DESIGN AND REALIZATION FOR RADAR CROSS SECTION REDUCTION OF PATCH ANTENNAS USING SHORTED STUBS METAMATERIAL ABSORBERS

Thesis submitted for the fulfillment of requirements for the degree of

DOCTOR OF PHILOSOPHY

in

Electronic Engineering

by

DHAWAN SINGH

UNIVERSITY OF
KWAZULU-NATAL

INYUVESI
YAKWAZULU-NATALI

HOWARD COLLEGE OF AGRICULTURE, ENGINEERING AND SCIENCE
UNIVERSITY OF KWAZULU-NATAL, DURBAN - 4041
SOUTH AFRICA

STUDENT NO.: 216075791

MARCH 2019

DESIGN AND REALIZATION FOR RADAR CROSS SECTION REDUCTION OF PATCH ANTENNAS USING SHORTED STUBS METAMATERIAL ABSORBERS

Student:

Er. Dhawan Singh

Supervisor:

Prof. (Dr.) Viranjay M. Srivastava

This thesis submitted in fulfillment of the requirements

for the degree of Doctor of Philosophy: Electronic Engineering

in

Howard College of Agriculture, Engineering & Science

University of KwaZulu-Natal, Durban

South Africa.

As the candidate's supervisor, I have approved this thesis for submission.

Signed…… Date 8 March 2019

Name: Prof. (Dr.) Viranjay M. Srivastava

DECLARATION 1 – PLAGIARISM

I, **DHAWAN SINGH** with Student Number **216075791** with the thesis entitled **"DESIGN AND REALIZATION FOR RADAR CROSS SECTION REDUCTION OF PATCH ANTENNAS USING SHORTED STUBS METAMATERIAL ABSORBERS"**
hereby solely declare that:

(i) The research reported in this thesis, except where otherwise indicated, is my original research work.

(ii) This thesis has not been submitted for any degree or examination at any other university.

(iii) This thesis does not contain other person's data, pictures, graphs or other information unless specifically acknowledged as being sourced from other persons.

(iv) This thesis does not contain other person's writing unless specifically acknowledged as being sourced from other researchers. Where other written sources have been quoted, then:

a. Their words have been re-written but the general information attributed to them has been referenced;

b. Where their exact words have been used, then their writing has been placed inside quotation marks and referenced.

(v) Where I have reproduced a publication of which I am an author, co-author or editor, I have indicated in detail which part of the publication was actually written by myself alone and have fully referenced such publications.

(vi) This thesis does not contain text, graphics or tables copied and pasted from the Internet, unless specifically acknowledged, and the source being detailed in the thesis and in the references sections.

DHAWAN SINGH 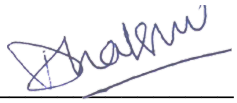 Date 8 March 2019

DECLARATION 2 - PUBLICATIONS

DETAILS OF CONTRIBUTION TO PUBLICATIONS that form part and/or include research presented in this thesis (include publications that have been submitted, *in the press* and published and give details of the contributions of each author to the experimental work and writing of each publication).

JOURNAL PUBLICATIONS

1. **Dhawan Singh and Viranjay M. Srivastava**, "Design Implementation of Concentric Loops with Stubs Metamaterial Absorber," *Wireless Personal Communications,* vol. 104, no. 1, pp 1-20, January 2019. **(Included in Chapter 3).**
2. **Dhawan Singh and Viranjay M. Srivastava**, "RCS Reduction of Patch Array using Shorted Stubs Metamaterial Absorber," *Journal of Communication (JOCM),* vol. 13, no. 12, pp. 702-711, December 2018. (**Included in Chapter 5**).
3. **Dhawan Singh, Aditi Thakur, and Viranjay M. Srivastava**, "Miniaturization and Gain Enhancement of Microstrip Patch Antenna with Defected Ground and EBG," *Journal of Communication (JOCM),* vol. 13, no. 12, pp. 730-736, December 2018. (**Included in Chapter 2**).
4. **Dhawan Singh and Viranjay M. Srivastava**, "A Comparative Analysis for Radar Cross Section of Patch Antenna using Shorted Stubs Metamaterial Absorber," *Journal of Engineering Science and Technology (JESTEC),* vol. 13, no. 11, pp. 3532-3546, November 2018. **(Included in Chapter 5).**
5. **Dhawan Singh and Viranjay M. Srivastava**, "An analysis of RCS for Dual-Band slotted patch antenna with a thin dielectric using Shorted Stubs Metamaterial Absorber," *AUE-International Journal of Electronics and Communication*, vol. 90, pp. 53-62, June 2018. **(Included in Chapter 6).**
6. **Dhawan Singh and Viranjay M. Srivastava**, "Low Radar Cross Section of Patch Antenna using Shorted Stubs Metamaterial Absorber," *International Journal of Microwave and Optical Technology (IJMOT),* vol. 13, no. 3, pp. 194-202, May 2018. **(Included in Chapter 5).**

7. **Dhawan Singh and Viranjay M. Srivastava**, "Dual Resonances Shorted Stub Circular Rings Metamaterial Absorber," *AUE-International Journal of Electronics and Communication*, vol. 83, pp. 58-66, January 2018. (**Included in Chapter 4**).

CONFERENCES PUBLICATIONS

8. **Dhawan Singh and Viranjay M. Srivastava**, "Polarization-Insensitive Cylindrical Shaped Frequency Selective Surface," *IEEE 10th international conference on Development in eSystem Engineering (DeSe-2017),* Paris, France, 14-16 June 2017, pp. 1-6. **(Included in Chapter 2).**

9. **Dhawan Singh and Viranjay M. Srivastava**, "3-D Cylindrical Shaped Frequency Selective Surface," *IEEE 4th International Conference on Advance Computing and Communication Systems (ICACCS-2017),* Coimbatore, India, 6-7 January 2017, pp. 1-6. **(Included in Chapter 2).**

10. **Dhawan Singh and Viranjay M. Srivastava**, "Triple Band Regular Decagon Shaped Metamaterial Absorber for X- Band Applications," *IEEE International Conference on Computer Communication and Informatics (ICCCI-2017),* Coimbatore, India, 5-7 January 2017, pp. 411-415. **(Included in Chapter 2).**

11. **Dhawan Singh and Viranjay M. Srivastava**, "Metamaterial Absorber Based on Concentric Rings with shorted stubs," *IEEE International Conference on Engineering and Technology (ICET-2016),* Coimbatore, India, 16-17 December 2016, pp. 159-163. **(Included in Chapter 3).**

PREFACE

The research work in this thesis was implemented by Dhawan Singh, under the supervision of Professor Viranjay M. Srivastava at the Discipline of Electrical, Electronic and Computer Engineering, Howard College, University of KwaZulu-Natal, Durban.

Some parts of this thesis have been published in the International Journal of Electronics and Communication. Some parts of this have been published in Wireless Personal Communications and International Journal of Microwave and Optical Technology. While some part of this thesis is published in the Journal of Communication and in the Journal of Engineering Science and Technology.

Some part of this thesis has been presented at Paris, France in the IEEE 10^{th} international conference on Development in eSystem Engineering and in the 4^{th} International Conference on Advance Computing and Communication Systems conference held at Coimbatore, India. Also, parts of this thesis gives augmentation published in the International Conference on Engineering and Technology held at Coimbatore, India. Last but not the least some part of it is presented at IEEE International Conference on Computer Communication and Informatics at Coimbatore, India.

ACKNOWLEDGMENTS

First and foremost, I am grateful to Almighty God, the most generous and merciful, who has created the mankind with knowledge, wisdom, and power. Who bestowed self-confidence, capability, and strength in me to bring this research work to completion and not letting me down anytime.

I render my thanks and special appreciation to my guide Dr. Viranjay M. Srivastava. He has been a very good mentor and collaborator since my research started at Howard College, UKZN back in the year 2016. As a mentor, he has provided me all liberty to explore on my own and provided time to time guidance and suggestions to recover when my steps faltered. As a collaborator, he has dedicated countless hours to discuss, criticize and explore new solutions together with me in many aspects of several research topics. It was a great pleasure to work with him.

I wish to extend my warm and sincere thanks to Mr. Lousber Greg, Senior Technician and in charge of Howard College Fabrication Laboratory for the constant help and knowledge contribution to ensure the success of the project. I would also like to thank Mr. Divesh Maharaj and Mr. Raj for the generous support throughout the years, and for helping me with my research work.

I am so lucky to have Aditi as my wife. She has been always a source of encouragement and supporting me in my journey towards completion. Your love and understanding encourage me to finish this work. I will hold you and cherish you forever. We are so blessed to have Aadit and Harshit as our wonderful kids. Finally, I devote my deep love and gratitude to my family. My merciful parents gave their unconditional love to me and exerted their best to support my study. I cannot end without thanking my two brothers, sister in laws, my mother in Law and brother in law, whose constant encouragement, love and support I relied on throughout my research in completing this project. May God bless each and every one of you.

Finally, I would like to thank all my colleagues and friends. We have had really wonderful time and great fun during past few years.

I would like to gratefully acknowledge the immense support of the College of Agriculture, Science and Engineering and also to the Centre of Excellence (CoE) in the School of Engineering for providing the available resources to undertake this research.

ABSTRACT

This thesis is devoted to analyzing of the Radar Cross Section (*RCS*) of rectangular patch antenna using Metamaterial Absorber (*MMA*) and the analysis of its reducing techniques. The addressed theme has a great complexity and it covers various areas that include designing and optimization of target geometrical model of rectangular patch antenna structures and making it compatible with respect to metamaterial geometry. Analyses have been made to optimize and validate the structure performances that include numerical methods for electromagnetic field computation, *MMA* behavior, characterization, extraction of parameters, antenna radiation performance analyses, simulation, fabrication, testing, and optimization with back validating the designs.

The *MMA* structure finds its applications in antenna designing for the reduction of *Monostatic* and *Bistatic RCS* in stealth platform for lower detectable objects. However, there is still more emphasis needed to devote for in-band frequency response for low *RCS* of the antenna. Therefore, making these assumptions, we have been proposing novel designs of single-band, dual-band, and triple-band *MMA* structures. These structures provide significant scattering characteristics and offering flexibility to the designer to control and tune the resonant frequency, based on the specific applications as compared to that of the other *MMAs* in the microwave regime of the Electromagnetic (EM) spectrum.

To explore the research scope, a three dimensional Frequency Selective Surface (FSS) structure has been analyzed and its simulation responses with respect to parametric analyses have been made. The research investigation further extended to Electronic Band Gap (EBG) Structure and Defected Ground Structure (DGS). A hybrid structure of patch antenna is proposed and designed for an inset feed rectangular microstrip patch antenna operating at 2.45 GHz in the Industrial, Scientific, and Medical (ISM) band. This hybrid structure claims the size reduction, bandwidth, and gains enhancement.

The main focus of this research work is limited to determine the potential and practical feasibility of *MMA's* to enhance the stealth performance of rectangular patch antennas. For this purpose, *Monostatic* and *Bistatic RCS* simulation and measurements are carried out in an anechoic chamber and practical methods for Radar Cross Section reduction are discussed and analyzed.

Table of Contents

List of Figures

List of Tables

List of Symbols

Absorbance	$A(\omega)$
Angle of incidence	θ
Angular Frequency	ω
Characteristic impedance	Z_0
Conductivity	σ
Decibel	dB
Decibel square meter	dBsm
Diameter	D,d
Dielectric constant of the substrate	ε_r
Efficiency	η
Free-space wavelength	λ_o
Gigahertz	GHz
Kilo	K
Propagation Constant	k
Millimeter	mm
Patch thickness	h
Permittivity of free space	ε_0
Permeability of free space	μ_0
Polarization sensitivity	ϕ
Reflectance	$R(\omega)$
Reflection coefficient	Γ/ S_{11}
Reflective Index	n
Relative Permeability	μ_r
Relative Permittivity	ε_r
Resistance	Ω
Speed of light 3x 10^{-8} m/s	c
loss tangent	$tan\ \delta$
Transmittance	$T(\omega)$
Transmission Coefficient	S_{21}
Wavelength	λ

List of Abbreviations

Artificial Magnetic Conductor	AMC
Cylindrical Shaped Frequency Selective Structure	CSFSS
Double Negative	DNG
Double Positive	DPS
Electric Field	E
Electronic Band-gap	EBG
Electromagnetic	EM
Epsilon-negative	ENG
Finite Difference Time Domain	FDTD
Frequency Selective Surface	FSS
Full-Width Half Maximum	FWHM
Left-handed metamaterials	LHM
Inductor, Capacitor	LC
Magnetic Field	M
Metamaterial Absorber	MMA
mu-negative	MNG
Negative-Index	NIM
Printed Circuit Boards	PCB
Perfect Electric Conductor	PEC
Radiation Absorbent Material	RAM
Radar Cross Section	RCS
Single Negative	SNG
Voltage Standing Wave Ratio	VSWR
Terahertz ($1x10^{12}$ Hz)	THz
Transverse Electric Field	TE
Transverse Electromagnetic	TEM
Transverse Magnetic Field	TM

Chapter-1

Introduction

In this section, background, introduction and the problem statement will be discussed. Moreover, the section also contains the objectives, scope of the study, motivation, research questions, contribution, and organization of this thesis.

1.1. Background

Metamaterials have attained tremendous attraction and increasing attention due to their unique Electromagnetic (EM) behavior. Great diversity or varieties of metamaterial have been proposed with different characteristics such as negative refractive index, huge chirality, magnetic conductivity, nonlinearity, tunable, and photonics [1-6]. So it has emerged as a new technology for both the scientific and the engineering community [7]. The various application of metamaterials are in the areas of superlens [8], metamaterial antennas [9], sensors technology [10], invisibility cloak [11], metamaterial absorber (MMA) [12] etc. In *MMA*, the effective capacitive and inductive response of the *MMA* structure could be altered by varying the geometry of the structure and hence set up the resonant frequency. The *MMA* unit cell behaves as a combination of lumped inductive and capacitive elements which get coupled to the incident electric and magnetic fields of *EM* radiation. The *MMA* unit cell structure is arranged in a periodic pattern and etched on the thin dielectric substrate layer [13]. The structure has the ability to modify the *EM* waves in such a way that the input impedance response of the *MMA* structure approximates to the free space impedance and hence, the condition of resonance achieved [14]. These properties play an imperative role in sophisticated antenna technology and offer better performance, capability, reliability, miniaturization, functions, and more flexibility.

The main objective of this thesis is to deeply analyze the characteristics of metamaterial absorber and to use that to improve the stealth performance of microwave antennas. Three types of *MMA* are proposed. (i) A passive tuned single-band circular ring shorted stubs metamaterial absorber. (ii) A passive tuned dual-band circular ring with shorted stubs *MMA.* These *MMA* structures operate and tuned throughout *X-band* to *Ku-band*. (iii) A triple band decagonal shaped *MMA* has been proposed operating in 8 GHz, 10 GHz and 12 GHz,

respectively in X-band. Different physical parameters are studied for these topologies with both numerical and measured results, and the working mechanisms behind these phenomena are explained by studying surface current distribution, the angle of incidence and polarization sensitivity. Some potential applications of these structures are also discussed. Then, various antennas based on metamaterials are designed, including single-band patch antenna, dual-band slotted-patch antenna, and an antenna array. All the antennas are designed using simulation, fabrication and then verified through experiments. Their performances have been reportedly improved compared with previously reported antennas.

1.2. Problem Statement

There are various constituents, which govern and disassemble the performance of the *MMA* structure as well as antenna radiations and Radar Cross Section (*RCS*) performance. The critical factors and problems that need to devote utmost attention and immediate considerations are:

(i) *Shape and parameters of elements*, the unit-cell geometry of *MMA* structure that is used in the microwave regime of the electromagnetic spectrum require to be very simple because of the fabrication cost associated with it. In the microwave regime of the electromagnetic spectrum, the development of novel geometrical shapes of *MMA* structures is an attractive area for researchers.

(ii) *Dielectric substrate material and thickness*, the dielectric substrate plays an imperative part in influencing the overall loss of the impinged *EM* wave and is decided by the thickness of the substrate. In order to make refractive index high, the thickness should be as small as possible and should not affect impedance matching condition.

(iii) *The oblique angle of incidence and polarization sensitivity*, one of the major prerequisite of *MMA* structure is its behavior and response for oblique angle of incidence (θ) and polarization sensitivity (ϕ), and it is required to be highly insensitive to incidence *EM* wave.

(iv) *Miniaturization*, the *MMA* structure thickness and dimensions should be reduced without degradation in absorbance performance, so as to meet low profile, miniaturization, and ease of fabrication requirements. Another problem with previously reported metamaterial antennas for *RCS* reduction is that low *RCS* achieved at the cost of the increased size of the substrate. Therefore, reducing and maintaining the metamaterial antenna structure periodicity without increasing its *RCS* offers a challenging task.

(v) *Compatibility between MMA and antenna structure*, it is one of the prime issues and it must be addressed properly so as to attain desired goals and objectives. The geometry of *MMA*

structure should be much simpler and well matched with the antenna. Otherwise, it would affect *MMA* characteristics as well as antenna radiation performances.

(vi) *Realization of low RCS*, the main task of this thesis is to design and realization of radar cross section reduction of patch antenna using shorted stubs metamaterial absorber. To accomplish this purpose, a passive tuned *MMA* with a single-band and dual-band need to be designed first. This would offer improved polarization and angular sensitivity, meanwhile, it must possess miniaturization and almost unity absorbance for different patch antennas configuration.

(vii) *To design and synthesize*, different patch antennas operating between *X-band* and *Ku-band* for a single-band and dual-band applications and evaluate their performance through simulations using the commercially available software.

(viii) *Comparison and back validate*, to compare simulation and measurements results at the end and back validate it again.

1.3. Objectives of the Research Work

In this research work, the issues that we have chosen to address includes thickness, morphology, absorbance, antenna radiation performances, and *RCS* reduction that comes with metamaterial antenna structures will be tackled. The objectives of these efforts are:

(i) To develop a single layer *MMA* absorber with almost unity absorbance: The single layer *MMA* has been designed, construct and test over its absorptivity for oblique angle of incidence and polarization of the electromagnetic waves. Aiming to improve the angular sensitivity, cross-polarization, reflection/transmission bandwidth, and band-separation.

(ii) To achieve miniaturized MMA structure: The *MMA* structure morphology namely thickness and dimensions should be reduced physically without absorbance performance degradation, so as to meet low profile, miniaturization, and ease of fabrication requirements. Moreover, one of the problems with previously reported *MMA* designs aiming towards *RCS* reduction achieved at the cost of the increased size of the substrate. Thus, this doesn't support miniaturization and turn out to be the unreliable and uneconomical solution. Therefore, we would try to achieve the *RCS* reduction without increasing the periodicity of the antenna structure.

(iii) Circular symmetry requirement: Another issue in designing a *MMA* structure is to analyze its response at an oblique angle of incidence and polarization sensitivity. To deal with these issues a circular ring-based topology is most commonly used because of better completeness and accuracy with regards to the angular stability, polarization sensitivity,

reflectance, transmittance coefficient, bandwidth, and band separation. Due to its regular arranged nature, the resonance frequency peak would occur in either of the two right angles or orthogonal coordinates.

(iv) To choose the substrate materials that can be strongly absorbed: Strong absorbance is still the main objective of absorbing material pursuit, and it is the most basic requirements of absorbing materials.

(v) To design a passive tuned *MMA* structure: A passive *MMA* unit cell structure is energized by the incident *EM* wave and the tuning is provided by the structural parametric variations. Unlike active tuned structure, it does not have special circuitry or extra biasing voltage that has been involved to achieve the desired results. This way, the passive *MMA* unit cell design offers simplicity, compactness, low cost, lightweight, and miniaturized of the absorber design.

(vi) To design a patch antenna for single-band and dual-band *MMA* applications, meanwhile maintain and preserve its radiation performances viz a viz gain, directivity with co polarization and cross polarization patterns, voltage standing wave ratio (*VSWR*), impedance (Z_{11}), and its radiation efficiency response should remain highly preserved.

(vii) Compatibility between antenna and *MMA* structure: It is imperative to preserve the absorbance and polarization characteristics of *MMA* along with antennas radiation performances. This is possible only if both structures are compatible to each other and loading of *MMA* into antenna won't affect their radiation performance.

(viii) To achieve better and improved *Monostatic* and *Bistatic RCS* reduction compared to previously proposed antenna's structure along with miniaturization. This is suitable for stealth platform.

(ix) To reduce mutual coupling between antennas: In case of antenna array as the gap between multiple antenna reduces, their performance starts degrading and that influence factors like gain and radiation efficiency because of the mutual coupling among them. By using *MMA* capability of suppressing surface waves propagation in a given frequency range, one can compensate for these losses.

1.4. Scope of the Research Work

Extensive analyses have been made for the behaviors of metamaterial structure. For this purpose, frequency selective surface (*FSS*), Electronic band-gap (*EBG*), Defected Ground Structure (*DGS*), and *MMA* structure have been discussed. The *FSS* is being widely used as *MMA* for stealth technology applications [15]. In which the surface attenuates signals for

out-of-band frequencies while in-band frequencies are absorbed. Over the past few decades, researchers have been devoting less attention to the three-dimensional *FSS* structure [16]. They carried out their researcher works in one or two-dimensional *FSS* metallic structure.

Keeping this in mind, we have designed a novel three-dimensional *FSS* structure, which is interesting, challenging and also offer excellent space utilization than its counterpart two-dimensional structure. With the utilization of three-dimensional space, the unit cell size of the *FSS* can be further reduced. A novel design of three-dimensional Cylindrical Shaped Frequency Selective Surface (*CSFSS*) based on a single circular ring structure has been proposed and its parametric analyses, variation for oblique angle of incidence and polarization sensitivity have been made.

Contrary to this *DGS* has been widely used for different applications such as radiation properties enhancement [17], bandwidth [18], mutual coupling reduction in antenna arrays [19] and antenna size reduction [20]. The *DG* plane is actualized by engraving off a shape in the metallic ground layer. Depending on the morphology of the defective shape structure, the impedance and surface current distribution get perturbed and this further modifies the associated capacitance and the inductance. Thus, results in assured propagation and excitation of the *EM* waves through the dielectric substrate.

Similarly, *EBG* structures are also widely used because of its unique properties and *EM* features such as electromagnetic band-gap and in-phase reflection to heighten antenna performance [21-24]. Making these considerations in this research work, we have designed a traditional microstrip patch antenna operating at 2.45 GHz resonant frequency. Then this antenna is modified by the defected ground structure. Once again antenna structure is altered and loaded with *EBG* structure. The *EBG* structure is designed and optimized such that resonance peak of antenna lies within its forbidden band-gap so that the surface wave excited by this patch antenna could be suppressed and prevent propagation. This improves the overall performance and functionality of the proposed antenna. Radiation characteristics such as S-parameters, directivity, gain, efficiency, bandwidth, *VSWR* and Z_{11} of microstrip antenna have been also analyzed for this hybrid structure.

However, this thesis work is mainly focusing on *MMA* structure and full devotion, dedication, and attention are being paid to metamaterial antennas and its applications to *RCS* reduction. For this purpose, a single- band, dual-band, and triple-band *MMA* structure have been studied and analyzed. A single-band patch antenna, dual-band slotted patch antenna, and

2 × 2 patch antenna arrays have been designed. These are being modified to metamaterial antennas and for its application to *RCS* reduction, meanwhile preserving *MMA* characteristics and antenna radiation performances.

1.5. Motivation

In stealth technology, it is very important to decrease the *RCS* of the target. An Antenna plays a crucial role and important contributor to *RCS* of the defense targets. Hence, the target is easy to capture on the basic radar system. So the antenna cannot be placed in stealth platform. Although, the conventional techniques for radar absorption such as shaping and Radar Absorbing Material/ Radar Absorbing Structure (*RAM/ RAS*) could not be implemented on the patch antenna because it might degrade the antenna performance.

With advancements in radar technology, the targets are easily identified and detectable, therefore it is primarily important to reduce its *RCS*. Thus, low *RCS* antenna is of prime concern and equal importance. The *RCS* of an antenna is all because of these two factors: Structural Mode *RCS* and Antenna Mode *RCS*. As we cannot change the antenna structure parameters since it influences the frequency response behavior. However, it has been found that when the antenna surrounded by *MMA* structure, it immensely reduces the *RCS* effect on the system without compromising with the performance of the antenna. Thus, one can minimize the structural mode *RCS* as low as possible and hence emerge as a new design technique.

As an application of *MMA* aiming for *RCS* reduction of the antenna, a simple patch antenna has been chosen first for this thesis work. Patch antennas are used to a great extent today owing to its advantages such as simple design geometry, linearly polarized, conformability to planar and non-planar structures, cost-effective, ease of implementation and compatible with the circuit board technology. Therefore, various of research is focusing on *RCS* reduction of patch antenna structure. One of the problems with previous *MMA* designs is *RCS* reduction achieved at the cost of the increased size of the substrate.

Thus, this doesn't support miniaturization and turn out to be the unreliable and uneconomical solution. So, we have tried to achieve the *RCS* reduction without increasing the periodicity of antenna unit cell structure. Again, it has been found that when the gap between multiple antennas reduces, their performance starts degrading and that influence factors like gain and radiation efficiency because of the mutual coupling among them. By using *MMA*

capability of suppressing surface waves propagation in a given frequency range, one can compensate for these losses.

Another objective of this thesis project is to design, construct and test a single-band, dual-band, and triple-band meta-material absorbers operating at *X-band* and *Ku-band*. This should offer better absorptivity, polarization insensitivity, miniaturized and ultra-thickens. During literature review, the authors have investigated that for radar and satellite applications in *Ku-band,* reduced-size planar patch antennas have been required to replace the huge-sized dish antenna.

It has been found that the *RCS* of dish antenna with an approximate size of 1 meter in 12 GHz is large enough, comparable to flat plate area and equivalent to antenna capture area. So an operational dish antenna would provide a very stable, nonfluctuating *RCS* and thus vulnerable to attack. Therefore, it is worthwhile and imperative to reduce the size of the antenna as well as make it less severe to incoming radar. Various researchers have been made to reduce the *RCS* of a planar patch antenna in *S, C* and *X-band.* However, little attention has been given to *Ku-band*, which is reserved for fixed and direct broadcast satellite communication.

An antenna designed at *Ku-band* is compact, cost-effective and offer better reliability. Whereas the conventional satellite antenna operating at *S, C and X-band* should require large dimension as the wavelength increases. If the antenna shall be able to transmit and receive, it should be able to operate on downlink frequencies according to *ITU* standard band (11.7 to 12.2 GHz), and for uplink frequency (14 to 14.5 GHz). So it is required to design a dual-band metamaterial antenna that could operate within these bands. In order to achieve the most effective metamaterial antenna design in this frequency range, a proper referenced design would be chosen first and then a series of optimization and tuning would be done based on it to obtain the proposed model. Finally, the simulated and experimental analysis for *Monostatic* and *Bistatic RCS* of determined metamaterial proposed antenna would be given.

1.6. Research Questions

This section contains and describes the list of questions with their answers that were posed and investigated during this research work.

Q1: What is metamaterial?

Answer: Metamaterials are artificial materials which can be created by various nanofabrication tools or engineering methods. Meta means beyond, which signify that it is a virtual material

and is made up of sub-wavelength meta-atoms of metals and dielectrics. The electric and magnetic permeability of metamaterial can be controlled, which rarely exists in natural materials. So it has emerged as a new technology for both the scientific and the engineering community.

Q2: Why circular ring symmetry has been chosen in this design problem?

Answer: Circular symmetry has been found highly symmetrical along all axis of rotation and found highly insensitive to the angle of incidence and polarization.

Q3: Why does passive tuned structure preferred over active tuned *MMA* structure?

Answer: The *MMA* unit cell can be designed as active or passive metamaterial structure. One trend is to implement a metamaterial absorber tuning circuit so that the frequency characteristics could be varied. *PIN* diodes, varactor diode, and voltage controlled active diodes are commonly used to switch on or off the top layer of *MMA*, result in the inductive or capacitive behavior of the *MMA* unit cell structure. Although these *MMAs* offer flexibility and dynamic tuning in design, their feasibility and implementation are restricted because of the requirement of various active components along with separate bias voltage for each active components.

That, in turn, brings complexity in design and do raise issues like miniaturization, complexity, economic cost, and fabrication of the design. On the other hand, the passive *MMA* unit cell structure is excited by the incident plane wave and the tuning is provided by the structural parametric variations of the unit cell only. Since, there is no special circuitry or extra biasing voltage that has been involved to achieve the desired results. This way, the passive *MMA* unit cell design offers simplicity, compactness, low cost, lightweight, and miniaturized of the absorber design.

Q4: Why did *FR-4* substrate and copper patch choose over other available material?

Answer: *FR-4* and copper material are readily available, most popular and cheaper, so they have been chosen over other material.

Q5: How does the condition of resonance achieve in Metamaterial Absorber?

Answer: The condition of resonance achieves when the intrinsic impedance of the unit cell structure approximates with the free space impedance and comes out to unity.

Q6: What are the advantages of metamaterial patch antenna over traditional patch antenna?

Answer: A metamaterial patch antenna is currently in trends because of its various properties that include low profile, miniaturized, simple design, improved radiation performances, offers low *RCS* capability and, compatible with circuit board technology. Thus, it offers tremendous applications in the areas of satellite communication, radio broadcasting, antenna radomes, electromagnetic shielding, improving the purity of the received signal, act as a band-pass or band-stop filter, artificial magnetic conductor (*AMC*) and wireless communication.

Q7: Why does *MMA* prefer over the rest of structure for *RCS* reduction?

Answer: Many techniques have been proposed for the *RCS* reduction of the rectangular patch antenna such as *RAM/RAS*, *EBG*, *FSS*, and *AMC* structure. However, it has been found that these structures behave efficiently and quite effectively for out-of-band *RCS* reduction. While for in-band *RCS* reduction of the patch antenna, *MMA* is preferred owing to its almost unity absorbance, miniaturization and insensitive to oblique angle of incidence, and polarization mechanism.

Q8: What are the advantages of dual-band Antenna over simple antenna?

Answer: A dual-band antenna is used in applications where transmission and reception should be done using the same antenna and thus provides an alternative to broadband antennas. To brace the increasing requirement of a sophisticated wireless communication system, numerous dual-band patch antennas have been proposed, those are competent of desegregation for more than one communication system into a single scheme.

Q9: Why has dual-band slotted patch antenna been preferred over other dual-band patch antenna structures in this thesis work?

Answer: It has been observed that dual-band behavior in rectangular patch antenna can be obtained by modifying the natural modes of a rectangular radiating patch through coupled-slot technique with suitable feed placement. This coupled-slot technique claimed to reduce the radiating element size up to about 32%. Hence, this design achieves miniaturization that serves the basis of this research work and helps us to accomplish primarily goal.

Q10: Why have patch antennas been considered in this thesis work?

Answer: Patch antennas are popularly used owing to its attractiveness in term simplicity, low profile, cost-effective, simple fabrication, linearly polarized, conformal and adaptability with other components of wireless communication. However, it comes at the cost of small bandwidth, lower gain, and increased the cross-polarization effect.

Q11: What are the limitations of proposed *MMA* structures?

Answer: This proposed *MMA* structure is an ultra-thin, almost unity absorbance magnitude, polarization insensitive and capable of being used with printed circuit board (PCB) design technology. Because of its simplicity, single layered and the commonly available *FR-4* substrate, it is low profile and cost-effective structure. However, it has been found that the high absorbance of *MMA* structure actualized at the expense of narrow bandwidth, which is proportional to the thickness of the structure and dielectric constant of the material used.

Therefore, large bandwidth could be obtained by either increasing the *MMA* structure thickness or replace the structure with multilayer *MMA* structure or alternatively choose a material with low dielectric constant. This would result in loss of its claim for ultra-thickness and also increase complexity in structural designing. Moreover, this will effect on the *MMA* magnitude. So, it is a compromise between absorbance, thickness, and bandwidth.

1.7. Contribution of the Thesis

The Radar Cross Section reduction is the latest topic of research in today's technology world. When technology becomes more sophisticated and advances there is a need to provide the stealth capability so that it is difficult to find and attack. It has been found then an antenna is one of the main contributors for *RCS* and the older techniques like *RAM* /*RAS* cannot be implemented because it might degrade the antenna performance. It has been found that if the antenna is loaded with *MMA*, it effectively reduces the *RCS* of the antenna along with preserving antenna's radiation performances.

In this context, we have attempted to enhance the stealth capability of the patch antennas for single-band, dual-band and for a 2×2 antenna arrays with implementing and loading of novel shorted stubs with rectangular bars *MMA* structures at the top of the substrate. These designs find its applications in military and stealth platform for satellite and wireless communication.

1.8. Organization of the Thesis

Chapter 1 presents some theoretical aspects related to metamaterial structures, a patch antenna, and radar cross-section. These aspects have been described with respect to thesis objectives, the scope of study and motivation of this research work. Questions have been also addressed that raised during this research work. The contribution of the thesis and organization of the research work is discussed at the end.

Chapter 2 covers the literature review of the metamaterials. Extensive backgrounds of the previously proposed metamaterials structure have been given. Then *FSS*, *EBG*, and *DGS* structure have been studied and analyzed to inspect their performance behavior. For this purpose, a three dimensional cylindrical shaped structure and its parametric performances with respect to the height, radius, and polarization sensitivity for Transfer Electric (*TE*) and Transfer Magnetic (*TM*) modes for oblique angle of incidence have been analyzed. Subsequently, an inset feed rectangular microstrip patch antenna operating at 2.45 GHz in the Industrial, Scientific, and Medical (*ISM*) band has been modified with *DGS* plane and its miniaturization and radiation performances have been evaluated. This design is then modified and loaded with mushroom-type *EBG* structure on the top of dielectric *FR-4* substrates. The overall performance and functionality of the patch antenna with respect to S-parameters, directivity, gain, efficiency, bandwidth, *VSWR* and Z_{11} of have been performed and compared. Furthermore, a triple band regular decagon shaped *MMA* for X-Band applications has been designed and its behavior with respect to simulated response, normalized input impedance and surface current distribution has been specified to understand the absorption mechanism.

Chapter 3 explains a passive tuned single-band *MMA* structure that is consisted of two concentric loops separated by stubs and modified with rectangular bars operating between *Ku-band* and *X-band*. Its parametric sensitive response with respect to shorted stubs length, rectangular bars length, thickens of the *FR-4* substrate have been determined. The *MMA* structure variations with regards to the oblique angle of incidence and polarization sensitivity for *TE* and *TM* modes of *EM* wave have been depicted. To validate the results, surface current distribution has been given. In the end, the simulated results are compared with the measured results.

Chapter 4 concerns with the design characterization of tunable dual-band shorted stubs circular rings metamaterial absorber structure designed at 17 GHz and 18 GHz. Parametric analyses have been performed to study the behaviour of circular ring radius, shorted stubs

length and rectangular bar length with respect to the resonance frequency. The simulation and the measurements of *MMA* are performed under the assumption of the normal angle of incidence. However, the effect of polarization sensitivity responses on the *MMA* structure are also considered for both *TE* and *TM* modes. Analyses for surface current distribution, normalized input impedance response and the comparison of the results with the previously proposed structure have been made.

Chapter 5 presents the comparative analysis for in-band *RCS* reduction of 10 GHz single-band patch antenna using shorted stubs *MMA.* Three different *MMA* loaded rectangular patch antennas design are simulated, analyzed and tested in this section. Their outcomes are compared with the conventional patch antenna design without loading *MMA* structure. The antennas characteristics and radiation performances have been evaluated for Scattering Coefficient (S_{11}), Z_{11}, *VSWR*, radiation efficiency, gain, and directivity. The *Monostatic* and *Bistatic RCS* behavior of the proposed antennas have been observed for horizontal and vertical polarization.

Subsequently, a novel design approach for the out-of-band radar cross section reduction of a conventional 2×2 patch antenna array operating in 7.54 GHz using shorted stubs metamaterial absorber (*MMA*) operating at 10 GHz has been proposed. Its scattering parameters characteristics, polarization sensitivity along with antenna radiation performances have been analyzed. In the end, its *Monostatic* and *Bistatic RCS* response has been observed for the horizontal as well for vertical polarization.

Chapter 6 focusses on analysis of *RCS* for dual-band slotted patch antenna with a thin dielectric using shorted stubs *MMA.* A dual-band slotted patch antenna has been proposed for *Ku-band* applications. A rectangular patch with a pair of bent slots at each side of the center has been designed and resonant at 11.95 GHz and 14.25 GHz with respect to *ITU* standard. A dual resonance ultrathin *MMA* based on circular rings and shorted stubs operating at same frequency bands have been designed. Its behavior for polarization sensitivity and oblique angle of incidence has been also observed. Antenna radiation performances with co polarization and cross polarization patterns have been studied. The *Monostatic* and *Bistatic RCS* of the proposed design is analyzed for the horizontal as well for vertical polarization.

Finally, we concluded the thesis with the presentation of the conclusions and recommend the future scope of the work in **Chapter 7**. Analyses in this dissertation are compared with previously published results and with simulated results using three dimensional

electromagnetic tools. Validation of applications with antennas is carried by manufacturing prototypes and comparing measured performance with analysis and three dimensional electromagnetic simulations.

Chapter-2

Study and Analyses of Metamaterials for FSS, EBG, and MMA Structures

In order to achieve the objectives and goals those have stated in the introduction section, we are studying and analyzing the behavior and properties of metamaterial structure. Knowledge of the previous studies on the metamaterial structure design is much essential and desired before any improvement and progress could be made, so this is given in the literature review section. We shall also study the physics of the *FSS, EBG, DGS,* and *MMA*. For this purpose, a 3-D *CSFSS* structure has been analyzed and its parametric analyses are made to achieve stop-band and pass-band behavior.

Its frequency response for the oblique angle of incidence and polarization sensitivities has been considered extensively. After this, attention has been paid to *EBG* structure and a hybrid microstrip antenna consisted of *EBG* and *DGS* has been proposed. Its behaviors with respect to antenna radiation performances are analyzed in the end. Furthermore, a triple band regular decagon shaped *MMA* for an *X-Band* application has been designed. Its behavior with respect to simulated response, normalized input impedance, and surface current distribution has been specified to understand the absorption mechanism. This would set the background for the coming chapters.

2.1. Literature Review

The recent technological advancement and the latest research in metamaterials have pioneered the door to tremendous innovative antenna applications. A novel metamaterial structure efficiently manipulates the reflection and transmission of the impinging *EM* wave. Metamaterials are artificial materials which can be created by various nano-fabrication tools or engineering methods. Meta means beyond, which signify that it is a virtual material and these are usually arranged in repeating patterns of meta-atoms of metals and dielectrics, at scales of subwavelength.

The electric and magnetic permeability of metamaterial can be controlled, which rarely exists in natural materials. So, it has emerged as a new technology for both the scientific and the engineering community [25]. The geometry, size, shape, and orientation of metamaterial

give them their unique properties that are capable of manipulating and influencing *EM* wave. The size and the period of unit cells of most metamaterials are much smaller than operating wavelength. This leads to several potential and diverse applications in the areas of superlens [26], metamaterial for high-gain antennas, [27], sensors detection and infrastructure monitoring [28], radomes [29], invisibility cloak [30], optical filters [31], as metamaterial absorber [32] and benefits go beyond a shadow of a doubt that is impossible with conventional designs.

Metamaterials can be characterized by an effective complex permittivity

$$\varepsilon_{eff}(\omega) = \varepsilon'_{eff}(\omega) + j\varepsilon''_{eff}(\omega) \tag{2.1}$$

and permeability

$$\mu_{eff}(\omega) = \mu'_{eff}(\omega) + j\mu''_{eff}(\omega) \tag{2.2}$$

By carefully selecting metamaterial structure parameters such as geometry, size, shape, orientation and alignment $\varepsilon_{eff}(\omega)$ and $\mu_{eff}(\omega)$ could be adjusted. It is realizable to develop and create metamaterials which demonstrate properties such as negative refraction index and backward wave propagation i.e. $n(\omega) < 0$.

Explorations of metamaterial structure for manipulating *EM* wave initiated at the end of the 19th century. However, a first material exhibiting negative-index properties were proposed theoretically by Victor Veselago in 1967 [33]. He coined the term “left-handed material” for the metamaterial because of the double negative material, as it simultaneously produces negative index values for permittivity and permeability. Metals, semiconductors, and ionized gases have negative permittivity, and ferrite materials possess negative permeability properties within the range of a certain frequency.

However, no known material with both negative permittivity and permeability were identified due to lack of materials resources and insufficient computation technology. Finally, this has only been experimentally demonstrated in 1999 by Pendry et al [34, 35]. He invented a virtual way to synthesis left-handed metamaterials (*LHM*). Afterward, the majority of metamaterial structures demonstrating unlike *EM* properties such as epsilon-negative (*ENG*), mu-negative (*MNG*), double positive (*DPS*), and double negative (*DNG*) have been proposed [36-40].

2.1.1. Classification of Metamaterials

Most dielectric materials available in existence have positive values of permittivity and permeability so they are named as *DPS* (double positive) materials. *DPS* materials are also called right-handed material as *EM* radiation can propagate through these medium and the vectors *E*, *H*, and *k* form a right-handed symmetry and shown in Figure 2.1.

Metamaterials with only one of ε or μ negative are named as *SNG* (single negative) materials. They are categorized into two types based on the negative effective parameter. They are named as *ENG* (epsilon-negative) and *MNG* (mu-negative). In *ENG*-material permeability is greater than zero and permittivity are less than zero. One common example of such medium is Plasma. While in *MNG*-materials, permittivity is greater than zero and permeability is less than zero. Some antiferromagnetic and ferromagnetic materials possess this behavior.

Over the last two decades, the research and experiments have been carrying with materials with simultaneously negative values of ε and μ materials. But it does not exist in nature, so they have produced artificially. Such artificial materials are named double negative metamaterials (*DNG*). The *DNG* materials are also called as left-handed materials as *EM* radiation can propagate through these medium and the vectors *E*, *H*, and *k* form a left-handed

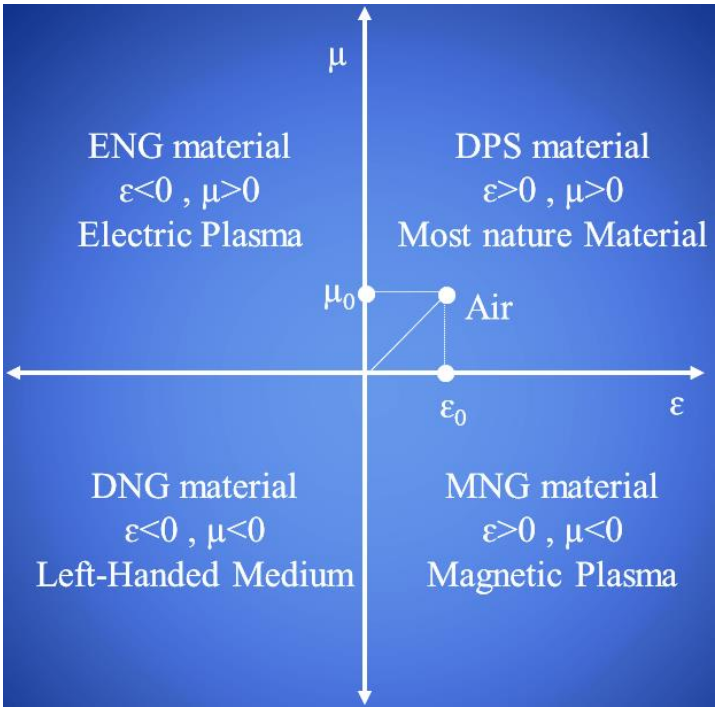

Figure 2.1 Classification of metamaterials.

symmetry. Both *DPS* and *DNG* are impedance matching materials and the phenomenon of backward wave propagation is exhibited.

For many applications such as metamaterial absorbers, the important parameter is the surface impedance which is not easily available in the required frequency range. For such applications, 2-D metamaterials, also called metasurfaces are used to obtain the required surface impedances.

2.1.2. Types of Metamaterials

As an interdisciplinary area, metamaterial structures can be categorized into distinct classes based on different standards. From the point of view resonant frequency, they can be classified as *EM* metamaterials, chiral metamaterial, nonlinear metamaterial, *FSS* metamaterial, tunable metamaterial, terahertz metamaterials, and photonic metamaterials as shown in Figure 2.2. From a spatial arrangement point of view, they are also classified as 1-D metamaterials, 2-D metamaterials, and 3-D metamaterials based on their geometry.

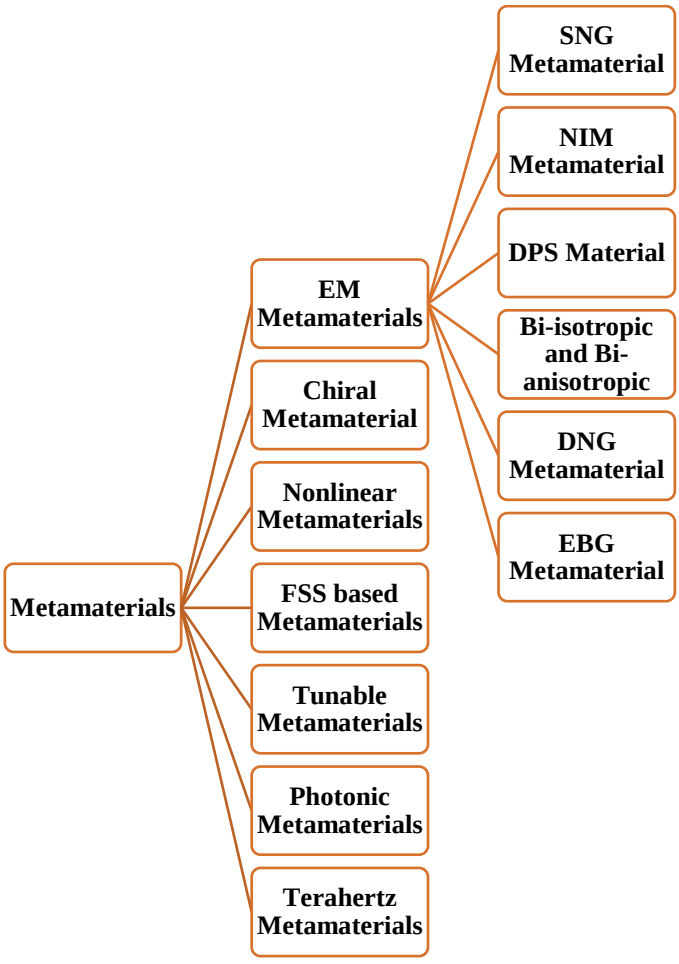

Figure 2.2 Types of metamaterials.

From a material point of view, they can be categorized as metallic and dielectric metamaterials. The electromagnetic metamaterial is further classified into *SNG* metamaterial, negative-index (*NIM*) metamaterial, *DPS* material, Bi-isotropic and Bianisotropic, *DNG* metamaterial, and *EBG* metamaterial. In this work, we will have been designing and analyzing *FSS* metamaterial with stressing on 3-D *CSFSS* and *EM* metamaterial with focusing on *EBG* and *MMA* metamaterial in the microwave frequency range.

2.2. Frequency Selective Surface (FSS)

A frequency selective surface is a periodic metallic structure etched on a dielectric substrate. It might be a patch, aperture, split-ring or hybrid elements type shape. Each shape of the *FSS* structure element has its own merits and applications. The *FSS* structure can efficiently control the transmission and reflection of the incident *EM* depending on its physical and geometrical construction of the surface and therefore may exhibit a low-pass, high-pass, band-pass and band-stop filter characteristics.

In antenna based systems, it is required to use some kind of filters, which possess the bandpass and bandstop filtering characteristics. This behavior is well governed by *FSS* and also it has been used in a variety of the applications including antenna radomes [29], filters [41], Cassegrainian antenna [42], reflectors to provide dual or multiband frequency operation [43], polarizer [44], artificial magnetic conductor [45, 46] and in the satellite communication to control the transmission and reflection. Recently, the *FSS* is being widely used as metamaterial absorbers (*MMA*) in radar absorbing materials for stealth technology applications [47]. In which the surface attenuates out-of-band frequencies while in-band frequencies are absorbed.

According to *Babinet's principal*, the patch type structure acts as a bandstop filter and the slot/ aperture kind structure behaves as a bandpass filter [31]. It is found that same behavior could be achieved if we convert the two-dimensional *FSS* structure into a three-dimensional *FSS* structure which offers design flexibility along with various new challenges [48-51]. For low-frequency applications such as radome antenna, one of the design challenges with two-dimensional *FSS* unit cell is miniaturization. Generally, by increasing the size of *FSS* unit cell, one can drift the reflection and transmission scattering parameters towards the lower side of the frequency band and the resultant dimensions of *FSS* unit cell will become large. Thus, it will become difficult to place large sized *FSS* unit cells within curved surfaces and also becomes impractical to realize large size circuit boards. Thus put a limitation on space and add up additional cost also.

One of the issues in designing a two-dimensional tunable *FSS* metallic structure exists because these *FSS* unit cells consist of active lumped components like *PIN* diode, a varactor diode and voltage-controlled diodes [52-54]. However, this tunable *FSS* required a large number of active lumped components. That raises issues like miniaturization, fabrication complexity, complication is to analyze its response at a different angle of incidence and must be highly polarization insensitive response. However, the major issues with this 3-D *FSS* are their complicated topologies. Most of them require extra assembly process after fabrication, which would increase undesirable errors and uncertainties. So, increasing the 3-D *FSS* structure further would cause the increase in length/periodicity of unit cell structure and hence that will increase the size of the unit cell. One of the solutions to address these problems are to reduce the size of 3-D *FSS* unit cell structure, which will solve two problems simultaneously:

(i) A miniaturized unit cell structure, and
(ii) Highly polarization insensitive to oblique angle of incidence.

To deal with these issues a circular ring-based topology is most commonly preferred because of its better completeness and accuracy with regards to the angular stability, polarization sensitivity, bandwidth and band separation [55]. Moreover, the design should be simple, symmetrical along all axis and circular symmetrical in nature. Since it has been observed that the circular symmetrical *FSS* structures are more polarization insensitive then rest of the unit cell structure because of its rotational symmetry. The results described here have been published in [56].

So, the design procedure consists of four stages:

(i) A flat two-dimensional circular ring *FSS* metallic structure has been designed.
(ii) This circular ring *FSS* structure is mapped into a desired 3-D *CSFSS*, aiming for low-frequency application covered in next section in detail.
(iii) Passband and stopband behavior of 3-D *CSFSS* are being analyzed.
(iv) The angular stability and polarization sensitivity of a 3-D *CSFSS* have been considered.

2.2.1. 3-D Cylindrical Shaped Frequency Selective Surface (CSFSS)

Over the past few decades, less attention has been paid to the 3-D *FSS* structure [57, 58]. A novel design of a 3-D *FSS* is interesting, challenging and also offer excellent space utilization than its counterpart two-dimensional structure. The research for new geometrical shapes of *FSS*

structures, which higher selective and close band frequency response including significant improvement in terms of the angular and polarization stability.

Recently, 3-D *FSS* structure shows more flexibility in design and performance to control the frequency response compared to its 2-D *FSS* analogues without using active component [59, 60]. Few kinds of literature have analyzed the polarization sensitivity response of 3-D *FSS* [61-62], in which a lesser extent oblique angle of incidence has been emphasized or polarization sensitivity has been achieved at the cost of increasing unit cell size. This would extend the structure size approximates to half of the wavelength, where wavelength corresponds to the center resonant frequency.

Even though, the increase in unit cell size would result in degradation and reduction of the polarization sensitivity frequency response for oblique angle of incidence [56]. In this framework, the band-pass, band-stop, angular stability and polarization sensitivity of a cylindrical shaped frequency selective structure (*CSFSS*) have been considered, which is required to design *FSS* structure. These issues are necessary to fully analyze the *CSFSS* structure design. This section gives the argumentation published in [63].

2.2.2. Design of 3-D CSFSS

The scattering parameters of the *CSFSS* structure have been studied. This *CSFSS* offers greater flexibility and tuned to the particular resonant frequency by varying the height of the cylinder. Therefore, in order to attain the particular frequency responses of *CSFSS* structure, the geometrical parameters like length, width, thickness of the substrate (*t*), radius of the cylinder (*Rin* , *Rout*), width of the cylinder (*w*) and height of cylinder (*h*) of the *FSS* structure need to be well optimized.

The frequency response of *CSFSS* is also analyzed at a different angle of incidence of EM wave. A full-width half maximum (*FWHM*) bandwidth analysis of *CSFSS* is also observed. The purpose of this work is to design a 3-D *CSFSS* that could be tuned between pass-band and stop-band by varying the height of the cylinder and offer lower resonant frequency than its counterpart two dimensional (2-D) circular *FSS* flat structure.

By extending the 2-D ring resonator to 3-D space, the resonant frequency could be minimized without increasing the size of the ring. Thus the dimension of a unit cell of the proposed *FSS* is reduced, miniaturized and more unit cells can be placed within a limited space compared to its previous 2-D flat surface.

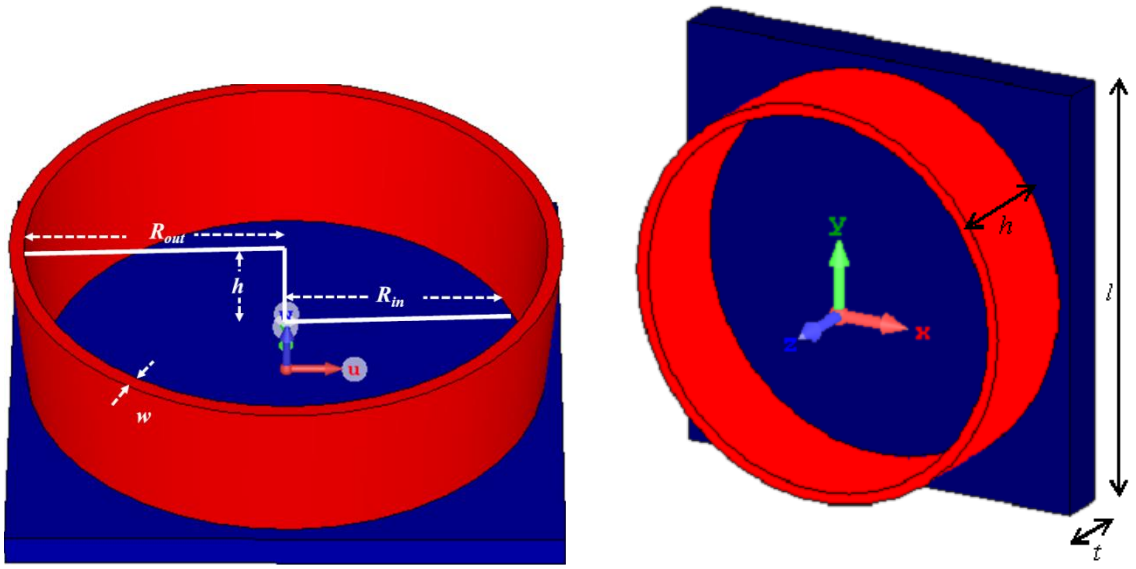

(a) (b)

Figure 2.3 The geometry of Cylindrical Shaped Frequency Selective Surface (CSFSS) with their dimensions. (a) front view and (b) perspective view.

A 3-D *CSFSS* consists of most popular and low-cost copper patch with a conductivity of $5.8x10^7$ *s/m* printed on the top of the FR-4 dielectric substrate (ε_r) with the relative permittivity and loss tangent (*tan δ)* values are 4.3 and 0.025, respectively, by the mean of standard photolithographic technique. The top layout view for a single unit cell of a circular ring is depicted in Figure 2.3(a).

This ring is then modified by raising its height and thus converted it into a cylindrical structure as shown in Figure 2.3(b). The dimensions of the proposed structure are depicted in Table 2.1. All the structural parameters are adjusted and optimized to obtain sharp resonance peaks at the desired resonant frequency of 6.09 GHz.

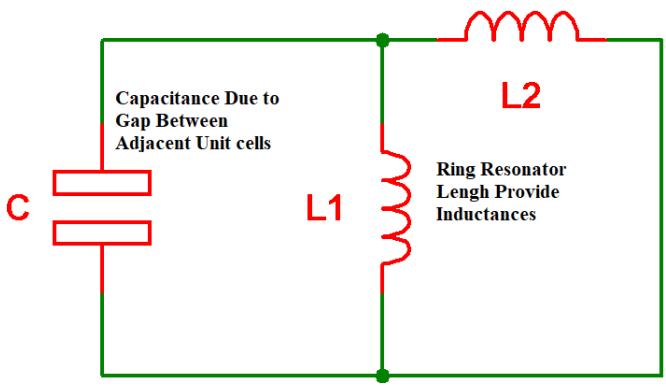

Figure 2.4 Equivalent circuit model of CSFSS.

Table 2.1 The dimensions of a 3-D CSFSS unit cell.

Description	Dimensions (mm)	Parameters
Length/ Width of Substrate	18	l
Thickness of Substrate	0.1	t
Height of Cylinder	5	h
The inner radius of Cylinder	8	R_{in}
The outer radius of Cylinder	8.5	R_{out}
Width of cylinder	0.5	w

Since the accurate values of equivalent circuit model are difficult to determine therefore, we limit our study to behavioral analysis and response of equivalent circuit model. A *CSFSS* structure can be modeled as a parallel *LC* tuned circuit, where the ring resonator length provides the inductance and the gap between two adjacent neighboring unit cells provides the capacitance. At a normal angle of incidence ($\theta = 0^0$), as the three-dimensional cylinder introduced, it adds an inductive reactance in series with the parallel tuned circuit, caused to modify the condition of resonance. As

$$\left(X_{L1} \,||\, X_c\right) + X_{L2} \tag{2.3}$$

Thus, the modified tuned resonant circuit frequency becomes:

$$\omega_r{}^2 = \frac{1}{L_1 C} + L_2 \omega_r$$

Where $L_2\omega_r$ is the series reactance introduced in the circuit because of the height of the cylinder as depicted above equivalent circuit model of *CSFSS* in Figure 2.4. Thus:

$$\omega_r{}^2 - L_2\omega_r - \frac{1}{L_1 C} = 0$$

So the modified resonant frequency is given by:

$$\omega_r = \frac{L_2}{2} \pm \sqrt{\frac{L_2{}^2}{4} + \frac{1}{L_1 C}} \tag{2.4}$$

From the Equation (2.4), it is cleared that $\omega_r \propto L_2$ .When $X_{L2} \approx 0$ and replacing $L_1 = L$. This is the condition of resonance for a series or parallel resonator:

$$\omega_r = \frac{1}{\sqrt{LC}} \tag{2.5}$$

And the impedance of this circuit is given by:

$$Z(\omega) = -j\left(\frac{1}{C}\right)\left(\frac{\omega}{\omega^2 - \omega_r{}^2}\right) \tag{2.6}$$

As

$$\lim_{\omega \to \pm\omega_r} Z(\omega) = \infty$$

So the parallel *LC* resonator circuit behaves as a band stop filter when the impedance approaches infinity. Also, the resonant frequency can be tuned by varying capacitance or inductance. As:

$$C = \varepsilon \frac{A}{d} \tag{2.7}$$

Where ε is the absolute permittivity, *A* is the area of the loop and *d* is the distance between two conducting plates and the inductance varies because of the well-known relation as:

$$L = \frac{N^2 \mu A}{h} \tag{2.8}$$

Since *N* (number of turns) is *1* for a single turn, *h* is the length of the cylinder, μ is the absolute permeability and *A* is the area of the loop and found to be

$$A = \pi(R_{out}{}^2 - R_{in}{}^2) \tag{2.9}$$

2.2.3. Stop-band Behavior of 3-D CSFSS

For the simulation analysis, a frequency domain solver is employed. By applying periodic boundary conditions and applying perfect electric conductor to the boundary surface perpendicular to the incident electrical field (*E*). While applying the perfect magnetic conductor surfaces to the boundary surface normal to the incident magnetic field (*H*). The surfaces perpendicular to propagation vector (*k*) are configured as open ports. The incident input port is Z_{max} and the output port is Z_{min}, where the reflection and transmission would take place. The fundamental simulation results are obtained in the form of *S-parameter.*

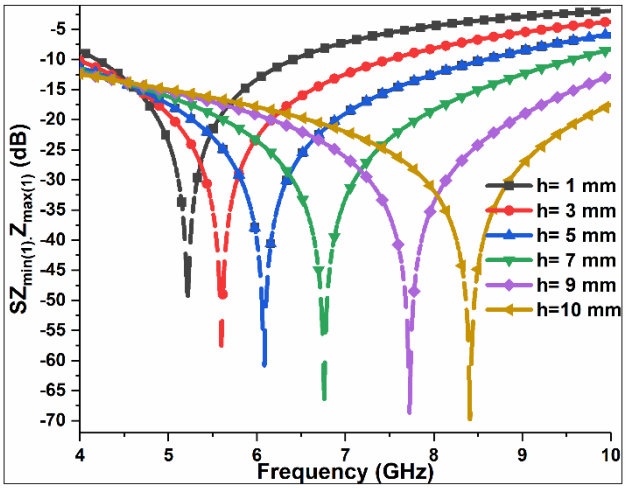

Figure 2.5 Transmission response of 3-D CSFSS structure.

The combination of $SZ_{min(1)}.Z_{max(1)}$ and $SZ_{min(2)}.Z_{max(2)}$ represents the transmissions coefficient and the combination of $SZ_{max(1)}.Z_{max(1)}$ and $SZ_{max(2)}.Z_{max(2)}$ represents the reflections coefficient for both *TE* and *TM* field of the incident *EM* wave, respectively.

A graph for transmission coefficient $SZ_{min(1)}.Z_{max(1)}$ for *TE* wave is plotted between different values of height (*h*) to the resonant frequency as shown in Figure 2.5. From the graph, it is clear that the resonant frequency is highly influenced by the height response. An increase in resonant frequency is observed with the increase in cylinder height and its response can be tuned and controlled. This shows a patch type structure behavior and executes a stop-band filter response when the impedance approaches infinity. The resonant peak value of the transmission coefficient increases proportionally with the increase of *CSFSS* height.

A *FWHM* bandwidth analysis is also done and shows that the bandwidth almost remains unaffected. Table 2.2, depicts the transmission behavior of *CSFSS* unit cell and shows that the frequency shift occurred without substantially affecting the stop band characteristics.

Table 2.2 The effect of variations of height on the resonant frequency.

Variation of Height (mm)	**Resonant Frequency (f_r) in GHz**	**S_{21} (dB)**	**FWHM (BW=f_2-f_1)**	**% shift of Resonant Frequency (f_r)**
h=1	5.22	-49.24	7.6%	0
h=3	5.60	-57.51	7.22%	7.28
h=5	6.09	-60.82	8.11%	16.67
h=7	6.76	-66.38	7.16%	29.50
h=9	7.72	-66.66	7.72%	47.89
h=10	8.41	-69.72	6.51%	61.11

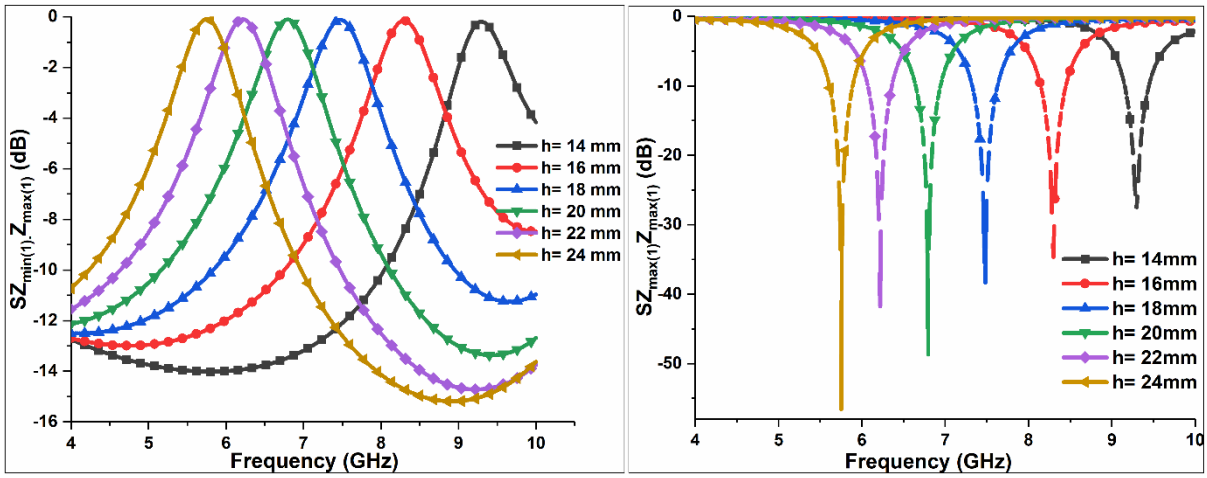

(a) (b)

Figure 2.6 Frequency response (a) Transmission and (b) Reflection response of 3-D CSFSS structure.

The transmission response (S_{21}), *FWHM* bandwidth and shift in resonant frequency are well maintained. The Equation 2.8 explains that as the height of resonator cylinder increases the net effective inductance decreases. Thus, a positive shift is in resonant frequency (f_r) with respect to the height is observed and hence the resonant frequency follows the Equation 2.5.

2.2.4. Pass-band Behavior of 3-D CSFSS

A significant change in the behavior of resonant frequency obtained when the height of CSFSS is increased further. A graph for transmission coefficient $SZ_{min(1).}Z_{max(1)}$ and reflection of height (h) versus the resonant frequency as shown in Figure 2.6(a) and (b), respectively. The stop-band response is now changed to pass-band response. With the increase in the height coefficient $SZ_{max(1).}Z_{max(1)}$ for *TE* electromagnetic wave is plotted against different values of *CSFSS* a reduction in the resonant frequency is observed. Table 2.3 depicts the reflection coefficient (S_{11}) behavior of *CSFSS* unit cell and shows that the negative frequency

Table 2.3 The effect of variations of height on the resonant frequency.

Variation of Height (mm)	**Resonant Frequency (f_r) in GHz**	**S_{11} (dB)**	**FWHM ($BW=f_2-f_1$)**	**% shift of Resonant Frequency (f_r)**
h=14	9.30	-27.49	1.93%	0
h=16	8.30	-34.66	1.48%	10.74
h=18	7.48	-38.38	1.34%	19.56
h=20	6.80	-48.70	0.80%	26.91
h=22	6.22	-41.78	1.26%	33.10
h=24	5.75	-56.59	0.57%	38.14

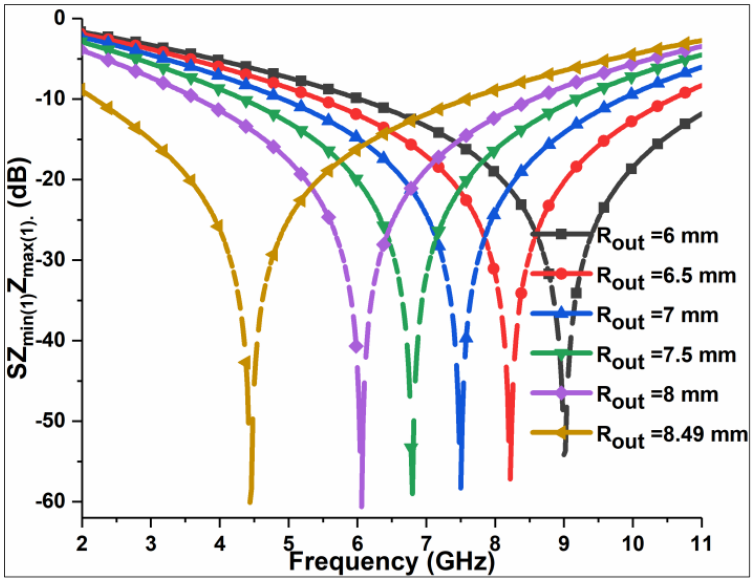

Figure 2.7 Resonance peak at a different value of $R_{out.}$

shift occurred without substantially affecting the pass-band characteristics. The reflection response (S_{11}), *FWHM* bandwidth and shift in resonant frequency are well maintained.

This behavior can be assumed because as the height of the *CSFSS* increased further, the tuned circuit inductance $L_1 \approx 0$, causes L_2 inductance comes in series with capacitance C resulting in bandpass behavior as shown in equivalent circuit model with the impedance of the circuit approaches to zero. Thus a parallel tuned circuit response will convert to series tuned circuit response.

2.2.5. Circumference Variation Behavior of 3-D CSFSS

A graph of transmission coefficient $SZ_{min(1).}Z_{max(1)}$ for *TE* modes at a normal angle of incidence have been plotted between different values of circumference by varying the outer radius (R_{out}) ranging from 6 mm to 8.495 mm versus the resonant frequency as depicted in Figure 2.7. The band stop frequency behavior of the 3-D *CSFSS* is shifted towards the lower resonant frequency as the value of the circumference outer radius increases.

At the value of R_{out} equals to 6 mm, the resonant peak formed at 9 GHz with -55.32 dB gain and as the value of R_{out} increased to 8.495 mm, the resonant peak occurred at 4.44 GHz with -69.9 dB gain. So a shift of -49.33 % obtained with sharp frequency gain. Thus, these results have been achieved without increasing the periodicity of the 3-D unit cell structure, hence support miniaturization. So, the variation in the circumference greatly influences the behavior of 3-D *CSFSS* unit cell structure.

2.2.6. Oblique Angle of Incidence Behavior of 3-D CSFSS

An important characteristic of the *CSFSS* unit cell is the analysis of the polarization sensitivity for a different angle of incidence of *TE* and *TM* field. For this purpose, the incident angle theta (θ) has been varied between 0^0 to 80^0 for both *TE* and *TM* field polarizations as shown in Figure 2.8. The graphical response of *TE* and *TM* modes for a normal angle of incidence for *EM* waves at height (h = 5 mm) is shown in Figure 2.9(a) and (b), respectively. At the value of h = 5 mm, Table 2.4 has been also drawn for the purpose of comparison.

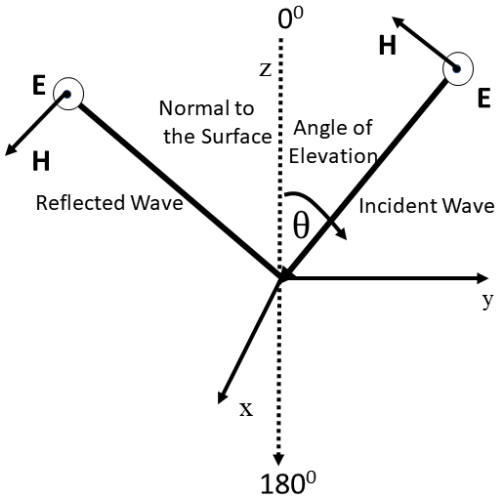

Fig. 2.8 Oblique angle of incidence theta (θ) measurement

For *TE* mode, at theta (θ = 0^0) the resonant peak frequency occurs at 6.08 GHz with the value of transmission parameter is -60.77 dB. As the angle of incidence varies from 0^0 to 60^0 the resonant frequency remains almost unaffected and equal to 6.04 GHz. When the angle of

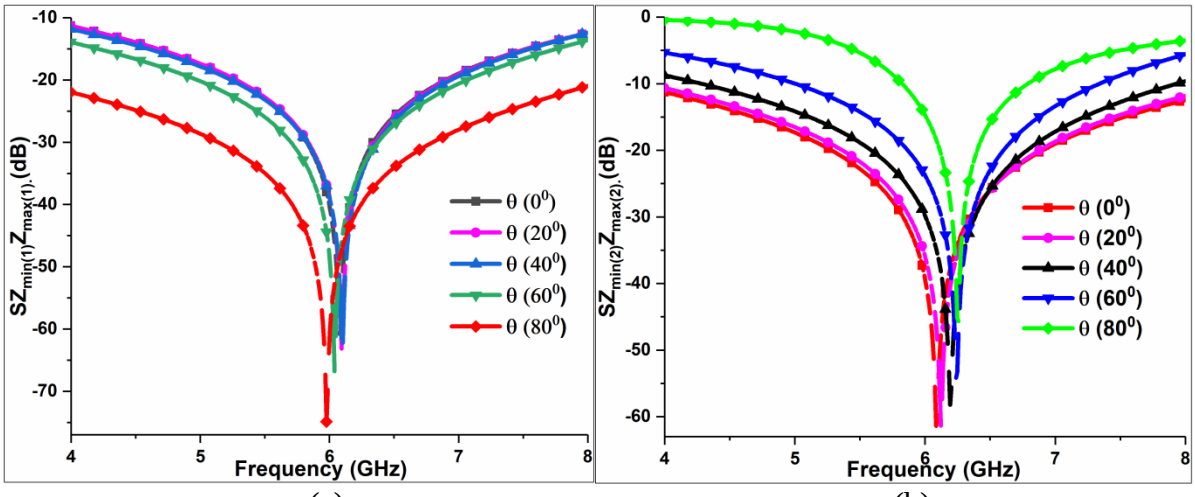

(a) (b)

Figure 2.9 Oblique angle of incidence for (a) TE and (b) TM mode at h = 5 mm

Table 2.4 TE and TM field polarization sensitivity analysis at h = 5 mm.

Angle(θ) for TE	Resonant Frequency (f_r) GHz	S_{21} in dB	Deviation (%)
0^0	6.08	-60.77	0
20^0	6.09	-63.16	0.30
40^0	6.10	-62.23	0.44
60^0	6.04	-66.79	0.59
80^0	5.98	-74.87	1.63
Angle(θ) for TM	**Resonant Frequency (f_r) GHz**	**S_{21} in dB**	**Deviation (%)**
0^0	6.09	-61.39	0
20^0	6.12	-61.33	0.59
40^0	6.19	-58.22	1.77
60^0	6.24	-54.15	2.51
80^0	6.26	-45.65	2.81

incident is modified to 80^0, the resonant frequency is slightly shifted and moves down to 5.98 GHz with a shift of 1.63 %.The value of the resonant peak of transmission parameter is well maintained and observe increased the incidence angle from 0^0 to 80^0.

For *TM* mode, at theta ($\theta = 0^0$) the resonant peak frequency occurs at 6.09 GHz with the value of transmission parameter is -61.39 dB. As the angle of incidence varies from 0^0 to 20^0 the resonant frequency remains almost unaffected and equal to 6.12 GHz. When the angle of incident is modified to 80^0, the resonant frequency is slightly shifted and moves up to 6.26 GHz with a shift of 2.81 %. The value of the resonant peak of transmission parameter at theta ($\theta = 80^0$) is well maintained always remain above 74.36%.

2.2.7. Variation of Angle of Incidence of 3-D CSFSS for TE Mode

For *TE* mode of *EM* wave, analyses have been observed at the oblique angle of incidence. The graph for the different values of outer radius R_{out} at an oblique angle of incidence for 3-D *CSFSS* have been shown in Figure 2.10(a) for the value of R_{out} equals to 7.2 mm. The curve corresponds to the value of R_{out} equals to 7.6 mm has been shown in Figure 2.10(b).

Similarly, the curve corresponds to the value of R_{out} equals to 8.0 mm has been shown in Figure 2.10(c) and the last one curve corresponds to the value of R_{out} equals to 8.49 mm has been shown in Figure 2.10(d), respectively. At Table 2.5, a polarization sensitive analysis at a different oblique angle of incidence for *TE* mode has been drawn for the purpose of comparison. The value of theta is varied between $\theta = 0^0$ to $\theta = 60^0$.

In Figure 2.10(a), for theta ($\theta = 0^0$), the resonant frequency peak (f_r) occurs at 7.22 *GHz* with the value of transmission coefficient (S_{21}) is -57.86 dB. As the angle of incidence varies from 0^0 to 60^0 the resonant frequency influence effectively and reduces to 6.80 GHz, while the value of transmission parameter (S_{21}) almost remains unaffected. When the angle of incident is modified to 60^0, the resonant frequency is slightly shifted and moves down to 6.80 GHz with a shift of -5.82 %.

In Figure 2.10(b), for theta ($\theta = 0^0$), the resonant frequency peak (f_r) occurs at 6.66 GHz with the value of transmission coefficient (S_{21}) becomes -57.06 dB. As the angle of incidence varies from 0^0 to 60^0 the resonant frequency influence effectively and become to 6.46 GHz, while the value of transmission parameter S_{21} changes slightly to -64.51 dB. When the angle of incident is modified to 60^0, the resonant frequency is slightly shifted and moves down to 6.46 GHz with a shift of -3.0 %.

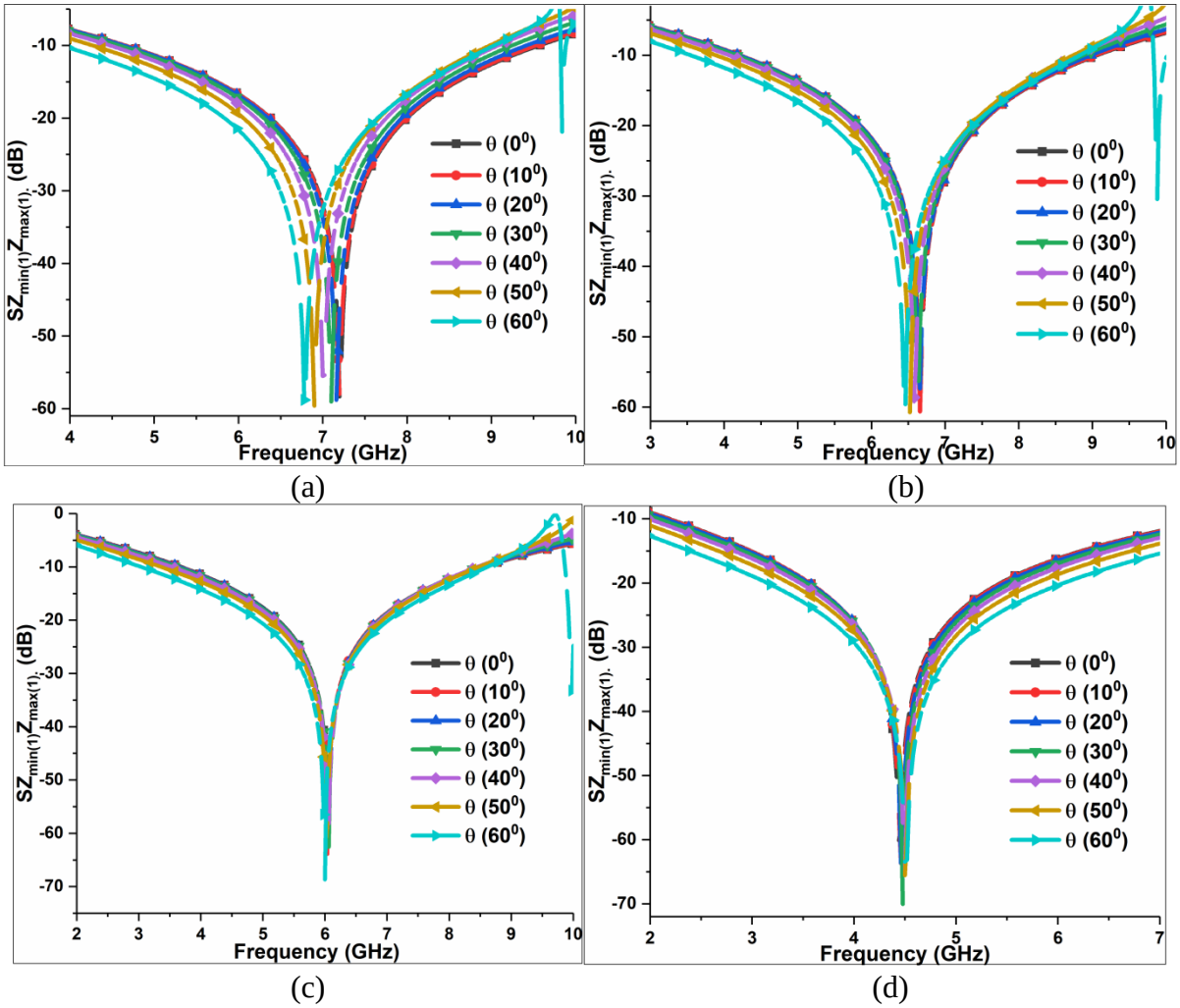

Figure 2.10 Graphs for oblique angle of incidence for TE mode (a) R_{out} = 7.2 mm, (b) R_{out} = 7.6 mm, (c) R_{out} = 8.0 mm, and (d) R_{out} = 8.49 mm.

In Figure 2.10(c), for theta ($\theta = 0^0$), the resonant frequency peak (f_r) occurs at 6.04 GHz with the value of transmission coefficient (S_{21}) becomes -57.06 dB. As the angle of incidence varies from 0^0 to 60^0 the resonant frequency negligibly affected and become to 6.02 GHz. While a sharp peak of transmission parameter S_{21} with value -67.18 dB appear. When the angle of incident is modified to 60^0, the resonant frequency remains almost stable and insensitive to any variation in the oblique angle of incidence and become equals to 6.02 GHz with a minor shift of -0.33 %.

In Figure 2.10(d), for the value of theta (θ) equals to 0^0, the first resonant frequency peak (f_r) occurs at 4.50 GHz with the value of transmission coefficient (S_{21}) becomes -59.05 dB. As the angle of incidence varies from 0^0 to 60^0 the resonant frequency influence slightly and

Table 2.5 TE modes polarization sensitivity analysis at different values of R_{out}.

	Angle(θ) for TE	Resonant Frequency (f_r) GHz	S_{21} in dB	Deviation (%)
R_{out} = 7.2 mm	**0^0**	7.22	-57.86	0
	10^0	7.22	-57.52	0
	20^0	7.18	-56.91	-0.55
	30^0	7.12	-56.71	-1.38
	40^0	7.04	-54.77	-2.49
	50^0	6.92	-57.30	-4.16
	60^0	6.80	-56.93	-5.82

	Angle(θ) for TE	Resonant Frequency (f_r) GHz	S_{21} in dB	Deviation (%)
R_{out} = 7.6 mm	**0^0**	6.66	-57.06	0
	10^0	6.66	-57.97	0
	20^0	6.66	-61.40	0
	30^0	6.64	-61.94	-0.30
	40^0	6.60	-60.12	-0.90
	50^0	6.54	-57.77	-1.8
	60^0	6.46	-64.51	-3.0

	Angle(θ) for TE	Resonant Frequency (f_r) GHz	S_{21} in dB	Deviation (%)
R_{out} = 8 mm	**0^0**	6.04	-57.06	0
	10^0	6.06	-60.09	0.33
	20^0	6.06	-61.10	0.33
	30^0	6.08	-58.77	0.66
	40^0	6.06	-58.47	0.33
	50^0	6.04	-62.83	0
	60^0	6.02	-67.18	-0.33

	Angle(θ) for TE	Resonant Frequency (f_r) GHz	S_{21} in dB	Deviation (%)
R_{out} = 8.49 mm	**0^0**	4.50	-59.05	0
	10^0	4.50	-64.23	0
	20^0	4.50	-62.80	0
	30^0	4.52	-69.57	0.44
	40^0	4.54	-67.85	0.89
	50^0	4.50	-59.05	0
	60^0	4.50	-64.23	0

become to 4.56 GHz, while the value of transmission parameter S_{21} also changes slightly When the angle of incident is modified to 60^0, the resonant frequency is slightly shifted and moves down to 4.56 GHz with a shift of 1.33 %.

2.3. Electronic Band-Gap Structure (EBG)

Electronic band-gap structures are usually compact and lightweight, low fabrication cost, minor losses and can be easily integrated into antennas design without degrading performance. *EBG* structures are widely used because of its unique properties and *EM* features such as electromagnetic band-gap and in-phase reflection to heighten antenna performance [64-67]. *EBG* structures possess interesting and unique properties such as it behaves like high impedance surface in the certain frequency band and behaves like a passband filter in others. Using these properties one can solve problems that arise when antenna's exiting source mount close to a ground plane.

Another scenario exists when several exiting sources etched close to each other conducting planes. This would result in mutual coupling and lead to degradation of antenna performance. *EBG* structures are used in this scenario to minimize coupling by creating a band-gap region, where surface waves get suppressed. Thus, enhances the efficiency of the antenna by re-reflecting back *EM* radiations in phase with respect to forwarding *EM* radiations. On the other hand, *EM* signals remain unperturbed for out-band frequency region.

For the fast and accurate analysis of periodic *EBG* structures, a single *EBG* unit cell behavior could be considered and studied with appropriate boundary conditions. The

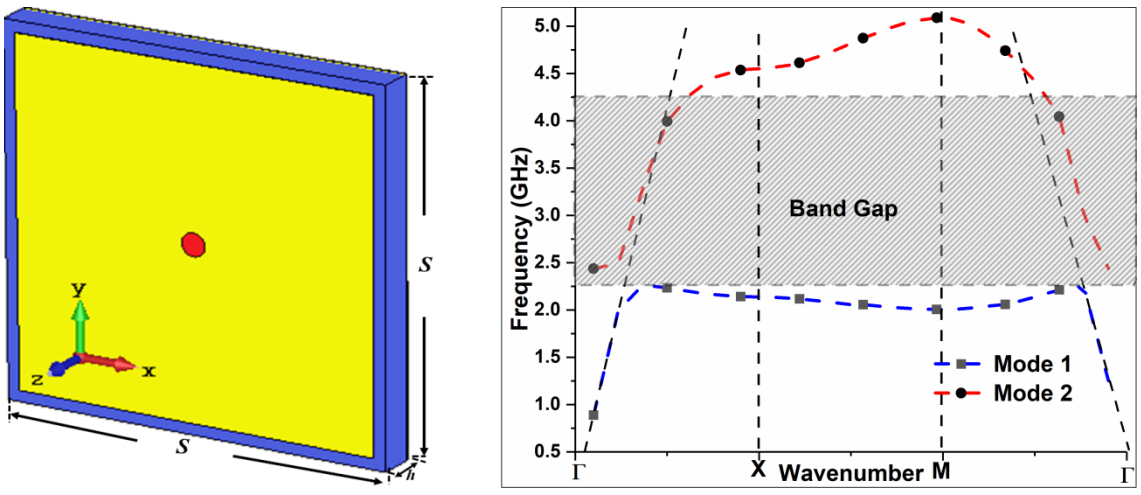

(a) (b)

Figure 2.11. The geometry of EBG unit cell. (a) perspective view and (b) Dispersion curve with dimensions: S = 16 mm, g = 1 mm, h = 1.5 mm, t = 0.035 mm, and via = 0.5 mm.

periodicity (*S*) of a single unit cell of *EBG* is 16 mm. A copper patch of 15 mm × 15 mm has been directly printed on *FR-4* substrate material of thickness 1.5 mm with relative permittivity (ε_r) 4.3 and tangent loss (δ) 0.025. A via of diameter 0.5 mm connecting the metal patch to the ground plane has been chosen and shown in Figure 2.11 (a). In an *EBG* equivalent frequency tuned circuit, the inductance is represented by via, while capacitance is governed by the gap (*g*) of 1 mm between the patches. A dispersion diagram of a unit cell of the mushroom-type *EBG* structure has been plotted and depicted in Figure 2.11 (b).

The frequency band-gap of the *EBG* structure has been adjusted between 2.25 GHz to 4.25 GHz using parameter sensitivity analysis. Parameter sensitivity is the deviation in frequency response with the structural parameters variations. Therefore, the parameters like periodicity (*S*), gap width (*g*), a substrate thickness (*h*), dielectric constant (ε_r) of the *EBG* have been varied and tuned along with vias diameter as it also has a trivial effect. All parameters are optimized to cover the operating frequency of 2.45 GHz.

2.3.1. Antenna Design using Defected Ground Structure(DGS) with EBG

The Defected ground structure (*DGS*) is periodic or non-periodic defects in the ground plane of microstrip and coplanar structure. The *DGS* plane behavior can be realized by etching off a specific geometry in the ground plane. Depending on the geometry and dimensions of the defective shape, the impedance and surface current distribution get perturbed and this further modifies the associated capacitance and the inductance values. Thus, results in assured propagation and excitation of the *EM* waves through the dielectric material. The *DGS* has been widely used for different applications such as radiation properties enhancement [68], bandwidth [69], mutual coupling reduction in antenna arrays [70], antenna size reduction [71], and so forth. DGS also has some disadvantages like as we introduce some slots or defects in the ground plane, this will result in back lobes. Due to which some of the energy get dissipated, which in turn decreases the directional gain. DGS increases Specific absorption rate (SAR) value and hence it is not suitable in mobiles and wearable devices applications.

Making these considerations in this design, we have designed a traditional microstrip patch antenna operating at 2.45 GHz resonant frequency. Then this antenna is modified by the defected ground structure. Once again antenna structure is altered and loaded with *EBG* structure. The *EBG* structure is designed and optimized such that resonance peak of antenna lies within its forbidden band-gap so that the surface wave excited by this patch antenna could be suppressed and prevent propagation. This section gives augmentation published in [72].

The basic geometry of a conventional microstrip patch antenna designed with inset feed has been shown in Figure 2.12(a). The top layer is the radiating rectangular patch (copper), backed by most popular and readily available flame retarded (FR-4) substrate of height h = 1.5 mm. The substrate is grounded using a copper layer. The dimensions of the antenna are as follow: periodic length S_L = 64 mm, periodic width S_W = 67 mm of the substrate with length L = 28.88 mm, and width W = 35 mm of the radiating patch. A standard thickness of 35 µm has been considered which is compatible with *PCB* fabrication technology. The antenna is operational at 2.45 GHz of *ISM* band.

This referenced antenna is then modified with the defected ground plane as shown in Figure 2.12(b). Which result in modification of resonant frequency and it gets shifted to the lower band. So, when the antenna is optimized back to 2.45 GHz resonant frequency, the exiting patch dimensions get modified and become equals to *L* = 25.1 mm, and *W* = 25 mm.

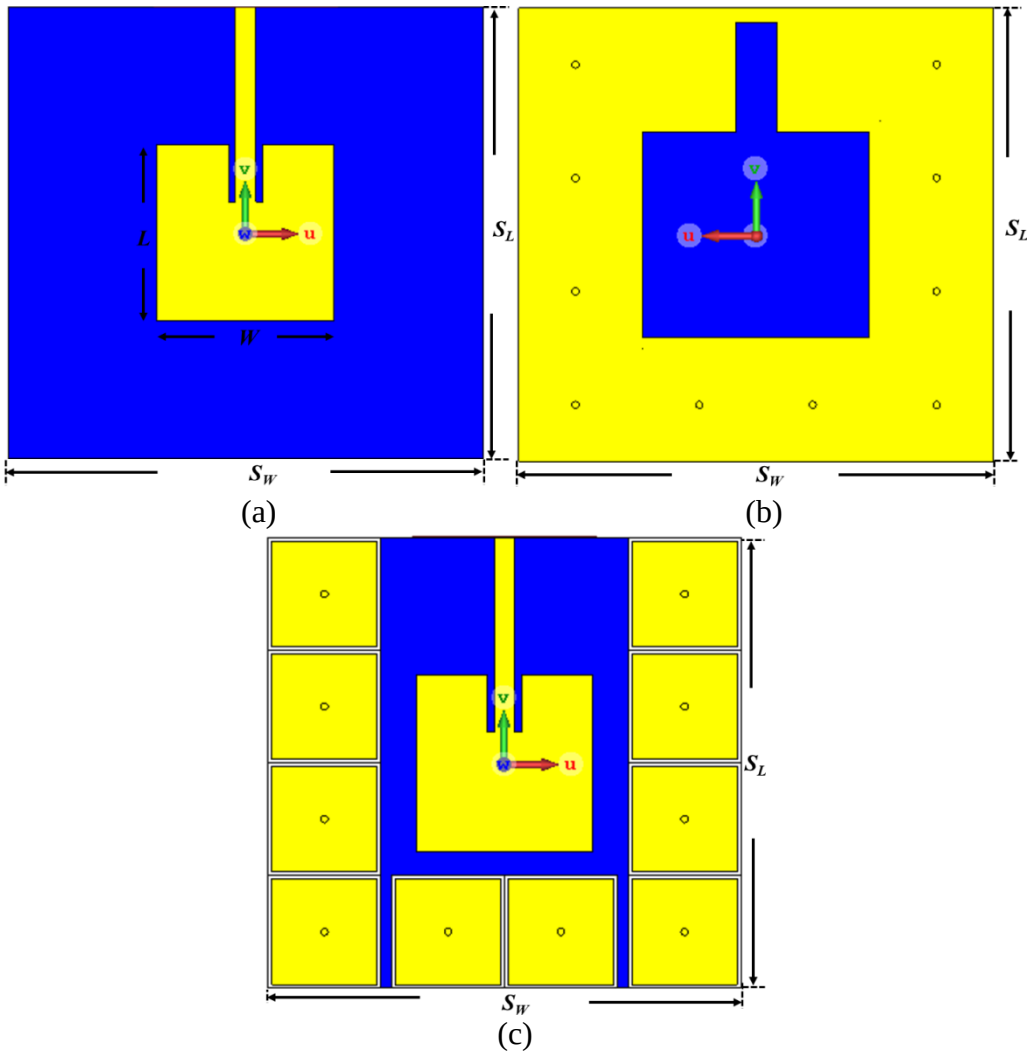

Figure 2.12 Microstrip patch antenna (a) referenced antenna (b) antenna with defected ground structure, and (c) proposed antenna (DGS+ EBG).

This indicates a miniaturization to 37.9 % of patch size when get modified with *DG* plane. Finally, this antenna structure has been further modified with periodic mushroom-typed *EBG* to study the effect of *EBG* on overall antenna radiation performance and depicted in Figure 2.12(c).

2.3.2. Microstrip Patch Antenna Radiation Performances

A comparison of antenna radiation performances has been made and shown in Figure 2.13. For the referenced antenna, the value of the S_{11} parameter has been observed at 2.45 GHz and equal to -34.65 dB. The antenna is then modified with *DG* plane with resonant frequency peak adjusted to 2.45 GHz with -29.02 dB. Finally, this structure has been modified by loading with

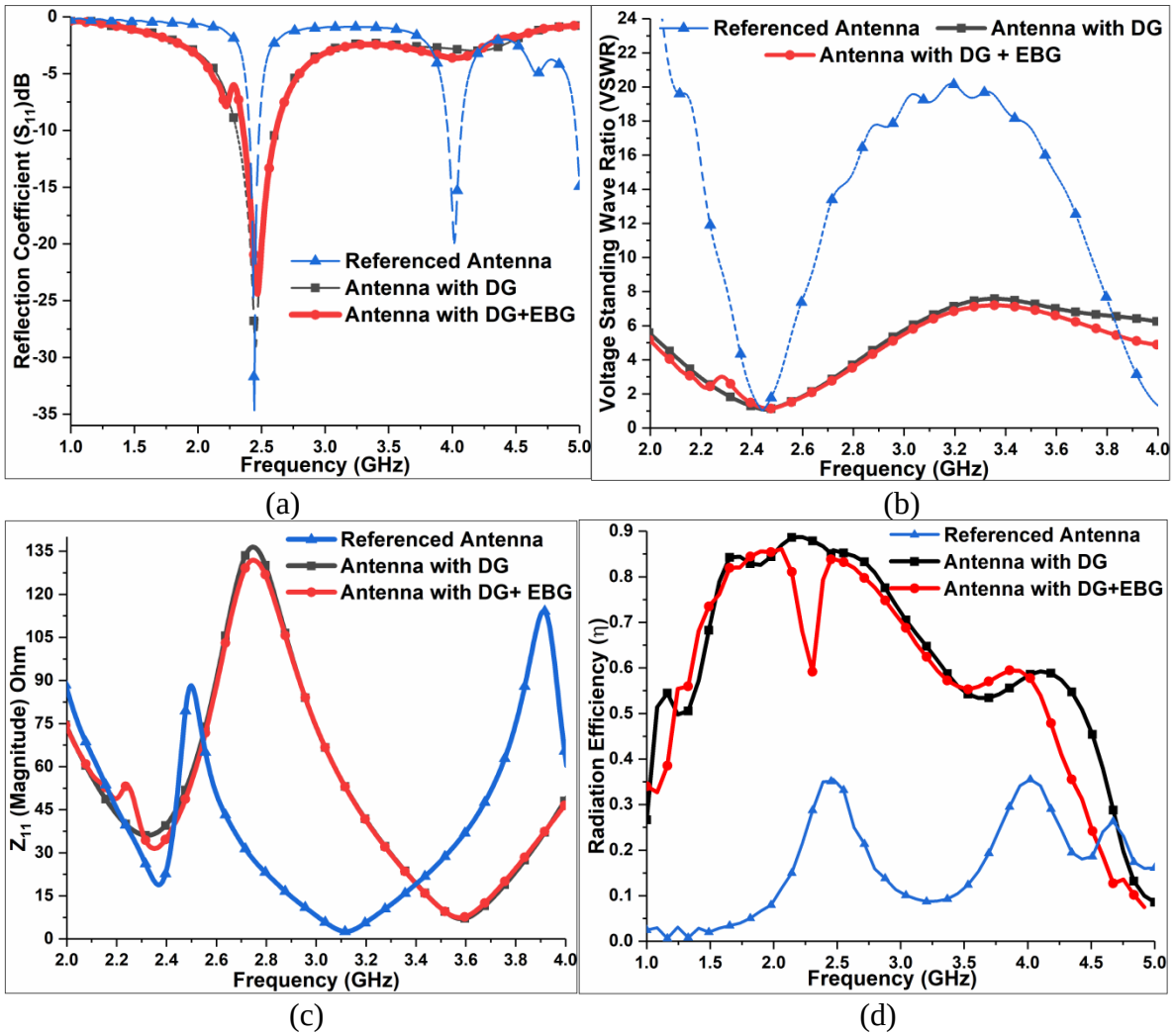

Figure 2.13 Comparison of antenna radiation performances (a) scattering coefficient (S_{11}) (b) VSWR (c) Z_{11} (magnitude), and (d) radiation efficiency (η).

Table 2.6 Antenna radiation performance comparison.

Structure/Performance Parameters	Referenced Antenna	Antenna with DG	Antenna with DG +EBG
Frequency (f_0) GHz	2.45	2.45	2.47
Return Loss (S_{11}) dB	-34.65	-29.02	-24.40
Bandwidth (-10 dB) MHz	72	304	256
VSWR	1.04	1.07	1.13
Impedance (Z_{11}) Ω	50.87	47.14	46.83
Radiation Efficiency (η)	35.1 %	85.06 %	83.97 %
Directivity (dBi)	6.68	4.48	4.68
Gain (dB)	2.12	3.77	3.84

EBG structure and which results in a slight shift of resonance frequency to 2.47 GHz with S_{11} approaches to -24.40 dB and shown in Figure 2.13(a). For the referenced antenna, the value of *-10 dB* bandwidth is very small and equal to 72 MHz, whereas after modifying it with *DG* plane it effectively enhances to 304 MHz. But after loading of *EBG* structure slightly reduces the bandwidth to 256 MHz that is still larger than the referenced antenna.

To further analyze the behavior of proposed patch antenna on antenna radiation performances, an analysis of voltage standing wave ratio (*VSWR*), impedance (Z_{11}) and radiation efficiency (η) have been made. The results show that for reference antenna, the value for *VSWR* comes out 1.04 and 1.07 for an antenna with *DG* plane, whereas for a proposed model with *DG* and *EBG* it comes out to be 1.13 as shown in Figure 2.13(b). All values of *VSWR* remain within the acceptable range of 1 to 1.5.

The value for Z_{11} (magnitude) for referenced antenna observed of 50.87 Ω and 47.14 Ω for an antenna with *DG* plane at 2.45 GHz, whereas for proposed model the value of Z_{11} reduces to 46.83 Ω at 2.47 GHz as shown in Figure 2.13(c). All these values are approximated to 50 Ω matching impedance. Similarly, for reference antenna, the value of radiation efficiency (η) is very less and is equal to 35.1%. But when it modified with *DG* plane it effectively enhances to 85.06 %. For the proposed model with *DG* plane and *EBG*, the value of η marginally reduces to 83.97 % and depicted in Figure 2.13(d). For better clarification and understanding, a comparison of antenna radiation performance has been given and tabularized in Table 2.6.

2.3.3. Directivity and Gain Comparisons Between Referenced and Proposed Antenna

The antenna directivity polar plot comparisons between referenced and proposed antenna for *E-Plane* and *H-Plane* have been given in Figure 2.14. The results indicate that for *E-Plane*, the referenced patch antenna main lobe magnitude is 6.68 dBi with 3 dB angular width is 87^0 and for proposed microstrip antenna, it reduces to 4.48 dBi with 3 dB angular width is 92.3^0. For the proposed model with *DG* and *EBG* structure, the value of main lobe magnitude is 4.68 dBi with 3 dB angular width is 89.2^0 as depicted in Figure 2.14(a).

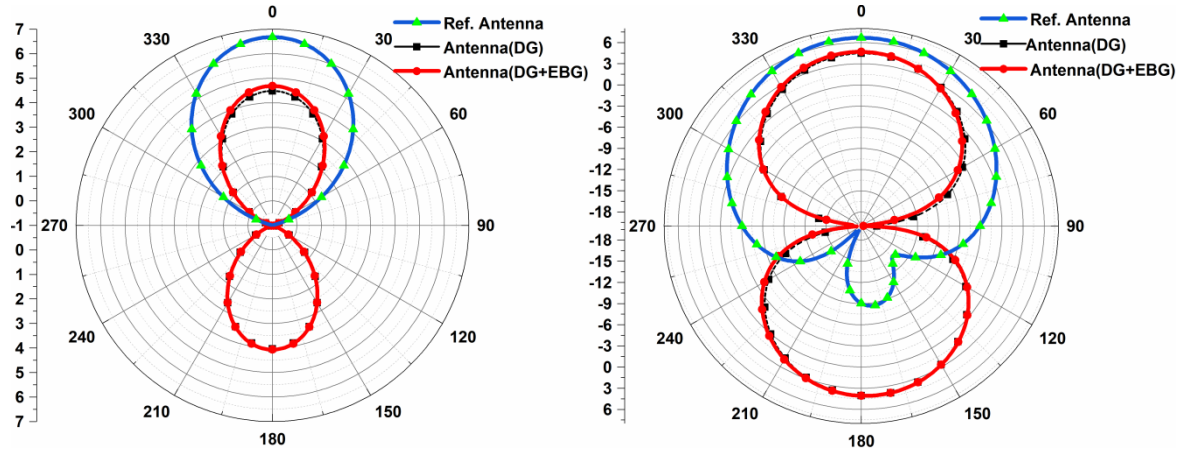

(a) (b)

Figure 2.14 Polar plot comparison of antenna directivity for (a) E-Plane and (b) H-Plane.

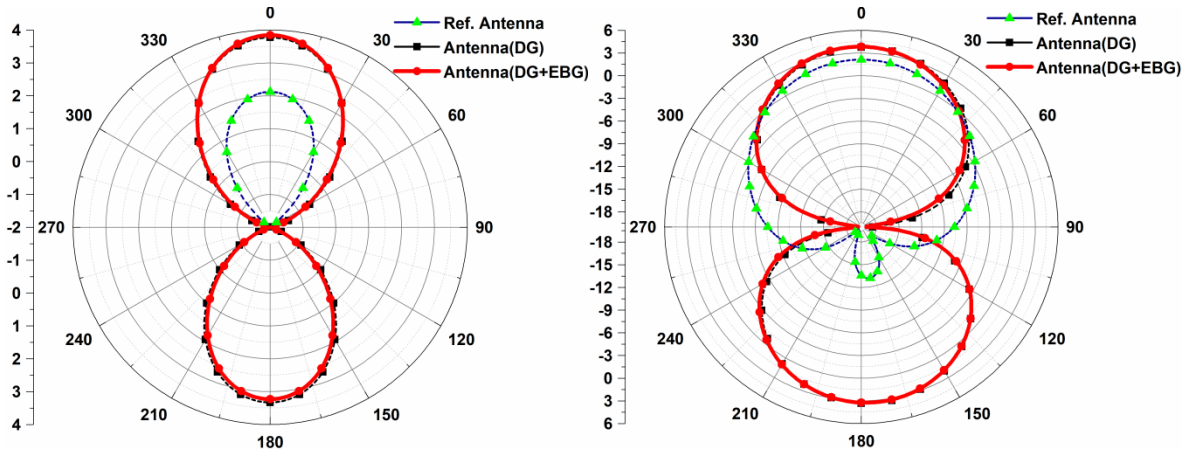

(a) (b)

Figure 2.15 Polar plot comparison of antenna gain for (a) E-Plane and (b) H-Plane.

For *H-Plane*, the reference patch main lobe magnitude is 6.68 dBi with 3 dB angular width is 92.3^0 and for an antenna, with *DG* plane it reduces to 4.48 dBi with 3 dB angular width is 74^0. For the proposed model with *DG* and *EBG* structure, the value of main lobe magnitude is 4.69 dBi with a 3dB angular width of 72.2^0 as depicted in Figure 2.14(b). A polar plot

comparison for antenna gain has been given in Figure 2.15. The results indicate that for *E-Plane*, the reference patched antenna main lobe magnitude is 2.12 dB with beam width is 87^0 and for an antenna, with *DG* plane it increases to 3.77 dB with beam width is 92.3^0. For the proposed model with *DG* and *EBG* structure, the value of main lobe magnitude further enhances to 3.84 dB with a beam width of 89.2^0 as depicted in Figure 2.15(a).

For *H-Plane*, the reference patch main lobe magnitude is 2.12 dB with beam width is 92.3^0 and for an antenna, with *DG* plane it increases to 3.77 dB with beam width is 74^0. For the proposed model with *DG* and *EBG* structure, the value of main lobe magnitude further enhances to 3.85 dB with a beam width of 72.2^0 as depicted in Figure 2.15(b).

This concludes that when the referenced antenna is modified with *DG* plane and *EBG*, its antenna gain enhances to 81.1 %. So, the proposed antenna would require less power in the line of sight transmission and therefore would lead to a reduction in hardware cost as the number of repeaters required reduces. The beam width has been also reducing in the proposed antenna as compared to the conventional antenna. This would lead to a concentrate and focus power in the line of sight transmission for long distance transmission.

2.3.4. 2-D Comparisons for Directivity and Gain

In Figure 2.16, two-dimensional comparisons of antenna directivity and gain have been made between 1 to 5 GHz of the frequency band. The analysis indicates that when the antenna is loaded with *DG* and *EBG* structure, the value of directivity remains high for the entire band-gap of *EBG* structure that lies between 2.37 to 4.31 GHz and shown in Figure 2.16(a). However, a minor fluctuation is observed between 3.67 to 3.92 GHz, where

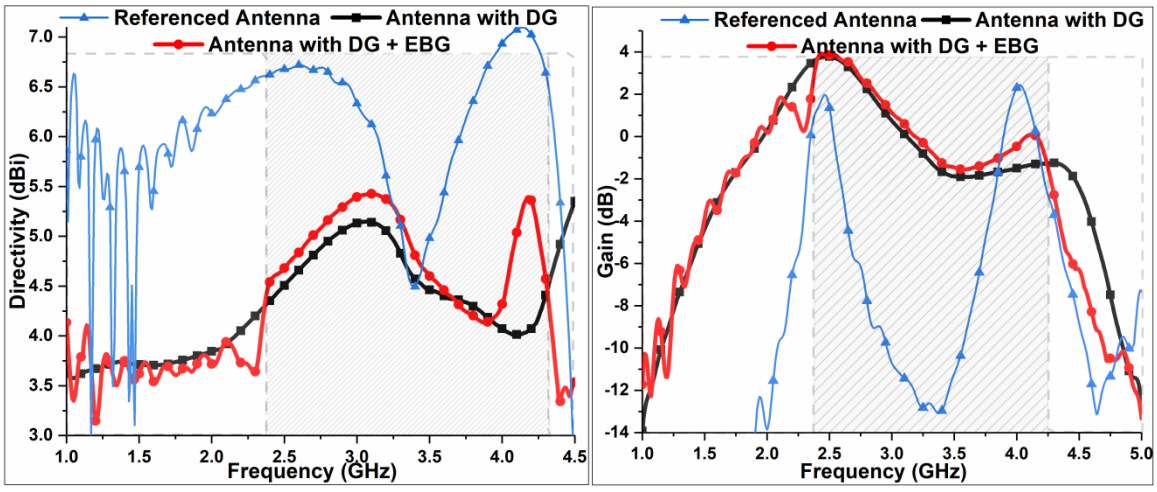

(a) (b)

Figure 2.16 Two-dimensional comparisons for (a) directivity and (b) gain.

antenna with *DG* plane value slightly increases. On the other hand, the value of gain remains high for the entire bandgap of *EBG* structure that lies between 2.41 to 4.24 GHz and shown in Figure 2.16(b).

2.4. Metamaterial Absorber (MMA)

Researchers have been demonstrating and proposed various *MMA* structure ranging from microwave to THz regimes, infrared to the visible light region, single-band to wideband, and dual-band to multi-band range of *EM* radiation based on the target applications. *MMA* has attracted notable interest and offers excellent features including narrow dimensions, lightweight, near-unity absorbance, ultra-thin thickness, wide angles of incidence, and highly polarization insensitivity. This is making it potential rival and thus currently replacing the traditional absorbers.

MMA is obtained by modifying frequency selective surface (*FSS)* structure. A *FSS* is a patch or aperture/slot/grid type element and their properties could be tuned and engineered to exhibit band-pass, band-stop, low-pass or high-pass filter characteristics, depending on design modification. In *MMA,* the effective inductance and capacitance of the unit cell structure could be altered by varying the geometry of the structure and hence set up the resonant frequency. The *MMA* unit cells behave as a combination of lumped inductive and capacitive elements which get coupled to the incident electric and magnetic fields of *EM* radiation.

MMA is an array of periodically arranged patches etched on the dielectric substrate in the metallic screen and exhibits almost unity absorbance. The structure has the ability to modify the *EM* radiations in such a way that the input impedance of the structure becomes closely matched with the free space impedance and hence the condition of resonance achieves. Thus, offers further reduction in size, versatility with enhanced potentialities.

However, *MMA's* absorbance highly relies on structural morphology and composed materials for the purpose of fabrication. It is the most relevant periodic structure, offers better alternate to *FSS, EBG,* Artificial Magnetic Conductor (*AMC*) structure for several intended applications in microwave regime of the electromagnetic spectrum such as satellite communication, such as in stealth technology for low *RCS,* in solar-photovoltaic and thermo-photovoltaic cells to enhance the functioning of photo-detectors by heightening absorption mechanism, and wireless communication. In antenna design, its intended applications are

gain/directivity enhancement, increase isolation by reducing cross polarization, mutual coupling reduction, and in-band and out-of-band *RCS* reduction.

2.4.1. Triple Band Regular Decagon Shaped Metamaterial Absorber

The design characteristics of metamaterial absorber have been investigated for X-band applications. For this purpose, a primary regular decagon shaped loop structure has chosen, and its multiband response has been studied and analyzed [73]. The schematic diagrams are shown in Figure 2.17. Where top view layout of one-unit cell for the proposed structure is depicted in Figure 2.17(a), while the back view is shown in Figure 2.17(b), the cross-sectional view is given in Figure 2.17(c), respectively. At last, Figure 2.17(d) shows the side view of the proposed structure along with its respective parameters.

The *MMA* is a three-layer structure composed of metal/dielectric/metal layer. The three regular decagon structures are fabricated on the top of the substrate. The electric field is enhanced by the coplanar coupling of metallic rings, while the magnetic field is enhanced by the mutual coupling between the front rings and back metal layer. The *EM* wave response can

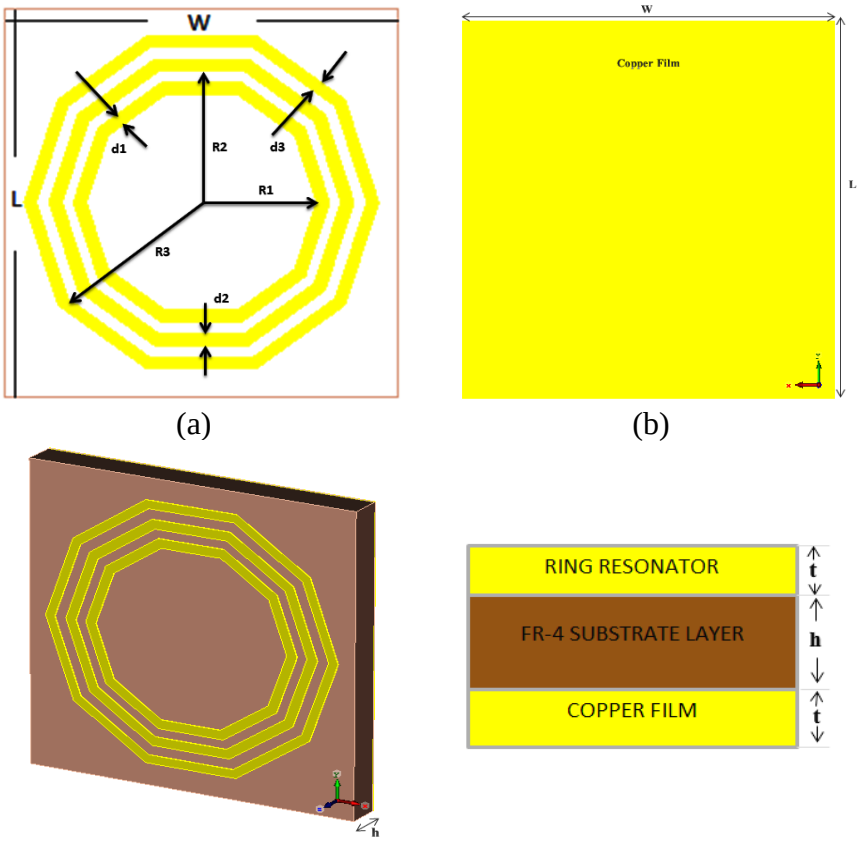

(a) (b)

(c) (d)

Figure 2.17 The geometry of triple band regular decagon shaped metamaterials absorber (a) top view (b) bottom view (c) perspective view, and (d) side view.

Table 2.7 The dimensions of absorber unit cell.

Description	Parameters	Dimensions (mm)
Width/Length of Substrate	W/L	7.6
Height of Substrate	h	0.8
Height of Metallic Rings	t	0.017
Radius of 1st Ring	R1	2.23
Radius of 2nd Ring	R2	2.7
Radius of 3rd Ring	R3	3.2
Thickness of 1st Ring	d1	0.24
Thickness of 2nd Ring	d2	0.28
Thickness of 3rd Ring	d3	0.22

be tuned by varying the physical parameters of the front rings, back metallic layer and the substrate layer. The absorber consists of triple ring resonator structure on the top, a lossy FR-4 substrate with the value of relative permeability (ε_r) is 4.3 and *tan δ is* 0.02 placed at the center and a metallic bottom plane.

The top and bottom plane consist of same copper metal with conductivity (σ) equal to 5.8×10^7 s/m. On the back of the substrate, the full ground plane is placed to make a zero transmitted wave. But the existence of a ground plane at the back also causes the back-reflected wave. So, a thick dielectric substrate is used to solve this problem. The results described here have been published in [83].

For impedance matching, the parameters like the thickness of the metal and dielectric layer should be optimized. In simulations, the thickness of the top metal layer and ground metal plane has kept equal to 17 μm. Whereas, the thickness (t) of the dielectric FR-4 substrate layer is optimized to 800 μm. The rest of the parameters have been tabulated in Table 2.7. Where, the radius of three consecutive rings have been designated as *R1*, *R2,* and *R3*. Where, *d1*, *d2,* and *d3* signify their corresponding thickness, respectively.

By careful analysis, it is observed that the radius of three regular decagon shaped rings has been estimated by the relation given in Equation (2.10), corresponding to their respective absorption peaks:

$$R = \frac{C}{\omega_r \sqrt{\varepsilon_{reff}}} \tag{2.10}$$

Where ω_r is the resonant frequency of the regular decagon-shaped and ε_{reff} is the effective relative permittivity of the lossy FR4 substrate. So, it is clear that the radius is inversely proportioned to the resonant frequency. So, as we decrease the radius of the regular decagon ring the corresponding resonant frequency increases and as we increase the radius of the ring the corresponding resonant frequency decreases.

The resonant frequency not only depends on the radius but also on the other factors like the substrate permittivity, thickness of the substrate, thickness of the metal layer and top layer, the width of the rings, the capacitive coupling between rings. Since, this is a multiple rings structure, so the resonant frequencies also depend on capacitive coupling between adjacent unit cells along with the dimensions of the unit cell. These all parameters vary the inductance and capacitance of the complete unit cell as given in Equation (2.5). As the length of the decagon shaped ring wire increases the inductance also increases, which raises the resultant radius and because of this the resonant frequency decreases and as the length of the decagon shaped ring wire decreases the inductance also decreases, which reduces the resultant radius and because of this the resonant frequency increases.

Similar phenomena will be observed because of the smaller gap between the neighboring decagon shaped metallic rings or because of the adjacent unit cells outer metallic rings coming close to each other, resulting in increase of the capacitance causing the resonant frequency decreases and the reverse effect will take place when the capacitances will reduce due to either the decagon shaped metallic rings going far from each other or the decagon shaped metallic rings are placed far apart from each other resulting in increases of the resonant frequency. Along with thickness of three decagon shaped metallic rings, all parameters are optimized so that the absorber achieves the highest absorption at sharp edges of 8 GHz, 10 GHz, and 12 GHz, respectively.

2.4.2. Frequency Response Analysis

It has been found that the loop structures are highly polarization insensitive in nature for the oblique angle of incidence of *EM* wave. Since, a regular decagon shaped loop structure has been chosen, which is found to be very symmetrical to ring shape structure. Thus, the unit cell structure has been analyzed for the normal angle of incidence using finite differential time domain (*FDTD*) technique [65]. The incident *TEM* wave is excited along the *z*-axis (Figure 2.17) with the electric field components along the *y*-axis and magnetic field components along the *x*-axis.

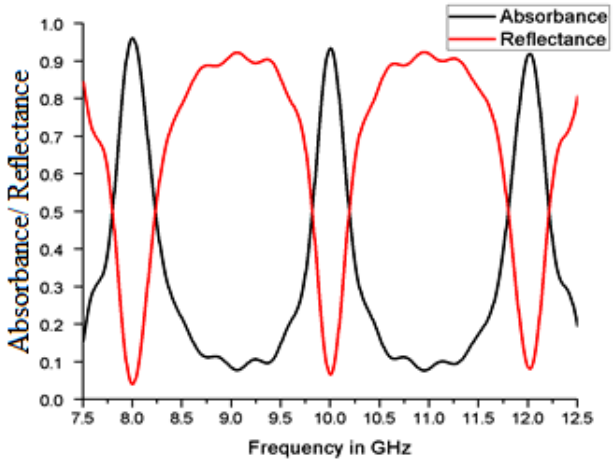

Figure 2.18 Simulated reflectance and absorbance of the proposed metamaterial absorber.

The simulated absorbance as a function of time domain under a normal angle of incidence *EM* wave has been depicted in Figure 2.18. From the result, it can be seen that the proposed structure exhibits three distinguished absorption peaks sharply at 8 GHz, 10 GHz and 12 GHz with corresponding absorbance peak values of 96 %, 93.36 %, and 91.88 % respectively. The value of the reflection coefficient (S_{11}) at these consecutive resonant peaks of 8 GHz, 10 GHz, and 12 *GHz* has been found to be approaching to zero, which is clearly reflected in Figure 2.18.

All absorbance peak values have been found above 91.88 %. The *MMA* exhibits, a response with *FWHM* bandwidth is 457.9 MHz, 400.3 MHz, and 455.5 MHz, which is found to be equivalent to 5.72 %, 4.00 %, and 3.80 %, respectively of the respective resonant frequency. These three distinct absorption peaks are distributed exactly across the entire X-bands. By carefully varying the thickness of these three rings, the location of absorption peaks could be adjusted and thus, we would make *MMA* suitable for the applications in the range of microwave, optical and terahertz regime.

2.4.3. Normalized Input Impedance Response

The parameters optimization of *MMA* have been accomplished by tuning and adjusting the radius of three rings, their related thickness, the height of the top metallic ring layers, adjusting the values of dielectric constant, loss tangent, the morphology of the dielectric substrate to get the response at desired resonant frequency. So that, the *MMA* structure's normalized input impedance approximates to the free space impedance at desired resonant frequencies. For the purpose of comparison, a graph has been plotted of normalized input impedance (Z_{11}) and resonant frequencies for real part and imaginary part of Z_{11} and shown in

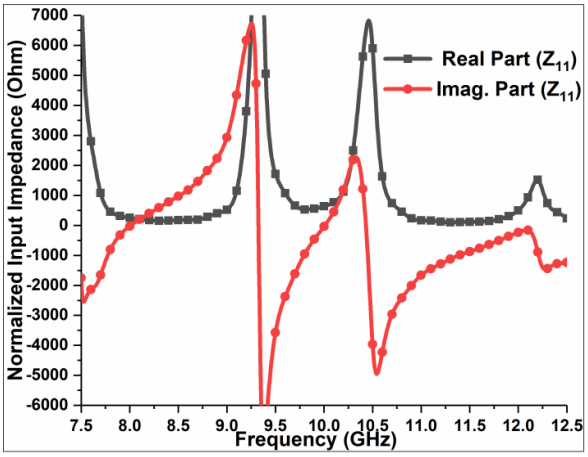

Figure 2.19 Normalized input impedance of the proposed absorber.

Figure 2.19. It is clear that, the real and imaginary parts of Z_{11} approach to zero and resonant at 8 GHz, 10 GHz, and 12 GHz, respectively. However, for other frequencies, the real and imaginary parts of Z_{11} possess different values.

2.4.4. Surface Current Distribution Analysis

The simulated surface current distribution of a single unit cell is given in Figure 2.20. The

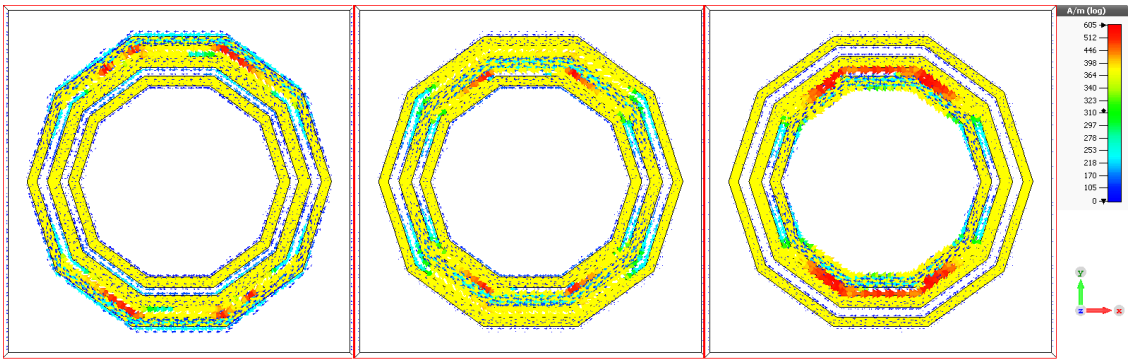

(a) (b) (c)

Figure 2.20 The Surface current distribution with top layer at (a) 8 GHz (b) 10 GHz, and (c) 12 GHz.

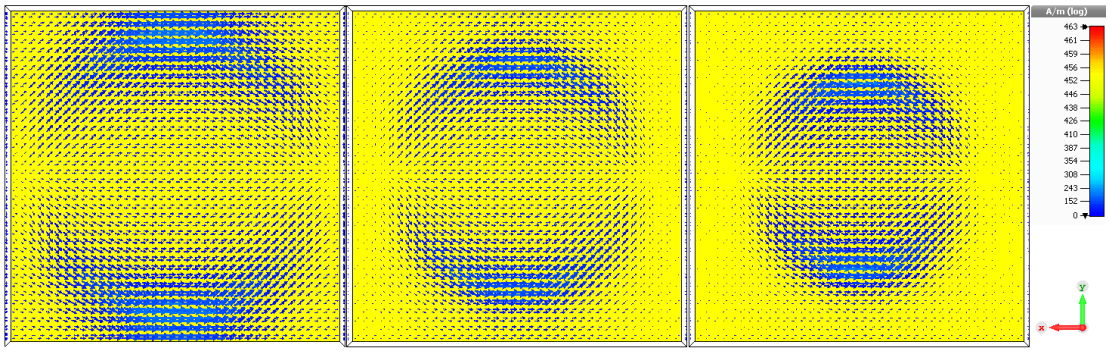

(a) (b) (c)

Figure 2.21 The Surface current distribution bottom layer at (a) 8 GHz (b) 10 GHz, and (c) 12 GHz.

Figure 2.20(a) to (c) shows the surface current distribution for the top decagon shaped metallic rings and the Figure 2.21(a) to (c) shows the surface current distribution for the bottom metallic layer for clear understanding. By analyzing the unit cell structure corresponds to top metallic rings and bottom metal layer it is concluded that the regular decagon shaped *MMA* is properly operating at each resonance frequency.

The concentration of current corresponds to 8 GHz resonant frequency is given by the largest ring of Figure 2.20(a) for the top view and Figure 2.21(a) for the bottom view, the middle resonance of 10 GHz frequency is given by the middle ring of Figure 2.20(b) for top view and Figure 2.21(b) for bottom view and the highest resonant frequency of 12 GHz is given by the smallest ring corresponding to the Figure 2.20(c) for top view and Figure 2.21(c) for bottom view. At the resonant frequencies, the value of reflectance coefficient parameter (S_{11}) is minimized. This is because the normalized input impedance of *MMA* structure approximates to the free space impedance. Therefore, results in maximized absorbance at the corresponding resonant frequency.

2.5. Chapter Summary

In this chapter 2, literature review of metamaterials, classification of metamaterials, and types of metamaterials have been studied. Then, a 3-D *CSFSS* has been proposed. The results show that the length of the resonant cylinder has a significant influence on the frequency response characteristics of the *FSS* and the *CSFSS* shows a stop-band, pass-band frequency response behavior. The polarization sensitive analysis of 3-D *CSFSS* for *TE* mode of *EM* wave has been demonstrated along with the effect of circumference variation by changing the *Rout*. The analysis shows the circumference of the resonant cylinder has a significant influence on the frequency response characteristics of the 3-D *CSFSS.* The frequency response peak could be tuned to the lower frequency just by varying the value of R_{out}. Again, the 3-D *CSFSS* unit cell structure found unaltered to any variation of oblique angles of incidence. At the value of *Rout* equals to 8 mm, the structure found highly polarization insensitive along with sharp resonant frequency peak at 6.04 GHz.

With the utilization of three-dimensional space, the unit cell size of the *FSS* can be further reduced. So, this design provides an extra degree of freedom when compared with its previous counterparts. Even though, by varying the height of *CSFSS* the reflection and transmission level at any frequency can be tuned and controlled. So it opens the way to fabricate a controllable and tunable *CSFSS*. This structure finds its applications in the area of stealth

technology, wireless communication, space communication, satellite communication, space vehicle navigation, metamaterial absorbers, radar and other communication areas.

Furthermore, we have proposed an inset feed microstrip antenna operating at 2.45 GHz of *ISM* band. Its behavior has been analyzed after modifying it with the defected ground plane and then loading it with mushroom-typed *EBG* structure. It has been observed that when the antenna is modified with *DG* structure, it doesn't only miniaturize the exited patch but also enhances the bandwidth, gain, and radiation efficiency. Furthermore, when the antenna is loaded with *EBG* structure, it enhances antenna directivity and gains. On the other hand, bandwidth and radiation efficiency are marginally affected. It has been also observed that the antenna directivity and gain increase throughout the band-gap of *EBG*. Whereas, the rest of parameters remain highly preserved.

Finally, a triple band regular decagon shaped *MMA* has been proposed. The proposed absorber exhibits three absorbance peaks for a normal angle of incidence with the magnitude of 96 %, 93.36 %, and 91.88 % at 8 GHz, 10 GHz and 12 GHz, respectively. The absorber exhibits a response with *FWHM* bandwidths are 457.9 MHz, 400.3 MHz and 455.5MHz, which is equivalent to 5.72 %, 4.00 %, and 3.80 %, respectively of the corresponding resonant frequency. A time domain analysis has been done which support only normal angle of incidence of EM wave. So frequency domain analysis for oblique angle of incidence analysis has been left for future work.

The absorption mechanism is explained by impedance matching between absorber and air. The analysis and results of triple band regular decagon shaped metamaterial absorber shows a good agreement between them and make it best suited at X-band regime. This *MMA* structure finds its applications in antenna designing and reduction of *Monostatic* and *Bistatic RCS* in military and stealth platform for lower detectable objects.

Chapter-3

Single-band Shorted Stubs Metamaterial Absorber

In this chapter, a novel design of a passive tuned *MMA* absorber using concentric loops with shorted stubs and split rectangular bars at GHz frequency has been proposed. The tuning is provided by the mean of varying the length of shorted stubs and split square rectangular bars. The parametric sensitivity response, in which a *MMA* structure has been analyzed under the influence of parameters such as inner radius (R_{in}), shorted stub length (a), and rectangular bar length (b). These parameters have been analyzed thoroughly. The results reveal that by varying the length of rectangular split bars and stubs distance between concentric rings, it is possible to obtain desired frequency response with near unity absorbance.

This mechanism results in significant scattering characteristics response along with flexibility to designer to control and optimize the resonant frequency in the microwave regime of the electromagnetic spectrum. The simulation response and analytical measurements have been analyzed under the assumption of the normal angle of incidence. The angular sensitivity response of *MMA* unit cell structure under an oblique angle of incident (θ) and polarization sensitivity (ϕ) for *TE* and *TM* modes of *EM* wave have been also analyzed. The proposed *MMA* analyzed under different parameters, which includes the effective magnetic permeability, effective electric permittivity, a normalized input impedance characteristics response and surface current distribution.

3.1. Metamaterial Absorber

Earlier, the design of a perfect *MMA* had been proposed with the absorbance magnitude of 88 % at 11.5 GHz of resonant frequency operating at *X-band* along with *FWHM* bandwidth of *4 %* by *Landy et. al.*[10]. Due to their small dimensions, lightweight and almost unity absorbance, various *MMAs* have been proposed and designed such as dipole [74], Jerusalem cross [75], square [76], circular [14], Pentagon [77], hexagon [78] and hybrid [13] loop structures, thus replacing the traditional absorbers. *MMA* has various properties and offer excellent features including near-unity absorbance [79], ultra-thin thickness [80], wide angles of incidence [55, 81] and polarization insensitivity [82], makes it suitable for antennas designs [83, 84], for the reduction of *RCS* in stealth technology [85, 86], in solar-photovoltaic and

thermo-photovoltaic cells to enhance the functioning of photo-detectors by heightening absorption mechanism [87] and also in wireless communication [88].

These structures have been consisting of an electrical ring resonator at the top, a dielectric layer in the middle, and a full metallic layer at the bottom, such that the net transmission approaches to zero. With these designs, both the effective permittivity and permeability altered or tuned in such a way to match the normalized impedance of structure to free space impedance, so that the absorbance can be maximized. A wide variety of methods have been proposed in the literature to improve the frequency response of *MMAs* [89-92].

The *MMA* unit cell can be designed as an active or passive metamaterial structure. *Zhang et. al.* [93] have demonstrated an active photo-excited tunable *MMA*. The silicon used to fill the gap in the metallic resonator and varying the location of the silicon insertion in the different critical regions results in frequency modulation of the resonance absorption peak. *Ma et. al.* [94] have proposed active tunable metamaterial absorber using varactor diodes and split ring resonator. The absorption frequency of the *MMA* can be tuned continuously by changing the bias voltage on both ends of the varactor diode. *Li et. al.* [95] have proposed an active tunable low-frequency absorber that uses *PIN* diodes loaded frequency selected surface (*FSS*) to provide tuning of the resonance frequency. *Qi et. al.* [96] have proposed a tunable *MMA* model based on the voltage-controlled diode, which acts as a variable resistor, whose impedance can be tuned by varying bias voltages and thus the absorbance achieved.

These active components commonly function as a switch to turn ON or OFF the top metallic *MMA* layer, result in the inductive or capacitive behavior of the *MMA* unit cell structure [97, 98]. Although this *MMA* offers flexibility and dynamic tuning in design, their feasibility and implementation are restricted because of the requirement of various active components along with separate bias voltage for each active components. That, in turn, brings complexity in design and do raise issues like miniaturization, economic cost, and fabrication of the design.

On the other hand, the passive *MMA* unit cell structure is excited by the incident *EM* wave and the tuning is provided by the structural parametric variations of the unit cell only. Since, there is no special circuitry or extra biasing voltage that has been involved to achieve the desired results. This way, the passive *MMA* unit cell design offers simplicity, compactness, low-cost small dimensions, lightweight and miniaturized of the absorber design.

Another issue in designing a frequency selective surface-based *MMA* is to analyze its response at a different angle of incidence and polarization sensitivity [99]. To deal with these issues a circular ring-based topology is most commonly used because of better completeness and accuracy with regards to the angular stability, polarization sensitivity, reflectance and transmittance coefficient, bandwidth and band separation [85]. Due to its regular arranged nature, the resonance frequency peak would occur in either of the two right angles or orthogonal coordinates.

It has been observed that in some particular designs geometry, the gap or spacing of the ring resonator with its adjacent neighboring resonator is very small. Such that it doesn't leave any space to drift the reflection and transmission coefficient band towards the lower side of the frequency band by increasing the resonator radius. One of the solutions to the problem is that it can be replaced by the large sized rings along with increasing and scaling the dimension of the structure again. This doesn't offer high flexibility. Thus, it becomes very difficult to realize large size circuit boards.

In this chapter, a novel design of the ring resonator using the concentric circle and square split with shorted stubs at *GHz* frequency has been introduced and some parts of it have been published in [79, 100].

3.2. Single-band Shorted Stubs Metamaterial Absorber (MMA)

In this thesis work, the design of the passive tuned concentric loops with shorted stubs *MMA* has been designed and analyzed [100]. However, the design of a perfect *MMA* must be simple, low profile, controllable, tunable, significant stable for the angle of incidence and highly polarizations insensitive to the impinged *EM* wave. By making these initial assumptions, we have proposed a simple *MMA* design based on concentric loops with shorted stubs and split rectangular bars.

The geometry of the *MMA* unit cell with all its parameters value has been shown in Figure 3.1. Whilst, the corresponding values of frequency response peaks for absorbance, reflectance and transmittance have been depicted in Figure 3.2. The *MMA* consists of the metallic patch at the top while at the bottom; a full copper layer is placed. So that transmission coefficient value could reduce to zero.

Both layers consist of same copper metal with a conductivity of 5.8×10^7 s/m**.** The metallic patch is printed on a low-cost *FR-4* substrate by means of standard photolithographic

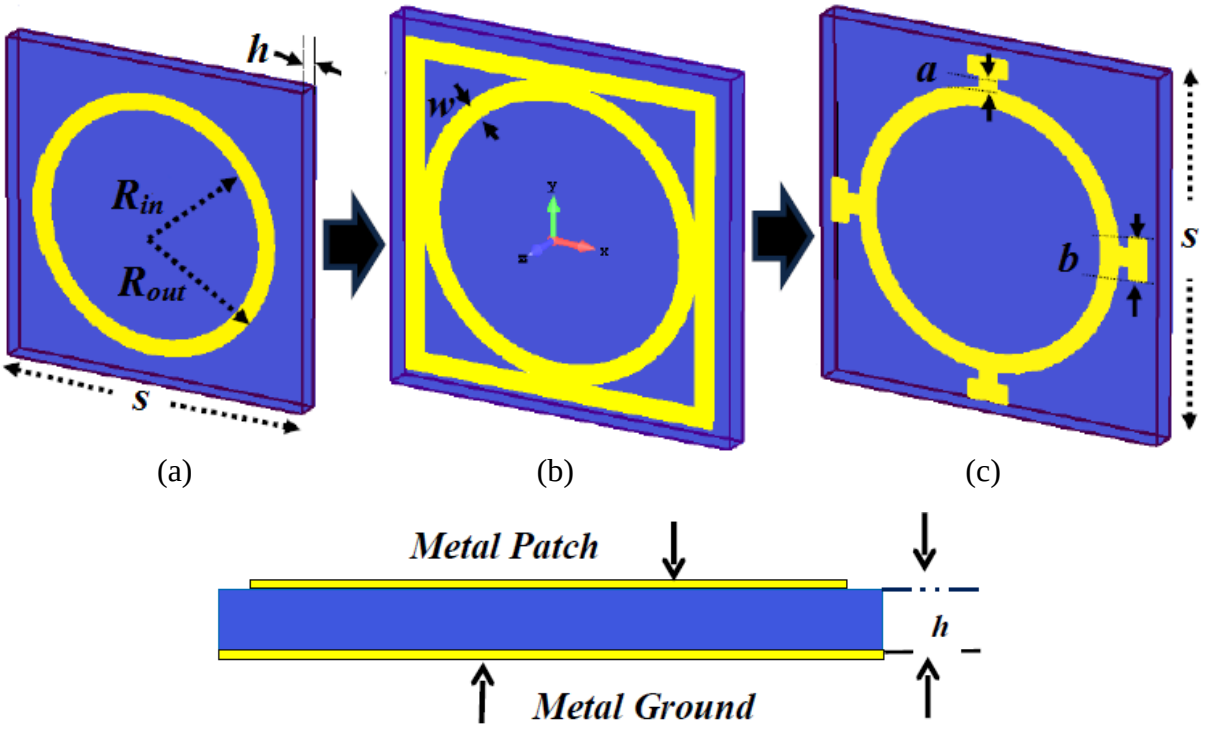

Figure 3.1 (a) Single circular loop (b) concentric circle and square loops (c) modified structure with shorted stubs and split rectangular bars, and (d) side view of the proposed MMA. Unit cell dimensions: S = 4.43 mm, R_{in} = 1.59 mm, R_{out} = 1.79 mm, h = 0.31 mm and w = 0.2 mm.

techniques of the dielectric substrate with the relative permittivity (ε_r) and loss tangent (*tan δ)* values are 4.3 and 0.025, respectively. By proper optimization of the metallic patch structure on a substrate, the *MMA* with nearly unity absorption magnitude can be formulated.

At a normal angle of incident *EM* wave, a simple circular ring unit cell *MMA* structure is designed and simulated as shown in Figure 3.1(a). Then the design parameters are adjusted and optimized. For *TE* and *TM* modes, the resonance peak appeared at the frequency of 15.99 GHz with 99.99 % unity absorbance corresponding to *FWHM* bandwidth of 4.74% in *Ku-band* as shown in Figure 3.2(a).

After this, the structure is modified and new design consists of two vertically aligned concentric loops one underneath another is formed as depicted in Figure 3.1(b). The simulation result reveals that a reduction in the resonant frequency peak from 15.99 GHz to 12.17 GHz with an absorbance value of 98.19 % and *FWHM* bandwidth of 5.62 % has been observed as shown in Figure 3.2(b).

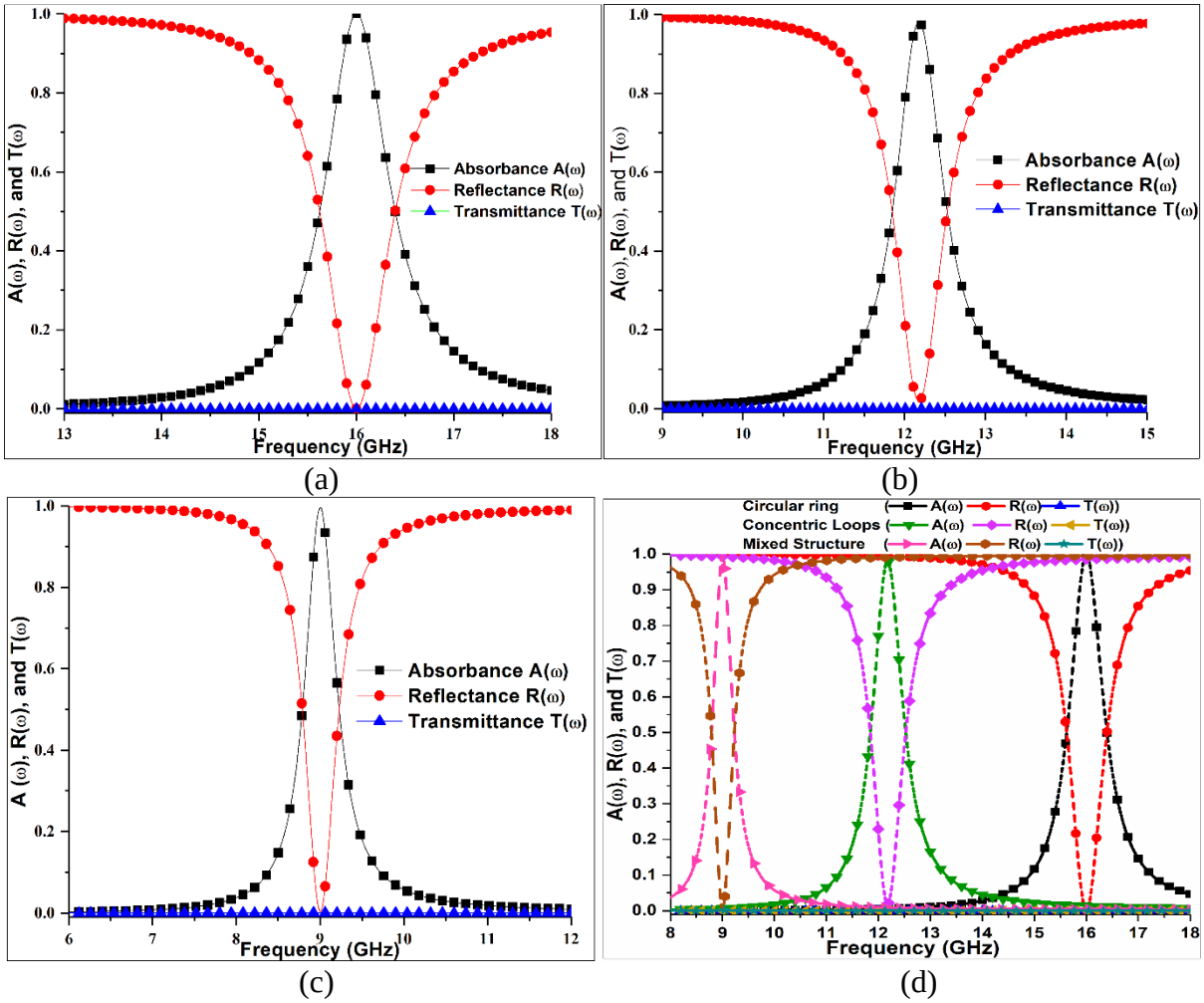

Figure 3.2 Resonance curves for (a) circular ring (b) concentric circle and square (c) modified split ring with shorted stubs, and (d) comparisons of all structure.

Later, the *MMA* unit cell is further modified by splitting the square loop and the concentric loops are shorted using stubs in a manner that the *MMA* unit cell structure always remains symmetrical and extremely insensitive to polarization sensitive and oblique angle of incidence resulting further drift towards lower resonant frequency as shown in Figure 3.1(c). Simulation result reveals that a continuous reduction in the resonant frequency peak from 12.17 GHz to 9 GHz while maintaining the absorbance value to *99.68 %* and *FWHM* bandwidth of 4.95 % in *X-band* as depicted in Figure 3.2(c).

On combining all, we conclude that frequency shift of 3.82 GHz is obtained between 1st resonant peak and 2nd resonant peak, while, the frequency shift of 3.17 GHz is found between 2nd resonant peak and 3rd resonant peak. A passive frequency tuning between 1st to 3rd resonant peaks of 6.99 GHz is achieved, which cover almost the entire *X- band* and *Ku-band* of the frequency spectrum as shown in Figure 3.2(d).

3.3. Design Principle of Metamaterial Absorber (MMA)

The design principal of *MMA* begins with making assumptions that the *MMA* surface is an effectively homogeneous medium, the *EM* wave incident upon a surface may be reflected, transmitted or absorbed [101, 102]. For the efficient design of *MMA*, it is necessary to minimize the reflection and transmission parameter. The expression of absorbance is presented as:

$$A(\omega) = 1 - T(\omega) - R(\omega) \tag{3.1}$$

Where $A(\omega)$, $T(\omega)$ and $R(\omega)$ are the Absorbance, transmission, and reflection spectrum with the function of frequency ω, respectively [103, 104]. They are related to scattering coefficient (S) for *TE* and *TM* modes of impinged *EM* wave, as:

$$T(\omega) = |S_{21}|^2 = |S_{12}|^2 \text{, and}$$

$$R(\omega) = |S_{11}|^2 = |S_{22}|^2 \tag{3.2}$$

Where, $|S_{21}|^2$ is the transmission scattering coefficient and $|S_{11}|^2$ is the reflectance scattering coefficient. So the Equation (3.1) is modified to:

$$A(\omega) = 1 - |S_{21}|^2 - |S_{11}|^2 \tag{3.3}$$

In order to achieve almost unity absorbance, according to the formula of Smith's parameter inversion [105]:

$$S_{21} = S_{12} = \left[\cos(n_{eff} k_0 h) - \frac{j}{2}\left(Z_{eff} + \frac{1}{Z_{eff}} \right) \sin(n_{eff} k_0 h) \right]^{-1} e^{-jk_0 h} \tag{3.4}$$

$$S_{11} = S_{22} = \left[\frac{j}{2}\left(\frac{1}{Z_{eff}} - Z_{eff} \right) \sin(n_{eff} k_0 h) \right] t \tag{3.5}$$

Where $k_0 = \omega/c$ is the free space wave number, ω and c are the angular velocity and speed of light in vacuum, and h is the height of the substrate [106]. The definition for the effective refractive index is

$$n_{eff}(\omega) = n'_{eff}(\omega) + j n''_{eff}(\omega) \tag{3.6}$$

and for complex wave impedance index

$$Z_{eff}(\omega) = Z_{eff}^{'}(\omega) + jZ_{eff}^{''}(\omega) \tag{3.7}$$

Where the refractive index

$$n_{eff}(\omega) = \sqrt{\mu_{eff}(\omega)\varepsilon_{eff}(\omega)} \tag{3.8}$$

and wave impedance is given by

$$Z_{eff}(\omega) = \sqrt{\frac{\mu_{eff}(\omega)}{\varepsilon_{eff}(\omega)}} \tag{3.9}$$

When $Z_{eff}(\omega)$ approaches 1, effective wave impedance matching with free space impedance $Z_0(\omega)$, so the Equation (3.4) and Equation (3.5) reduce to:

$$S_{12} = S_{21} = \left[\cos(n_{eff}k_0h) - j\sin(n_{eff}k_0h)\right]^{-1} e^{-jk_0h} \tag{3.10}$$

$$S_{11} = S_{22} = \frac{j}{2}\left(\frac{1}{Z_{eff}} - Z_{eff}\right)\sin(n_{eff}k_0h) = 0 \tag{3.11}$$

Equation (3.11) indicated that when Z_{eff} approaches to 1, there will be no reflection from the *MMA* surface, given by

$$\left|S_{11}\right|^2 = \left|S_{22}\right|^2 = R(\omega) \approx 0$$

This corresponds to the condition where the *MMA* wave impedance is matched to that of free space impedance $Z_0(\omega)$. However, when $Z_{eff}(\omega) \approx 1$ the transmission term solely left and according to the *Euler's Identity*, Equation (3.10) can be transformed to:

$$S_{12} = S_{21} = \left[e^{-jn_{eff}k_0h}\right]^{-1} e^{-jk_0h} \Rightarrow S_{12} = S_{21} = \left[e^{jn_{eff}k_0h}\right] e^{-jk_0h}$$

So,

$$S_{12} = S_{21} = e^{j(n_{eff}-1)k_0h}$$

By using Equation (3.6),

$$S_{12} = S_{21} = e^{j(n_{eff}^{'}-1)k_0h} e^{-n_{eff}^{''}k_0h} \tag{3.12}$$

Therefore, the electromagnetic wave transmission rate reduces to:

$$T(\omega) = |S_{21}|^2 = |S_{12}|^2 = e^{-2n''_{eff}k_0h} \tag{3.13}$$

From Equation (3.8), it is clear that transmission rate depends and concerned with the n''_{eff} [107]. Whilst, the wave vector (k_0) and thickness (h) of *MMA* is always remained fixed. So, it is necessary to have a large value of imaginary part of refractive index component [10, 83, 108]. When n''_{eff} approaches to infinity, then

$$\lim_{n''_{eff}\to\infty} T(\omega) = \lim_{n''_{eff}\to\infty} e^{-2n''_{eff}k_0h} = 0 \tag{3.14}$$

Thus, from Equation (3.1), A(ω) = 1 is achieved. This is the condition for unity absorbance. So, the Equation (3.14) indicates that n''_{eff} is the main parameter that is responsible for absorbance.

In addition, we conclude that the overall loss of the impinged *EM* wave in the substrate is decided by the thickness for h of the substrate and in order to make n'' high, the thickness (h) should be as small as possible but should not affect impedance matching condition. However, it is possible to determine the values of effective wave impedance and effective refractive index directly from the results for S_{11} and S_{21} as given in Equation (3.4) and (3.5), respectively [109].

$$n_{eff} = \frac{1}{k_0 d}\cos^{-1}\left(\frac{1}{2S_{21}}(1 - S_{11}^2 + S_{21}^2)\right) \tag{3.15}$$

$$Z_{eff} = \sqrt{\frac{(1+S_{11})^2 - S_{21}^2}{(1-S_{11})^2 - S_{21}^2}} \tag{3.16}$$

When the effective wave impedance matches to free space impedance such that $Z_{eff}(\omega)$ approaches to 1, then Equation (3.9) reduces to

$$\mu_{eff}(\omega) = \varepsilon_{eff}(\omega) \tag{3.17}$$

and Equation (3.8) reduces to

$$n_{eff}(\omega) = \varepsilon_{eff}(\omega) \Rightarrow n_{eff}(\omega) = \mu_{eff}(\omega) \tag{3.18}$$

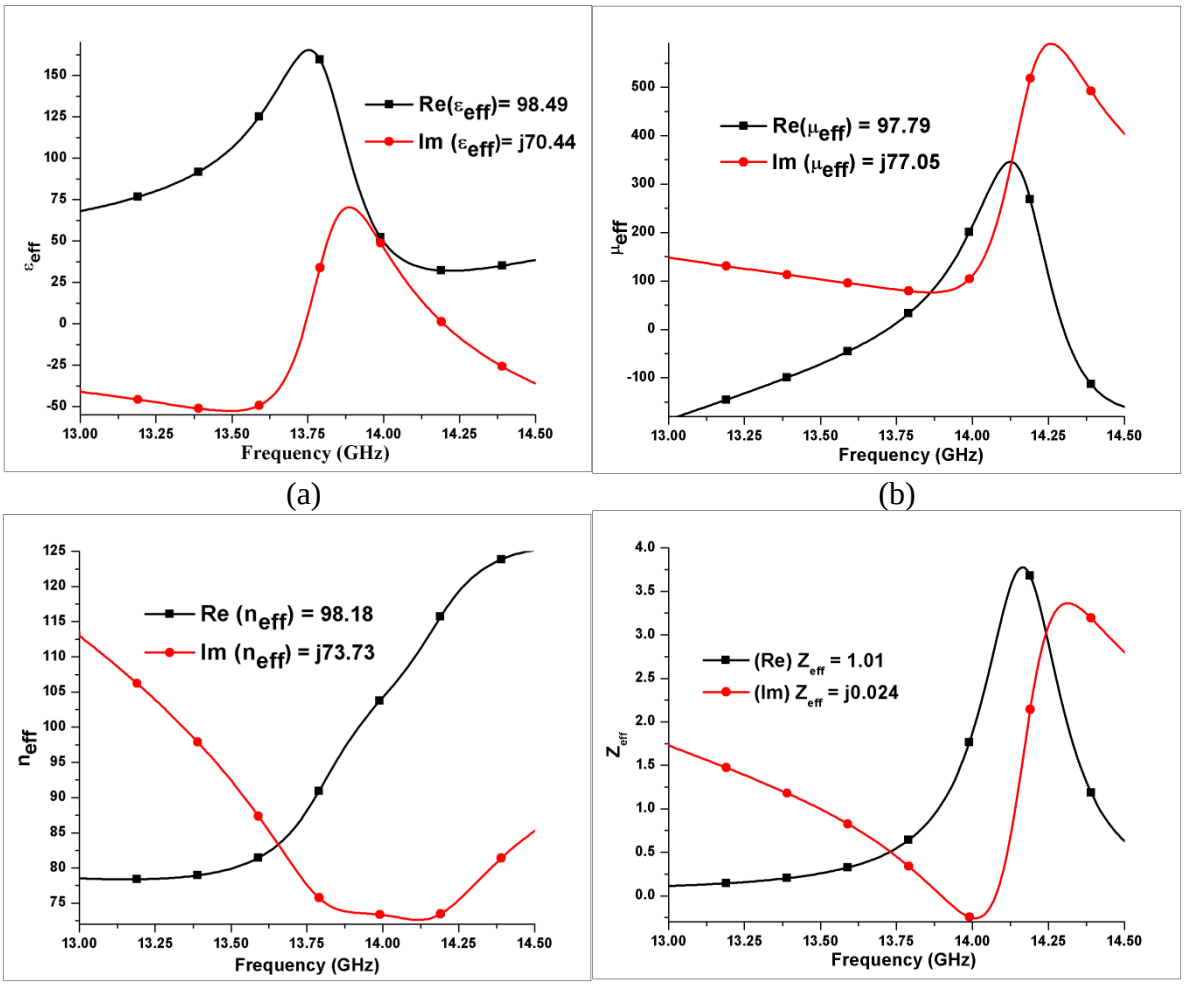

Figure 3.3 Resonance curves for the Real and Imaginary part of (a) effective electric permittivity ($\varepsilon_{eff}(\omega)$) (b) effective magnetic permeability ($\mu_{eff}(\omega)$) (c) effective refractive index ($n_{eff}(\omega)$), and (d) effective wave impedance ($Z_{eff}(\omega)$).

The refractive index is calculated by the *Kramers–Kronig* relation and by arranging the relations, the effective magnetic permeability and effective electric permittivity can be extracted directly from S-parameters as given in Equation (3.15) and Equation (3.16) [110-112]. At, 13.89 GHz for the proposed *MMA* the real and imaginary parts of the effective electric permittivity $\varepsilon_{eff}(\omega)$, effective magnetic permeability $\mu_{eff}(\omega)$, effective refractive index $n_{eff}(\omega)$ and effective wave impedance $Z_{eff}(\omega)$ have been given in Figure 3.3(a), (b), (c) and (d), respectively.

The values for $\varepsilon_{eff}(\omega)$ is found to be (98.49 + j 70.44) and for $\mu_{eff}(\omega)$ is (97.79 + j77.05), which is almost equal. Also, the value for $n_{eff}(\omega)$ is (98.18 + j73.73) and is well matched according to Equation (3.8) and the $Z_{eff}(\omega)$ value comes to be (1.01 + j0.024) and that matches the condition for free space impedance.

3.4. Sensitivity Response Analysis

The *MMA* unit cell consisted of the metallic patch at the top while at the bottom; a full copper layer is placed. So that transmission coefficient value would reduce to zero. Both layers consist of same copper metal with a conductivity of 5.8×10^7 s/m. The metallic patch is printed on a low-cost *FR-4* substrate by means of standard photolithographic techniques with a relative permittivity (ε_r) of the dielectric substrate is 4.3 and the loss tangent (tan δ) is 0.025.

By proper optimizing the metallic patch structure on a substrate, *MMA* with nearly unity absorption magnitude can be formulated. The simulated response of the tuned *MMA* is carried out using a Finite Integration Technique (*FIT*) based *CAD* solver. Along the direction of *x-axis* and *y-axis* the unit cell boundary conditions has been assigned, while Z_{max} is assigned as an open (Add Space) along the direction of wave propagation and Z_{min} as a Perfect Electric Conductor (*PEC*) as shown in Figure 3.4.

The simulation results have been adjusted by setting appropriate no. of floquet modes. The sensitivity response of *MMA* structure has been simulated, analyzed and optimized. This is further divided in following two types namely parametric sensitivity and angular sensitivity response.

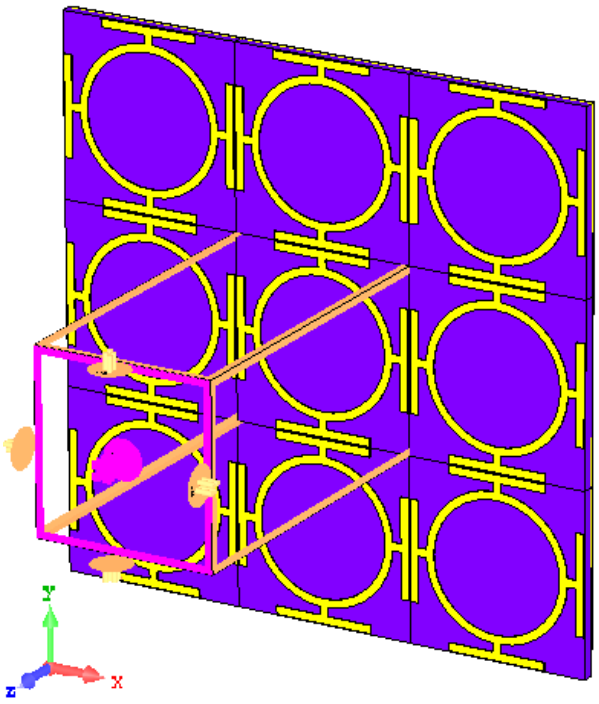

Figure 3.4 Simulation of proposed MMA unit cell structure.

3.4.1. Parametric Sensitivity Response

Parametric sensitivity is defined as the deviation in frequency response with the rate of change of parameters such as shorted stub length (a) and rectangular bar length (b). This is observed in order to find out and study the sensitivity, behaviour and reliability of *MMA* on these parameters. By varying these parameters, the inductance and capacitance of the tuned *MMA* are adjusted to achieve the condition of resonance. As the inductance and capacitance are defined as

$$X_L = \omega_L L \; ; \;\; X_C = \frac{1}{\omega_C C} \tag{3.19}$$

Therefore, at only one resonant frequency these two reactance values would become equal. This is called the condition of resonance and follows Equation (2.5). In other words, the condition of resonance occurs when effective wave impedance matched to the free space impedance and the resonant frequency can be tuned by varying inductance or capacitance, as given in Equation (2.7) and (2.8). Therefore, the *MMA* can be tuned by varying stub length (a) and bar length (b) and then finally the results get optimized.

(a) Effect of Shorted Stubs Length on Resonant Frequency

A graph is plotted for resonant frequencies versus absorbance for the different values of shorted stubs length (a). Whose values vary between 0 to 0.20 mm as depicted in Figure 3.5 and its comparison is made in Table 3.1. It is being shown in Figure 3.5 that increase in the values of 'a' results in a continuous reduction in the resonant frequency from

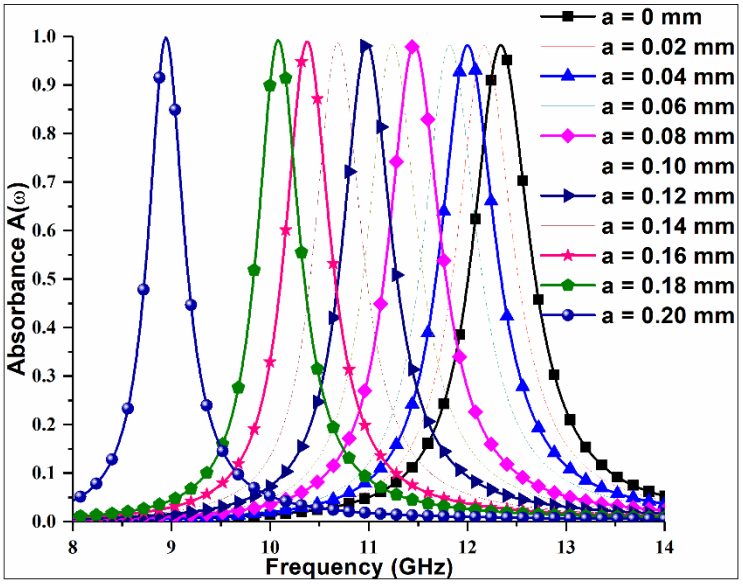

Figure 3.5 Variation of shorted stubs length (a).

Table 3.1 Variations of shorted stubs length (a).

	Stub Length (a) mm	Resonant Frequency (f_r) GHz	Absorbance Magnitude (%)	Deviation (%)
Bar length (b)=3.983 mm	0	12.34	98.22	0
	0.2	12.17	98.17	1.38
	0.4	12.00	98.16	2.76
	0.6	11.82	98.16	4.21
	0.8	11.46	98.25	7.13
	1.0	11.24	98.36	8.91
	1.2	10.98	98.45	11.02
	1.4	10.69	98.68	13.37
	1.6	10.38	98.96	15.88
	1.8	10.08	99.21	18.31
	2.0	8.94	99.73	27.55

12.34 GHz to 8.94 GHz with the absorbance magnitude of above then 98.16 % achieved for all the results.

Therefore, almost unity absorbance is observed with a total frequency shift of 27.55 %. This behavior of *MMA* is predicted because of the variation in the capacitance of the *MMA*, Which gets modified every time as the value of 'a' changes. The gap between the adjacent neighboring *MMA* unit cell changes with the variation in the values of 'a'. Therefore, as the distance or the gap between the neighboring unit cell reduces, it increases the effective capacitance *MMA* unit cell, which is inversely proportioned to the distance between unit cell as given in Equation (2.7) and the area of the unit cell and the relative permittivity is assumed fixed.

Thus, the resonant frequency of the *MMA* structure decreases. So, by adjusting the gap between adjacent neighboring unit cell or varying *a*, we can control and optimize the resonant frequency of the *MMA.* In Table 3.1, the value of the rectangular bar length keep fixed to 3.983 mm and then the stub length varied. The absorbance values are maintained well above 98.16 % while a continuous reduction in the resonant frequency observed till a = 0.2 mm.

(b) Effect of Split Bars Length on Resonant Frequency

The frequency shift occurs without substantially affecting the absorbance characteristics. The absorbance minima and bandwidth in the curve are reasonably maintained, only shifted to a lower frequency. A graph is plotted for resonant frequencies and absorbance at different

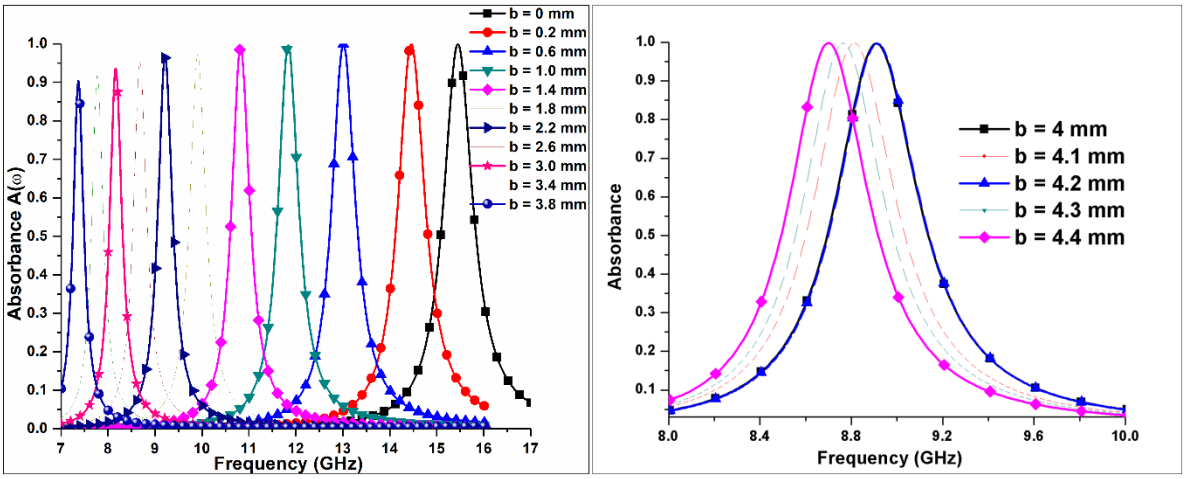

(a) (b)

Figure 3.6 Variation of rectangular bars length (a) between 0 to 3.8 mm and (b) between 4 to 4.4 mm.

values of split rectangular bars length (*b*), varies between 0 to 3.8 mm as shown in Figure 3.6(a) and its comparison is given in Table 3.2. It is clear from the figure that, as we start increasing the values of 'b' from 0 to 3.8 mm, a continuous shift in f_r has been observed from 15.46 GHz to 7.37 GHz towards the lower resonant frequency. So, a total of 52.33 % of a shift in resonant frequency observed.

The value of absorbance is well maintained until 'b' becomes 11.84 GHz then it starts decreasing but always keeps the absorbance magnitude well above 90.33 %. So the length of the rectangular bar plays an important role in moldings the behavior of *MMA*, as it increases the inductance which in turn reduced the resonant frequency as stated in Eq. (2.5) and Eq. (2.8).

Table 3.2 Variation of rectangular bars length (b) between 0 to 3.8 mm.

	Bar length (b) in mm	Resonant Frequency (f_r) GHz	Absorbance Magnitude (%)	Deviation (%)
Stub Length (a)= 0.2 mm	0	15.46	99.97	0
	0.2	14.46	99.90	6.47
	0.6	13.01	99.93	15.85
	1.0	11.84	99.56	23.42
	1.4	10.83	98.92	29.95
	1.8	9.91	97.04	35.90
	2.2	9.22	96.61	40.36
	2.6	8.68	95.00	43.86
	3.0	8.17	93.61	47.15
	3.4	7.78	91.92	49.68
	3.8	7.37	90.33	52.33

Another important behavior is observed during simulation response analysis of tuned *MMA*, that when we increase the rectangular bar length (*b*) further from 4 to 4.4 mm, the resonant frequency starts increasing. At b = 3.8 mm, the value of f_r is 7.37 GHz with the absorbance of 90.33 %, while at b = 4.0 mm, it becomes 8.91 GHz with the absorbance of 99.65 % as shown in Figure 3.6(b). Again, increasing the value of 'b' would result in positive/negative minor shift in resonant frequency.

Therefore, this behavior is observed because of the edges of rectangular bar start colliding and meeting with each other and forming the square loop again. These abnormalities in the *MMA* results are caused because of *MMA* structure transition from Figure 3.1(c) to Figure 3.1(b). This justifies and verifies the superiority and requirement of the proposed structure above the previous two proposed structures.

Thus, the simulation results summarize that the modified structure has potential to act as a tuned circuit with almost unity absorbance. The resonant frequency of modified structure could be adjusted by varying the width of the stubs and also the length of rectangular patches belongs to the split rectangular.

(c) Thickness of the Dielectric Substrate of the MMA Structure

The thickness of the proposed structure [100] Substrate is very small in the proposed model and is adjusted to 0.31 mm, so fulfilling its promise for an ultra-thin metamaterial absorber structure. The numerical simulation shows above 90.33% absorbance for frequency ranges

Table 3.3 Comparing results with some other MMA reported previously.

Metamaterial Absorber	References	Centre Frequency f_0 (GHz)	Unit Cell Size (mm)	Thickness of dielectric (mm)	FWHM	Polarization Insensitive
Our Work	[100]	8.94	4.43	0.31 (0.0092 λ_0)	5.011%	Yes
Ghosh et al	[113]	10.05	7.1	2 (0.067 λ_0)	72.64% (43% at -10dB)	No
Lee et al	[114]	10	14.2	0.6 (0.02 λ_0)	11%	Yes
Liu et al	[115]	11.11	40	0.8 (0.0296 λ_0)	20 %	Yes
Soheilifar and Sadeghzadeh	[116]	9.88	7.35	0.25 (0.0082 λ_0)	4.35%	Yes
Cheng et al	[117]	10.91	6	0.4 (0.0145 λ_0)	-	Yes

from 7.37 GHz to 15.99 GHz through circular to modified *MMA* design, which is in good agreement with the experimental results.

The proposed *MMA* structure has been compared with previously proposed *MMA*, operating with center frequency lies in X-band in Table 3.3. It is definitely clear that the thickness of structure is improved over [113], [114], [115] and [117], while [116] structure is found ultra-thinner. Also, structure [113], [114] and [115] offer better *FWHM* bandwidth as compare to proposed structure, whereas in [116] bandwidth response is poor and [117] has not performed the bandwidth analysis. The entire structures offer better polarization insensitivity except the structure given by [113]. Therefore, the proposed structure is in good agreement and provides an alternative for ultrathin passive tuned *MMA*.

3.4.2. Angular Sensitivity Response

The Angular sensitivity response for the proposed *MMA* structure corresponding to the oblique angle of incidence (θ) and polarization sensitivity (ϕ) are of utmost importance and prime concern. Without analyzing these response results the *MMA* structure would not be realized. Since, majority of the structures act substantially good under the influence of normal angle of incidence and polarization sensitivity. However, as the angle (θ, ϕ) varies, its absorbance magnitude starts reducing and the behavior of *MMA* turns poor and unreliable.

(a) TE and TM modes for oblique angle of incidence

For a homogeneous medium at a normal angle of incidence of *EM* wave on the surface of *MMA*, the *Fresnel Reflectivity* represented by

$$R(\omega) = \left| \frac{Z_{eff}(\omega) - Z_0(\omega)}{Z_{eff}(\omega) + Z_0(\omega)} \right|^2 \tag{3.20}$$

At unit absorbance condition, the effective wave impedance becomes equal to free space impedance and Equation (3.20) reduces to zero. But for the oblique angle of incidence, the zero reflection condition changes and it varies as the angle of incidence changes. For the *S-polarized* light in which the electric field of *EM* wave is perpendicular to the *MMA* plane. The *Fresnel Reflectivity* is given as:

$$R_{\perp}(\omega) = \left| \frac{Z_{eff}(\omega)\cos\theta_i - Z_0(\omega)\cos\theta_t}{Z_{eff}(\omega)\cos\theta_i + Z_0(\omega)\cos\theta_t} \right|^2 \tag{3.21}$$

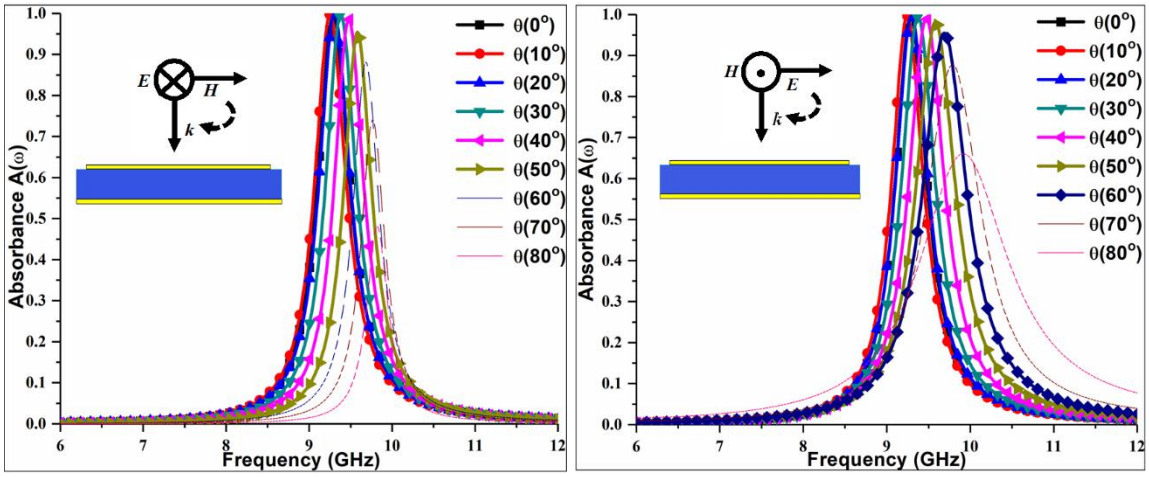

(a) (b)

Figure 3.7 Oblique angle of incidence for (a) TE mode and (b) TM mode.

For the *P-polarized* light in which the electric field of *EM* wave is parallel to the *MMA* plane. The *Fresnel Reflectivity* is given as:

$$R_{\parallel}(\omega) = \left| \frac{Z_{eff}(\omega)\cos\theta_t - Z_0(\omega)\cos\theta_i}{Z_{eff}(\omega)\cos\theta_t + Z_0(\omega)\cos\theta_i} \right|^2 \tag{3.22}$$

At oblique angle of incidence, the *MMA* shows incapability in circulating the current between two copper metallic layers lying above and beneath the dielectric substrate and is governed by the relationship given above for *TE* and *TM* mode. So, the angular sensitivity response analysis have been made from 0^0 to 80^0 corresponds to *TE* and *TM* modes of electromagnetic *EM* waves in Figure 3.7 and results are summarized in Table 3.4.

Table 3.4 Oblique angle of incidence for TE and TM modes of EM wave.

Angle(θ) for TE	**Resonant Frequency (f_r) GHz**	**Absorbance (%)**	**Deviation (%)**	**Angle (θ) for TM**	**Resonant Frequency (f_r) GHz**	**Absorbance (%)**	**Deviation (%)**
0^0	9.29	99.63	0	0^0	9.28	99.60	0
10^0	9.26	99.70	-0.32	10^0	9.25	99.66	-0.32
20^0	9.31	99.93	0.22	20^0	9.29	99.62	0.11
30^0	9.38	99.83	0.97	30^0	9.38	99.46	1.08
40^0	9.48	98.68	2.05	40^0	9.48	99.15	2.16
50^0	9.58	95.38	3.12	50^0	9.58	98.20	3.23
60^0	9.68	88.10	4.20	60^0	9.69	95.49	4.42
70^0	9.76	74.05	5.06	70^0	9.79	87.73	5.50
80^0	9.82	48.05	5.70	80^0	9.92	66.04	6.90

As θ varies, the resonance frequency, the bandwidth and the maximum absorption peak undergoes a small shift but almost unaffected. The analysis has been made at a resonant frequency of 9.29 GHz for *TE* mode as depicted in Figure 3.7(a). At $\theta = 0^0$ the first resonance peak observed at 9.29 GHz with the absorbance of 99.63 %. At $\theta = 10^0$, the value of resonance peak shifted towards negative direction by 0.32 % and become equals to 9.26 GHz with the absorbance of 99.70 %. Then the incident angle is extended to 20^0, 30^0, 40^0 and 50^0.

It is observed that above 90% the absorbance is maintained for the incident angle of 50^0 the resonant frequency becomes 9.58 GHz with a shift of 3.12 % while maintaining the absorbance magnitude of above 95.38 %. Then, the value of absorbance starts decreasing. At $\theta = 70^0$, the resonant frequency becomes 9.76 GHz with a shift of 5.06 % and the absorbance magnitude of 74.05 %. This is observed to be the utmost angle where *MMA* maintains at least 50% of absorbance for the incident *EM* waves.

For *TM* mode the resonant frequency occurred at 9.28 GHz as depicted in Figure 3.7(b). At $\theta = 0^0$ the first resonance peak observed at 9.28 GHz with the absorbance of 99.60 %. When the angle of incident is altered to 10^0, the value of resonance peak slightly shifted towards negative direction by 0.32 % and become equals to 9.25 GHz with the absorbance of 99.66 %. Then the incident angle is extended to 20^0, 30^0, 40^0, 50^0 and 60^0, respectively.

It is observed that above 90% the absorbance is maintained for the incident angle of 60^0 with the resonant frequency of 9.69 GHz and a shift of 4.42 % while maintaining the absorbance magnitude of above 95.49%. Then, the value of absorbance starts decreasing. At $\theta = 80^0$, the resonant frequency becomes 9.92 GHz with a shift of 6.90 % and the absorbance magnitude of 66.04 %. This is observed to be the utmost angle where *MMA* maintains at least 50% of absorbance for the incident *EM* waves.

(b) TE and TM mode of Polarization Sensitivity

A polarization sensitivity analysis has also been made for polarization angle (ϕ) between 0° to 90° for both *TE* and *TM* modes of *EM* field. Their results are depicted in Figure 3.8(a) and (b), respectively. The analysis has been made at the resonance frequency of 9.29 GHz for *TE* and 9.28 GHz for *TM* mode respectively. It is observed that the variation in polarization angle (ϕ) from 0° to 90° for both *TE* and *TM* modes have no effect on the resonance frequency and it will remain almost same and maintained the absorbance magnitude of above 99.60 %. That proves the high polarization insensitivity nature of proposed *MMA* structure.

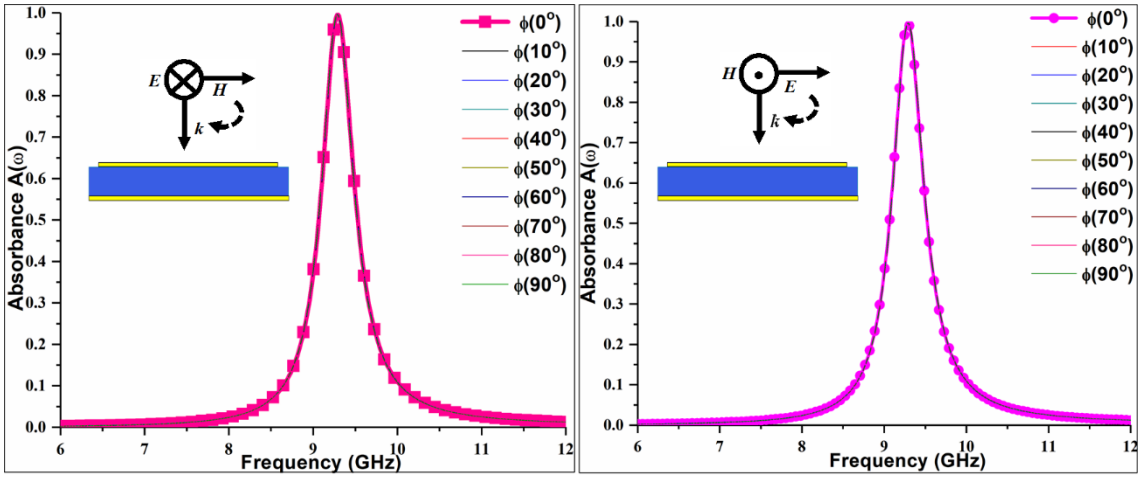

(a) (b)

Figure 3.8 Polarization sensitivity response (ϕ) for TE mode and (b) TM mode.

3.5. Surface Current Distribution Analyses

The simulated surface current distribution analysis for a single unit cell of *MMA* structure has been depicted in Figure 3.9. The Figure 3.9(a) shows the front view for surface current distribution resonant at 9.29 GHz. Whereas, the back view of surface current distribution for *TE* modes of *EM* wave has been given in the Figure 3.9(b). The *MMA* unit cell structure surface current distribution analyses indicate that it is operating and behaving properly at the corresponding resonant frequency. The concentration of surface current has been observed in the entire metallic unit cell structure.

This indicates that the rectangular bar length (b) and shorted stubs length (a) play an equal role in the circular loop to decide the resonant frequency. The top layer and bottom

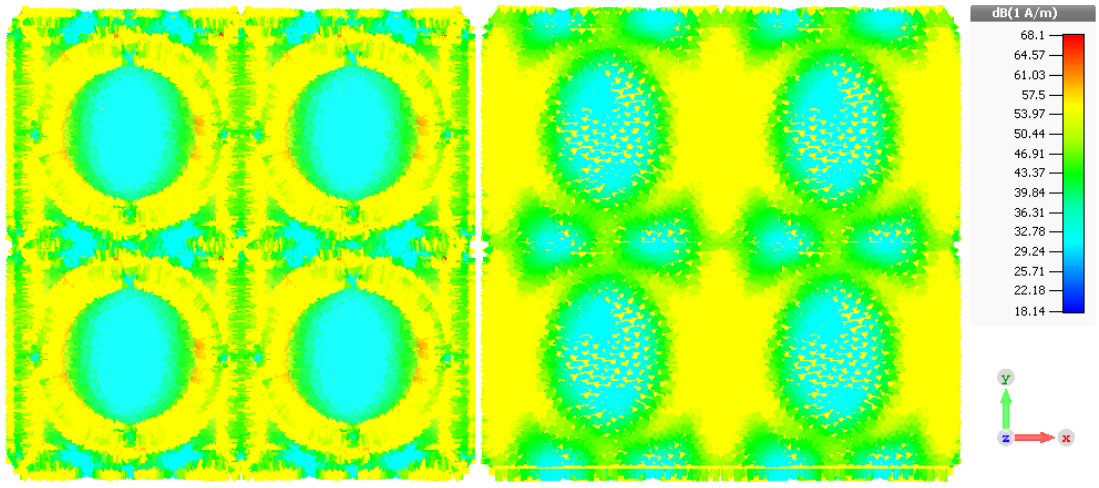

(a) (b)

Figure 3.9 Surface current distribution (a) front view and (b) back view of the proposed MMA structure.

layers resonance are perfectly matched. At the point of resonance, the reflection coefficient value reduces to minima. This is because of the closely matched effective input wave impedance of *MMA* structure to free space impedance. Thus, this would results in maximized absorbance at the corresponding resonant frequency.

3.6. Fabrication and Measurement of MMA

The unit cell of the proposed *MMA* is simulated with the boundary conditions, which means that the absorber is an infinite array and hardly fabricated in reality. To investigate its scattering parameters in practice, a model of 120×150 mm^2 composed of 726 unit cell has been considered for fabrication. This composite structure is fabricated of metallic copper layers for patch and ground plane and flame retardant FR4 for dielectric substrate and shown in Figure 3.10. The dimension of the proposed metamaterial absorber has been optimized by

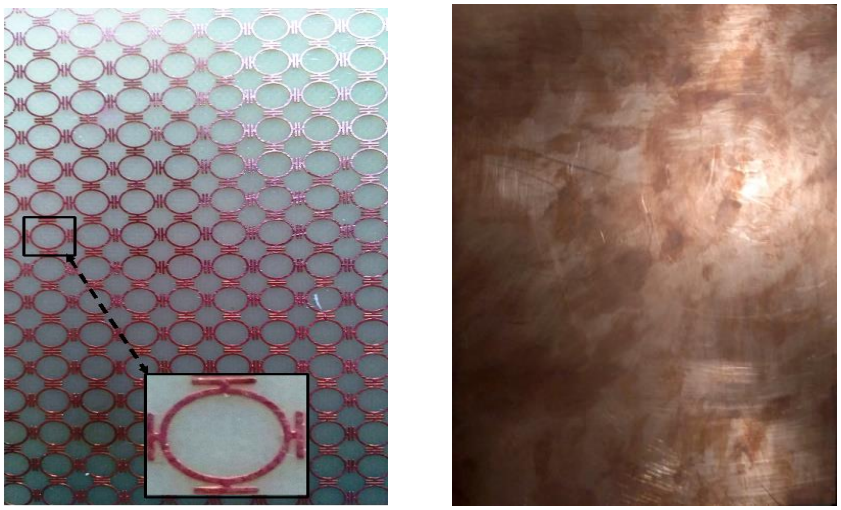

(a) (b)

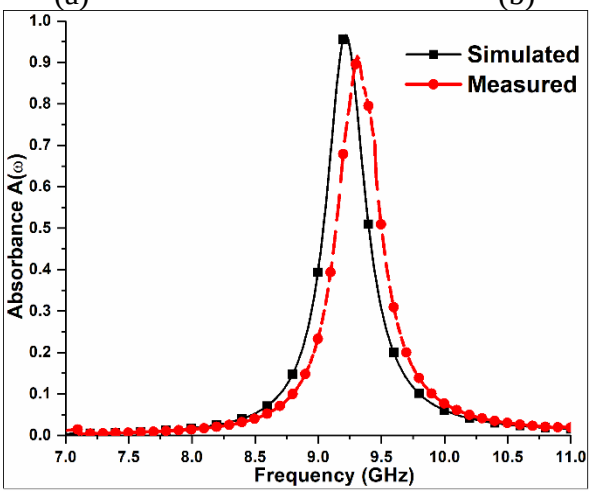

(c)

Figure 3.10 120 mm × 150 mm panel (a) front view (b) back view, and (c) measured results of the proposed *MMA* structure.

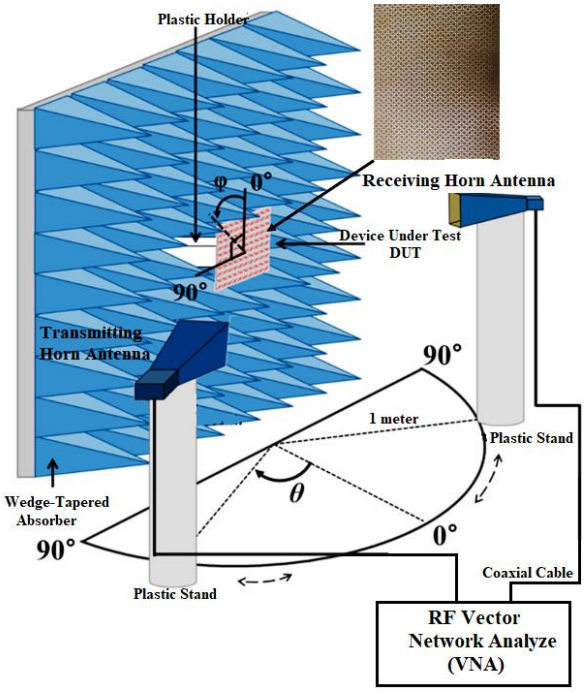

Figure 3.11 Block diagram of the experimental setup

simulation. The size of both stub length and rectangular bar considered for fabrication is 0.2 mm, which resonates at 9.22 GHz with the absorbance magnitude of 96.61 %. The front and back view of the fabricated model has been shown in Figure 3.10(a) and Figure 3.10(b), respectively. While the measured and the simulated absorbance magnitudes are given in Figure 3.10(c).

This clarifies the overall absorbance performance of *MMA* structure calculated by experimental reflection coefficients values. Because of the size constraints, fabrication processing errors and measurement precision, there is a slight frequent deviation of 9.306 GHz with the absorbance of 91.5% has been observed in the *MMA* structure. This concludes that the measured results are in good agreement with the simulated results.

The block diagram of experimental setup for *MMA* structure has been shown in Figure 3.11. The MMA structure is placed in an Anechoic Chamber. Which is a non-reflecting chamber also known as wedge-tapered absorber. Two horn antennas are used, where one antenna will act as a transmitting antenna and other will act as receiving antenna. both the antennas are kept 1-meter distance from the device under test (DUT). The output from each antenna has been recorded by using a vector network analyzer (VNA) for the oblique angle of incidence (θ).

3.7. Chapter Summary

In this chapter, a novel design of a passive tuned *MMA* structure is made up of a circular ring modeled with stubs and rectangular bars extending from *Ku-band* to *X-band* has been studied. The lowest resonant frequency peak obtained at 7.77 GHz with absorbance peak response of 90.33 %, while the highest resonant frequency peak obtained at 15.46 GHz with absorbance peak response of 99.97 %. The electromagnetic simulations result shows that the length of the rectangular bar and shorted stubs have a significant influence on determining the frequency characteristics of *MMA* and add an extra degree of freedom to the structure.

The center frequency of *MMA* can be tuned easily by varying the length of the rectangular bar and shorted stubs only while the other parameters kept unchanged. With the proposed configuration, the designer always has flexibility in adjusting the resonant frequency. This also allows varying the spacing between the adjacent neighboring loops, which is an important aspect while fabricating the design. So it opens the way to fabricate controllable and tunable *MMA*.

The *MMA* structure has been observed for the oblique angle of incidence and polarization. The structure has been found highly polarization insensitive. The surface current distribution analysis shows that the current is circulated properly in the loop and then the simulated and measured results are compared at the end and the results are well matched and justified.

This structure finds its applications in the field of stealth technology for low *RCS* antenna design. There the antenna designers can find out the possibility of using the same antenna aperture for the multi-band frequency operation. Thus, it explores and offers feasibility to use the same structure and combine the different feed antennas onto the aperture of a single reflector antenna. Hence, instead of multiple antennas, a compact antenna system can be realized that cover less space and so suitable for military planes, space aircraft, missiles, ships, and other sensitive vehicles. Consequently, the *MMA* may be used as a shield in a specific frequency band, whilst performing field transmission in another nearby band because of its tuning nature.

Chapter-4

Dual-band Shorted Stubs Metamaterial Absorber

Over the last one decade, the dual resonances *MMA* structure has gain tremendous attention for the presents and succeeding wireless communication applications. This includes satellite navigation and control, reduction of *RCS* for stealth technology applications, radar frequency identification and wireless handheld applications.

In this chapter, we have proposed and analyzed the design characteristics of a dual-band shorted stubs circular rings *MMA* structure. Parametric studies are essentially required. So that, the behavior of *MMA* and its effects upon the resonance frequency for the variation of circular ring radius (R_{in}), shorted stubs length (a), and rectangular bar length (b) could be evaluated. The effect on transmission characteristics response of polarization sensitivity and oblique angle of incidence are studied for *TE* and *TM* modes of *EM* wave. The behavior for surface current distribution and normalized input impedance characteristics are also required to be observed, so that our simulation results would become accurate and valid. Ultimately, proposed *MMA* structure fabrication and measurement have been made to validate and justify our research work model.

4.1. Design of Dual-band Shorted Stubs Metamaterial Absorber

An absorber based on metamaterial structure neither reflects nor transmits the incident *EM* wave [118-120]. It absorbs all the incoming *EM* waves and therefore, almost disables the transmission, reflection and scattering signals. However, the *MMA* absorbance relies upon its morphology and fabrication material types [102, 121]. Various works have been reported previously in conjunction to the *MMA* structure ranging from microwave to THz regimes, infrared to the visible light region, single-band to wideband, and dual-band to multi-band range of *EM* radiation based on the target applications [73, 88, 114, 116, 122, 123].

It has been observed that if the input impedance response of the *MMA* structure approximates to the free space impedance. This would produce a perfect *MMA* absorber with the sharp resonance response [124]. Researchers have observed that the unique characteristics for metamaterial structure could be obtained by employing several nano-fabrication designing tools and engineering techniques [9, 125, 126]. This influences the inductive and capacitive

behavior of the *MMA* structure. Therefore, modifies the resonant frequencies and results in near unity absorbance with light-weight, ultra-thickness and narrow dimensions *MMA* structure. Thus, this *MMA* structure proposes better substitute to *FSS*, *EBG*, and *AMC* structure. It has several applications in the field of antenna design for gain enhancement [85], enhancing isolation by reducing cross polarization [127], mutual coupling reduction [128], for the reduction of *RCS* in stealth technology [129-131], in solar-photovoltaic and thermo-photovoltaic cells to enhance the functioning of photo-detectors by heightening absorption mechanism [87, 132].

The *MMA* offers further miniaturization, versatility, and increased capabilities. The *MMA* has successfully interacted with the frequency bands across the entire electromagnetic spectrum from radio frequency range to microwave, terahertz, across the infrared spectrum and almost covers visible wavelengths [81, 133-135]. It has been observed that circular ring structures can achieve high *EM* wave absorbance as compared to the other unit cell structures because of its simplicity, circular symmetry along all axis and more polarization insensitive [55]. In the dual-band, triple-band and multi-band *MMA* structures, it has been analyzed that the frequency separation distant limitation occurs. It appears difficult to overcome the drawbacks and reduce the distance between resonances peaks so that they become quite close to each other, otherwise, cost in poor absorbance.

This limitation was overcome by the modified circular ring unit cell structure. In this research work, a unit cell of the *MMA* has consisted of four circular rings and each

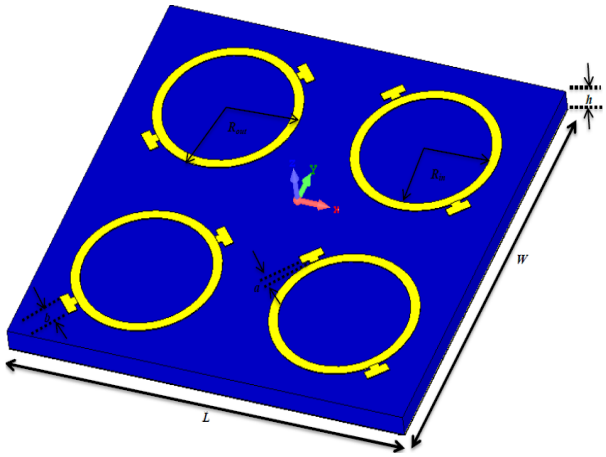

Figure 4.1. Dual-band shorted stub circular rings metamaterial absorber.

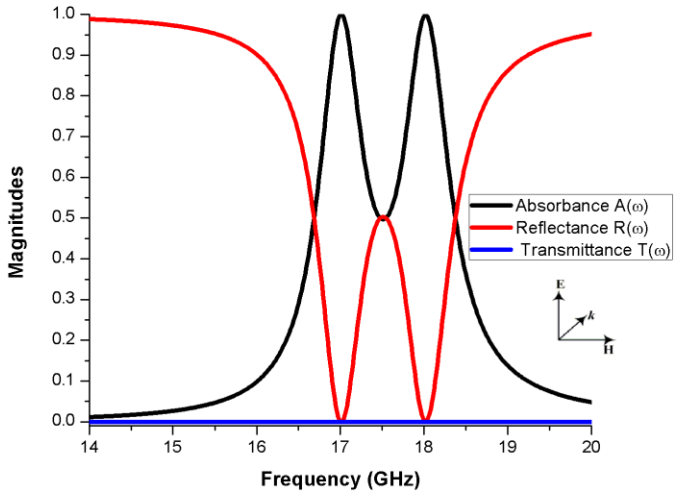

Figure 4.2. Absorbance, reflectance, and transmittance response for dual-band MMA at 17 GHz and 18 GHz.

circular ring has modeled with stubs and rectangular bars to obtain a sharp dual band resonance peaks with close separation distance between two resonant frequencies is obtained as close as 1 GHz compared to the other dual-band [136-139], triple-band [140] or multi-band [141] circular ring which is 2 GHz or more as in Figure 4.2. Adding of shorted stubs and rectangular bars on the circular ring structure provides the significant scattering characteristics response along with the flexibility to the designer to control and optimize the resonant frequency. This is in accordance with the specific application against its previous counterpart *MMA's* in the microwave regime of the electromagnetic spectrum.

The circular ring structure has been considered in this research work because of its simplicity, symmetrical nature along with all axis, and highly insensitive to the angle of incidence and polarization. The design of dual resonances shorted stub circular ring metamaterial absorber unit cell structure has been depicted in Figure 4.1. The proposed *MMA* unit cell structure consists of a lossy *FR-4* substrate with relative permittivity of the dielectric substrate (ε_r) is 4.6 and the value of loss tangent (*tan δ)* is 0.019. The dielectric substrate has been sandwiched by two copper metallic patch layers with the conductivity of 5.8×10^7 s/m.

The top copper metallic patch has been constructed by four circular rings. Then further modification has been made on the circular ring structure by introducing several shorted stubs and rectangular bars in a way that the right half of the patch looks exactly the mirror image of the left half of the patch. These copper metallic stubs and bars possess inductive behavior; hence, the resonant frequency peaks could be modified and adjusted. The size of these copper stubs and bars connected to each circular ring are tuned and adjusted to obtain dual resonance

Table 4.1 Parameters of proposed MMA.

Description	Parameters	Dimensions (mm)
Length/Width of Substrate	L,W	8.86
Height of substrate	h	0.4
Inner Radius	R_{in}	1.38
Outer Radius	R_{out}	1.58
Width of the ring	w	0.2
Stub Length	a	0.075
Thickness of metal	t	0.017
Bar Length	b	0.5

peaks at 17 GHz and 18 GHz with the absorbance of 99.99 % and 99.83 %, respectively as shown in Figure 4.2. All the parameters of the structure are well optimized to obtain sharp resonance peaks at the corresponding frequencies. This chapter gives the augmentation published in [142].

Since these parameters play a significant role in influencing the frequency response curve. Therefore, to achieve the specific frequency characteristics curve, the geometrical parameters such as length, width of the substrate (L, W), thickness of the substrate (h), thickness of the patch and metal layer (t), radius of the circular ring (R_{in}, R_{out}), width of the circular ring (w), stubs length (a) and bar length (b) of the *MMA* unit cell structure need to be well optimized as shown in Table 4.1. The size of the substrate for the unit cell has been chosen to 8.86 mm × 8.86 mm × 0.4 mm (W × L × h). A full copper ground plane is used making the transmittance reduce to zero for all frequency. An additional advantage of using full copper ground plane makes the analyses more simplified by just minimizing reflectance coefficient so that to maximize absorbance magnitude. By proper optimization, all the parameters, condition for surface impedance of the structure matched with free space impedance are achieved. Hence, *MMA* with almost unity absorbance magnitude can be developed.

4.2. Frequency Response Analysis

The transmission coefficient, $SZ_{max(2).}Z_{max(1)}$ and reflection coefficient, $SZ_{max(1)}.Z_{max(1)}$ (scattering parameters) of the *MMA* unit cell structure have been studied for both *TE* and *TM* mode using a Finite Integration Technique (*FIT*) based *CAD* solver. For this purpose, a periodic unit cell boundary conditions have been assigned across *x-axis* and *y-axis*. The *z-axis* is set to

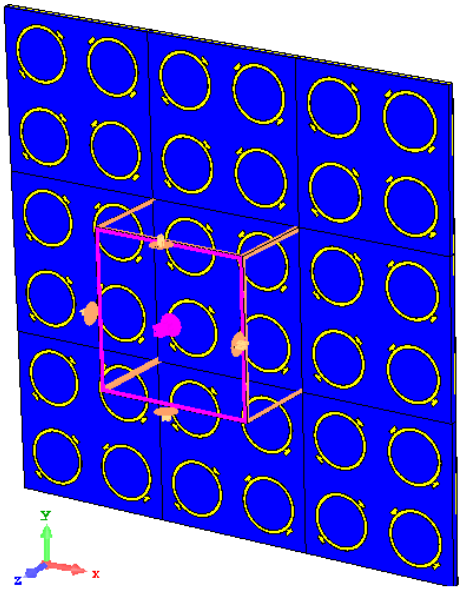

Figure 4.3 Geometry and parameters of the concentric rings metamaterial absorber.

be an open add space as depicted in Figure 4.3. For the *S*-parameter calculation, only two floquet ports have been considered because of its simple set-up and ability to analyze the response of the *MMA* structure from a different angle of incident for the incoming *EM* incident waves.

The sensitivity response of *MMA* has been simulated and analyzed. The sensitivity response analysis is considered in two ways.

(i) parametric sensitivity and

(ii) angular sensitivity.

Parameter sensitivity is the deviation in frequency response with the variation of parameters. So, the parameters like inner radius (R_{in}), stub length (a) and bar length (b) of *MMA* have been varied, in order to find out the sensitivity and dependency of *MMA* on these parameters. This would not only help us with analyzing the error due to inaccuracy in manufacturing but also give us an insight on how to shift the operating frequencies and obtained the desired results. Whereas, the angular sensitivity is defined as the behavior of the *MMA* structure observed at different values for angle of incidence and polarization sensitivity. So, this behavior is analyzed by changing theta (θ) and phi (ϕ) for the oblique angle of incidence and polarization sensitivity corresponds to the proposed *MMA* design.

4.3. Parametric Sensitive Response

In the *MMA* designed structure, the three 'R_{in}', 'a' and 'b' are primarily considered and their effect has been studied, whilst all the other parameters remain unchanged. Since these three parameters have the greatest influence on enhancing and modifying the absorbance and band gap between dual resonances of *MMA*.

4.3.1. Variation of Inner Radius (R_{in})

The effect of R_{in} on the resonance frequency of metamaterial absorber has been observed from the values R_{in} = 1 to R_{in} = 1.75 mm as shown in Figure 4.4. The simulated results of absorbance magnitudes of the proposed *MMA* for *TE* polarization field at a normal angle of incidence and the values of dual resonance peaks have been given in Table 4.2.As, R_{in} = 1 mm, the first resonance peak frequency (f_1) appears at 22.09 GHz and second resonance peak frequency (f_2) appears at 23.95 GHz with absorbance above 98 %. As the value of R_{in} increases, the whole dual resonance peaks start drifting towards the lower resonant frequency with an unchanged bandgap between frequency peaks. Whilst, absorbance magnitude remains unaltered and approximate to unity absorbance.

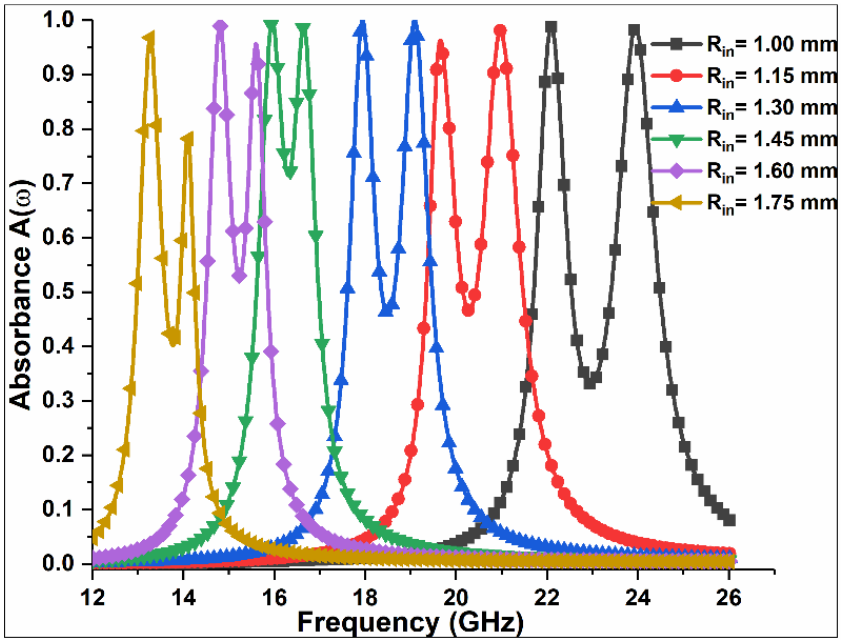

Figure 4.4 Effects on dual resonance peaks with the variation in R_{in}.

Table 4.2 Effects of the inner radius on the resonance frequency of MMA.

Inner Radius (mm)	**1st/2nd Resonance peaks (GHz)**		**1st /2nd Absorbance at resonance (%)**		**% shift of Resonant frequency (f_r)**	
R_{in}	**f_1**	**f_2**	**$A_1(\omega)$**	**$A_2(\omega)$**	**f_{r1}**	**f_{r2}**
1.0	22.09	23.95	99.48	98.33	0	0
1.15	19.66	20.98	96.36	98.32	11	12.4
1.30	17.94	19.09	99.99	99.99	18.79	20.29
1.45	15.96	16.65	99.68	98.79	27.75	30.48
1.60	14.81	15.60	99.11	95.66	32.96	34.86
1.75	13.27	14.1	96.74	78.85	39.93	41.13

As, R_{in} approaches 1.60 mm, the absorbance magnitude start falling down and reached to 95.66 % for second resonance peak frequency (f_2), while for the first resonance peak frequency (f_1) the absorbance magnitude remains well above 99 %. After this, a poor frequency response with low absorbance has been observed for R_{in} equals to 1.75 mm and above. Similarly, a poor frequency response with low absorbance has been observed for R_{in} less than 1.00 mm.

4.3.2. Variation of Shorted Stubs Length (a)

The effect of 'a' on the resonance frequency of metamaterial absorber has been observed from the values a = 0 to a = 1.1 mm as in Figure 4.5. The simulated results of absorbance magnitudes of the proposed *MMA* for *TE* polarization field at a normal angle of incidence and the values of dual resonance peaks have been given in Table 4.3. At a = 0 mm, the first resonance peak frequency (f_1) appears at 17.31 GHz and second resonance peak frequency

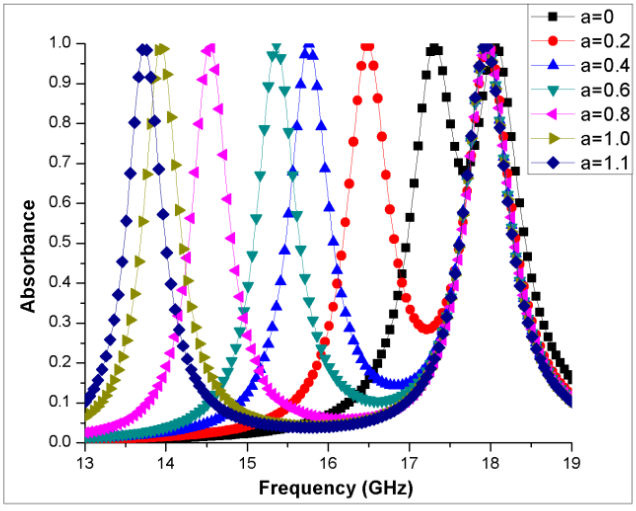

Figure 4.5 Effects on dual resonance peaks with the variation in stub length (a).

Table 4.3 Effects of different stub length on the resonance frequency of MMA.

Stub Length (mm)	1st/2nd Resonance peaks (GHz)		1st /2nd Absorbance Magnitude (%)		% shift in Resonant frequency (f_r)	
a	**f_1**	**f_2**	**$A_1(\omega)$**	**$A_2(\omega)$**	**f_{r1}**	**f_{r2}**
0	17.31	18.06	99.94	99.86	0	0
0.2	16.48	17.98	99.99	99.79	4.79	0.44
0.4	15.76	17.95	99.99	99.68	8.95	0.61
0.6	15.36	17.94	99.68	99.68	11.27	0.66
0.8	14.55	17.97	99.49	99.80	15.94	0.50
1.0	13.94	17.95	99.49	99.81	19.47	0.61
1.1	13.74	17.95	99.17	99.73	20.62	0.61

(f_2) appears at 18.06 GHz with absorbance magnitude above 99 %. As the value of stub length increases, the absorbance magnitude remains unaltered and approximate to unity absorbance. A minor shift in resonance frequency peak (f_{r2}) appears, whilst the first resonance peak (f_{r1}) values changing continuously and reached to 20.62 % from its initial value as stub length (a) approaches to 1.1 mm.

4.3.3. Variation of Split Square Patch Bars Length (b)

The effect of different 'b' on the resonance frequency of metamaterial absorber has been observed from the values b = 0.25 to b = 2.50 mm as shown in Figure 4.6. The simulated results of absorbance magnitudes of the proposed *MMA* for *TE* polarization field at normal the angle of incidence and the values of dual resonance peaks have been given in Table 4.4. At b = 0.25 mm, the first resonance peak frequency (f_1) appears at 17.41 GHz and second resonance peak frequency (f_2) appears at 17.98 GHz with absorbance above 99 %.

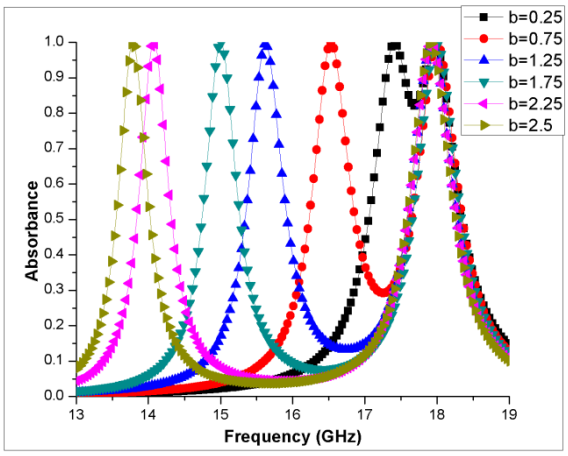

Figure 4.6 Effects on dual resonance peaks with the variation in bar length (b).

Table 4.4 Effects of different bar length on the resonance frequency.

Bar Length (mm)	**1st/2nd Resonance peaks (GHz)**		**1st /2nd Absorbance Magnitude (%)**		**% shift in Resonant frequency (f_r)**	
b	**f_1**	**f_2**	**$A_1(\omega)$**	**$A_2(\omega)$**	**f_{r1}**	**f_{r2}**
0.25	17.41	17.98	99.87	99.87	0	0
0.75	16.53	17.98	99.82	99.82	5.05	0
1.25	15.62	17.93	99.56	99.85	10.28	0.28
1.75	15.00	17.98	99.96	99.96	13.84	0
2.25	14.09	17.92	99.99	99.99	19.07	0.33
2.50	13.79	17.91	99.83	99.99	20.79	0.39

As the value of rectangular bar length increases, the absorbance magnitude remains unaltered and approximate to unity absorbance. The second resonance frequency peak (f_{r2}) almost remain unchanged, whilst the first resonance peak (f_{r1}) values changing continuously and reached to 20.79 % from its initial value as rectangular bar length (b) approaches to 2.50 mm.

4.4. Angular Sensitivity Response

In the *MMA* designed structure, the Angular sensitivity response for the oblique angle of incidence and polarization sensitivity characteristics are of prime concern and importance. Since most of the structures behave significantly well under a normal angle of incidence and polarization sensitivity but as the angles (θ, ϕ) vary, the absorbance decreases and their behavior become poor and unpleasant. This is all because of the incapability of the *MMA* structure to drive the circulating current in the *FR-4* substrate between two copper metallic layer. At a normal angle of incidence, this *MMA* structure has almost unity absorbance and the circular symmetrical nature of this structure makes it highly insensitive to different angle of incidence and polarization sensitivity. So, the angular sensitivity response for the *MMA* designs have been made corresponds to *TE* and *TM* modes of *EM* waves.

4.4.1. TE and TM Modes for Oblique Angle of Incidence (θ)

For *TE* and *TM* modes, the oblique angles of incidence theta (θ) are of prime concern and importance in *MMA* design. Hence, the simulation and analysis have been made at the oblique angle of incidence for *TE* and *TM* mode of *EM* wave and depicted in Figure 4.7. For *TE* mode, at any angle of incidence, the electrical component of incident *EM* wave is always tangential

to the surface of *MMA*. For the analysis of *TE* mode, the value of theta (θ) is varied between θ = 0^0 to θ = 70^0 as shown in Figure 4.7(a). At θ = 0^0, the first dual resonance peaks appear at 17.05 GHz and 18.04 GHz frequencies with the almost unity absorbance.

Till θ = 20^0, the resonance peaks and absorbance magnitudes remains unaltered. At θ = 30^0, a slight change is observed and dual resonance peaks start shifting towards lower resonant frequencies and become 17 GHz and 18 GHz frequencies, while the absorbance magnitude remains quite stable to 98.64 % and 99.55 %, respectively.

When the incident angle is altered to θ = 40^0, the resonant frequency is again shifted to lower frequency range and become equal to 16.93 GHz and 17.98 GHz with the absorbance magnitude of 94.07 % and 99.10 %. The incidence angle is then altered to θ = 50^0, then the

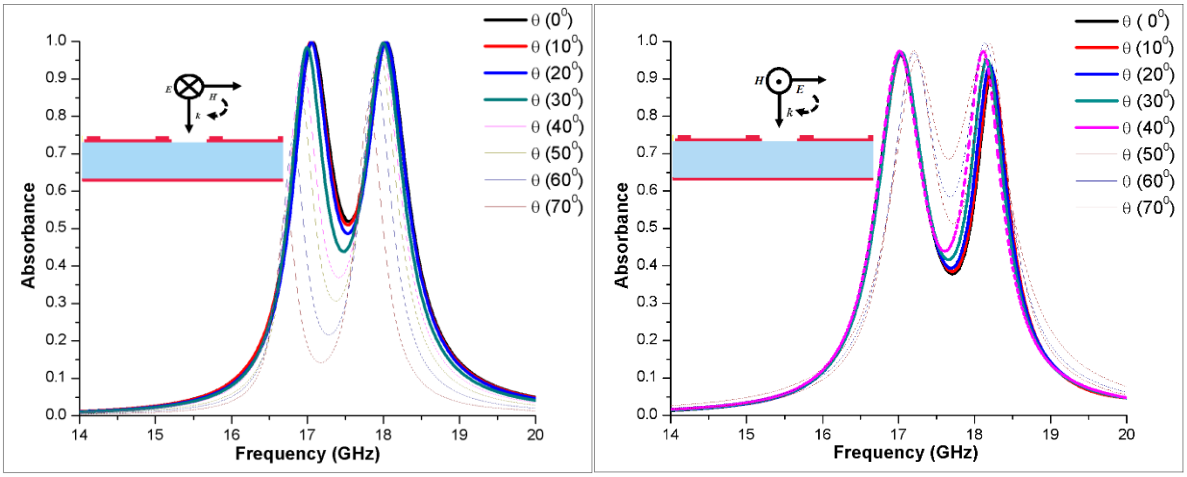

(a) (b)

Figure 4.7 Absorbance for oblique angles of incidence theta (θ) from 0^0 to 70^0 for (a) TE mode and (b) TM mode of MMA.

the resonant frequency is again shifted to lower frequency range and become equal to 16.90 GHz and 17.94 GHz with the absorbance magnitude of 85.87 % and 97.27 %. It is observed that the second resonance manages to maintain high absorbance which is 93.19 % at 17.89 GHz for incident angle as large as 60^0.

The incidence angle is then increased until 70^0. This is found to be the maximum angle that enables the absorber to absorb at least 55.28 % for first resonance peak shifted at 16.72 GHz, while the second resonance peak observes at 17.81 GHz with 82.80 % absorbance for the incident *EM* wave. For *TM* mode, at any angle of incidence, the magnetic component of incident *EM* wave is always tangential to the surface of *MMA*. For the analysis of *TM* mode, the value of theta (θ) is varied between θ = 0^0 to θ =70^0 as shown in Figure 4.7(b).

At $\theta = 0^0$, the first dual resonance peaks appear at 17.03 GHz and 18.23 GHz frequencies with the absorbance magnitude of 96.13 % and 91.08 %. Till $\theta = 30^0$, the first resonance peak remains at the same position whereas the second resonance peak slightly shifted to 18.16 GHz with the absorbance magnitudes 97.48 % and 94.93 % respectively. At $\theta = 40^0$, now the dual resonance peaks start moving closer to each other with the frequency peaks shifted slightly to 17.02 GHz and 18.11 GHz with the band gap of 1.09 GHz and along with the absorbance magnitude of 97.41 % and 97.37 % respectively. As the value of theta (θ) is varied from 0^0 to 70^0, the absorbance magnitude throughout maintained a value equally and above then 95.05 % and 91.08 % for the first and second peak respectively. While the bandgap reduces continuously and at $\theta = 70^0$, it becomes as close as 0.86 GHz with the dual resonance peaks at 17.23 GHz and 18.09 GHz with the absorbance of 95.05 % and 93.74 %, respectively.

4.4.2. TE and TM Modes of Polarization Sensitivity (ϕ)

For *TE* and *TM* modes, the polarization sensitivity phi (ϕ) is of equal concern and priority in *MMA* design to the oblique angle of incidence. These two characteristics have the capability to overcome the shortfalls in designing *MMA* in single polarization state and small operating angle. Hence, the simulation and analysis have been made at the polarization angle phi (ϕ) both *TE* and *TM* mode of *EM* wave and given in Figure 4.8. For the analysis of *TE* mode, the value of phi (ϕ) is varied between $\phi = 0^0$ to $\phi = 90^0$ as shown in Figure 4.8(a). At $\phi = 0^0$, the first dual resonance peaks appear at 17.07 GHz and 18.03 GHz frequencies with the almost unity absorbance. Till $\phi = 20^0$, the resonance peaks and absorbance magnitudes for the first peak remain same while for second peak it varies slightly. At $\phi = 30^0$, a slight change is observed and dual resonance peaks start shifting towards higher resonant frequencies and become 17.09 GHz and 18.05 GHz frequencies, while the absorbance magnitude changes to 96.29 % and 86.36 %, respectively.

When the polarization angle is altered to $\phi = 50^0$, the resonant frequencies are shifted again and become equal to 17.16 GHz and 18.20 GHz with the absorbance magnitude of 93.32 % and 72.05 % respectively. The values of absorbance magnitude for dual resonance peaks are lowest at this polarization angle. As the angle changes to $\phi = 60^0$, the absorbance magnitude starts increasing again with a continued increase in dual resonance frequency peaks with the values of 17.18 GHz and 18.35 GHz. Whilst, the absorbance magnitude of

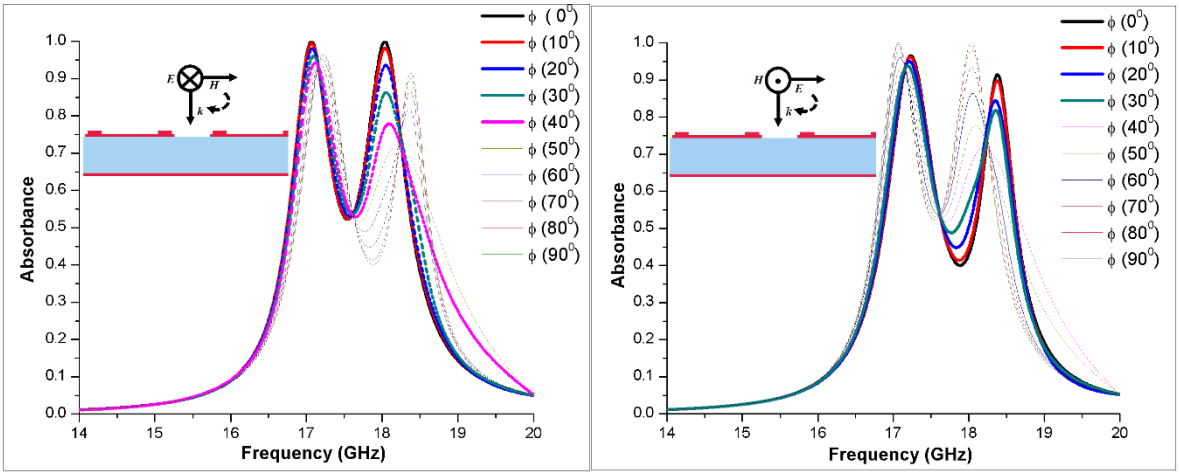

(a) (b)

Figure 4.8 Absorbance for different polarization angles for phi (ϕ) from 0^0 to 90^0 for (a) TE mode and (b) TM mode of MMA.

93.32 % and 82.10 % are observed. The polarization angle is then increased to 90^0. At this point, the *MMA* found high polarization insensitive with dual resonance peaks occurs at 17.23 GHz and 18.37 GHz with the absorbance magnitude of 96.10 % and 91.67 %, respectively for the impinged *EM* wave. For the analysis of *TM* mode, the value of phi (ϕ) is varied between $\phi = 0^0$ to $\phi = 90^0$ as shown in Figure 4.8(b).

At $\phi = 0^0$, the first dual resonance peaks appear at 17.23 GHz and 18.38 GHz frequencies with the absorbance magnitude of 96.50 % and 91.62 % respectively. As the polarization angle phi (ϕ) varies from $\phi = 0^0$ to $\phi = 90^0$, the resonant frequency continuously drifting down with the change in absorbance magnitude. At $\phi = 40^0$, the dual resonant peak frequencies are found at 17.16 GHz and 18.22 GHz with the absorbance magnitude of 93.32 % and 71.88 %, respectively. The values of absorbance magnitude for dual resonance peaks are lowest at this polarization angle. As the angle changes and increased further the absorbance magnitude starts increasing and at $\phi = 90^0$, the dual resonance frequency peaks occur at 17.06 GHz and 18.04 GHz with almost unity absorbance magnitude of 99.97 % and 99.99 %, respectively for the incident *EM* wave.

4.5. Comparison of Results with Previous Proposed MMA Structures

To further validate and justify the importance of proposed structure [142], a comparison has been made between previously proposed structures and given in Table 4.5. The frequency separation distance between f_1 and f_2 is larger in [122], [136], [137], [138] and [141] structure, whereas it is smaller in [126] and maintained same in [124]. The thickness of the

Table 4.5 Comparisons of MMA with the previously proposed structure

MMA Absorber	References	Unit Cell Size (mm)	Dielectric Thickness (mm)	Centre Frequency (GHz)		Absorbance A(ω) (%)		FWHM (%)		Polarization Sensitivity
				f_1	f_2	f_1	f_2	f_1	f_2	
Ayop et al	[122]	9	0.8	9	11	95.59	91.35	5.12	3.08	Till 82º
Ayop et al	[124]	18	0.8	9	10	97	97.77	3.59	3.31	Yes
Jamilan et al	[126]	20	1.5	5.6	6	97	99	no	no	Till 60º
Dincer et al	[136]	30	1.6	4.42	5.62	90	99.7	7.46	3.55	Yes
Li et al	[137]	12	0.5	11.15	16.01	99.99	99.99	2.87	3.87	Till 60º
Peng et al	[138]	10	0.8	4.06	6.66	99.60	95.83	no	no	Till 50º
Liu et al	[141]	10	0.4	9.4	11.7	98	99	no	no	Till 75º
Our Work	[142]	8.86	0.4	17	18	99.99	99.83	4.9	5.07	Till 70º

FR-4 Substrate plays an important role in determining the absorbance of the dual-band *MMA* structure. For unity absorbance, it is kept as small as possible and equal to *0.40 mm*; hence keeps its promise for an ultra-thin *MMA* structure.

It is observed that the thickness of *MMA* is improved over [122], [124], [126], [136], [137] and [138], while [141] structure possesses same thickness. Only structure [137] claims better absorbance then our proposed structure. Also, structure [122] and [136] claims better *FWHM* bandwidth compare to our proposed model, while it is not performed in [126], [138] and [141] structure and other remained structures offer poor bandwidth response compare to the proposed structure. All structures offer polarization sensitivity response but the degree of sensitivity varies significantly. Hence, the proposed structure is a good alternative for dual-band ultrathin tuned *MMA* with unity absorbance.

4.6. Surface Current Distribution

The simulated surface current distribution of a single unit cell of *MMA* has been shown in Figure 4.9. The Figure 4.9(a) shows the surface current distribution resonant at 17 GHz while, Figure 4.9(b) shows the surface current distribution resonant at 18 GHz. By analyzing the *MMA* unit cell structure, it is concluded that the dual resonance *MMA* structure has been properly operating at each resonance frequency.

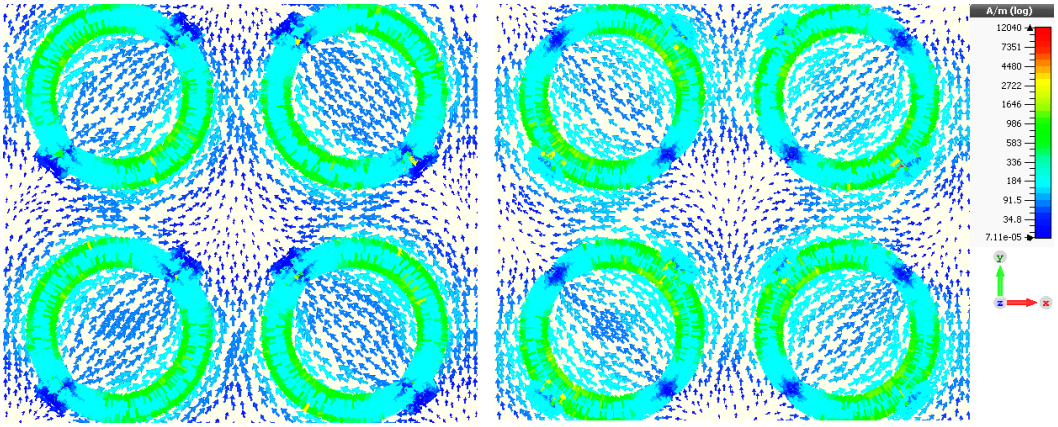

(a) (b)

Figure 4.9. Surface current distribution for shorted stub circular rings MMA at (a) 17 GHz and (b) 18 GHz.

The concentration of surface current found at right half and left half of the circular rings facing opposite to each other to correspond to 17 GHz resonant frequency at Figure 4.9(a). Similarly, the concentration of surface current found at right half and left half of the circular rings facing to each other to correspond to 18 GHz resonant frequency at Figure 4.9(b). As the resonance achieved, the value of return loss (S_{11}) reduces to a minimum because of the closely matched normalized input impedance of *MMA* to free space impedance and thus, the resultant absorbance magnitude at the corresponding resonant frequency has been maximized.

4.7. Normalized Input Impedance Response

A *MMA* unit cell physical parameters optimization have been achieved to obtain the specific dual resonant frequencies by adjusting and tuning the inner radius (R_{in}) stub length (a), bar length (b), relative permittivity (ε_r), loss tangent ($tan\ \delta$), thickness (h) and length/width (L/W) of the dielectric substrate.

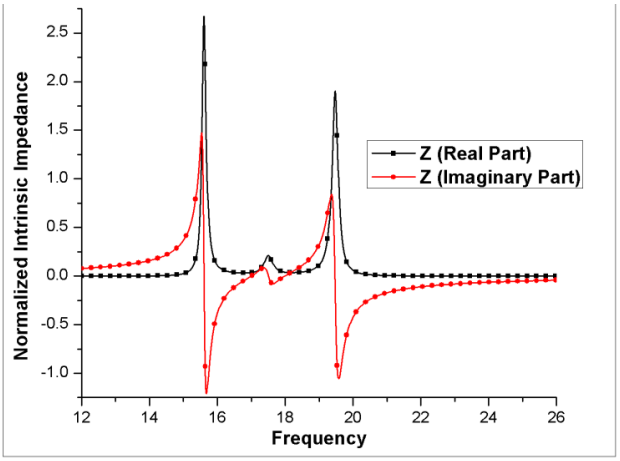

Figure 4.10 Normalized input impedance of the proposed absorber.

The *EM* wave responses for dual resonance peaks can be tuned so that normalized input impedance of the *MMA* is well matched with the free space impedance. A graph has been plotted between normalized input impedance versus resonant frequencies as depicted in Figure 4.10. In the figure, the real and imaginary parts of normalized input impedance approach to zero at sharp resonant peak frequencies of 17 GHz and 18 GHz, respectively. While at all other frequencies the values of real and imaginary parts are found totally different.

4.8. Fabrication and Testing

The dimension of dual resonances shorted stub circular rings metamaterial absorber has been optimized by using simulation technique. The prototypes of *MMA* unit cell structure have been made up using metallic copper and flame retardant *FR-4* using printed circuit

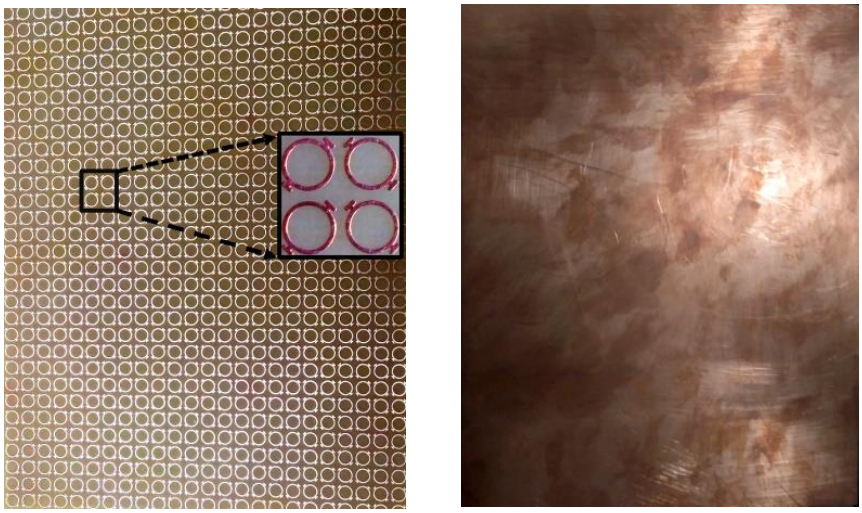

(a) (b)

Figure 4.11 120 mm × 150 mm proposed MMA (a) Front view and (b) back view.

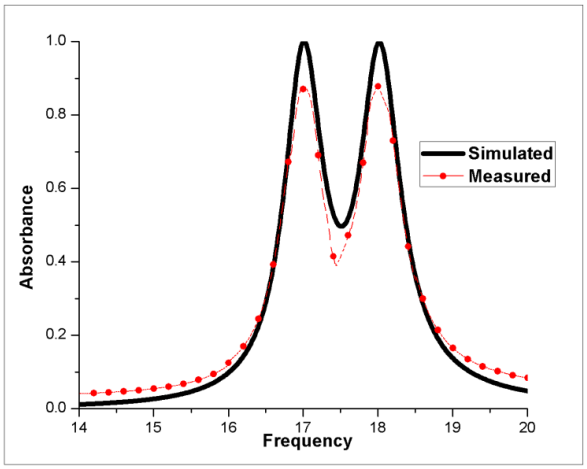

Figure 4.12 Measured results of the proposed MMA absorber.

board (*PCB*) technology as shown in Figure 4.11. For the purposed *MMA* structure, a finite ground of 120 mm × 150 mm has been chosen. The measured S-parameters are shown in Figure 4.12 along with the simulated results, these illustrate the performance of the *MMA* in term of the absorbance calculated by experimental reflection coefficients. Because of the limitation on size and some very common errors during the fabrication process, then measurement precision, a slight frequency shift has been observed as shown in Figure 4.12.

In the dual resonance absorber, the first absorbance peaks have been found a 16.99 GHz with the absorbance of 87%, while second absorbance peak has been obtained at 17.99 GHz with the absorbance of 88%. Hence, the measured results are in excellent agreement with simulated ones and the overall absorbance of more than 87% has been recorded.

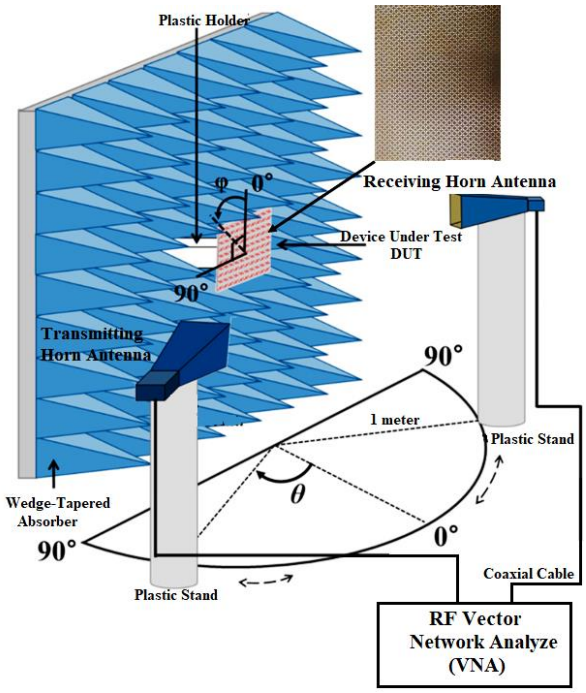

Figure 4.13 Block diagram of the experimental setup

The block diagram of experimental setup for *MMA* structure has been shown in figure 4.13. The MMA structure is placed in an Anechoic Chamber. Which is a non-reflecting chamber also known as wedge-tapered absorber. Two horn antennas are used, where one antenna will act as a transmitting antenna and other will act as receiving antenna. both the antennas are kept 1-meter distance from the device under test (DUT). The output from each antenna has been recorded by using a vector network analyzer (VNA) for the oblique angle of incidence (θ).

4.9. Conclusion

By considering the research work results, we evaluate and conclude to the points that

(i) All the three parameters, input radius (R_{in}), stubs length (a) and bar length (b) has greatly influenced in determining the dual frequency resonance peaks.

(ii) R_{in} has been found responsible to set the location of dual resonances frequency peak.

(iii) Stubs length (a) and rectangular bar length (b) are responsible for varying and adjusting the band gap between the resonant frequency peaks.

(iv) The oblique angle of incidence and polarization sensitivity has a negligible effect on transmission characteristics response.

(v) The surface current distribution and normalized input impedance characteristics made our simulation results more clear.

(vi) Finally, fabrication and testing of the *MMA* unit cell structure validate our research work model.

This dual resonance *MMA* structure is an ultra-thin, almost unity absorbance magnitude and compatible with *PCB* design technology. Because of its low profile, single layer structure and the readily available *FR-4* substrate, it is very simple and cost-effective structure. However, the unity absorbance *MMA* structure realized at the cost of narrow bandwidth that is related directly to the thickness and dielectric constant of the substrate. The bandwidth of *MMA* can be enhanced by increasing the substrate thickness or making a multilayer *MMA* structure or decreasing the dielectric constant value. However, it would, in turn, reduce the absorbance magnitude. So, it's a trade-off between absorbance, thickness, and bandwidth.

4.10. Chapter Summary

In this research work, a novel design of a unit cell structure consisted of four circular rings has been studied. Each circular ring has modeled with stubs and rectangular bars to obtain sharp dual band resonant peaks at 17 GHz and 18 GHz with absorbance peak response of 99.99 % and 99.83 %, almost unity absorbance. The corresponding full width at half maximum (*FWHM*) bandwidth at these resonant frequencies is 4.90 % and 5.07 %, respectively. A close separation distance between two resonant frequencies is obtained as close as 1 GHz compared to the other dual band and multiband circular ring which is 2 GHz or more. Then, an analysis has been also made to find out the behavior of *MMA* for oblique angle of incidence and polarization sensitive analysis.

The results show that the *MMA* structure is highly insensitive to any variation in the angle of incidence and polarization. Then, an analysis has been conducted for surface current distribution and normalized input impedance characteristics which show a good agreement with the simulated results. Finally, the *MMA* design has been fabricated and tested and the results are well matched with the simulated ones. Hence, this research work adds flexibility in design and offer opportunities to modify and adjust the resonant frequency of the *MMA* structure design. Hence, this dual resonance *MMA* absorber finds application in antenna design, where it would be used to reduce the Antenna *RCS* for in-band and out-band range of frequency extending from *X-band* to *Ku-band* radar and that is being left for future work. This *MMA* structure is suitable for the wide range of applications in stealth technology for *RCS* reduction in missile, ship, aircraft, drones and many more.

Chapter-5

RCS Reduction of Patch Antennas using Single-Band Shorted Stubs MMA

In this Chapter, we shall analyze the techniques for *RCS* reduction of a patch antenna using the single-band shorted stubs metamaterial absorber. The *EM* behaviors and parametric variations of single-band shorted stubs metamaterial absorber have been studied and analyzed in chapter 3. However, in this chapter *MMA's* application as *RCS* reduction of the single-band patch antenna is the topic of interest that will be explored in details. This chapter is subdivided mainly into three sections:

In Section 5.1, a novel design for the In-band low *RCS* of rectangular patch antenna has been proposed. This idea is based on the metamaterial absorber *MMA* composed of shorted stubs and rectangular bars. The *RCS* of the *MMA* loaded rectangular patch antenna has been simulated, analyzed and matched with referenced rectangular patch antenna operating at the resonant frequency of 10 GHz.

In Section 5.2, we shall design three entirely different dimensions patch antennas and load them with a different configuration of *MMA* unit cells such as to determine the effects of variations of dimensions on the overall performance of antenna along with determining its effects on *RCS*. Finally, for the purpose of long-distance communications, a patch array is designed and then this is loaded with *MMA* and its performance and *RCS* is determined, studied, and discussed in Section 5.3.

5.1. In-band RCS Reduction of Patch Antenna using MMA

An absorber based on metamaterial structure transformed into a new research focus whose effective bulk material properties could be tuned by slightly altering material parameters and thus offers various properties and excellent features such as near unity absorbance has been designed and proposed ranging in the microwave regime, THz, infrared and visible light spectrum [88, 103, 143]. It offers characteristics like ultra-thin [144], wide angle of incidence [145] and highly polarization insensitive [146].

It can be a single to wide-band, dual-band and multi-band [13, 79, 142, 147]. Thus, make it suitable for several intended applications such as antenna designs [148], in solar-photovoltaic

and thermo-photovoltaic cells to enhance the functioning of photo-detectors by heightening absorption mechanism [87, 149], for the reduction of *RCS* in stealth technology [150-153] and wireless communication [154].

In stealth technology, it is very important to decrease the *RCS* of the target. The *RCS* of any physical object is directly related to the reflected part of the incidence *EM* wave and it is determined by the body shape, size and constituent material of the objects. In military platform for communication, the antenna is one of the indispensable instrument that is more susceptible and main contributor for *RCS*. Without compromising radiation performances, the reduction of *RCS* for the antenna has been a topic of immense interest. Although, the conventional techniques for radar absorption such as shaping and *RAM/ RAS* could not be implemented on the patch antenna because it might degrade the antenna performance [155, 156]. With advancements in radar technology, the targets are easily identified and detectable, therefore it is prime important to reduce its *RCS* [157]. Thus, low *RCS* antenna is of prime concern and equal importance.

The *RCS* of an antenna is because of these two factors:

(i) Structural Mode *RCS* and

(ii) Antenna Mode *RCS*.

As we cannot change the antenna structure parameters since it influences the frequency response behavior. However, it has been found that when the patch antenna surrounded by *MMA* structure, it immensely reduces the *RCS* effect on the system without compromising with the performance of the antenna [158, 159]. Thus, one can minimize the structural mode *RCS* as low as possible and hence emerge as a new design technique.

Various techniques have been proposed for the *RCS* reduction of the rectangular patch antenna. For out-band *FSS, EBG* structure and *AMC* structures have been employed for reduction of *RCS* of the antenna and *MMA* has been employed for reduction of *RCS* of the antenna [160-162]. But, there is still more emphasis needed for in-band frequency response for low *RCS* of the antenna. Therefore, we have proposed a metamaterial absorber based on shorted stubs at 10 GHz. This *MMA* is utilized to enhance the in-band stealth capability of patch antenna by loading it around the exiting source and has been covered in this section.

5.1.1. Design of Single-band Shorted Stubs MMA at 10GHz

Figure 5.1 shows a novel design of a passive tuned *MMA* absorber that operates at *X-band*. It consists of concentric loops with shorted stubs and split rectangular bars. The *MMA* tuning to 10 GHz is provided by the mean of varying length of shorted stubs and split square rectangular bars. The periodicity (S_2) and the thickness (h_1) for the shorted stubs *MMA* is designed to 5 mm and 0.4 mm, respectively. The front view and side view of *MMA* absorber have been shown in Figure 5.1(a) and Figure 5.1(b), respectively.

All the parameters of *MMA* are optimized and adjusted to obtain a sharp frequency resonance peak at 10 GHz. In Figure 5.2(a), a resonance curve has been drawn between absorbance $A(\omega)$, reflectance $R(\omega)$ and transmittance $T(\omega)$. An absorbance of 99.95 % achieves and that approximates to unity absorbance. Then, effective wave impedance $Z_{eff}(\omega)$ graph has been plotted in Figure 5.2(b), where its value comes to be (0.998 - j 0.85) and that matches the condition for free space impedance. It states that when $Z_{eff}(\omega)$ approaches to 1, there will be no reflection from the *MMA* surface.

The *MMA* structure response at an oblique angle of incidence (θ) and polarization sensitivity (ϕ) has been analyzed and justified for *TE* modes of *EM* waves as depicted in Figure 5.2(c) and 5.2(d), respectively. The simulation result verifies that the *MMA* performs well at any polarization of incident EM wave and operate at wide operating angles where absorbance is above 94 % for θ equals to 50^0 and remains 72.58 % for θ equals to 70^0. While the *MMA* remains insensitive for entire polarization angle from 0^0 to 90^0. The total thickness

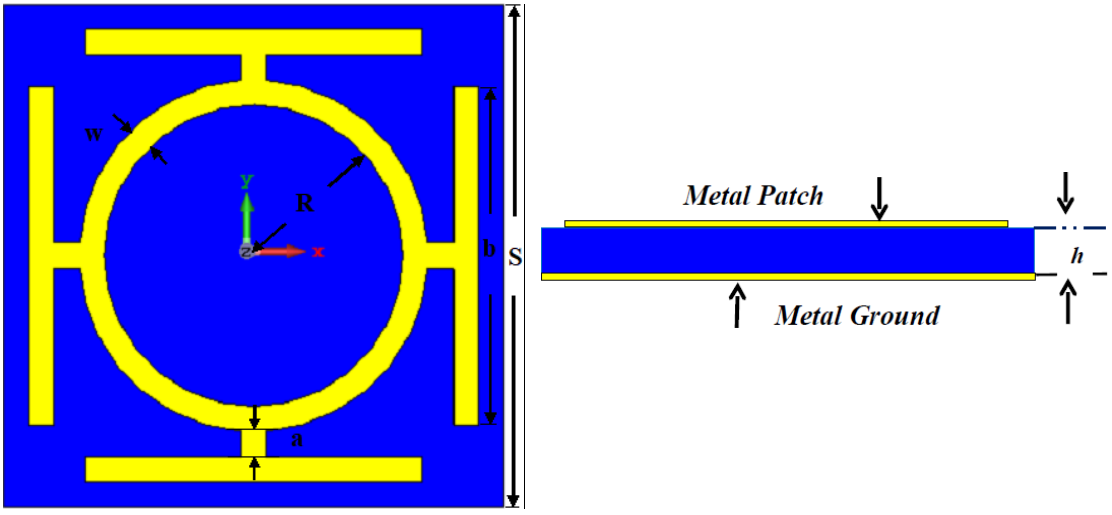

(a) (b)

Figure 5.1 Metamaterial absorber (a) front view and (b) side view. Unit cell dimensions: S = 5 mm, R = 1.5 mm, a = w = 0.25 mm, h = 0.40 mm.

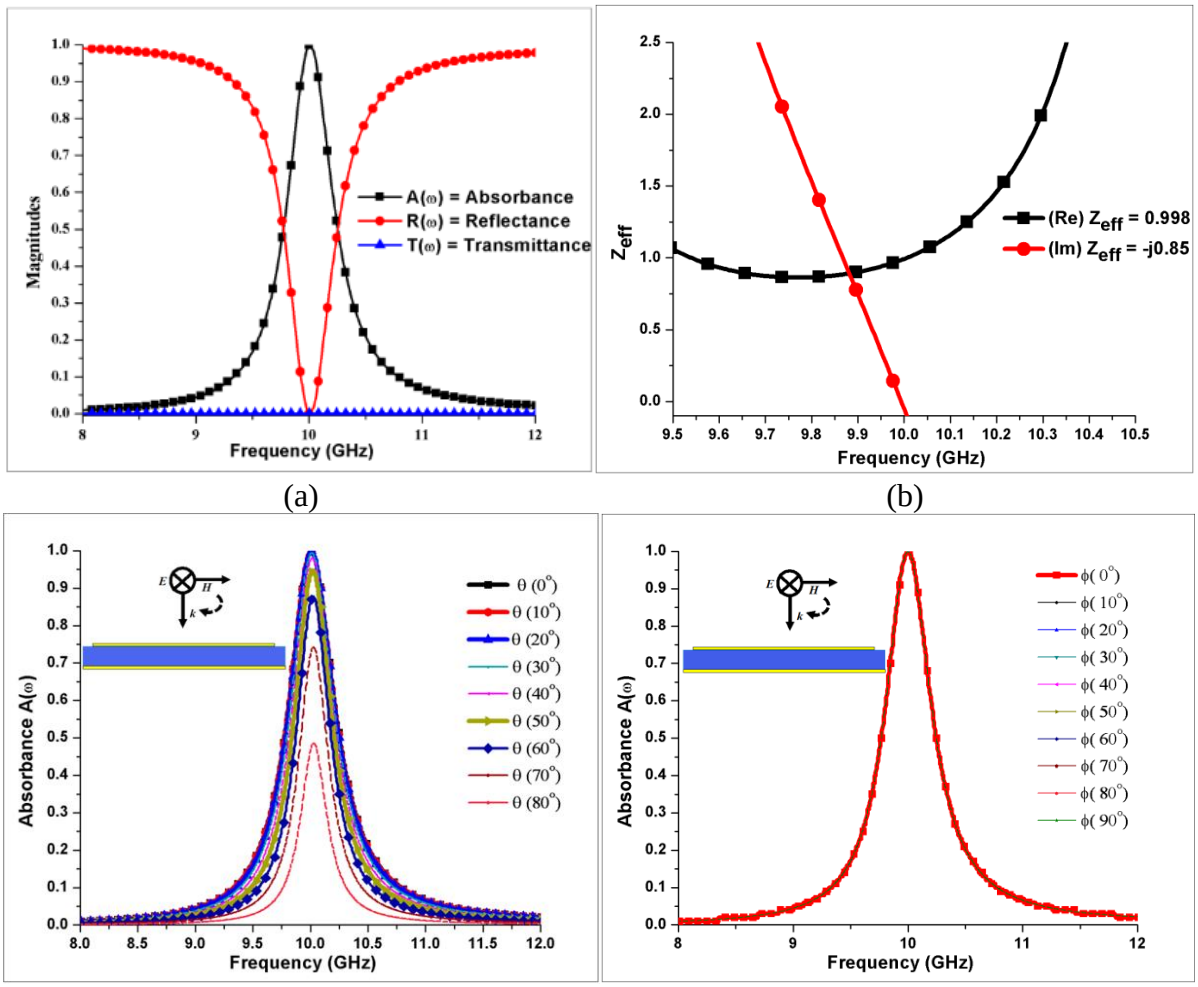

Figure 5.2 Resonance curves for (a) A(ω), R(ω) and T(ω), (b) effective wave impedance (Z_{eff} (ω)) (c) oblique angle of incidence (θ), and (d) polarization sensitivity (ϕ) for TE modes of MMA at 10 GHz.

of the modified designed absorber has been adjusted to only 0.013 λ_0, where λ_0 is the free-space wavelength at the resonant frequency.

5.1.2. Design Analysis of Patch Antenna with or without MMA

A microstrip antenna also called patch antenna are becoming very popular antennas in the microwave frequency range because of its simplicity, linearly polarized, conformability to planar and non-planar structures, cost-effective, ease of implementation and compatible with the circuit board technology [129,163,164]. A patch antenna finds its application in handheld devices, Global Positioning Systems (*GPS*), satellites and radar communications, wireless fidelity (*Wi-Fi*), biological imaging and radio frequency identification.

The simplest form of patch antenna made up of a rectangular metallic patch placed at the

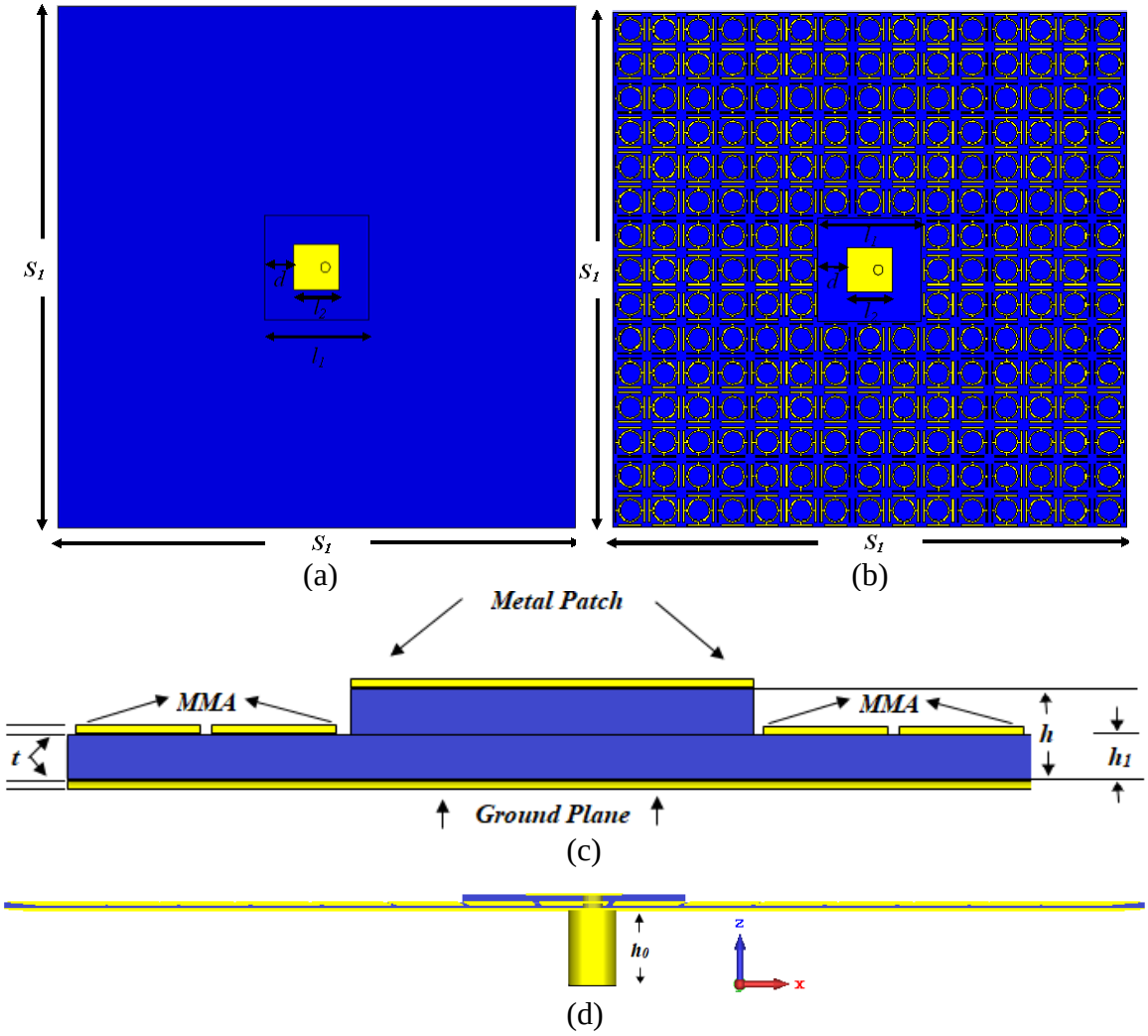

Figure 5.3 Coaxial feed patch antennas (a) proposed antenna, (b) MMA loaded patch antenna, (c) side view of the modified antenna, and (d) side view with a coaxial feed.

top of a dielectric substrate of reasonable height and fixed dielectric constant value underneath covered by a metallic ground plane. The rectangular patch length is approximate to half of the wavelength corresponds to that frequency [153,165-167]. The size and bandwidth of a patch antenna can be determined and greatly influenced by the dielectric constant of a substrate [168-170].

It has been found that the antenna bandwidth could be heightened by raising the substrate height or by decreasing the substrate permittivity but results in an increase of periodicity. The results described in this section have been published in [171]. Although increasing the substrate permittivity decreases the periodicity but reduces the efficiency and bandwidth of the rectangular patch antenna. Also, the bandwidth can be increased by increasing the patch width, while resonant frequency can be adjusted by varying the patch length.

The following equations are used to calculate the length (L_s) and width (W_s) of the patch antenna [155,164]:

$$\Delta L = 0.412 \frac{(\varepsilon_{reff} + 0.3)\left(\frac{W_s}{h_1} + 0.264\right)}{(\varepsilon_{reff} - 0.258)\left(\frac{W_s}{h_1} + 0.8\right)} h_1 \tag{5.1}$$

The effective length of the patch becomes

$$L_s = L_{eff} - 2\Delta L \tag{5.2}$$

The effective length (L_{eff}), for resonant frequency (f_0), is given as:

$$L_{eff} = \frac{c}{2 f_0 \sqrt{\varepsilon_{reff}}} \tag{5.3}$$

and

$$\varepsilon_{eff} = \frac{\varepsilon_r + 1}{2} + \frac{\varepsilon_r - 1}{2}\left[1 + 12\frac{h_1}{W_s}\right]^{-\frac{1}{2}} \tag{5.4}$$

The resonance frequency corresponds to any TM_{mn} mode is given as:

$$f_0 = \frac{c}{2\sqrt{\varepsilon_{reff}}}\left[\left(\frac{m}{L_s}\right)^2 + \left(\frac{n}{W_s}\right)^2\right]^{1/2} \tag{5.5}$$

Here, m and n are modes with respect to L_s and W_s respectively. For resonance, the width is given as:

$$W_s = \frac{c}{2 f_0 \sqrt{\frac{\varepsilon_r + 1}{2}}} \tag{5.6}$$

The aim of this research work is to analyze a radar absorbing technique to decrease the *RCS* of the rectangular patch antenna without any degradation in its system performance. First, the reference patch antenna has been designed as depicted in Figure 5.3(a). It is designed to operate at 10 GHz resonant frequency by varying its physical parameters and then their values are optimized. The periodicity (S_1) of patch antenna is 75 × 75 mm with the length of the radiating patch (l_2) is 6.50 mm. The length of the central substrate (l_1) is 15 mm

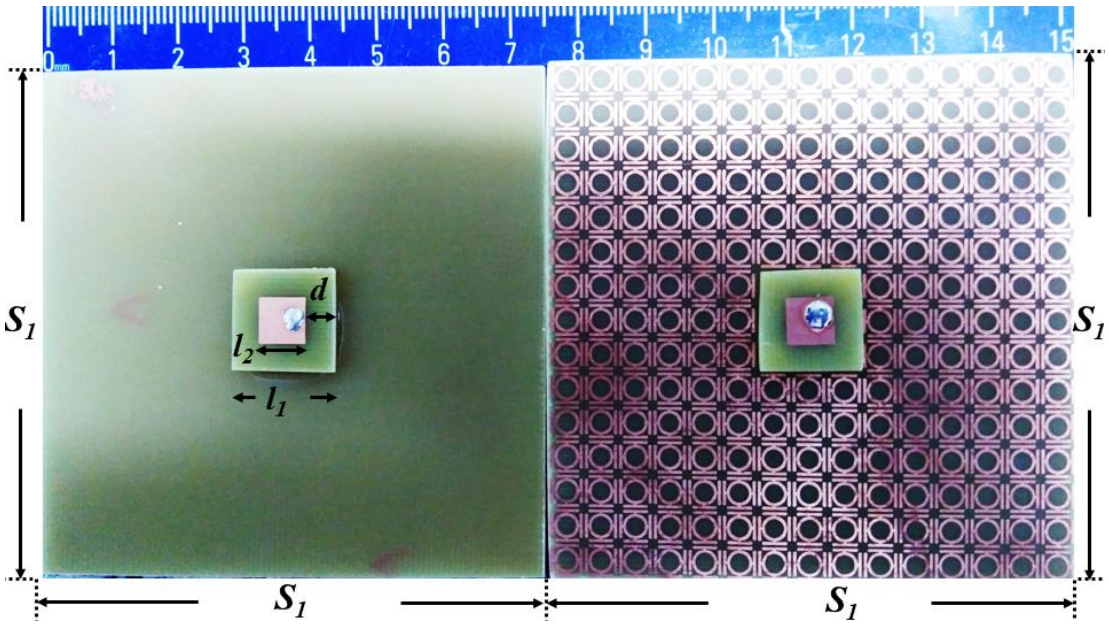

(a) (b)

Figure 5.4 Fabricated coaxial-feed patch antenna (a) referenced [139] and (b) proposed antenna.

whereas the central substrate height (h) is 1 mm. The thickness of the other area (h_1) is 0.4 mm. A low cost and most popular flame retardant *FR-4* with $tan\delta$ and ε_r values are 0.025 and 4.3, respectively selected for this research work.

A standard thickness (t) of 0.035 mm has been considered for copper ground plane and patch antenna that is suitable for designing in printed circuit board (*PCB*) technology. The patch antenna has been fed by coaxial feed and the central position of coaxial probe found an equivalent to 50 Ω matching the impedance at the position, pos_x =1.27 mm and pos_y = 0. This is shown in Figure 5.3(d). Now the rectangular patch antenna's frequency response is optimized at 10 GHz. Then, the antenna structure is modified and loaded with 15 × 15 *MMA* unit cell.

A total of 3 × 3 *MMA* unit cells are etched off from the center for the rectangular patch antenna as depicted in Figure 5.3(b) and its side view are shown in Figure 5.3(c). A 4.25 mm of space is left between *MMA* and patch antenna to minimize the mutual coupling and keep the antenna radiation performance unaffected. The referenced (standalone) antenna as well as proposed (*MMA* loaded) antenna has been fabricated using printed circuit board technology and shown in Figure 5.4.

5.1.3. Radiation Performance Comparison of Referenced and Proposed Antenna

A comparison has been made between the scattering coefficient (S_{11}) values for reference antenna and the *MMA* loaded proposed antenna and is presented in Figure 5.5(a). The results indicate that the S_{11} value for referenced antenna resonant at 10 GHz comes out to be -41.87 dB. While for the proposed antenna, the scattering coefficient (S_{11}) marginally shifted to 9.99 GHz with -49.66 dB, and the bandwidth remains almost unaffected.

The measured value for the proposed antenna has been shown and compared with both results. The result shows that measured values are within accepted range (below -10dB). This concludes that the introduction of shorted stubs *MMA*s on patch antenna has no effect on the antenna performance and it remains preserved simultaneously.

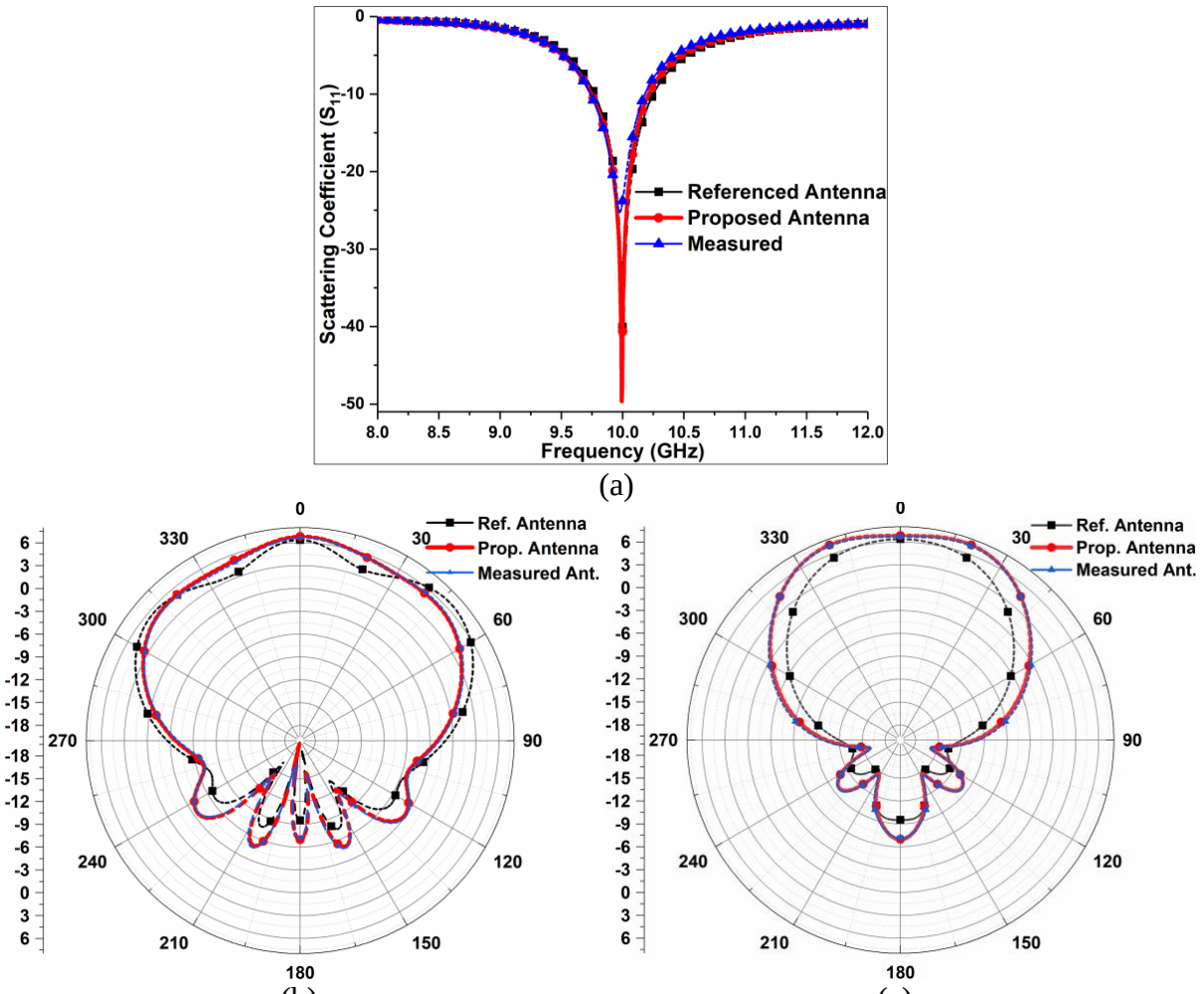

Figure 5.5 Frequency responses (a) scattering coefficient (S_{11}) (b) E-Plane, and (c) H-plane radiation performance.

A polar plot radiation pattern comparison for $\phi = 0^0$ and $\phi = 90^0$ are simulated, analyzed and depicted in Figure 5.5(b) and Figure 5.5(c), respectively. The results indicate that for *E-Plane* the referenced patch antenna main lobe magnitude is 6.68 dBi with a beamwidth of 90.6^0 and for the proposed antenna, the main lobe magnitude is 6.80 dBi with a beamwidth of 120.6^0. For *H-Plane* the referenced patch antenna main lobe magnitude is 6.35 dBi with a beamwidth of 66.9^0 and for the proposed antenna, the main lobe magnitude is 7.25 dBi with a beamwidth of 82.7^0.

Comparative analyses have been made for *E-plane* and *H-plane* of the referenced structure for co-polarization (*Cop*) and cross-polarization (*Xp*) polar plots as depicted in Figure 5.6. For E-Plane, the proposed antenna main lobe magnitude is 6.8 dBi with *Xp* isolation of 82.5 dBi at 10 GHz as shown in Figure 5.6(a). For H-Plane, the proposed antenna main lobe magnitude is 7.25 dBi with *Xp* isolation of 24.65 dBi at 10 GHz as depicted in Figure 5.6(b). Therefore, when the referenced antenna is modified with the *MMA*, it enhances the antenna radiation performance for *E-Plane* as well as for *H-Plane*, respectively. Also, there are isolations of 82.5 dBi and 24.65 dBi observed between copolar and cross-polar patterns for the referenced antenna. So, the *E-plane* and *H-plane* radiation patterns indicate that desirable antenna directivity is attained with suppressed cross-polar radiations.

This concludes that the rectangular patch antenna structure modified with the shorted stubs *MMA* has no effect on the radiation pattern and overall performance remains well kept.

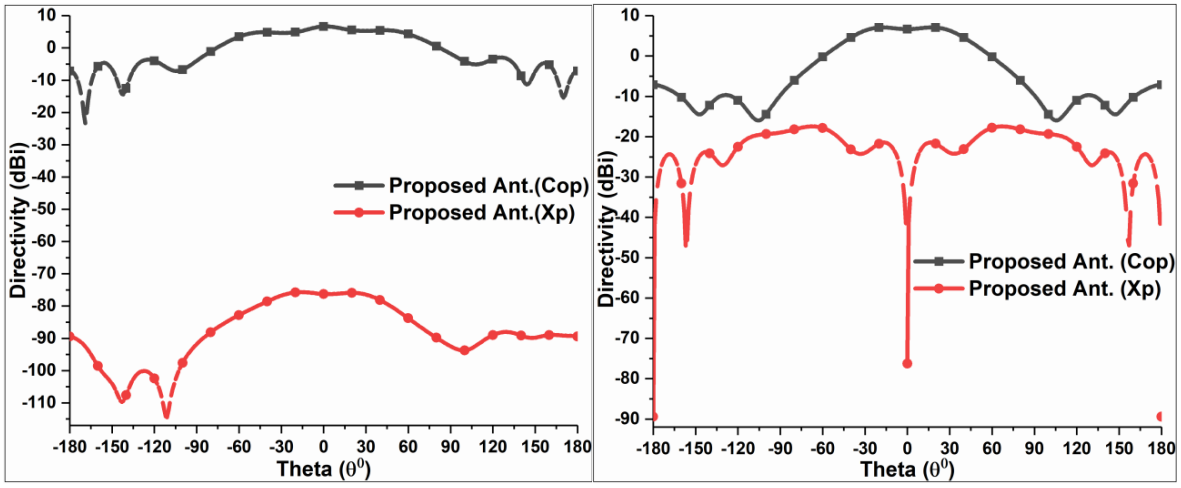

(a) (b)

Figure 5.6 Comparisons of co-polarization and cross-polarization patterns of the proposed antenna for (a) E-Plane and (b) H-plane.

5.1.4. In-band RCS Reduction of the Proposed Patch Antenna

Since this research work is mainly focused on *RCS* reduction of patch antenna using *MMA*, so a complete analysis for *Monostatic* and *Bistatic RCS* have been performed [171]. This indicates that *MMA* greatly enhances the stealth capability of rectangular patch antenna by reducing its *RCS* as shown in Figure 5.7(a). It has been found that the *Monostatic RCS* values decreased in all direction through the entire *X-band*. However, the significant reduction in *RCS* of *MMA* loaded rectangular patch antenna is obtained in 9.89 GHz frequency with reduction of 21.22 dBsm, whereas at 10 GHz the value for low *RCS* is decreased up to 7.40 dBsm with respect to the referenced antenna.

The *Bistatic RCS* of patch antenna has been simulated and analyzed at 10 GHz. At $\phi = 0^0$, the *Bistatic RCS* of the *MMA* loaded patch antenna reduced throughout the angle theta (θ) with a significant reduction in between -83^0 to 84^0. The largest reduction is analyzed of

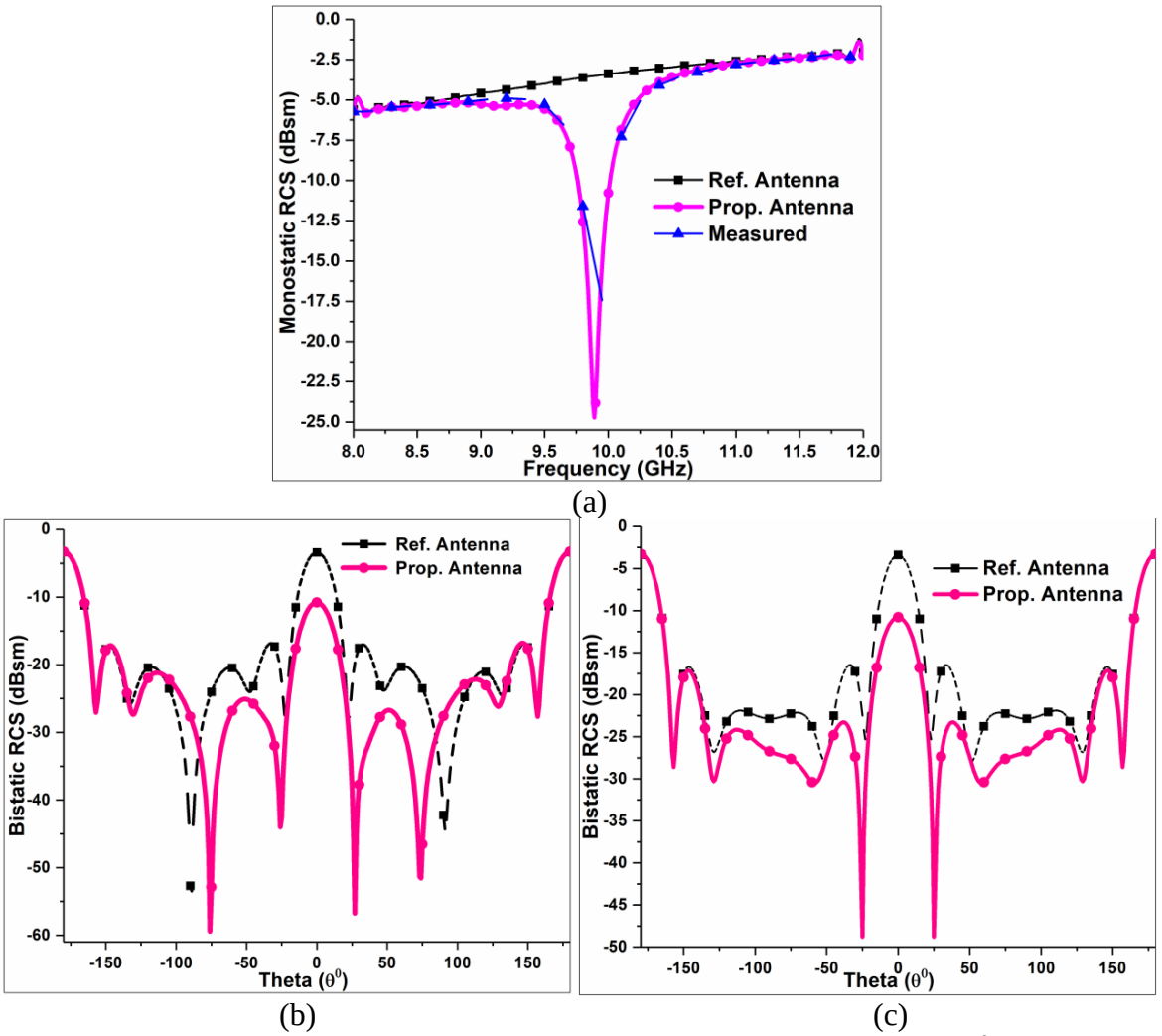

Figure 5.7 Analysis of RCS for (a) Monostatic RCS (b) Bistatic RCS at $\phi = 0^0$ and (b) $\phi = 90^0$ of the referenced and proposed antenna at 10 GHz.

33.21 dBsm at -76^0 and 37.07 dBsm at 27^0 between referenced patch antenna and *MMA* loaded rectangular patch antenna as shown in Figure 5.7(b). Similarly, at $\phi = 90^0$, the *Bistatic RCS* of the *MMA* loaded patch antenna reduced throughout the angle theta (θ) with significant reduction obtained in between -167^0 to 167^0. The largest reduction is analyzed of 26.31 dBsm at -25^0 and 26.31 dBsm at 25^0 between referenced patch antenna and *MMA* loaded rectangular patch antenna and also depicted in Figure 5.7(c).

5.1.5. Comparisons with Previously Proposed Structures

To validate the novelty of the proposed structure [171], comparisons have been made with previously reported *MMA* structures for the *RCS* reduction and tabulated in Table 5.1. It has been found that dimension of the proposed structure is 2.5 λ_0, where λ_0 is the free-space wavelength at the resonant frequency. This is equivalent to the structure [154] and [129] dimensions, whereas the structure [173] found to have smallest dimensions than rest of all. However, the structure [172] has largest dimensions among all and that would probably result in poor *RCS* performance.

The thickness of dielectric substrate plays an imperative role in ascertaining the *MMA* structure absorbance magnitude. To obtain sharp absorbance peak, its thickness is being adjusted to *0.4 mm* so that, this *MMA* structure upkeeps its promises for ultra-thickness. It has been found that the thickness of proposed *MMA* structure is 0.013 λ_0 and that is improved over [172] and [173]. Whereas, the structure [129] offers ultra-thickness amongst all the remaining structures. The structures [129], [172] and [173] offer polarization sensitivity

Table 5.1 Comparisons with previously proposed structures.

Low RCS Patch Antenna	References	Dimensions (mm)	Thickness of MMA (mm)	A (ω) Peaks (GHz)	Polarization	Maximum RCS Reduction (dBsm)
Zhang et al	[129]	82.5 × 82.5 (2.5λ_0)	0.3 (0.0092λ_0)	9.15	Till 60^0	15
Liu et al	[154]	135 × 135 (2.5λ_0)	0.5 (0.0093λ_0)	5.57	Yes	16.6
Our Work	[171]	75 × 75 (2.5λ_0)	0.4 (0.013λ_0)	10	Yes	21.22
Baskey et al	[172]	154 × 154 (3.33λ_0)	1 (0.021λ_0)	6.35	Till 60^0	18
Mol et al	[173]	≈ 110.75 × 104 (2λ_0)	1.6 (0.028λ_0)	5.262	Till 60^0	Not clearly defined

responses up to 60^0, while it is completely analyzed in structure [154] and proposed structure. The maximum *RCS* reduction has been claimed better by proposed model of 21.22 dBsm at *X-band*, while the remaining structures offer poor in-band *RCS* response compare to the proposed structure. However, it is not clearly predicted in structure [173].

Hence, the proposed structure not only preserves and maintains the antenna radiation performances but also, upkeeps it promises for the maximum in-band *RCS* reduction of the patch antenna.

5.2. Comparative Analyses for RCS Reduction of Patch Antennas

A comparative design principle has been adopted to study and analyze the performance of shorted stubs *MMA* absorber which is placed and loaded around patch antennas having three different configurations. The results are simulated, analyzed, measured, and finally compared. The results show a significant reduction in *Monostatic* as well *Bistatic RCS* of patch antennas while preserving its radiation performance. The results given in this section have been published in [174].

5.2.1. Analyses of Patch Antennas with and without MMA

The length of the radiating patch (L) is 6.50 mm and the length of the central substrate (L_1) is 15 mm whereas the central thickness of the substrate (h_1) is 1 mm. The thickness of the area (h) around exiting source is 0.4 mm which is compatible and specifically designed to load *MMA* absorber for unity absorbance. All the parameters are optimized to resonant at 10 GHz and their tabular description has been given in Table 5.2. Each design has been fed by coaxial feed with its central approximates to 50 Ω matching the impedance at the position, pos_x = 1.25 mm and pos_y = 0 as shown in Figure 5.8.

Table 5.2 Antenna parameter descriptions.

Description	Dimensions (mm)	Parameters
$\mathbf{L_s/W_s}$	35/55/75	Periodicity of Structure
$\mathbf{L_1}$	15	Central Substrate Length
$\mathbf{h_1}$	1	height of substrate
L	6.50	Length of Patch
$\mathbf{g_s}$	3.5	Gap b/w Patch and MMA
t	0.035	Thickness of metal
Pos_x	1.25	Position of Probe
h_0	5	Height of connector

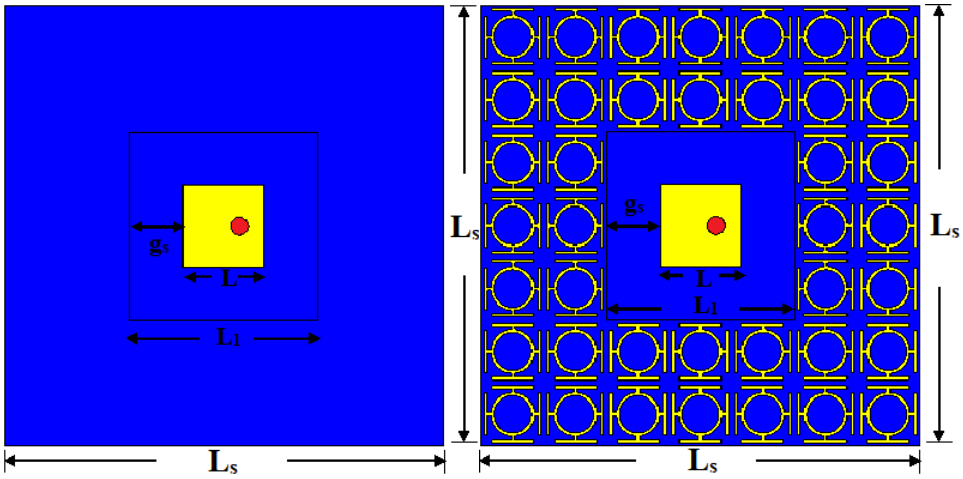

(a) (b)

Figure 5.8 Coaxial feed patch antenna 35 mm × 35 mm design 1. (a) Referenced antenna and (b) MMA loaded antenna.

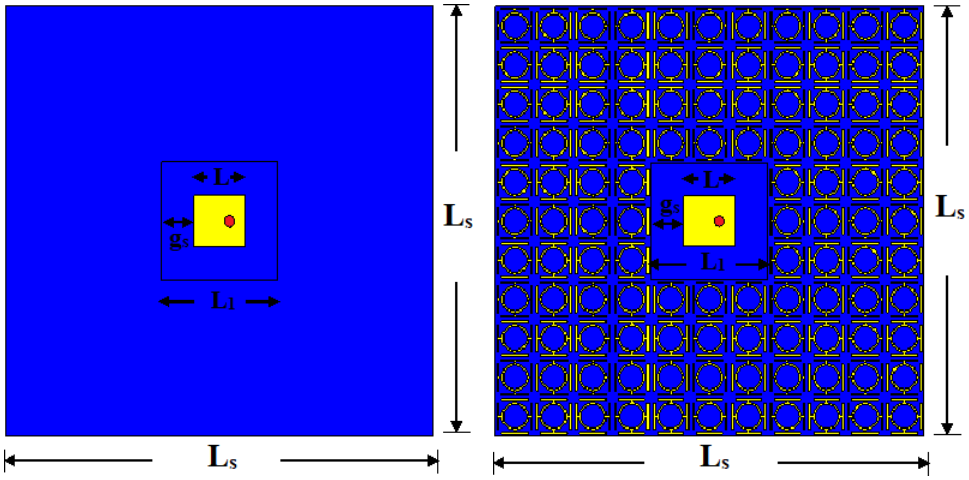

(a) (b)

Figure 5.9 Coaxial feed patch antenna 55 mm × 55 mm design 2. (a) Referenced antenna and (b) MMA loaded antenna.

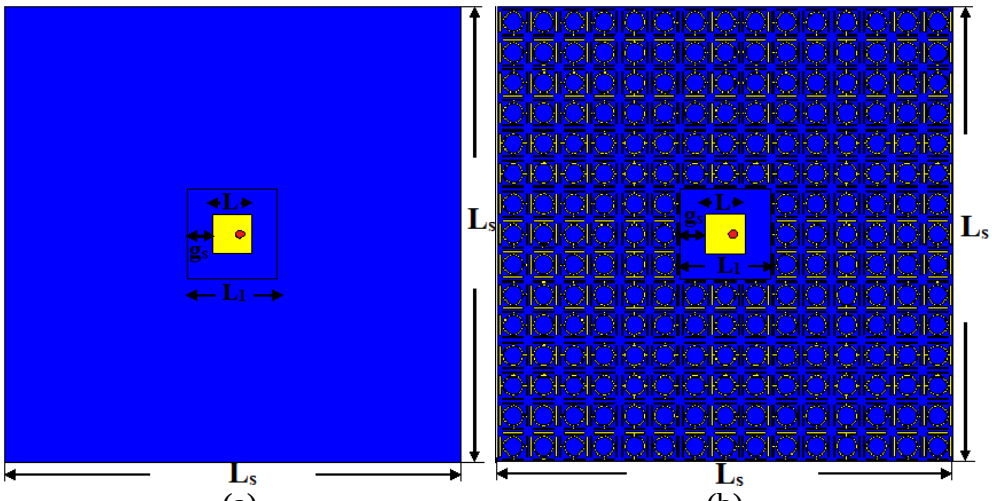

(a) (b)

Figure 5.10 Coaxial feed patch antenna 75 mm × 75 mm design 3. (a) Referenced antenna and (b) MMA loaded antenna.

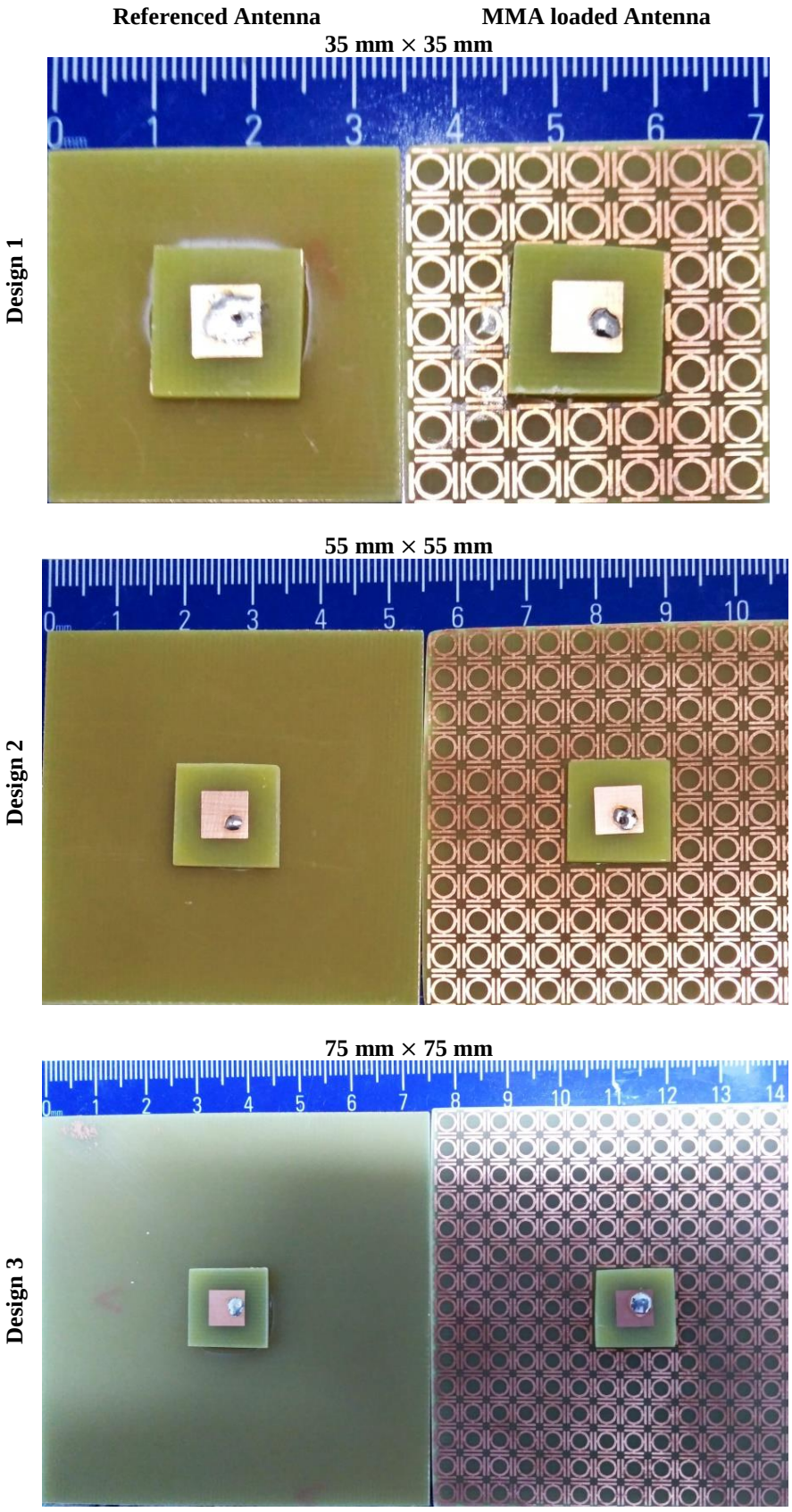

Figure 5.11 Fabricated coaxial feed patch antenna with and without MMA.

This technique has been adopted for our research work because of its simplicity and uncomplicated impedance matching characteristics. The outer conducting layer of the *SMA* connector is connected to the ground plane, while the center conductor is fed through the substrate and ground-plane by drilling hole and electrically connected to the patch antenna. To minimize the mutual coupling and keep the antenna radiation performance unaffected a small gap *(g_s)* of 3.5 mm has been left between *MMA* and each design.

This research work has been divided into three design models to evaluate the possibility and capability of *MMA* structure in enhancing the stealth capability along with to study the effects of *MMA* on patch antenna radiation performance.

(i) *Design 1,* Initially, a referenced patch antenna of periodicity 35 mm x 35 mm is designed with and without two *MMA* layers and its radiation performance is simulated and analyzed as depicted in Figure 5.8.

(ii) *Design 2,* This referenced patch antenna is then modified and extended to four layers of *MMA* with the periodicity of 55 mm x 55 mm as shown in Figure 5.9.

(iii) *Design 3,* Finally, this structure is further extended, where the exiting source is loaded with six layers of *MMA* structure with the periodicity of 75 mm x 75 mm as depicted in Figure 5.10.

It has been analyzed that as we start increasing the number of *MMA* layers around exiting source the resonant frequency (f_0) response remains almost unaffected. All designs are fabricated with and without *MMA* structure and have been given in Figure 5.11.

5.2.2. Antenna Radiation Performances Analyses

To study the effect of *MMA* structure on patch antenna radiation performances, comparative analyses have been made and tabularized in Table 5.3. The radiation performance curves have been analyzed and shown in Figure 5.12.

For Design 1, the referenced antenna achieved resonance at 10 GHz frequency with scattering coefficient (S_{11}) value of -48.17 dB. Although, after loading with *MMA* layers its resonance peak slightly moves to 9.96 GHz with S_{11} equal to -44.39 dB.

For Design 2, the referenced antenna resonance peak appears at 10.01 GHz frequency with S_{11} value corresponds to -35.45 dB and after loading with *MMA* layers its resonance slightly shifted to 9.98 GHz with the S_{11} value reached to -35.62 dB.

For Design 3, the referenced antenna resonance remains unaltered to 10 GHz frequency with S_{11} value of -34.49 dB and after loading with *MMA* layers its resonance slightly shifted to 9.99 GHz with S_{11} value of -38.49 dB as shown in Figure 5.12(a).

For Design 1, the value of return loss parameter increases marginally after loading *MMA* structure. While for Design 2 and Design 3 after loading *MMA* layers the values slightly diminished. This behavior is observed because of a shift in matching impedance (Z_{11}) with the increase in the periodicity of the structure as shown in Figure 5.12(b). For Design 1, the shift in Z_{11} for modified patch antenna with respect to 50 Ω matching impedance is 3.06 Ω and for Design 2, it starts reducing and becomes equal to 2.77 Ω. While for Design 3, the value of Z_{11} approaches to 50 Ω matching impedance and reduces as close as 0.4 Ω.

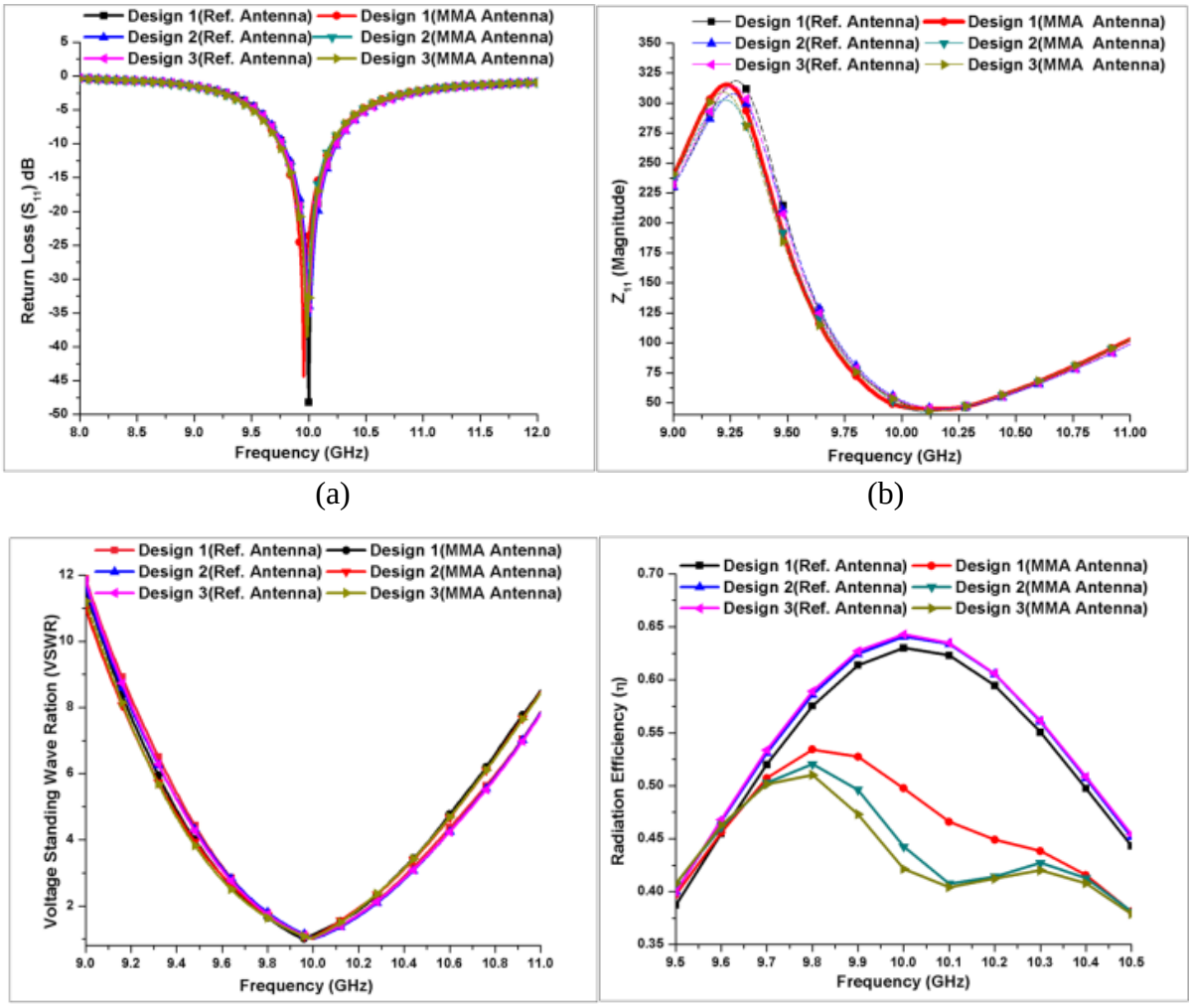

Figure 5.12 Comparison of radiation performance curves. (a) Return loss (S_{11}) (b) impedance (Z_{11}) (c) voltage standing wave ratio (VSWR), and (d) radiation efficiency (η).

Table 5.3 Antennas radiation performances comparison.

Structure/Performance Parameters	Design 1		Design 2		Design 3	
	Referenced Antenna	MMA Modified	Referenced Antenna	MMA Modified	Referenced Antenna	MMA Modified
Size	35 mm × 35 mm		55 mm × 55 mm		75 mm × 75 mm	
Frequency (f_0) GHz	10	9.96	10.01	9.98	10	9.99
Return Loss (S_{11}) dB	-48.17	-44.39	-35.45	-35.62	-34.49	-38.49
Bandwidth (-10 dB) MHz	456	460	468	436	468	460
Total Efficiency (η)	63.02	53.43	64.09	52.06	64.29	51.04
VSWR	1.01	1.14	1.04	1.06	1.04	1.05
Impedance (Z_{11}) Ω	50.27	46.94	52.03	47.23	51.33	49.60

A comparison of -10 dB bandwidth, voltage standing wave ratio (*VSWR*), and radiation efficiency (η) between referenced antenna and *MMA* modified patch antenna for all three designs have been made. The analysis indicates that the bandwidth remains almost unaltered for all design models. The simulated value of *VSWR* for all design remains within the acceptable range from 1.0 to 2.0 as depicted in Figure 5.12(c). Similarly, a simulation analysis is made to find out the efficiency of the antenna and a small reduction in Radiation Efficiency (η) has been observed after loading with *MMA* and shown in Figure 5.12(d).

5.2.3. Antenna Directivity and Gain Analyses

Analyses of directivity and gain between referenced antenna and *MMA* loaded patch antenna have been made and its polar plots have been drawn in Figure 5.13.

For *E-Plane* in Design 1, the reference patch main lobe magnitude is 6.83 dBi and for *MMA* loaded antenna it is reduced to 5.57 dBi. For Design 2, the reference patch antenna main lobe magnitude becomes 7.11 dBi and after loading *MMA* it is slightly increased to 7.45 dBi. For Design 3, the reference patch main lobe magnitude becomes 6.69 dBi and after loading *MMA* it is increased to 6.96 dBi.

For *H-Plane* in Design 1, the reference patch main lobe magnitude is 6.79 dBi, while for *MMA* loaded antenna, it is unexpectedly reduced to 3.36 dBi. For Design 2, reference patch main lobe magnitude becomes 3.52 dBi and after loading *MMA* it is sharply increased to 7.45 dBi. For Design 3, the reference patch main lobe magnitude becomes 6.35 dBi and after

loading *MMA* it is increased to 7.16 dBi. So the directivity performance for Design 1 remained poor while for Design 2 and Design 3 its performance increases after loading *MMA*.

For *E-Plane* in Design 1, the reference patch main lobe gain magnitude is 4.82 dB and for *MMA* loaded antenna it is sharply reduced to 2.54 dB. For Design 2, the reference patch

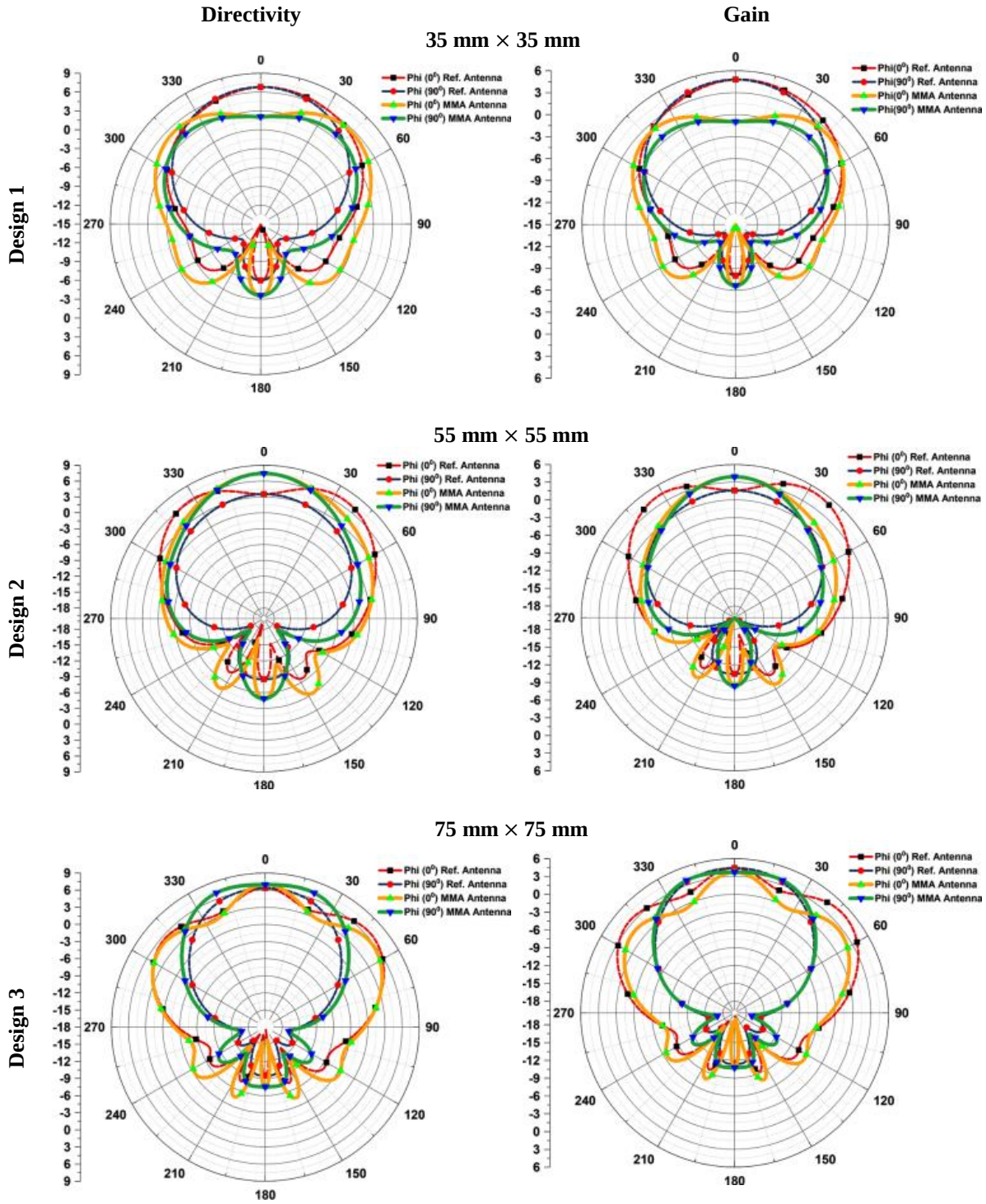

Figure 5.13 Comparisons for directivity and gain of the proposed models.

antenna main lobe magnitude becomes 5.17 dB and after loading *MMA* it is reduced to 3.91 dB. For Design 3, the reference patch main lobe magnitude becomes 4.77 dB and after loading *MMA* it is also reduced to 3.71 dB.

Table 5.4 Comparisons of antennas directivity and gain for E-Plane and H-Plane.

Structure/Performance Parameters (10 GHz)		Phi (ϕ)	Directivity (dBi)	Gain (dB)
Design 1	Referenced	0^0	6.83	4.82
	Antenna	90^0	6.79	4.79
	MMA	0^0	5.57	2.54
	Modified	90^0	3.66	0.63
Design 2	Referenced	0^0	7.11	5.17
	Antenna	90^0	3.52	1.59
	MMA	0^0	7.45	3.91
	Modified	90^0	7.45	3.91
Design 3	Referenced	0^0	6.69	4.77
	Antenna	90^0	6.35	4.43
	MMA	0^0	6.96	3.71
	Modified	90^0	7.16	3.91

For *H-Plane* in Design 1, the reference patch main lobe magnitude is 4.79 dB while for *MMA* loaded antenna it is unexpectedly reduced to 0.632 dB. For Design 2, the reference patch main lobe magnitude becomes 1.59 dB and after loading *MMA* it is increased to 3.91 dB. For Design 3, the referenced patch main lobe magnitude becomes 4.43 dB and after loading *MMA* it is marginally reduced to 3.91 dB. So, the results show a poor gain performance for Design 1, whereas for Design 2 it is affected marginally and for Design 3, it is remained well kept and tabularized in Table 5.4.

5.2.4. Monostatic RCS Reduction Analyses for Patch Antennas

As compared to conventional antenna geometry, *Monostatic RCS* of the *MMA* loaded patch antenna is almost polarization independent. The *Monostatic RCS* of the conventional antenna and *MMA* loaded patch antenna for *x-polarization* and *y-polarization* incidence wave have been shown with its measured values in Figure 5.14.

For Design 1, it has been found that the value for *Monostatic RCS* reduced throughout the observation band after loading it with *MMA* as shown in Figure 5.14(a). At 10 GHz resonant frequency, the reduction in *Monostatic RCS* for *MMA* loaded antenna is -26.39 dBsm for

x-polarization and -28.17 dBsm for *y-polarization.* However, the significant peak reduction is obtained at 9.93 GHz with -28.82 dBsm for *x-polarization* and at 9.95 GHz with 30.16 dBsm for *y-polarization.* So, a maximum difference of 9.61 dBsm observed for *x-polarization* and 10.82 dBsm for *y-polarization* between referenced and proposed antenna.

For Design 2, at 10 GHz resonant frequency, the reduction in *Monostatic RCS* for *MMA* loaded antenna is -18.32 dBsm *for x-polarization* and -17.90 dBsm for *y-polarization.* Whereas, the significant peak reduction is obtained at 9.91 GHz with -31.89 dBsm and -48.04 dBsm for *x-polarization* and as well for *y-polarization* respectively as shown in Figure 5.14(b). A maximum difference of 22.67 dBsm observed for *x-polarization* 38.56 dBsm for *y-polarization* between referenced and proposed antenna.

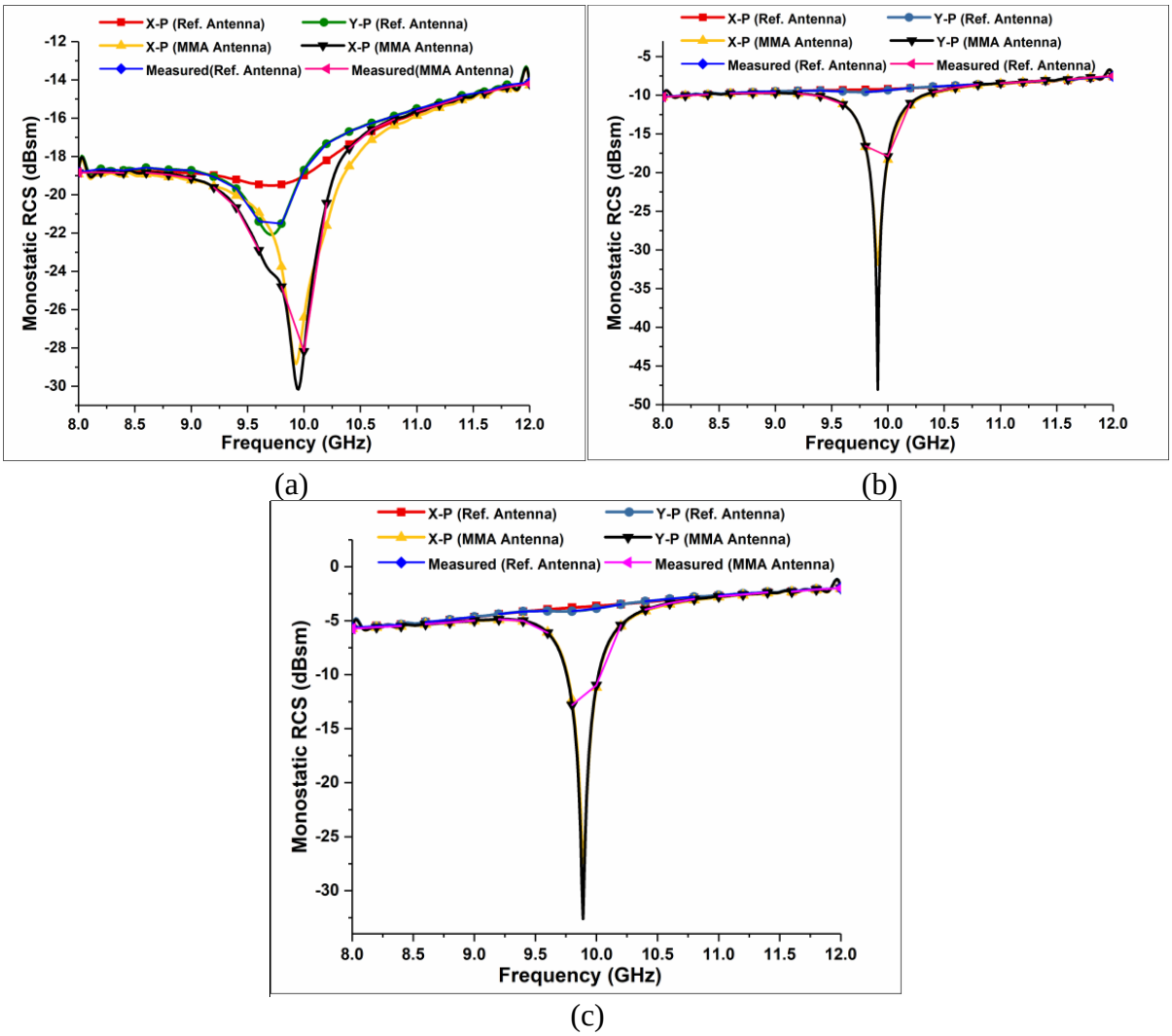

Figure 5.14 Comparison of x-polarization and y-polarization for Monostatic RCS (a) Design 1 (b) Design 2, and (c) Design 3.

For Design 3, at 10 GHz resonant frequency the reduction in *Monostatic RCS* for *MMA* loaded antenna is -11.17 dBsm *for x-polarization* and -10.96 dBsm for *y-polarization.* Although, the significant peak reduction is obtained at 9.89 GHz with -27.39 dBsm and -32.62 dBsm for *x-polarization* as well as for *y-polarization* respectively as depicted in Figure 5.14(c). So, a maximum difference of 23.68 dBsm observed for *x-polarization* 28.59 dBsm for *y-polarization* between referenced and proposed antenna. Small deviations in simulated and measured results are found during fabrication, handling, and testing of structure and cannot be avoided. Thus, the measured *RCS* values for antennas are in good agreements with the simulation results.

5.2.5. Bistatic RCS Reduction Analyses for Patch Antennas

A simulation analysis of conventional patch antenna and *MMA* loaded patch antenna has been also made for *Bistatic RCS* of horizontal and vertical polarization as depicted in Figure 5.15. The *Bistatic RCS* of the referenced antenna and proposed *MMA* modified antenna has been simulated and analyzed at 10 GHz. Vertical polarization curves for all designs have been also given. Since the structure is almost polarization independent so its behaviors are not considered here.

For Design 1 at $\phi = 0^0$, the *Bistatic RCS* of the *MMA* loaded antenna reduced significantly throughout the angle theta (θ) between -83^0 to 84^0. However, the maximum difference is observed of 36.03 dBsm at 34^0 and 16.40 dBsm at -34^0, respectively. At $\phi = 90^0$, the *Bistatic RCS* of the *MMA* loaded antenna reduced significantly for theta (θ) with a major reduction in between -144^0 to 144^0. However, the maximum difference is observed of 13.48 dBsm at 50^0 and -50^0, respectively between referenced and *MMA* loaded antenna.

For Design 2 at $\phi = 0^0$, the *Bistatic RCS* of the *MMA* loaded antenna reduced significantly throughout the angle theta (θ) between -82^0 to 82^0. However, the maximum difference is observed of 44.17 dBsm at 59^0 and 33.89 dBsm at -54^0, respectively. At $\phi = 90^0$, the *Bistatic RCS* of the *MMA* loaded antenna reduced significantly throughout the angle theta (θ) with a major reduction in between -176^0 to 176^0. However, the maximum difference is observed of 13.80 dBsm at 33^0 and -33^0, respectively between referenced and *MMA* loaded antenna.

For Design 3 at $\phi = 0^0$, the *Bistatic RCS* of the *MMA* loaded antenna reduced significantly throughout the angle theta (θ) between -81^0 to 81^0. However, the maximum difference is found of 27.96 dBsm at 70^0 and 28.07 dBsm at -73^0, respectively. At $\phi = 90^0$, the *Bistatic RCS* of the

MMA loaded antenna reduced significantly throughout the angle theta (θ) with a major reduction in between -169^0 to 169^0. However, the maximum difference is noticed of -13.50 dBsm at 25^0 and -25^0, respectively between referenced and *MMA* loaded antenna.

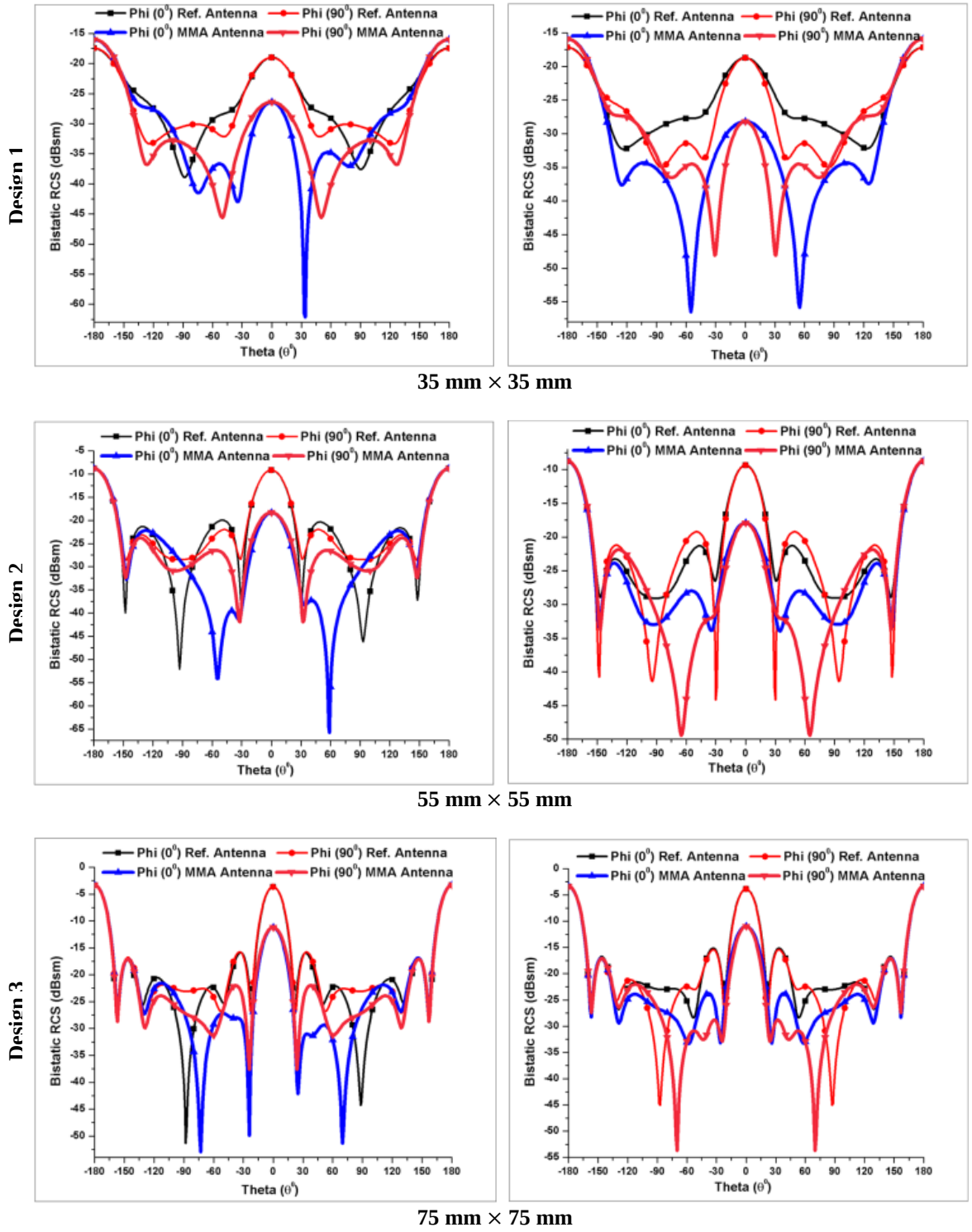

Figure 5.15 Comparisons of Bistatic RCS for referenced patch antennas at 10 GHz.

5.3. Design of Patch Antenna Array using Shorted Stubs Metamaterial Absorber

A novel design approach for the out-band *RCS* reduction of a conventional 2×2 patch antenna array using shorted stubs *MMA* operating in X-band has been proposed. A patch antenna array has been designed at a resonant frequency of 7.54 GHz. Simulation and experimental results exhibit that when patch antenna array is loaded with *MMA*, its *Monostatic* and *Bistatic RCS* response reduces significantly for the horizontal as well for vertical polarization. However, it has negligible influence on the radiation characteristics, whilst the bandwidth, gain and overall performance of patch array preserved simultaneously. Finally, a compatibility of observation achieved between simulated and measured results. This section gives the augmentation published in [175].

Owing to its advantages, patch antennas are used to a great extent today because of its simple design, linearly polarized, conformability to planar and non-planar structures, cost-effective, ease of implementation and compatible with the circuit board technology. Therefore, a lot of research is focusing on *RCS* reduction of single patch antenna structure [129, 153, 154]. But this type of antenna having some disadvantages and suffers from low radiation performance such as its narrow bandwidth, directivity, lower gain, and radiation efficiency.

Therefore, it cannot be used for long-distance communication especially in military applications, where a radar system is used to scan the electromagnetic beam quickly throughout the sky to detect the planes and missiles and contrariwise. Numerous techniques have been advised to improve its radiation preformation. One of the vital solutions is a combination of the patch antenna so-called antenna array. It has been found that when several antenna elements are combined to form an array, its overall radiation performance enhances furthermore [159, 176, 177].

One of the problems with previous *MMA* designs is *RCS* reduction achieved at the cost of the increased size of the substrate. Thus, this doesn't support miniaturization and turn out to be the unreliable and uneconomical solution [148, 178, 179]. So, we have tried to achieve the *RCS* reduction without increasing the periodicity of antenna unit cell structure. Again, it has been found that when the gap between multiple antennas reduces, their performance starts degrading and that influence factors like gain and radiation efficiency because of the mutual coupling among them. By using *MMA* capability of suppressing surface waves propagation in a given frequency range, one can compensate for these losses [118].

5.3.1. Linear Patch Array Antenna Design Aspects

For long distance communication, single element antenna is insufficient to fulfill the gain or radiation pattern requirement. Therefore, making an array could be a possible solution. The antenna array is a process of placing many antennas all together with an exact number of elements, amplitude, spacing, and phasing based on the target application.

Proper spacing and phasing are required so that the individual radiation will meet at the point of interest in a constructive way and in other direction they will cancel out each other because of destructive interference. So that we will get a very high directional pattern with higher directivity and gain in the desired direction without getting anything in the other direction that offers applications in radar and terrestrial communication. But practically, it does not cancel out in other directions leads to side lobes.

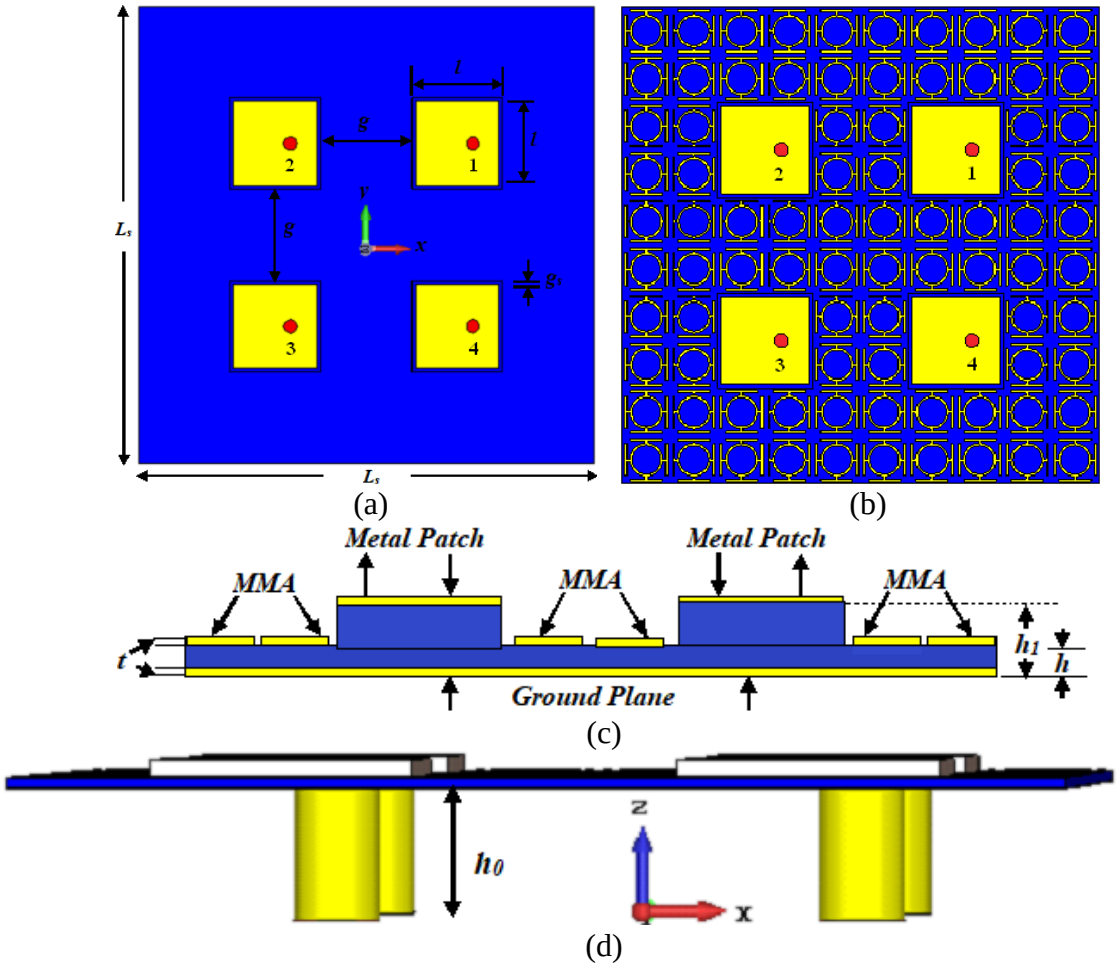

Figure 5.16 Coaxial feed patch antennas. (a) Proposed antenna array (b) MMA loaded antenna array (c) side view of the proposed antenna, and (d) side view with a coaxial feed.

Phase distribution to the individual element decides how the fields that are meeting at the point of interest and modifies the side lobe level and the main lobe direction. The surface area or aperture of the complete radiating structure is decided on the basis of a total number of elements and their spacing. A larger aperture size enhances its gain performance and a larger spacing enhances its directivity. For this research work, we have restricted our study to 2×2 antenna element.

A *λ/2* element spacing value has been chosen to avoid side lobes occurrence [180]. Although it increases directivity when the element spacing approaches to λ. Multiple unwanted grating lobes appear when element spacing value goes beyond λ so become impractical. Here, we have considered element spacing (g) of *λ/2* that approximates to 20 mm with respect to the central frequency of 7.5 GHz as shown in Figure 5.16(a). In this research work, the antenna elements are fed with the same amplitude, equal phase and uniform spacing results in a planar antenna array.

The basic structure of the proposed patch antenna array is depicted in Figure 5.16. It is designed to operate at 7.53 GHz resonant frequency by varying and optimizing its physical parameters. The top layer is the radiating patch made up of copper-backed by a most popular, low cost and readily available flame retardant *FR4* substrate with *tan* δ and ε_r are 0.025 and 4.3, respectively. The substrate is grounded using a copper layer. The periodicity (L_s) of Patch Antenna array is 50 mm × 50 mm with the length of the radiating Patch (l) is 9.17 mm. The length of the central substrate is 10 mm whereas the central substrate height (h_1) is 1 mm. The thickness of the remaining surrounded area (h) is 0.4 mm where *MMA* is designed.

All the parameters description has been given in Table 5.5. The design of a conventional patch antenna array has been shown in Figure 5.16(a) with its parameters. While Figure 5.16(b) shows the modified *MMA* loaded patch antenna array. A side view of the modified structure is depicted in Figure 5.16(c). The fabricated reference and proposed antenna array view have been given in Figure 5.17(a) and (b), respectively. The feeding technique used for the antenna is very important when we consider the RCS reduction of the antenna because it controls the antenna scattering characteristics. An antenna suffers from two types of scattering namely Structural Mode and Antenna Mode Scattering. If the antenna is fed by properly matched loads, there will be only structural mode scattering. But when the antenna is not fed by perfectly matched loads there will be both scatterings that mean a part of the energy will be reflected and reradiate back to space.

Table 5.5 Antenna parameter descriptions.

Description	Dimensions (mm)	Parameters
L_s	50	Periodicity of Structure
h_1	1	height of substrate
l	9.17	Length of Patch
g	10	Element Spacing
g_s	0.83	Gap b/w Patch and MMA
t	0.035	Thickness of metal
Pos_x	1.68	Position of Probe
h_0	5	Height of connector

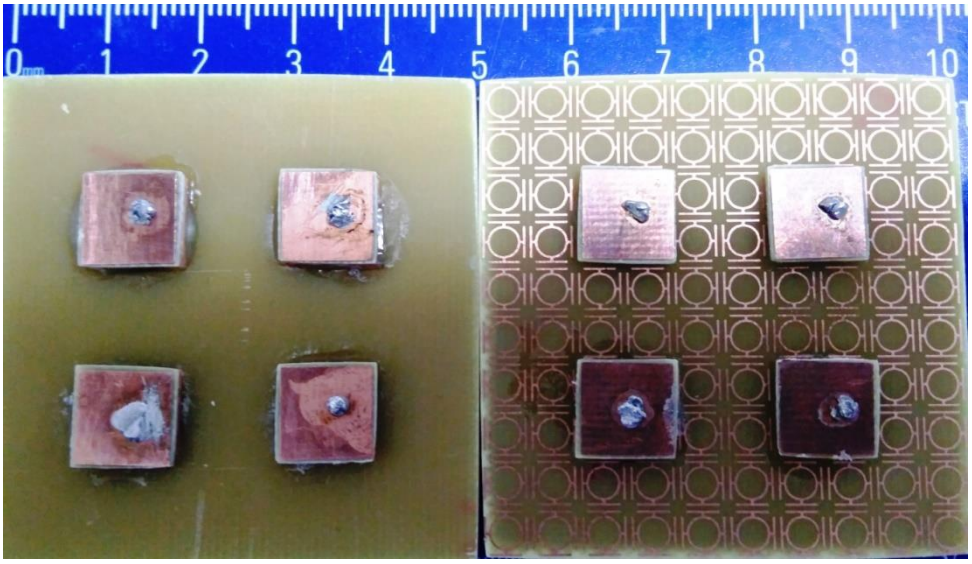

(a) (b)

Figure 5.17 Fabricated antenna array (a) referenced antenna array and (b) proposed antenna array structure.

A coaxial feed technique provides the low *RCS* Since its feeding network is on the other side of the dielectric material as compared to the microstrip feeding technique. So *MMA* absorber based technique is most suitable for the reduction of *RCS*. As we cannot change the antenna structure parameters since it influences the frequency response behavior. However, it has been found that when the Patch antenna surrounded by *MMA* structure, it immensely reduces the *RCS* effect on the system without compromising with the performance of the antenna. Thus, one can minimize the structural mode *RCS* as low as possible and hence emerge as a new design technique.

Each patch element has been fed by coaxial feed with its central position approximates to 50 Ω matching the impedance at the position, pos_x =1.68 mm and pos_y =0 *as* shown in Figure 5.16 (d). Its frequency response is optimized at 7.54 GHz. Then, the antenna structure is modified and loaded with 10 × 10 *MMA* unit cell. A total of 2 × 2 *MMA* unit cells are etched out for the antenna array. To minimize the mutual coupling and keep the antenna radiation performance unaffected a small gap (g_s) of 0.83 mm is kept between *MMA* and each patch element.

5.3.2. Linear Patch Antenna Array Design Analyses

A comparison of scattering parameters (S_{11}) has been made between the conventional antenna array and modified antenna array with the measured results and is shown in Figure 5.18. The S_{11} for a conventional antenna array occurs at 7.54 GHz with resonance peak magnitude of -24.52 dB. When it is loaded with *MMA* unit cells then the return loss (S_{11}) for a modified antenna array occurs at 7.57 GHz with resonance peak magnitude of -21.64 dB. The measured results for both structures has been also shown that indicates that for the conventional antenna the resonance peak for S_{11} is obtained at 7.53 GHz with the magnitude of -19.45 dB while for *MMA* loaded antenna array the value for S_{11} occurred at 7.55 GHz with the magnitude of -17.37 dB.

The value for -10 dB bandwidth for conventional antenna array came out to be 274 MHz that is 3.63 % of resonant frequency however for modified antenna array it came out to be 278 MHz that is 3.67 % of resonant frequency. So, a small increment in bandwidth is observed with a modified *MMA* loaded antenna array. An analysis of radiation pattern between the referenced antenna and *MMA* loaded patch antenna has been made and is shown in Figure 5.19.

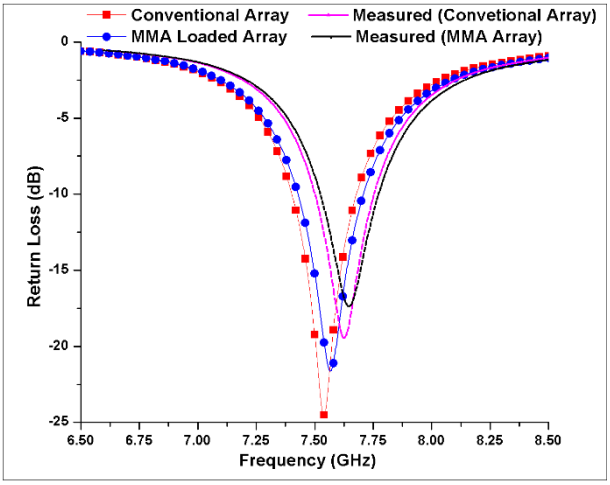

Figure 5.18 Comparisons of return loss (S_{11}) curve for patch antenna array.

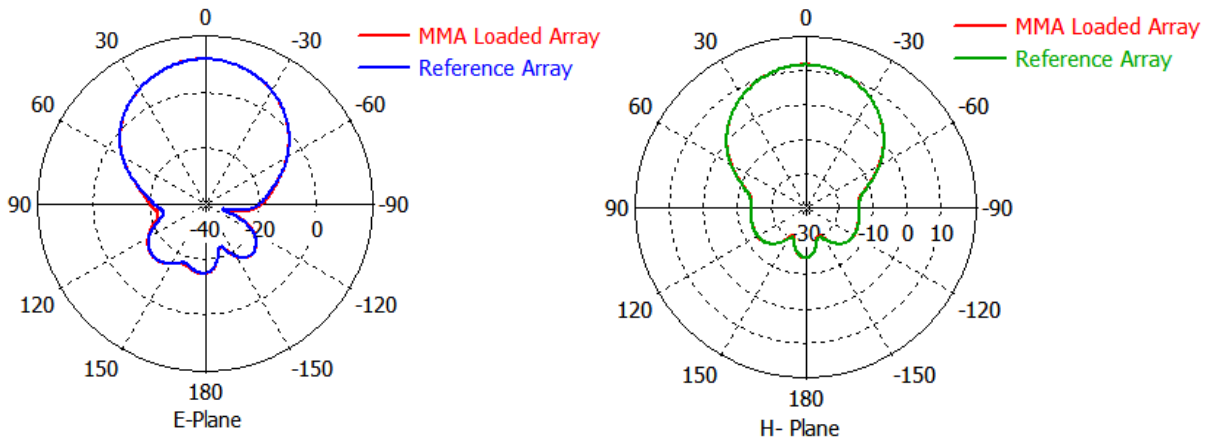

(a) (b)

Figure 5.19 Analyses of simulated radiation pattern between reference patch array antenna and MMA loaded patch antenna for (a) $\phi = 0^0$ and (b) $\phi = 90^0$.

For *E-Plane*, the reference patch array operating frequency resonant peak occurs at 7.54 GHz with main lobe magnitude is 11.6 dBi with the direction is at 0^0 and 3 dB angular width 49^0 while sidelobe level is -25.4 dB. For *MMA* loaded Patch array the is at 0^0 and 3 dB angular width 48.7^0 while sidelobe level is -25.4 dB as shown in Figure 5.19(a).

For *H-Plane*, the operating frequency resonant the peak occurs at 7.57 GHz with main lobe magnitude is 11.7 dBi with the direction reference patch array operating frequency resonant peak occurs at 7.54 GHz with main lobe magnitude is 11.6 dBi with the direction is at 0^0 and 3 dB angular width 50.5^0 while sidelobe level is -25.3 dB. For *MMA* loaded Patch array the operating frequency resonant peak occurs at 7.57 GHz with main lobe magnitude is 11.7 dBi with the direction is at 0^0 and 3 dB angular width 50.2^0 while sidelobe level is -25.4 dB as shown in Figure 5.19(b).

A comparison of voltage standing wave ratio (*VSWR*), impedance (Z_{11}) and radiation efficiency (η) has been made between the conventional antenna array and *MMA* loaded antenna array as depicted in Figure 5.20. The simulated value of *VSWR* for reference patch array operating at 7.54 GHz resonance frequency is 1.27, whilst for *MMA* loaded Patch array operating at 7.57 GHz resonance frequency is 1.30, which is within the acceptable range from 1.0 to 2.0 as depicted in Figure 5.20(a).

The simulated value of Z_{11} for reference patch array operating at 7.54 GHz resonance frequency is 52.59 Ω, whilst for *MMA* loaded Patch array operating at 7.57 GHz resonance frequency is 52.89 Ω, which is approximately matched to 50 Ω resistances as depicted in Figure 5.20(b).

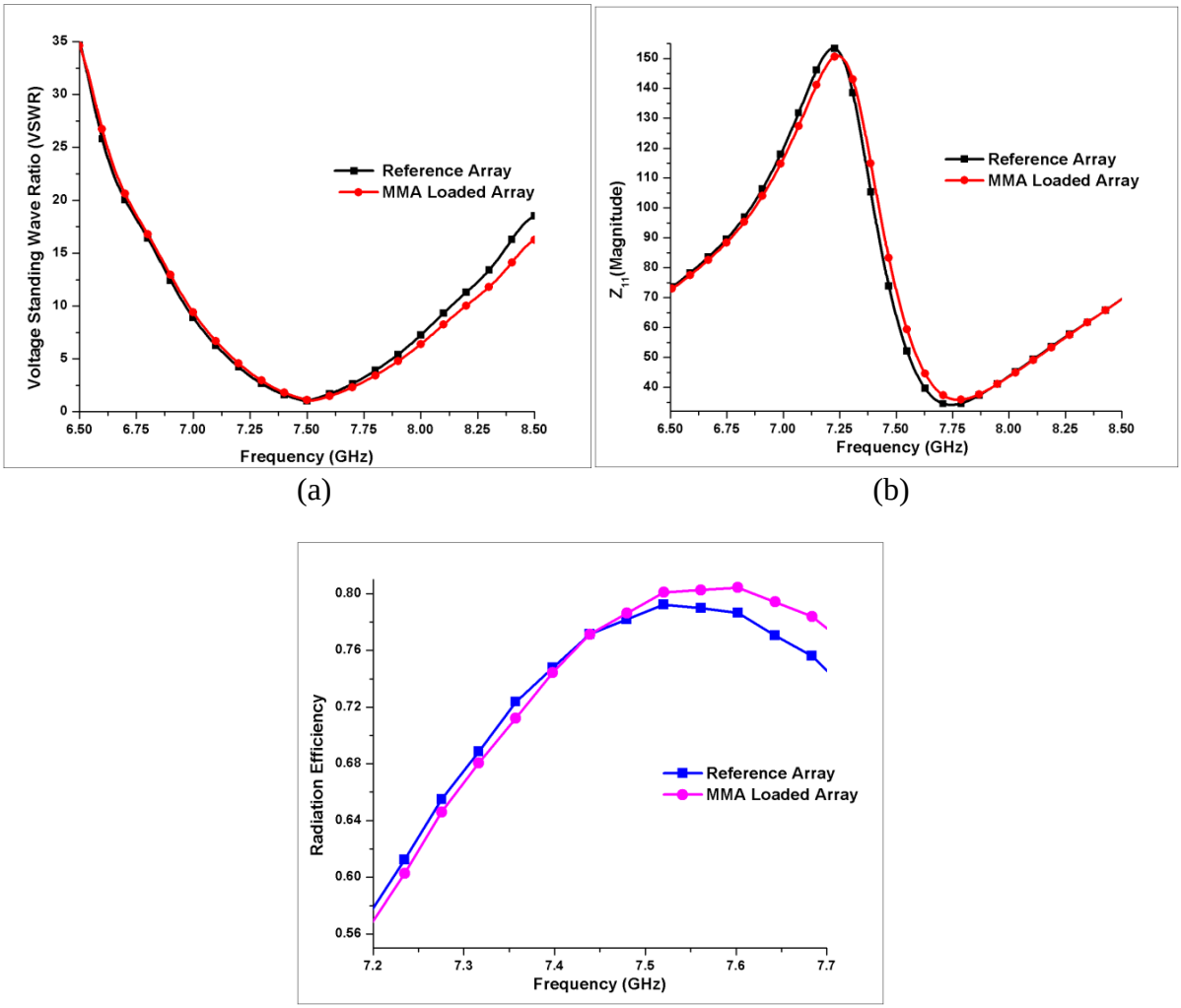

Figure 5.20 Comparisons of simulated results for (a) VSWR (b) Z_{11}, and (c) η of the referenced and proposed MMA loaded patch array.

Table 5.6 Comparisons of antennas performances.

Structure/Performance Parameters	Referenced Antenna	Proposed Antenna
Frequency (f)	7.54 GHz	7.57 GHz
Return Loss (S_{11})	-24.52	-21.64
Bandwidth (-10 dB)	274 MHz	278 MHz
	(3.63 %)	(3.67 %)
Directivity	11.6 dBi	11.7 dBi
Gain Value	9.22 dB	9.39 dB
Radiation Efficiency (η)	79.48	80.26
VSWR	1.27	1.30
Impedance (Z_{11})	52.59	52.89

Similarly, a simulation analysis is made to find out the efficiency of antenna and it has been found that for reference patch array operating at 7.54 GHz the radiation efficiency comes out to be 79.48 %, whereas for *MMA* loaded Patch array operating at 7.57 GHz a slight rise in radiation efficiency is found and equal to 80.26 % as shown in Figure 5.20(c).

Thus, the *MMA* loaded antenna not only enhances the stealth capabilities of the antenna array but antenna radiation performance including gain, directivity, bandwidth, and radiation efficiency are found to increase marginally. Complete comparisons of the entire antenna performances have been given in Table 5.6, that signify the relevance and importance of this proposed antenna array design.

5.3.3. Monostatic RCS Reduction Analyses for Patch Antennas Array

As compared to conventional antenna geometry, *Monostatic RCS* of the *MMA* loaded patch antenna array is almost polarization independent. *Monostatic RCS* of the conventional array and *MMA* loaded array for *x-p* and *y-p* incidence wave have been shown in Figure 5.21(a) and Figure 5.21(b), respectively with its measured values. A table has been also drawn for the purpose of comparison and is depicted in Table 5.7. From the figure, it has been found that the value for *Monostatic RCS* reduced throughout observation band after loading it with *MMA* unit cells. However, at 10 GHz resonant frequency, the significant peak reduction in *Monostatic RCS* for *MMA* loaded antenna array is -20.41 *dBsm* for *x-p* and -20.25 dBsm for *y-p* incidence wave.

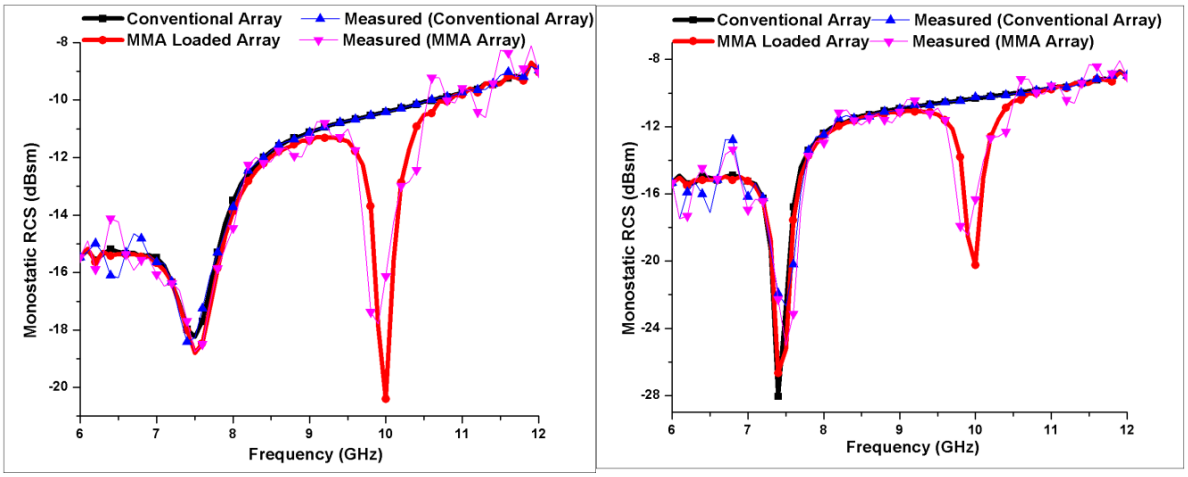

(a) (b)

Figure 5.21 Comparisons of Monostatic RCS for normal incidence (a) x-polarized incidence wave and (b) y-polarized incidence wave.

Table 5.7 Comparisons of Monostatic RCS for antenna array.

Structure / Frequency (GHz)	Referenced Antenna(dBsm)		Modified Antenna(dBsm)	
	x-p	y-p	x-p	y-p
6	-15.47	-15.33	-15.46	-15.35
6.5	-15.28	-15.04	-15.35	-15.14
7	-15.49	-15.25	-15.67	-15.23
7.5	-18.24	-22.62	-18.80	-25.22
8	-13.50	-12.40	-13.88	-12.52
8.5	-11.78	-11.37	-11.97	-11.47
9	-11.12	-10.93	-11.42	-11.16
9.5	-10.73	-10.60	-11.43	-11.28
10	-10.40	-10.32	-20.41	-20.25
10.5	-10.05	-10.02	-10.51	-10.46
11	-9.74	-9.70	-9.82	-9.79
11.5	-9.39	-9.37	-9.44	-9.44
12	-8.95	-8.95	-9.03	-9.03

A total reduction for *Monostatic RCS* is up to 10 dBsm *for x-p and* 9.93 dBsm for *y-p* incidence wave as compared with the referenced antenna. For conventional antenna array, the measured *Monostatic RCS* peaks are observed at -10.41 dBsm for *x-p* and -10.24 dBsm for *y-p*. Although for *MMA* loaded antenna, the measured *Monostatic RCS* peaks are observed at -16.12 dBsm for *x-p* and -16.32 dBsm for *y-p.* Minor deviations in simulated and measured results are recorded because of fabrication, handling, and testing of structure that can be ignored. Hence, the measured *RCS* values for antenna array are in good agreements with the simulation results.

5.3.4. Bistatic RCS Reduction Analyses for Patch Antennas Array

A simulation analysis of conventional array antenna and *MMA* loaded array antenna have been also made for *Bistatic RCS* and depicted in Figure 5.22. For horizontal polarization at $\phi = 0^0$, the *Bistatic RCS* of the referenced antenna array and proposed antenna array have been simulated and analyzed at 10 GHz. The *Bistatic RCS* of the *MMA* loaded antenna array reduced throughout the angle theta (θ) with a significant reduction in between -110^0 to 96^0. The maximum reduction between the referenced antenna array and *MMA* loaded antenna array observed of 11.75 dBsm at -32^0 and 22.08 dBsm at 32^0 respectively as shown in Figure 5.22(a).

At $\phi = 90^0$, the *Bistatic RCS* of the *MMA* loaded antenna array reduced significantly for angle θ in between -154^0 to 154^0. The maximum reduction between the referenced antenna

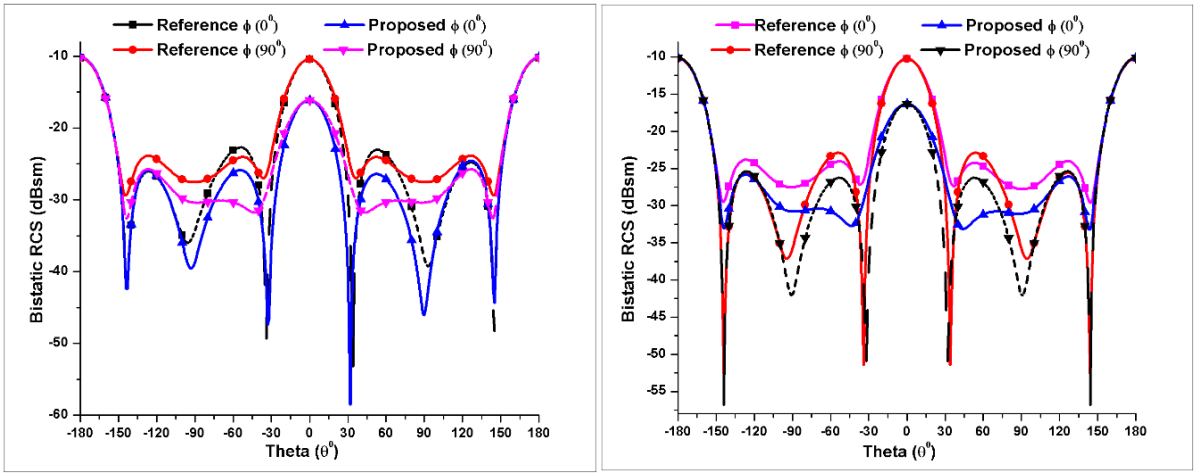

Figure 5.22 Comparisons of Bistatic RCS of the referenced array and proposed MMA antenna array for (a) horizontal and (b) vertical polarization at 10 GHz.

array and *MMA* loaded antenna array observed of 7.13 dBsm at -48^0 and 7.13 dBsm at 48^0, respectively.

For vertical polarization at $\phi = 0^0$, the *Bistatic RCS* of the referenced antenna array and proposed antenna array have been simulated and analyzed at 10 GHz. The *Bistatic RCS* of the *MMA* loaded antenna array reduced throughout the angle θ with a significant reduction in between -157^0 to 157^0. The maximum reduction between the referenced antenna array and *MMA* loaded antenna array observed of 7.94 dBsm at -48^0 and 8.23 dBsm at 48^0, respectively as shown in Fig. 9(b). At $\phi = 90^0$, the *Bistatic RCS* of the *MMA* loaded antenna array reduced significantly for angle θ in between -33^0 to 33^0. The maximum reduction between the referenced antenna array and *MMA* loaded antenna array observed of 16.51 dBsm at -32^0 and 16.51 dBsm at 32^0, respectively as shown in Figure 5.22(b).

5.4. Chapter Summary

In this chapter, a single-band low *RCS* rectangular patch antenna is presented, analyzed and is based on shorted stubs with rectangular bars *MMA* in Section 5.1. The reflection coefficient (S_{11}) and the radiation pattern of the modified antenna are also studied and it almost has a negligible effect on antenna performance. The co-polarization and cross-polarization patterns with respect to *E-Plane* and *H-Plane* of the proposed structure have been also analyzed. Effective isolation of *82.5 dBi* and *24.65 dBi* are observed for both planes and that indicated the suppression of cross-polar radiations. Further, Comparisons are made between the proposed antenna and the previously reported antennas that clearly justify the novelty of the proposed model. The results suggest that loading of shorted stubs *MMA* absorber plays an

important role and modified the antenna properties along with efficiently enhance the *RCS* capabilities of the rectangular patch antenna. The result shows a maximum *Monostatic* RCS reduction of 21.22 dBsm achieved for the proposed structure operation at X-band. This *MMA* absorber structure finds its various applications in military and defense area for the enhancement of *RCS* capabilities in the antenna.

In Section 5.2, comparative design analyses of *MMA* loaded patch antenna have been proposed. Analyses have been also made to study the effect of *MMA* on patch antenna before and after loading it. The results indicate that the radiation performance of the patch antenna has been affected marginally. Design 1 shows unsatisfactory directivity and gains response. Whereas for Design 2 and Design 3, directivity is enhanced with gain is affected slightly. A single patch antenna design has some limitations and suffers from low radiation performance such as narrow bandwidth, lower directivity, gain, radiation efficiency and less power handling capability. So it cannot be suitable for long-distance communication, especially in military applications. One of the vital solutions is to combine a number of antennas to form a patch array. It has been found that its overall radiation performance enhances and this is covered in Section 5.3.

In Section 5.3, we have proposed a shorted stubs metamaterial absorber operating at 10 GHz of the resonant frequency in X-band. A comparison has been made between reference antenna array and *MMA* modified antenna array. It has been found that when *MMAs* are loaded in a rectangular 2 × 2 patch antenna array, it significantly reduces the *RCS* of the structure throughout the observation band. Henceforth increase the stealth capability of the structure.

However, maximum resonance peak reduction is observed in 10 GHz at which *MMA* has been designed. The *Monostatic* and *Bistatic RCS* analysis have been made for *x-p* as well as for *y-p* of incidence wave. The overall radiation performance of antenna array with and without *MMA* remains preserved and unaffected. Even though, the gain, directivity, bandwidth and radiation efficiency found marginally increased. Because of the limitation on size and some very common errors during the fabrication process, then measurement precision, a slight variation in measured results observed with respect to simulated one.

These structures find its applications in stealth technology for military planes, space aircraft, missiles, ships, and other sensitive vehicles for long distance wireless communication and meant for lower detectable objects.

Chapter-6

RCS Reduction of Patch Antenna using Dual-Band Shorted Stubs MMA

In this chapter, we are proposing a dual-band slotted patch antenna with thin dielectric for *Ku-band* applications. A rectangular patch with a pair of bent slots at each side of the center has been designed that resonant at 11.95 GHz and 14.25 GHz with respect to *ITU* standard. For the perspective of In-band RCS reduction application, a dual resonance ultrathin shorted stubs *MMA* has been designed that operates at same frequency bands. Its behavior at an oblique angle of incidence and polarization sensitivity has been analyzed. The radiation performances of dual-band slotted patch antenna for S_{11}, -10 dB bandwidth, *VSWR*, and Z_{11} along with co polarization and cross polarization polar plots patterns for directivity and gain have been analyzed and observed. The *Monostatic* and *Bistatic RCS* response have been examined carefully and methodically for the referenced and proposed antennas. Finally, comparison of results with previously proposed dual-band antennas has been made to validate and justify the novelty of this proposed structure.

6.1. Introduction

In order to meet the miniaturization and compactness requirements of portable communication systems, the planar patch antenna design is a focused area [153, 157, 166, 181, 182]. For radar and satellite applications in *Ku-band,* these reduced-size planar patch antennas have needed to replace the huge-sized dish antenna [183-186]. It has been found that the *RCS* of dish antenna with an approximate size of 1 meter in 12 GHz is large enough, comparable to flat plate area and equivalent to antenna capture area [187]. Moreover, a fire control radar system is designed to emit a narrow and intense beam of radio waves to accurately track as well as lock the target, in order to minimize the chances of getting lost. So an operational dish antenna would provide a very stable, nonfluctuating *RCS* and thus vulnerable to attack. Therefore, it is worthwhile and imperative to reduce the size of the antenna as well as make it less severe to incoming radar.

Various researchers have been made to reduce the *RCS* of a planar patch antenna in *S*, *C* and *X-band* [171, 174, 175, 188, 189]. However, little attention has been given to *Ku-band*, which is reserved for fixed and direct broadcast satellite communication. An antenna designed

at *Ku-band* must be compact, cost-effective and offer better reliability. Whereas the conventional satellite antenna operating at *S, C and X-band* should require large dimension as the wavelength increases. Although, *Ku-band* suffers from rain fade and snow fade problems but can be mitigated by allocating appropriate link budget.

A higher power might overcome the losses because of rain fade and snow fade. Meanwhile, its uplink and downlink power can be increased to avoid interference in terrestrial terrains. If the antenna shall be able to transmit and receive, it should be able to operate on downlink frequencies according to *ITU* standard band (11.7 to 12.2 GHz), and for uplink frequency (14 to 14.5 GHz).

Therefore, it is required to design a dual-band antenna that could operate within these bands. In previous chapter 4, authors had designed "Dual resonance shorted stub circular rings metamaterial absorber" operating at 17 GHz and 18 GHz with absorbance peak response of 99.99% and 99.83%, respectively. Parametric analyses had been made to investigate the effect of variation of circular ring radius, shorted stubs length and rectangular bar length upon the resonance frequency. The effects at an oblique angle of incidence and polarization sensitivity were considered for both *TE* and *TM* modes till 70^0. The simulated surface current distribution of the structure had been also observed.

Compare to previous existing work, this proposed *MMA* structure has been modified to operate at 11.95 GHz and 14.25 GHz at *Ku-band* with respect to *ITU* standard. In this research work, the effects at an oblique angle of incidence (θ) and polarization sensitivity (ϕ) are considered only for *TE* mode. Intending to reduce in-band *RCS* of the patch antenna, a dual band slotted patch antenna is being designed to operate at the same resonance frequency. Its radiation performances that include S_{11}, -10 dB Bandwidth, voltage standing wave ratio (*VSWR)* and Impedance (Z_{11}) have been determined. Comparative analyses between referenced and proposed antennas have been made for directivity and gain of *E-plane* and *H-plane*. Its polar plots have been drawn, in accordance with co polarization and cross polarization patterns.

The In-band *Monostatic* and *Bistatic RCS* reduction of *MMA* has been achieved through loading it with dual-band shorted stubs metamaterial absorber on the top of the substrate. Finally, comparisons of results have been made with previously proposed structures. This indicates and clearly validates the performance of the proposed structure.

6.2. Dual Resonance Shorted Stubs Metamaterial Absorber Design

In this section, a dual resonance shorted stubs metamaterial absorber operating in *Ku-band* has been designed, simulated, analyzed and optimized. As shown in Figure 6.1, a unit cell of the *MMA* is composed of four circular rings and each circular ring has been modeled with shorted stubs and rectangular bars and centered at 11.95 GHz and 14.25 GHz resonant frequencies. The circular ring diameter has been adjusted to shift the complete frequency band, while the addition of shorted stubs and rectangular bars on the circular ring structure offers flexibility to adjust and tune the dual resonant frequency peaks [142]. Parameters of the proposed dual resonance *MMA* has been depicted in Table 6.1.

In Figure 6.2(a), the frequency response curves for dual resonance shorted stubs *MMA* between absorbance A(ω), reflectance R(ω) and transmittance T(ω) have been depicted with absorbance peaks of 99.89 % appeared at 11.95 GHz and 98.16 % appeared at 14.25 GHz respectively. In Figure 6.2(b), the simulated values for scattering coefficient (S_{11}) are -29.88 dB at 11.95 GHz and -17.36 dB at 14.25 GHz respectively. However, the measured values for S_{11} are -10.92 dB at 11.98 GHz and -10.96 dB at 14.26 GHz that are well above -10 dB, respectively.

Figure 6.2(c) shows the variation of resonant frequencies with an oblique angle of incidence (θ). For downlink frequency, the absorbance value remains above 94.89 % for θ

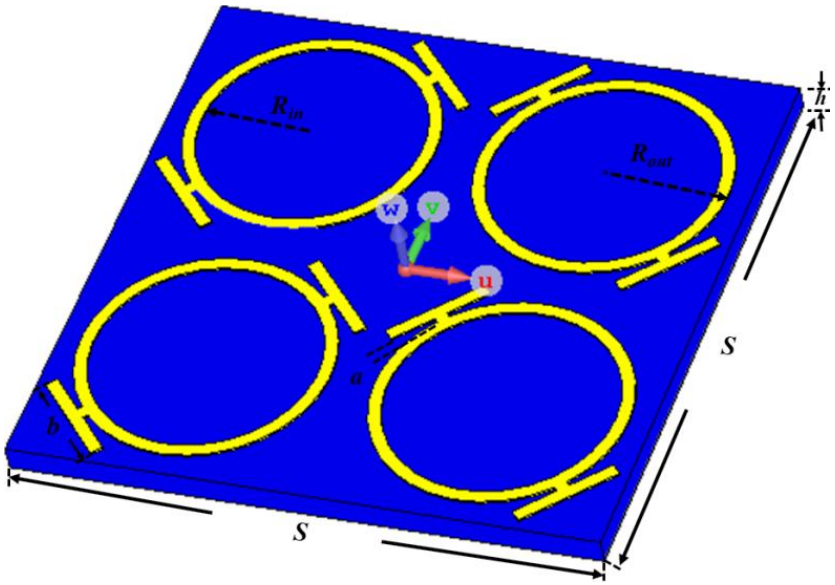

Figure 6.1 Dual-band circular rings with shorted stub metamaterial absorber.

Table 6.1 Parameters of proposed MMA.

Description	Parameters	Dimensions (mm)
Periodicity of Substrate	S	9.25
Height of substrate	h	0.4
Inner Radius	R_{in}	1.77
Outer Radius	R_{out}	1.97
The width of the ring	w	0.2
Stub Length	a	0.075
Thickness of metal	t	0.035
Bar Length	b	1.63

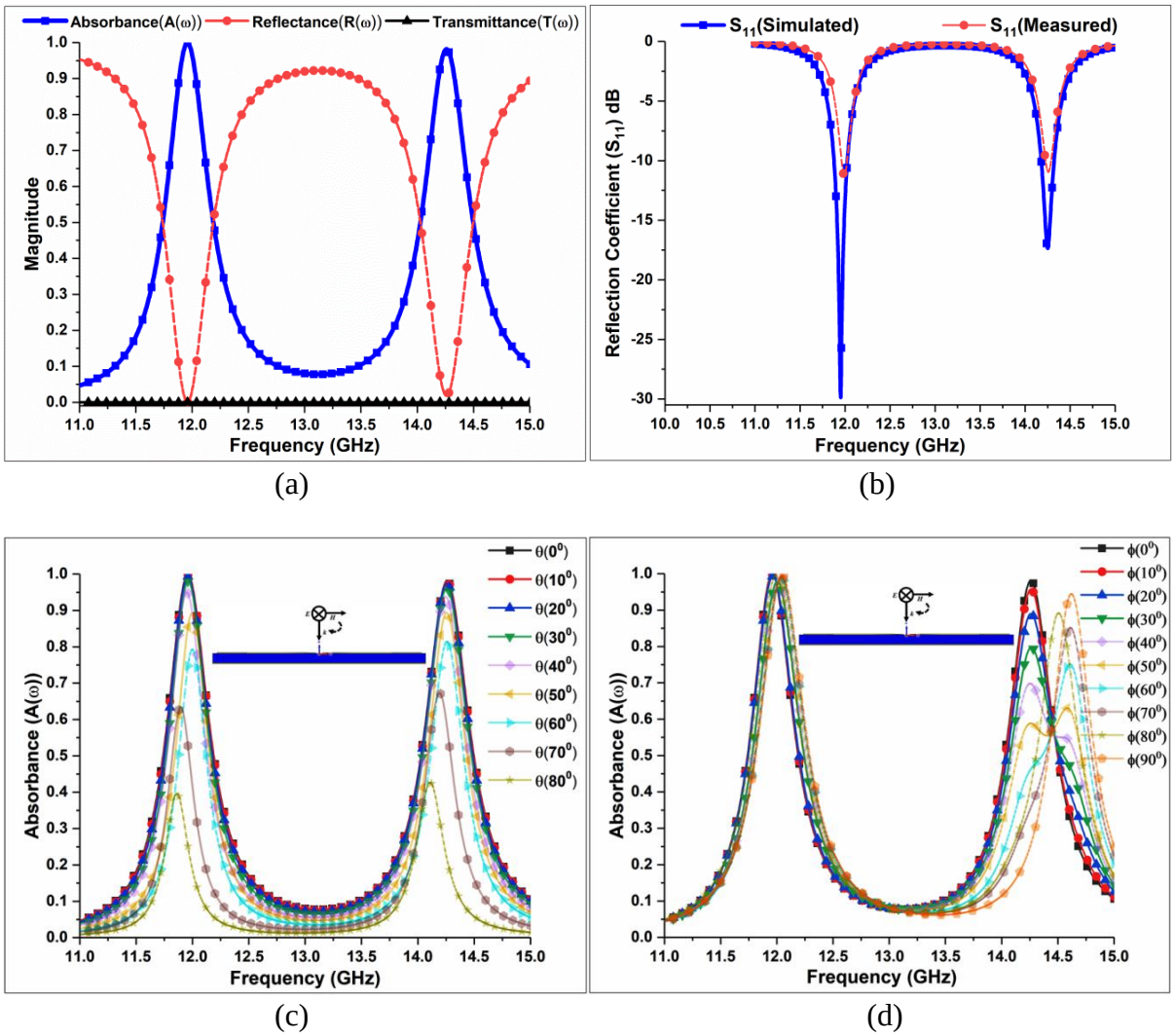

Figure 6.2. Frequency response curves for (a) A(ω), R(ω) and T(ω), (b) S_{11} simulated and measured results (c) oblique angle of incidence (θ), and (d) polarization sensitivity (ϕ) for TE modes of dual resonance shorted stubs MMA.

varies from 0^0 to 40^0. The resonant frequency starts varying at 60^0 with absorbance approaches to 79.30 % with frequency peak resonant at 12 GHz. For uplink frequency, the absorbance value remains above 93.81 % for θ varies from 0^0 to 40^0. At 60^0, the absorbance approaches to 81.45 % at the same resonant frequency.

A polarization sensitivity (ϕ) analysis has been also made to observe the behavior of *MMA* structure. For downlink frequency, the absorbance peaks remain above 97.70 % for ϕ varies 0^0 to 90^0. However, the resonant peak marginally shifted to 12.05 GHz at 90^0. For uplink frequency, the absorbance peaks remain above 58.87 % for ϕ varies of 0^0 to 90^0. However, the resonant peak shifted to 14.62 GHz at 90^0 with the absorbance of 94.46 %. This *MMA* absorber structure possesses circular symmetry, so *TM* mode analysis for θ and ϕ has not been considered in this research work.

6.3. Dual-band Slotted Patch Antenna Design

As the antenna is one of the crucial, integral and important parts of any communication system, significant research has been followed out to identify a low-profile planar dual-band antenna for wireless and satellite communication operating at *Ku-band* [190, 191]. A dual-band antenna is used in applications where transmission and reception should be done using the same antenna and thus provides an alternative to broadband antennas. To brace the increasing requirement of a sophisticated wireless communication system, numerous dual-band patch antennas have been proposed, those are competent of desegregation for more than one communication system into a single scheme [192-195].

Patch antennas are popularly used owing to its attractiveness in term simplicity, low profile, cost-effective, simple fabrication, linearly polarized, conformal and adaptability with other components of wireless communication. However, it comes at the cost of narrow bandwidth, lower gain, and increased cross-polarization effect [196, 197]. Making these considerations, authors have proposed a dual-band slotted patch antenna design operating at 11.95 GHz and 14.25 GHz resonant frequencies. The design of dual-band slotted patch antenna has been shown in Figure 6.3.

The whole radiating element of the proposed dual-band rectangular patch antenna is centered on the top of a copper ground plane of 27.75 mm × 27.75 mm. The patch has a side length of 5.46 mm and width of 4.44 mm, which is directly printed on an ultrathin flame

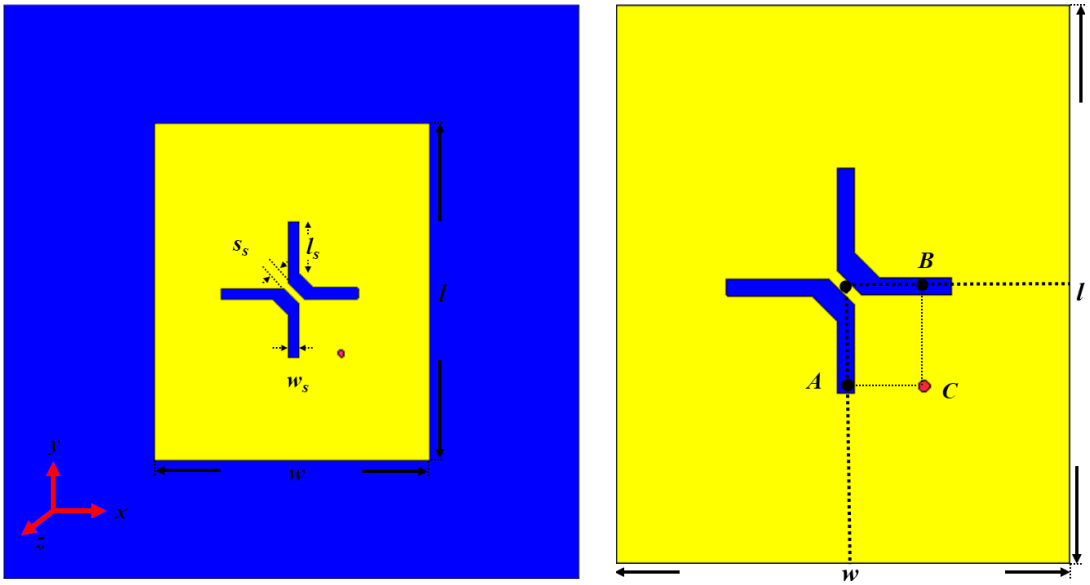

(a) (b)

Figure 6.3 Dual-band slotted patch antenna (a) front view and (b) coaxial-feed position.

retardant *FR-4* substrate material of thickness 0.4 mm with relative permittivity 4.3 and tangent loss 0.025 to reduce the cost.

A pair of bent slots of length (l_s) and width (W_s) is cut in the center of the patch, with a small spacing (S_s) between the two bent slots. The descriptions of the remaining antenna parameters have been tabulated in Table 6.2. In this work, a simple coaxial probe feeding has been employed owing to ease of impedance matching with low spurious radiation. The feed dimensions are optimized to achieve an impedance of 50 Ω.

Dual-band behavior is obtained by modifying the natural modes of a rectangular radiating patch through coupled-slot technique with suitable feed placement. This coupled-slot technique can reduce the radiating element size up to about 32% [198]. The dual-band

Table 6.2 Parameter descriptions of the antenna.

Description	Dimensions (mm)	Parameters
S_P	27.75	Periodicity of Structure
h	0.4	Thickness of substrate
l	5.46	Length of Patch
w	4.44	Width of Patch
l_S	2.08	Slot Length
W_S	0.17	Slot Width
S_S	0.23	Slot Spacing
t	0.035	Thickness of metal
Pos_x	0.8	Pin_inset_x
Pos_y	1	Pin_inset_y

behavior is obtained by reactively loading the patch antenna with bent slots [199]. This patch antenna design is linearly polarized.

The slotted structure behavior can be interpreted as that associated with two modes that arise from the perturbation of the TM_{01} and TM_{10} modes. A conventional rectangular patch without slots has the feed position corresponds to 50 Ω matching impedance situated along the line of the center of the patch width (point A) as shown in Figure 6.3(b). This mode of operation is the TM_{01} mode. By placing the feed along the line of the center of the patch length TM_{10} mode is achieved (point B).

After combining these points into a single feed position, both modes of operation can be achieved (point C). The frequency ratio between the upper and lower frequencies is mainly controlled by the aspect ratio of the patch whereas operating band frequency can be tuned by varying the slot length. All parameters are adjusted and optimized to obtain sharp dual-band peaks at 11.95 GHz and 14.25 GHz, respectively.

To analyze the future prospect and potential of dual-band *MMA* structure in enhancing the stealth capability of the referenced patch antenna, the radiating patch is designed with and

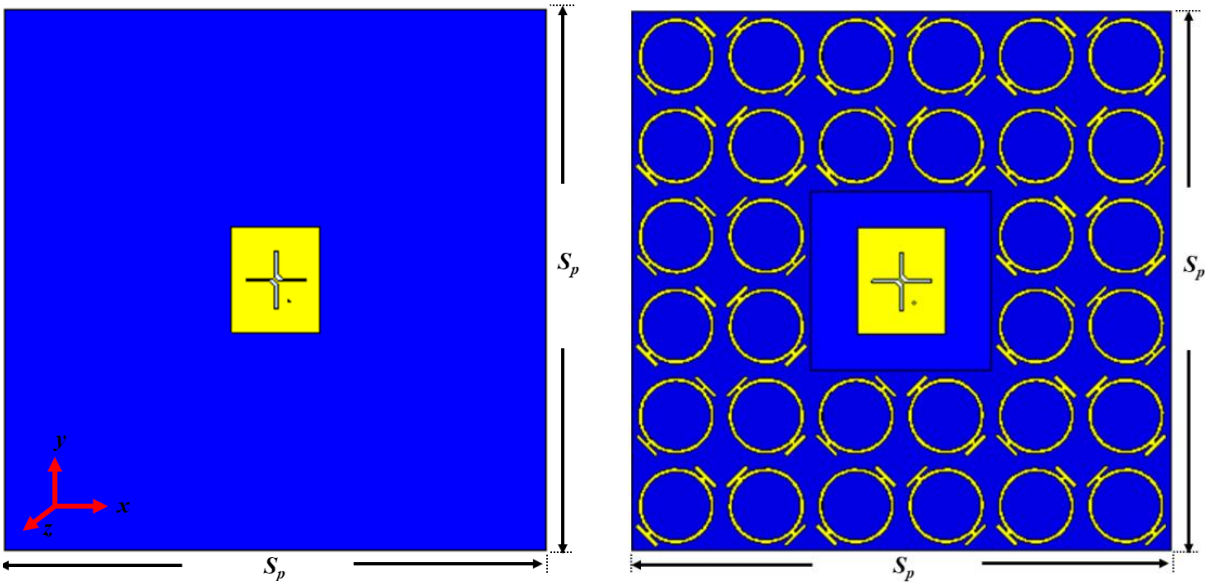

(a) (b)

Figure 6.4 Dual-band slotted patch antenna (a) referenced and (b) proposed antennas.

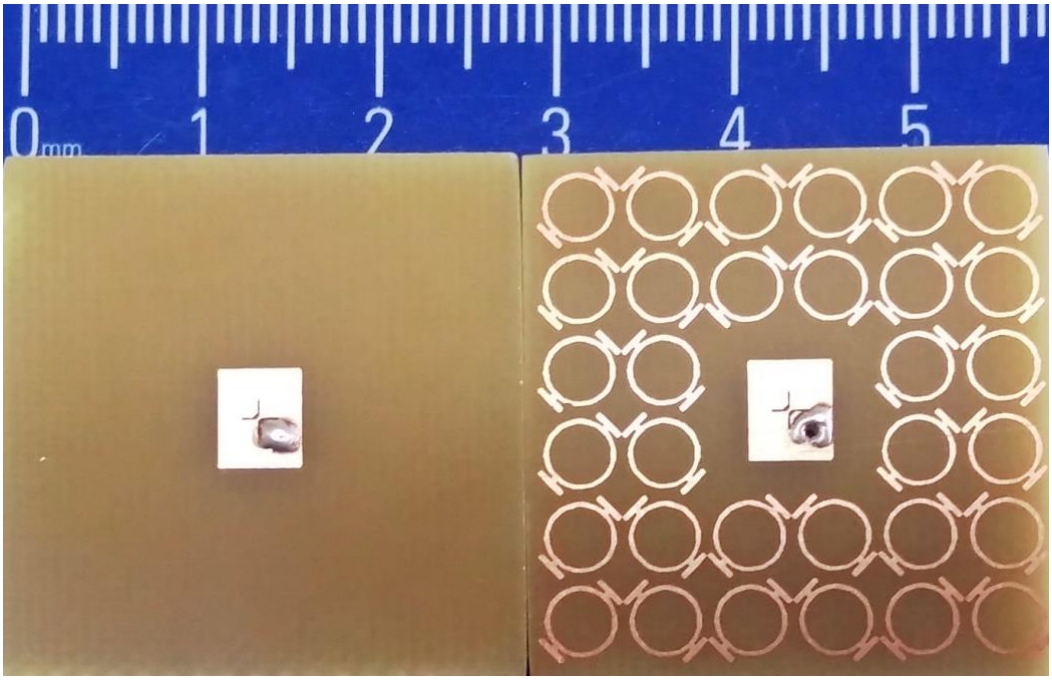

(a) (b)

Figure 6.5. Fabricated slotted patch antenna (a) referenced and (b) proposed Antennas.

without *MMA* by loading it with 3 × 3 *MMA* unit cells as depicted in Figure 6.4. The center *MMA* unit cell is cutout and etched by radiating patch as shown in Figure 6.4(b). The referenced antenna as well as *MMA* loaded antenna has been simulated, fabricated and measured as shown in Figure 6.5. The radiation performance of referenced antenna and *MMA* loaded patch antenna has been compared and analyzed as depicted in Figure 6.6. This chapter gives the augmentation published in [200].

It has been found that the value of scattering coefficient (S_{11}) for the referenced antenna has been obtained for the lower resonant frequency at 11.95 GHz with -27.78 dB, whereas upper resonant frequency peak appears at 14.25 GHz with -37.63 dB as shown in Figure 6.6(a). Although, after loading with dual-band *MMA*, its frequency response slightly affected and the lower resonant peak appears at 11.99 GHz with -24.90 dB, whereas the upper resonant peak appears at 14.28 GHz with -35.87 dB.

The measured results of a slotted patch antenna with and without *MMA* have been also recorded. This justifies and indicates that the simulated and measured results are in good agreements. To further analyze the behavior of dual-band *MMA* on antenna radiation performances, an analysis of *VSWR*, Z_{11} and -10 dB bandwidth have been made.

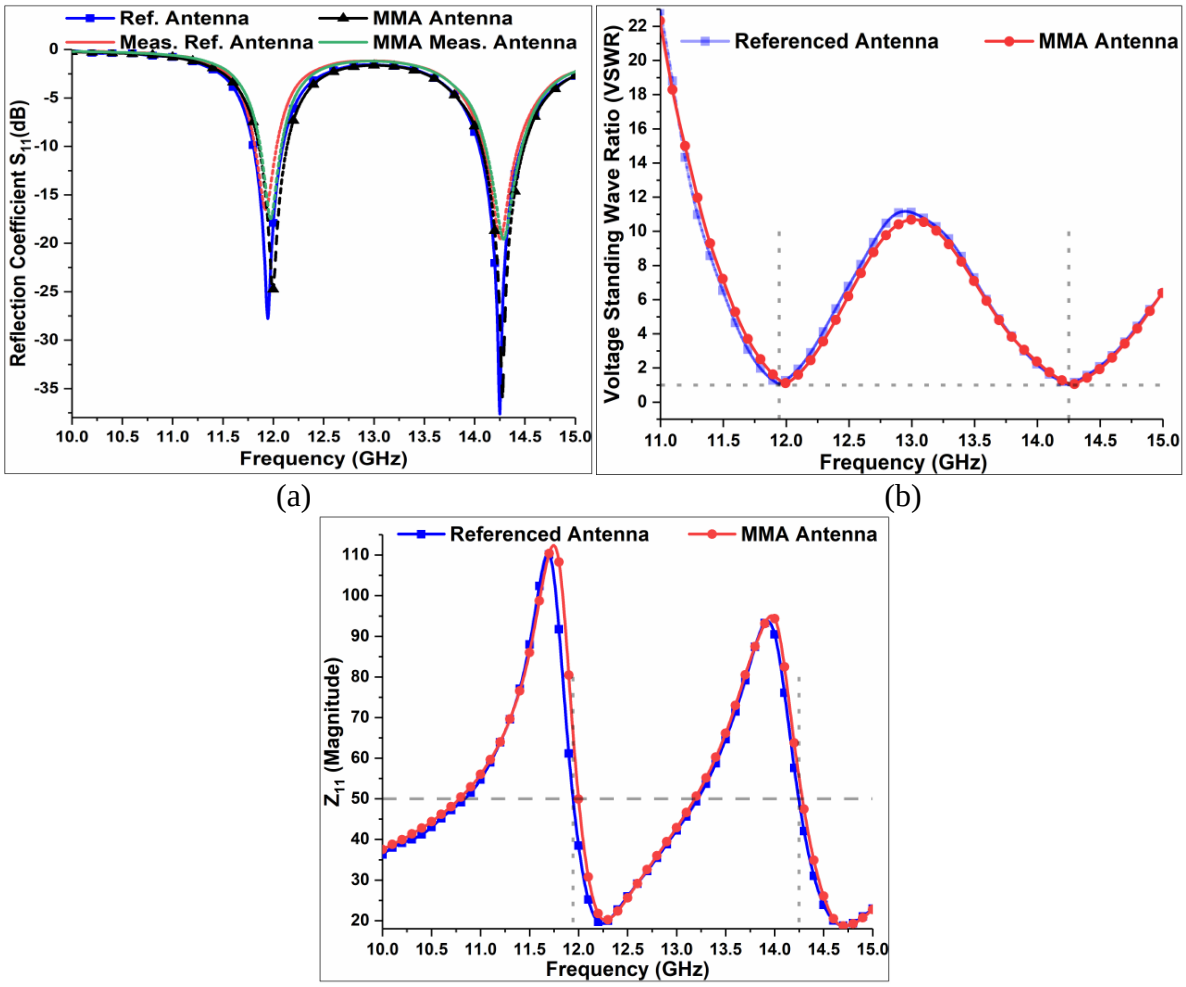

Figure 6.6 Radiation performance of Dual-band slotted patch antenna with and without MMA (a) S_{11} (b) VSWR, and (c) Z_{11}.

The results show that for reference antenna, the value for *VSWR* comes out 1.08 at 11.95 GHz and 1.03 at 14.25 GHz as given in Figure 6.6(b). Whereas for *MMA* loaded antenna, the value of *VSWR* comes out 1.12 at 11.99 GHz and 1.03 at 14.28 GHz respectively. All values of *VSWR* remain within the acceptable range of 1 to 1.5. The values of Z_{11} for referenced antenna observed of 49.69 Ω at 11.95 GHz and 49.28 Ω at 14.25 GHz, respectively.

While for *MMA* loaded antenna, its value slightly increased to 51.19 Ω at 11.99 GHz and 51.17 Ω at 14.28 GHz respectively and shown in Figure 6.6(c). For the referenced antenna, the value of -10 dB bandwidth is 285 MHz at 11.95 GHz and 420 MHz at 14.25 GHz. Whereas for *MMA* loaded antenna, the value for -10 dB bandwidth is 275 MHz at 11.99 GHz and 420 MHz at 14.28 GHz, So, the bandwidth remains almost unaffected after loading the referenced antenna with *MMA* structure. Complete descriptions of radiation performance parameters have been given in Table 6.3.

Table 6.3 Comparisons of antenna radiation performances.

Structure/Performance Parameters	Referenced Antenna		MMA Antenna	
Frequency (f_0) GHz	11.95	14.25	11.99	14.28
Reflection Coefficient (S_{11}) dB	-27.78	-37.63	-24.90	-35.87
Bandwidth (-10 dB) MHz	285	420	275	420
VSWR	1.08	1.03	1.12	1.03
Impedance (Z_{11}) Ω	49.69	49.28	51.19	51.17

Comparative analyses of directivity have been made between the referenced and proposed antennas for *E-plane* and *H-plane*. Its co polarization (*Cop*) and cross polarization (*Xp*) polar plots have been depicted in Figure 6.7.

For E- Plane, the referenced antenna main lobe magnitude is 7.19 dBi at 11.95 GHz with *Xp* isolation of 17.39 dB, while for the proposed antenna the main lobe magnitude is 7.54 dBi at 11.99 GHz with *Xp* isolation of 14.04 dB.

For H-Plane, the referenced antenna main lobe magnitude is 7.2 dBi at 11.95 GHz and proposed antenna main lobe magnitude is 7.54 dBi at 11.99 GHz, respectively and shown in Figure 6.7(a). There are the isolation of 17.4 dB and 16.69 dB between co-polar and cross-polar radiations for referenced and proposed antennas, respectively.

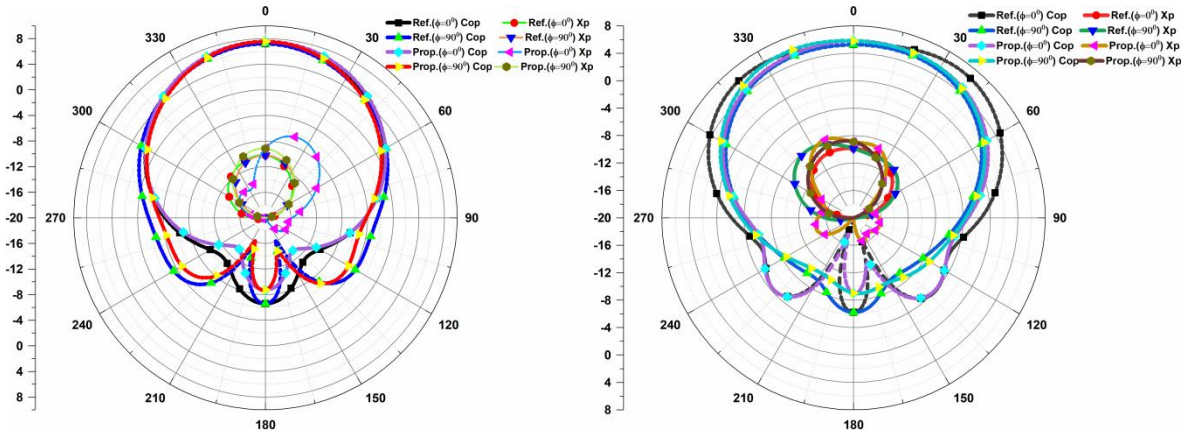

(a) (b)

Figure 6.7. Comparisons of directivity between referenced and proposed antennas (a) 11.95 GHz and 11.99 GHz (b) 14.25 GHz and 14.28 GHz for E-Plane and H-Plane.

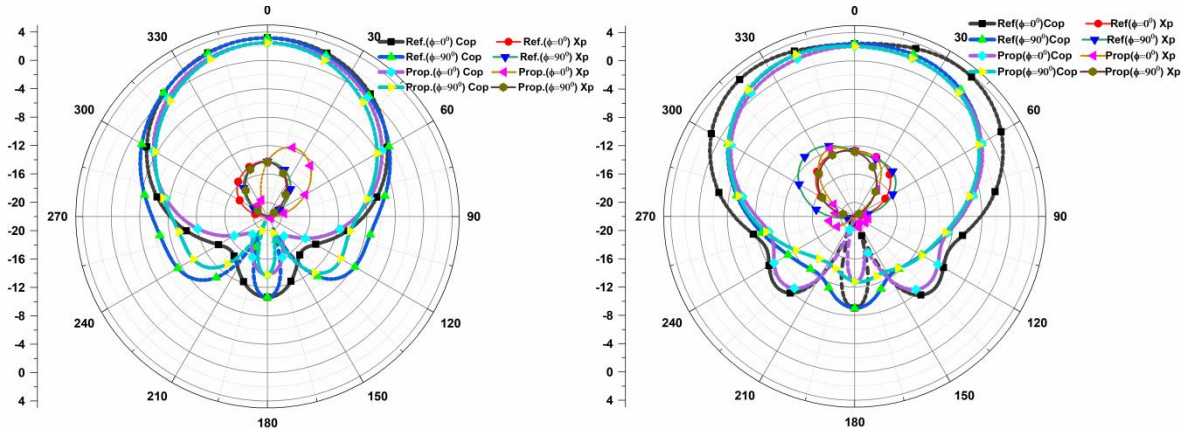

(a) (b)

Figure 6.8 Comparisons of gain between referenced and proposed antennas (a) 11.95 GHz and 11.99 GHz (b) 14.25 GHz and 14.28 GHz for E-Plane and H-Plane.

For E-Plane, the referenced antenna main lobe magnitude is 6.62 dBi at 14.25 GHz with *Xp* isolation of 16.41 dB and proposed antenna main lobe magnitude appears at 14.28 GHz is5.82 dBi with *Xp* isolation of 13.7 dB.

For H-Plane, the referenced and proposed antennas main lobe magnitudes are 5.25 dBi at 14.25 GHz and 6.1 dBi at 14.28 GHz, respectively and shown in Figure 6.7(b). There are the isolation of 13.32 dB and 14.79 dB between co-polar and cross-polar radiations for referenced and proposed antennas, respectively. The *E-plane* and *H-plane* radiation patterns indicate that desirable antenna directivity is attained with suppressed cross-polar radiations.

Polar patterns for gain analysis of *E-plane* and *H-plane* have been given between referenced and proposed antennas in Figure 6.8. All results have been tabulated in Table 6.4. These outcomes conclude that after loading exiting source with *MMA* its directivity enhanced whereas gain value affected marginally.

Table 6.4 Comparisons of directivity and gain.

Structure	Frequency (GHz)	Phi	Directivity	Gain
Referenced	11.95	0^0	7.19	3.18
Antenna		90^0	7.2	3.18
MMA Antenna	11.99	0^0	7.54	2.48
		90^0	7.54	2.48
Referenced	14.25	0^0	6.62	3.8
Antenna		90^0	5.25	2.43
MMA Antenna	14.28	0^0	5.82	2.05
		90^0	6.1	2.33

6.4. RCS Reduction of Dual-band Slotted Patch Antenna using MMA

A comparison of *Monostatic RCS* between referenced and proposed antenna has been given with its measured outcome in Figure 6.9. It has been observed that the *RCS* of proposed antenna almost remains polarization independent. The *Monostatic RCS* reduces throughout the analyzed frequency band between 10 GHz to 16 GHz after loading it with *MMA* and tabulated in Table 6.5. For *x-polarization* at 11.95 GHz, the value for *Monostatic RCS* for the referenced antenna is -20.03 dBsm and after loading it with *MMA*, its *RCS* peak appears at 11.99 GHz with -44.12 dBsm as depicted in Figure 6.9(a). So a reduction of 24.09 dBsm has been achieved. At 14.25 GHz, the value of *Monostatic RCS* for referenced and proposed antennas are -17.90 dBsm whereas it reduces to -25.76 dBsm at 14.28 GHz respectively. So a reduction of 7.86 dBsm has been achieved. The measured *Monostatic RCS* outcome of proposed antenna appeared at 11.9 GHz and 14.2 GHz with -34.55 dBsm and -25.88 dBsm, respectively.

This indicates that simulated and measured outcomes are within acceptable range and in good agreement. For y-polarization, the value of *Monostatic RCS* for referenced and proposed antennas are -21.13 dBsm and -30.04 dBsm at 11.95 GHz and 11.99 GHz, respectively as depicted in Figure 6.9(b).

Table 6.5 Comparisons of Monostatic RCS.

Frequency	**Referenced Antenna/MMA antenna**			
(GHz)	**x-polarization (dBsm)**		**y-polarization (dBsm)**	
10	-20.67	-20.78	-20.67	-20.77
10.5	-20.54	-20.66	-20.61	-20.71
11	-20.35	-20.60	-20.54	-20.84
11.5	-20.18	-21.01	-20.78	-21.79
11.95/11.99	-20.03	-44.12	-21.13	-30.04
12	-20.01	-41.14	-21.03	-29.17
12.5	-19.77	-19.92	-19.69	-20.11
13	-19.41	-19.41	-19.01	-19.33
13.5	-18.98	-19.10	-18.38	-19.21
14	-18.41	-19.94	-17.70	-26.74
14.25/14.28	-17.9	-25.76	-17.31	-19.76
14.5	-17.44	-20.67	-17.06	-18.08
15	-16.55	-16.92	-16.46	-16.85

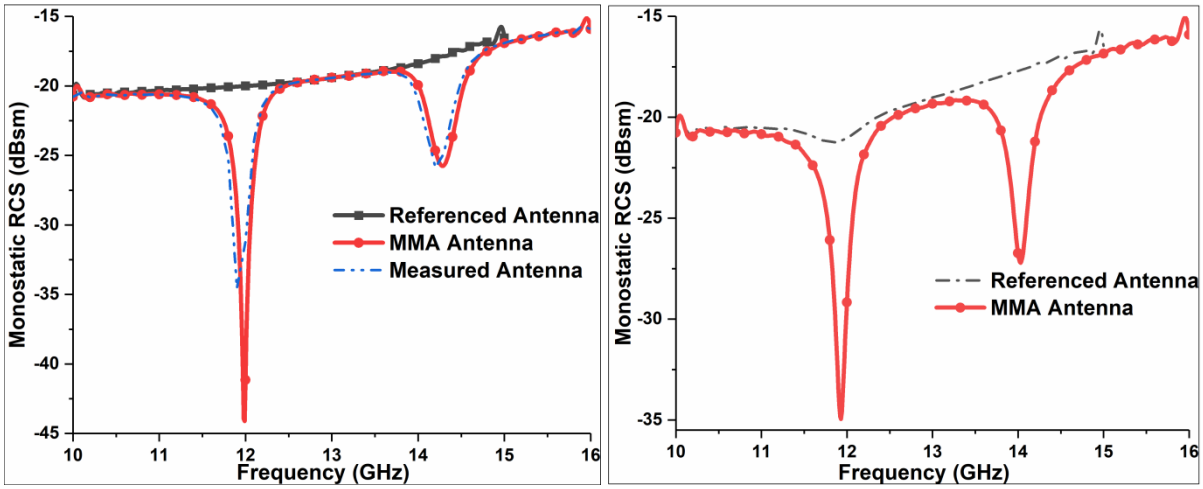

(a) (b)

Figure 6.9 Comparisons of Monostatic RCS of referenced and MMA loaded antennas (a) x-polarization and (b) y-polarization.

So a reduction of 8.91 dBsm has been achieved. The value of *Monostatic RCS* for referenced and proposed antennas are -17.31 dBsm and -19.76 dBsm at 14.25 GHz and 14.28 GHz respectively. So a reduction of 2.45 dBsm has been achieved. Because of polarization, the value of *Monostatic RCS* peaks shifted to 11.93 GHz and 14.03 GHz with the value of -34.96 dBsm and -27.21 dBsm, respectively for the proposed antenna.

A simulation analysis for *Bistatic RCS* between referenced and proposed antenna has been made for horizontal polarization as depicted in Figure 6.10. At lower frequency band, the

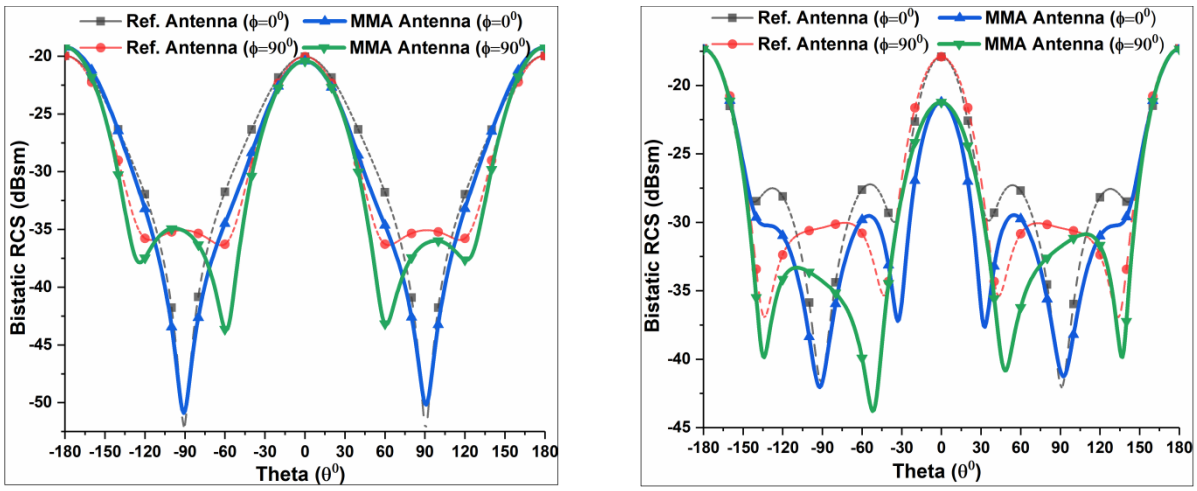

(a) (b)

Figure 6.10 Comparisons of Bistatic RCS of referenced and proposed antennas (a) 11.95 GHz and 11.99 GHz (b) 14.25 GHz and 14.28 GHz for horizontal-polarization.

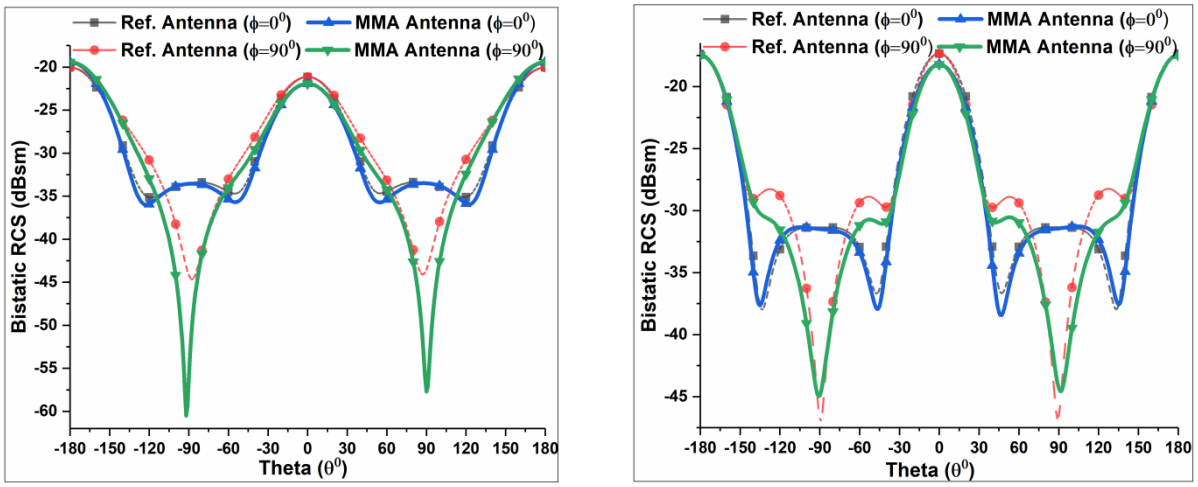

Figure 6.11 Comparison of Bistatic RCS of referenced and proposed antennas at (a) 11.95 GHz and 11.99 GHz (b) 14.25 GHz and 14.28 GHz for vertical-polarization.

proposed antenna *Bistatic RCS* reduced between -87^0 to 86^0 for theta (θ). Although, the maximum difference between referenced and proposed antenna is observed of 2.92 dBsm at 56^0 and 2.76 dBsm at -57^0, respectively. At $\phi = 90^0$, the *Bistatic RCS* of the *MMA* loaded antenna reduced significantly between -151^0 to 149^0.

However, the maximum difference between referenced and proposed antenna is observed of 6.91 dBsm at 61^0 and 7.54 dBsm at -59^0 respectively and shown in Figure 6.10(a). For the upper-frequency band, the proposed antenna *Bistatic RCS* reduced between -144^0 to 85^0 for theta (θ). Although, the maximum difference between referenced and proposed antenna is observed of 8.39 dBsm at 32^0 and 7.81 dBsm at -32^0, respectively. At $\phi = 90^0$, the *Bistatic RCS* of the *MMA* loaded antenna reduced significantly between -180^0 to 107^0. However, the maximum difference between referenced and the proposed antenna is observed of 7.14 dBsm at 51^0 and 11.22 dBsm at-53^0, respectively as shown in Figure 6.10(b).

A simulation analysis for vertical polarization has been made as shown in Figure 6.11. At lower frequency band, the proposed antenna *Bistatic RCS* reduced between -94^0 to 91^0 for theta (θ). Although, the maximum difference between referenced and proposed antenna is observed of 1.08 dBsm at 53^0 and 1.01 dBsm at -53^0, respectively. At $\phi = 90^o$, the *Bistatic RCS* of the *MMA* loaded antenna reduced significantly between -145^0 to 143^0. However, the maximum difference peak occurred between the referenced and proposed antennas are of 14.16 dBsm at 90^0 and 17.36 dBsm at -92^0, respectively and shown in Figure 6.11(a). For the upper-frequency band, the proposed antenna *Bistatic RCS* reduced between -99^0 to 96^0 for theta (θ). Although, the maximum difference between referenced and proposed antenna is observed of 1.91 dBsm

at 45^0 and 1.41 dBsm at -44^0, respectively. At $\phi = 90^0$, the *Bistatic RCS* of the *MMA* loaded antenna reduced between -83^0 to 80^0. The maximum difference between referenced and proposed antenna is observed of 1.64 dBsm at 56^0 and 1.86 dBsm at -57^0, respectively and shown in Figure 6.11(b).

6.5. Comparison of Results with Previously Reported Structures

To validate and justify the novelty of proposed structure, a comparison has been made with previously reported dual-band *MMA* structures designed for *RCS* reduction and tabulated in Table 6.6. For the purpose of balanced comparison, all structure dimensions and thickness have been measured with respect to center frequency (f_0). It has been found that the dimension of the proposed structure is $\lambda_0/0.83$ in term of a wavelength that is smaller than [153], [156] and [157]. The structure [156] has largest dimensions that would probably result in poor *RCS* performance. The dielectric substrate plays an important role in determining the absorbance of the dual-band *MMA* structure. For almost unity absorbance, it is being kept as small as possible and equal to 0.40 mm; hence upkeeps its promise for an ultra-thin *MMA* structure. Moreover, to make dual-band slotted patch antenna compatible with *MMA*, the overall thickness of the proposed antenna design has been also kept same for its low profile and ease of fabrication process.

Table 6.6 Comparisons with previously proposed structures.

Low RCS Patch Antenna	References	Dimensions (mm)	Thickness (mm)	Absorbance Peaks (GHz)	Polarization	Maximum RCS Reduction
Shater and Zarifi	[153]	52.5×52.5 ($\lambda_0/0.59$)	0.8 ($\lambda_0/38.86$)	8.4 and 10.9	Till 60^0	20 dBsm at 8.5 GHz and 10 dBsm at 11.2 GHz
Miao et al	[156]	130×130 ($\lambda_0/0.31$)	1.575 ($\lambda_0/25.71$)	5.8 and 9	Not performed	8 dBsm at 5.8GHz and 7 dBsm at 9GHz
Zhang et al	[157]	109×109 ($\lambda_0/0.51$)	1 ($\lambda_0/55.7$)	4.29 and 6.49	Till 60^0	8.59 dBsm at 4.29 GHz and 9.9 dBsm at 6.49 GHz
Our Work	[200]	27.75× 27.75 ($\lambda_0/0.83$)	0.4 ($\lambda_0/57.25$)	11.95 and 14.25 (ITU)	Yes	24.09 dBsm at 11.99 GHz and 7.86 dBsm at 14.28 GHz

It has been observed that the thickness of the proposed structure [200] is $\lambda_0/57.25$ that is improved over [153], [156] and [157]. The structure [166] offers the largest thickness among remaining structures. Structures [157] and [153] offer polarization sensitivity response up to 60^0, while it is not considered in [156]. The maximum *RCS* reduction has been claimed better by structure [153] for the second resonant peak only compare to our proposed model, while remained structures offer poor in-band *RCS* response compare to the proposed structure. Hence, the proposed structure not only preserves and maintains the antenna radiation performance but also offer an alternative for dual-band *RCS* reduction of the slotted patch antenna.

6.6. Chapter Summary

In this chapter, we have proposed an ultrathin dual-band slotted patch antenna loaded with *MMA* at 11.95 GHz and 14.25 GHz operating within *Ku-band*. Initially, we have analyzed the *MMA* behavior for oblique angle of incidence and polarization sensitivity and outcome shows that the structure remains highly polarization insensitive. Then a dual-band slotted patch antenna is designed and its radiation performance is optimized to investigate the in-band operation. The loading effect of *MMA* on antenna radiation performance has been also determined. Finally, *Monostatic* and *Bistatic RCS* for referenced and the proposed antenna has been evaluated.

The results indicate that directivity of proposed antenna enhances with a marginal reduction in antenna gain, whereas values of *VSWR,* -10dB bandwidth and Z_{11} remains well within the acceptable range. The in-band *Monostatic RCS* of the proposed antenna has been reduced significantly with a maximum reduction of 24.09 dBsm achieved. The *Bistatic RCS* of the proposed antenna has been reduced effectively and also bring down out-band RCS of proposed antenna throughout the observation band between 10 GHz to 16 GHz. Because of the tuning nature of dual-band shorted stubs *MMA* throughout *Ku-band*, it can operate and adjust to other frequencies based on target applications. This structure may provide alternatives to large bandwidth where dual-band operation is required that involve lot of complexity in antenna design. Thus, the proposed antenna is suitable for applications in military and stealth platform for satellite and wireless communication.

Chapter-7

Conclusions and Future Recommendations

7.1. Conclusions

In this thesis, we have demonstrated novel techniques to reduce the In-band *Monostatic* and *Bistatic* Radar Cross Section of patch antenna using metamaterial absorbers. For this purpose, we have designed single-band, dual-band and triple-band *MMA* structures in the microwave regime, ranging from X-band, Ku-band and Ka-band of the electromagnetic spectrum. The analytical, simulation and experimentally tested performance of the newly proposed *MMAs* have been determined. Moreover, the analysis and simulation of the circular ring shorted stubs *MMA* structure also has been explored to achieve the better angular stability than that of various reported *MMA* structure are examined in detail. In order to demonstrate the practicality of the proposed modified *MMA* structures, we have experimentally measured the reflection coefficient (S_{11}), radiation performances and *Monostatic RCS* for patch antenna and modified *MMA* loaded patch antenna at X-band and Ku-band, which provides the comparable frequency response as compared to that of the simulated response.

In chapter 1, we have explored the background, introduction and the problem of the statement of the metamaterial structure. This section also discussed the objectives, scope of the study, motivation, research questions, and contribution of the thesis in detail.

Knowledge of the previous studies on the metamaterial structure design is much essential and desired before any improvement and progress could be made, so this has given in the literature review section in chapter 2. The classifications and types of metamaterial structures are discussed. We have studied and analyzed the behavior of *FSS, EBG, DGS,* and *MMA*. For this purpose, a 3-D *CSFSS* structure has been analyzed and its parametric analyses are made to achieve stopband and passband behavior along with its response to the oblique angle of incidence and polarization sensitivity have been considered extensively. After this, attention has been paid to *EBG* structure and a hybrid microstrip antenna consisted of *EBG* and *DGS* has been analyzed. Its behaviors with respect to antenna radiation performances are analyzed in the end. Finally, a triple band regular decagon shaped *MMA* for an *X-Band* application has been designed. Its behavior for simulation, normalized input impedance, and surface current distribution have analyzed to understand the absorption mechanism.

In chapter 3, a novel design of a passive tuned *MMA* unit cell structure consisted of a circular ring modeled with stubs and rectangular bars extending from *Ku-band* to *X-band* has studied. The lowest resonant frequency peak obtained at 7.77 GHz with absorbance peak response of 90.33 %, while the highest resonant frequency peak obtained at 15.46 GHz with absorbance peak response of 99.97 %. The electromagnetic simulations result shows that the length of the rectangular bar and shorted stubs have a significant influence on determining the frequency characteristics of *MMA* and add an extra degree of freedom to the structure. The structure has been found highly polarization insensitive. The surface current distribution analysis shows that the current is circulated properly in the loop and then the simulated and measured results are compared at the end and the results are well matched and justified.

In chapter 4, the idea of single-band passive tuned structure is extended to dual-band passive tuned with shorted stubs *MMA*. The design consists of four circular rings that obtained sharp dual band resonant peaks at 17 GHz and 18 GHz with absorbance peak response of 99.99 % and 99.83 %, respectively. The corresponding full width at half maximum (*FWHM*) bandwidth at these resonant frequencies is 4.90 % and 5.07 %, respectively. A close separation distance between two resonant frequencies is obtained as close as 1 GHz compared to the other dual band and multiband circular ring which is 2 GHz or more. The behaviors of the structure for oblique angle of incidence with polarization sensitive have been observed and found highly polarization insensitive. Then, an analysis has been conducted for surface current distribution and normalized input impedance characteristics which show a good agreement with the simulated results. Finally, the *MMA* design has been fabricated and tested and the results are well matched with the simulated ones.

In chapter 5, the single-band shorted stubs *MMA* structure that we had studied in chapter 3 is used to reduce the In-band *RCS* of planar coaxial feed patch antenna operating at 10 GHz in X-band. The reflection coefficient (S_{11}) and the radiation pattern of the modified antenna are also studied. The co-polarization and cross-polarization patterns with respect to *E-Plane* and *H-Plane* of the proposed structure have been also analyzed. Effective isolation of 82.5 dBi and 24.65 dBi are observed for both planes and that indicated the suppression of cross-polar radiations.

The result shows a maximum *Monostatic RCS* reduction of 21.22 dBsm achieved for the proposed structure operation at X-band. Again, comparative design analyses of *MMA* loaded patch antenna have been proposed. Analyses have been also made to study the effect of *MMA*

on patch antenna before and after loading it. The results indicate that the radiation performance of the patch antenna has been affected marginally. Design 1 shows unsatisfactory directivity and gains response, whereas for Design 2 and Design 3, directivity is enhanced with gain is affected slightly. Then, we analyzed the In-band RCS behavior for 2 × 2 patch array when it is loaded with *MMA* structure. It has been found that it significantly reduces the *RCS* of the structure throughout the observation band. Henceforth increase the stealth capability of the structure. This suggests that loading of shorted stubs *MMA* absorber plays an important role and modified the antenna properties along with efficiently enhance the *RCS* capabilities of the rectangular patch antenna.

In chapter 6, the concept of chapter 4 is used to reduce the In-band *RCS* of an ultrathin dual-band slotted patch antenna operating at 11.95 GHz and 14.25 GHz within *Ku-band*. A passive tuned dual-band *MMA* is designed at the same frequency and its behavior for oblique angle of incidence and polarization sensitivity have observed. Then a dual-band slotted patch antenna is designed and its radiation performance is optimized to investigate the in-band operation. Finally, *Monostatic* and *Bistatic RCS* for referenced and the proposed antenna has been evaluated and shows a significant reduction in *RCS*. This structure may provide alternatives to large bandwidth where dual-band operation is required that involve lot of complexity in antenna design.

7.2. Future Recommendations

The frequency response of the proposed modified *MMA* structure is measured for the normal wave incidence only, which will be extended to study the effect of the angle of incidence and polarization states of the incidence wave in future. In addition to this, the design consideration, implementation, and analyses of the dual-band shorted stubs *MMA* structure for in-band *RCS* reduction of slotted patch antenna array in Ku-band has also been considered for the future perspective. Moreover, *RCS* behavior exploitation for the triple-band *MMA* implementation with regard to patch antenna in X-band (8 GHz, 10 GHz, and 12 GHz) will be considered in future communication.

This structure finds its applications in the field of stealth technology for low *RCS* antenna design. Where antenna designers can find out the possibility of using the same antenna aperture for the multi-band frequency operation. Thus, it explores and offers feasibility to use the same structure and combine the different feed antennas onto the aperture of a single reflector antenna. Hence, instead of multiple antennas, a compact antenna system can be realized that cover less

space and so suitable for military planes, space aircraft, missiles, ships, and other sensitive vehicles. Consequently, the *MMA* may be used as a shield in a specific frequency band, whilst performing field transmission in another nearby band because of its tuning nature.

References

[1] C. G. Meca, R. Ortuno, F. J. R. Fortuno, J. Marti, and A. Martinez, "Negative refractive index metamaterials aided by extraordinary optical transmission," *Optics Express*, vol. 17, no. 8, pp. 26-31, April 2009.

[2] D. Zarifi, M. Soleimani, and V. Nayyeri, "A novel dual-band chiral metamaterial structure with giant optical activity and negative refractive index," *Journal of Electromagnetic Waves and Applications*, vol. 26, no. 2-3, pp. 251-263, April 2012.

[3] Zijian Tian, Xuqi Wang, Weixiang Li, and Jing Fan, "Three-dimension isotropic negative permeability material made of eight-split-ring resonator," *AIP Advances 7*, vol. 7, no. 3, pp. 231- 237, March 2017.

[4] Ilya V. Shadrivov, Alexander B. Kozyrev, Daniel W. Vander Weide, and Yuri S. Kivshar, "Nonlinear magnetic metamaterials," *Optics Express*, vol. 16, no. 25, pp. 266-271, December 2008.

[5] Muhammad Rizwan, Hai B. Jin, Fida Rehman, Zhi L. Hou, Jing B. Li, Faheem K. Butt, and Zulfiqar Ali, "Dual-band tunable negative refractive index metamaterial with F-Shape structure," *Central European Journal of Physics*, vol. 12, no. 8, pp. 578–581, August 2014.

[6] G. Sinclair, "Theory of models of electromagnetic systems," *Proceedings of Institute of Radio Engineers*, vol. 36, no. 11, pp. 1364-1370, November 1948.

[7] Tang, Wen Xuan, Zhong L. Mei, and Tie J. Cui, "Theory, experiment, and applications of metamaterials," *Science China Physics, Mechanics and Astronomy*, vol. 59, no. 2, pp. 10-11, December 2015.

[8] Nicholas Fang, Hyesog Lee, Cheng Sun, and Xiang Zhang, "Sub-diffraction-limited optical imaging with a silver superlens," *Science*, vol. 308, no. 5721, pp. 534-537, April 2005.

[9] Stefan Enoch, Gerard Tayeb, Pierre Sabouroux, Nicolas Guerin, and Patrick Vincen, "A metamaterial for directive emission," *Physical Review Letters*, vol. 89, no. 21, pp. 901-904, November 2002.

[10] N. I. Landy, S. Sajuyigbe, J. J. Mock, D. R. Smith, and W. J. Padilla, "Perfect metamaterial absorber," *Physical Review Letter*, vol. 100, no. 20, pp. 1-4, May 2008.

[11] Archana Rajput and Kumar V. Srivastava, "Design of a two-dimensional metamaterial cloak with minimum scattering using a quadratic transformation function," *Journal of Applied Physics*, vol. 116, no. 12, pp. 11-15, September 2014.

[12] Dan Hu, Hong Y. Wang, Zhen J. Tang, Xi W. Zhang, Lin Ju, and Hua Y. Wang, "Design of a multiband terahertz perfect absorber," *Chinese Physics B*, vol. 25, no. 3, pp. 11-17, January 2016.

[13] Somak Bhattacharyya, Devkinandan Chaurasiya, Kumar V. Srivastava, Anamiya Bhattacharya, and Saptarshi Ghosh, "Compact multi-band polarisation-insensitive metamaterial absorber," *IET Microwaves, Antennas & Propagation*, vol. 10, no. 1, pp. 94-101, January 2016.

[14] Osman Ayop, Mohamad Kamal A. Rahim, Noor A. Murad, and Noor A. Samsuri, "Dual resonance circular ring-shaped metamaterial absorber with wide operating angle," *International Symposium on Antennas and Propagation (ISAP)*, Tasmania, Australia, 9-12 November 2015, pp. 1-4.

[15] Peng Wu, Fan Bai, Quan Xue, Xun Liu, and S. Y. Ron Hui, "Use of frequency-selective surface for suppressing radio-frequency interference from wireless charging pads," *IEEE Transactions on Industrial Electronics*, vol. 61, no. 8, pp. 3969-3977, August 2014.

[16] I. G. Lee and I. P. Hong, "3D frequency selective surface for stable angle of incidence," *Electronics Letters*, vol. 50, no. 6, pp. 423-424, March 2014.

[17] Ashwini K. Arya, M. V. Kartikeyan, and A. Patnaik, "Efficiency enhancement of microstrip patch antenna with defected ground structure," *International Conference on Recent Advances in Microwave Theory and Applications*, Jaipur, India, 21-24 November 2008, pp. 729-731.

[18] B. N. Ripin, S. N. C. Yusoff, A. A. Sulaiman, N. E. A. Rashid, and M. F. Hussin, "Enhancement of bandwidth through I-shaped defected ground structure," *IEEE International RF and Microwave Conference (RFM2013)*, Penang, Malaysia, 9-11 December 2013, pp. 477-481.

[19] F. Y. Zulkifli, E. T. Rahardjo, and D. Hartanto, "Mutual coupling reduction using dumbbell defected ground structure for multiband microstrip antenna array," *Progress in Electromagnetics Research Letters*, vol. 13, pp. 29-40, 2010.

[20] D. Fistum, D. Mali, and M. Ismail, "Bandwidth enhancement of rectangular microstrip patch antenna using defected ground structure," *Indonesian Journal of Electrical Engineering and Computer Science*, vol. 3, no. 2, pp. 428-434, August 2016.

[21] V. Ekke and P. Zade, "Implementation of EBG configuration for asymmetric microstrip antenna to improve radiation properties," *Journal of Telecommunication, Electronic and Computer Engineering*, vol. 9, no. 1, pp. 61-66, March 2017.

[22] S. Gnanasundar and K. U. Kiran, "Study of electromagnetic bandgap structures for antenna application," *IEEE 3rd International Conference on Signal Processing, Communication and Networking (ICSCN)*, Chennai, India, 26-28 March 2015, pp. 1-4.

[23] Cason Neo and Yee H. Lee, "Patch antenna enhancement using a Mushroom-like EBG structure," *IEEE Antennas and Propagation Society International Symposium (APSURSI)*, Orlando, USA, 7-13 July 2013, pp. 614-615.

[24] D. N. Elsheakh, H. A. Elsadek, E. A. Abdallah, H. Elhenawy, and M. F. Iskander, "Enhancement of microstrip monopole antenna bandwidth by using EBG structures," *IEEE Antennas and Wireless Propagation Letters*, vol. 8, pp. 959-962, September 2009.

[25] Ammar Armghan, Xinguang Hu, Shuai Yuan, and Jinsong Xia, "Negative refractive index metamaterial structure using SRR by incidenting the light horizontally," *Journal of Electromagnetic Analysis and Applications*, vol. 7, no. 11, pp. 276-282, November 2015.

[26] Alexandre Archambault, Mondher Besbes, and Jean J. Greffet, "Superlens in the Time Domain," *Physical Review Letters*, vol. 109, no. 9, pp. 51-54, August 2012.

[27] Yuandan Dong and Tatsuo Itoh, "Metamaterial-Based Antennas," *Proceedings of the IEEE*, vol. 100, no. 7, pp. 2271-2285, July 2012.

[28] Gizem Ekinci, Arda D. Yalcinkaya, Gunhan Dundar, and Hamdi Torun, "Split-ring resonator-based strain sensor on flexible substrates for glaucoma detection," *Journal of Physics: Conference Series*, vol. 757, no. 1, pp. 1-6, October 2016.

[29] Ben A. Munk, *Frequency selective surfaces: theory and design*, John Wiley & Sons, New York, USA, 2000.

[30] Debasish Banerjee, Chengang Ji, and Hideo Iizuka, "Invisibility cloak with image projection capability, *Scientific Reports*, vol. 6, no. 38965, pp. 1-6, December 2016.

[31] De H. Hu and Alan Tennant, "3D saw-tooth frequency selective surfaces," *Antennas and Propagation Conference*, Loughborough, United Kingdom, 12-13 November 2012, pp. 1-4.

[32] Anamiya Bhattacharya, Somak Bhattacharyya, Saptarshi Ghosh, Devkinandan Chaurasiya, and Kumar V. Srivastava, "An ultrathin penta-band polarization-insensitive compact metamaterial absorber for airborne radar applications," *Microwave and Optical Technology Letters*, vol. 57, no. 11, pp. 2519-2524, November 2015.

[33] Victor G. Veselago, "The electrodynamics of substances with simultaneously negative values of ε and μ," *Soviet Physics Uspekhi*, vol. 10, no. 4, pp. 509-14, 1968.

[34] J. B. Pendry, A. J. Holden, D. J. Robbins, and W. J. Stewart, "Magnetism from conductors and enhanced nonlinear phenomena," *IEEE Transactions on Microwave Theory and Techniques*, vol. 47, no. 11, pp. 2075-2084, 1999.

[35] J. B. Pendry, A. J. Holden, D. J. Robbins and W. J. Stewart, "Low-Frequency Plasmons for Thin-Wire Structure," *Journal of Physics: Condensed Matter*, vol. 10, no. 22, pp. 4785-4809, March 1998.

[36] D. R. Smith, Willie J. Padilla, D. C. Vier, S. C. Nemat Nasser and S. Schultz, "Composite medium with simultaneously negative permeability and permittivity," *Physical Review Letters*, vol. 84, no. 18, pp. 4184-4187, May 2000.

[37] R. W. Ziolkowski, "Design, fabrication, and testing of double negative metamaterials," *IEEE Transactions on Antennas and Propagation*, vol. 51, no. 7, pp. 1516-1529, 2003.

[38] Nader Engheta and R. W. Ziolkowski, "A positive future for double-negative metamaterials," *IEEE Transactions on Microwave Theory and Techniques*, vol. 53, no. 4, pp. 1535-1556, 2005.

[39] A. Erentok, Richard W. Ziolkowski, J. A. Nielsen, S. Schultz, R. B. Greegor, C. G. Parazzoli, M. H. Tanielian, Steven A. Cummer, B. I. Popa, Thomas Hand, D. C. Vier,

and S. Schultz "Low frequency lumped element-based negative index metamaterial," *Applied Physics Letters*, vol. 91, pp. 104-1043, 2007.

[40] G. V. Eleftheriades and K. G. Balmain, *Negative-Refraction Metamaterials: Fundamental Principles and Applications.* John Wiley & Sons, New York, USA, 2005.

[41] Maryam Majidzadeh, Changiz Ghobadi, and Javad Nourinia, "A reconfigurable frequency-selective surface for dual-mode multi-band filtering applications," *International Journal of Electronics*, vol. 104, no. 3, pp. 369-381, March 2017.

[42] M. Han, M. He, H. J. Sun, G. Q. Zhao, and H. Cheng, "Analysis of cassegrain antenna by using a dichroic sub-reflector," *IEEE International Conference on Microwave Technology and Computational Electromagnetics (ICMTCE)*, Qingdao, China, 25-28 August 2013, pp. 58-60.

[43] Jonathan M. Rigelsford, Sandra M. Benito, and Andrea Vallecchi, "A triband inductive frequency selective surface sub-reflector for satellite communication systems," *8th European Conference on Antennas and Propagation*, The Hague, Netherlands, 6-11 April 2014, pp. 898 – 900.

[44] M. Akbari, S. Gupta, S. Zarbakhsh, and A. R. Sebak,"A linear to circular polarizer based on frequency selective surface operating 30GHz applications," *17th International Symposium on Antenna Technology and Applied Electromagnetics (ANTEM)*, Montreal, Canada, 10-13 July 2016, pp. 1-2.

[45] B. Sanz Izquierdo, B. Liang, E. A. Parker, and J. C. Batchelor, "An application of active frequency selective surface to reconfigurable antenna technology," *Active and Passive RF Devices Seminar*, London, U.K, 17 February 2016, pp. 1-5.

[46] M.A. Hiranandani, A. B. Yakovlev, and A. A. Kishk, "Artificial magnetic conductors realised by frequency-selective surfaces on a grounded dielectric slab for antenna applications," *IET Proceedings Microwaves, Antennas and Propagation*, vol. 153, no. 5, pp. 487-493, October 2006.

[47] Haibing Xu, Shaowei Bie, and Jianjun Jiang, "Ultra-broadband and polarization-insensitive metamaterial absorber based on frequency selective surface," *IEEE International Congress on Advanced Electromagnetic Materials in Microwaves and Optics*, Chania, Greece, 19-22 September 2016, pp. 400-402.

[48] S. N. Azemi and W. S. T. Rowe, "Development and analysis of 3D frequency selective surfaces*," IEEE Asia-Pacific Microwave Conference Proceedings (APMC)*, Melbourne, Australia, 5-8 December 2011, pp. 693-696.

[49] S. N. Azemi, K. Ghorbani, and W. S. T. Rowe, "3D frequency selective surfaces," *Progress in Electromagnetics Research C*, vol. 29, pp. 191-203, May 2012.

[50] S. N. Azemi, K. Ghorbani, and W. S. T. Rowe, "3D frequency selective surfaces with close band spacing," *IEEE Asia-Pacific Microwave Conference Proceedings (APMC)*, Kaohsiung, Taiwan, 4-7 December 2012, pp. 454-456.

[51] S. N. Azemi, K. Ghorbani, and W. S. T. Rowe, "3D frequency selective surfaces with wideband response," *International Workshop on Antenna Technology: Small Antennas, Novel EM Structures and Materials, and Applications (iWAT)*, Sydney, Australia, 4-6 March 2014, pp. 212-215.

[52] Hui L. Liu, Kenneth L. Ford, and Richard J. Langley, "Design methodology for a miniaturized frequency selective surface using lumped reactive components," *IEEE Transactions on Antennas and Propagation*, vol. 57, no. 9, pp. 2732-2738, September 2009.

[53] Lili Liu, Chenchen Yang, Qunsheng Cao, Huangyan Li, and Yi Wang, "Smart-skins for radome using active frequency selective surface," *IEEE International Workshop on Electromagnetics: Applications and Student Innovation Competition (iWEM)*, Nanjing, China, 16-18 May 2016, pp. 1-3.

[54] X. G. Huang, Z. Shen, Q. Y. Feng, and B. Li, "Tunable 3-D bandpass frequency-selective structure with wide tuning range," *IEEE Transactions on Antennas and Propagation*, vol. 63, no. 7, pp. 3297 – 3301, July 2015.

[55] Garima Bharti, Ghanshyam Singh, Kumund R. Jha, and Rajeev Jyoti, "Circular ring frequency selective surface: A novel synthesis technique," *6th International Conference on Contemporary Computing (IC3)*, Noida, India, 8-10 August 2013, pp. 491-496.

[56] Dhawan Singh and Viranjay M. Srivastava, "3-D cylindrical shaped frequency selective surface," *IEEE International Conference on Advanced Computing and Communication Systems (ICACCS)*, Coimbatore, India, 6 -7 January 2017, pp. 1-6.

[57] Bingyuan Liang and Ming Bai, “Subwavelength three-dimensional frequency selective surface based on surface wave tunneling,” *Optics Express*, vol. 24, no. 13, pp. 697-702, June 2016.

[58] Amir K. Rashid, Bo Li, and Zhongxiang Shen, “An overview of three-dimensional frequency-selective structures,” *IEEE Antenna and Propagation Magazine*, vol. 56, no. 3, pp. 43-67, June 2014.

[59] Sultan Can, Emrullah Karakaya, Fulya Bagci, A. Evemen Yilmaz, and Baris Akaoglu, “A dual band double cylindrical ring 3D frequency selective surface,” *Electronics and Telecommunications Research Institute Journal*, vol. 39, no. 1, pp. 69-75, February 2017.

[60] C. Pelletti, G. Bianconi, R. Mittra, and Z. Shen, “Frequency selective surface with wideband quasi-elliptic bandpass response,” *Electronics Letters*, vol. 49, no. 17, pp. 1052-1053, February 2013.

[61] R. Dickie, R. Cahill, H. S. Gamble, V. F. Fusco, P. G. Huggard, B. P. Moyna, M. L. Oldfield, N. Grant, and P. de Maagt, “Polarisation-independent bandpass FSS,” *Electronics Letters*, vol. 43, no. 19, pp. 1013-1015, September 2007.

[62] I. L. Morrow and P. Thomas, “Compact frequency selective surface for polarisation transform” *Electronics Letters*, vol. 50, no. 2, pp. 64-65, January 2014.

[63] Dhawan Singh and Viranjay M. Srivastava, “Polarization-insensitive cylindrical shaped Frequency Selective Surface,” *IEEE 10th international conference on Development in eSystem Engineering (DeSe 2017)*, Paris, France, 14-16 June 2017, pp.1-6.

[64] Nabilah Ripin, Robiatun A. Awang, Ahmad A. Sulaiman, Noor H. Baba, and Suhaila Subahir, “Rectangular microstrip patch antenna with EBG structure,” *IEEE Student Conference on Research and Development (SCOReD)*, Pulau Pinang, Malaysia, 5-6 December 2012, pp. 266-271.

[65] F. Jing Liang and H. Y. David Yang, “Microstrip patch antennas on tunable Electromagnetic Band-Gap substrates,” *IEEE Transactions on Antenna and Propagation*, vol. 57, no. 6, pp.1612-1617, June 2009.

[66] Marina Mavridou, Alexandros P. Feresidis, and Peter Gardner, "Tunable double-layer EBG structures and application to antenna isolation," *IEEE Transactions on Antennas and Propagation*, vol. 64, no. 1, pp. 70-79, January 2016.

[67] Mohammad Shahidul Alam, Norbahiah Misran, Baharudin Yatim, and Mohammad T. Islam, "Development of electromagnetic band gap structures in the perspective of microstrip antenna design," *International Journal of Antennas and Propagation*, vol. 2013, pp.1-22, March 2013.

[68] L. H. Weng, Y. C. Guo, X. W. Shi, and X. Q. Chen, "An overview on defected ground structure," *Progress in Electromagnetics Research B*, vol. 7, pp.173-189, 2008.

[69] Yikai Chen, Shiwen Yang, and Zaiping Nie, "Bandwidth enhancement method for low profile E-shaped microstrip patch antennas," *IEEE Transactions on Antennas and Propagation*, vol. 58, no.7, pp. 2442-2447, July 2010.

[70] Kun Wei, Jianying Li, Ling Wang, Zijian Xing, and Rui Xu, "S-shaped periodic defected ground structures to reduce microstrip antenna array mutual coupling," *Electronics Letters*, vol. 52, no. 15, pp.1288-1290, July 2016.

[71] Pravin R. Prajapati, Gannavarapu G. Krishna Murthy, Amalendu Patnaik, and Machavaram V. Kartikeyan, "Design and testing of a compact circularly polarised microstrip antenna with fractal defected ground structure for L-band applications," *IET Microwaves, Antennas & Propagation*, vol. 9, no. 11, pp. 1179-1185, August 2015.

[72] Dhawan Singh, Aditi Thakur, and Viranjay M. Srivastava, "Miniaturization and gain enhancement of microstrip patch antenna with defected ground and EBG," *Journal of Communication (JOCM)*, vol. 13, no. 12, pp. 730-736, December 2018.

[73] Dhawan Singh and Viranjay M. Srivastava, "Triple band regular decagon shaped metamaterial absorber for X-band applications," *IEEE International Conference on Computer Communication and Informatics (ICCCI -2017),* Coimbatore, India, 5-7 January 2017, pp. 411-415.

[74] Li Sijia, Cao Xiangyu, Gao Jun, Zheng Yuejun, Zhang Di, and Liu Hongxi, "Fractal metamaterial absorber with three-order oblique cross dipole slot structure and its

application for in-band RCS reduction of array antennas," *Radio Engineering*, vol. 23, no. 4, pp. 1048-1054, December 2014.

[75] Wang G. Dong, Liu M. Hai, Hu X. Wei, Kong L. Hua, Cheng Li, and Chen Z. Quan, "Multi-band microwave metamaterial absorber based on coplanar jerusalem crosses," *Chinese Physics B*, vol. 23, no. 1, pp. 21-26, December 2013.

[76] Tian Liu and Sung S. Kim, "Design of wide-bandwidth electromagnetic wave absorbers using the inductance and capacitance of a square loop-frequency selective surface calculated from an equivalent circuit model," *Optics Communications*, vol. 359, pp. 372-377, January 2016.

[77] X. R. Guo, Z. Zhang, J. H. Wang, and J. J. Zhang, "The design of a triple-band wide-angle metamaterial absorber based on regular pentagon close-ring," *Journal of Electromagnetic Waves and Applications*, vol. 27, no. 5, pp. 629-637, March 2013.

[78] Mehdi Bahdorzadeh, Nooshin Feiz, and M. Alipoor, "Circuit model analysis of a polarization and wide-angle independent hexagonal shaped metamaterial absorber," *The Applied Computational Electromagnetics Society: ACES*, vol. 30, no. 8, pp. 909-914, August 2015.

[79] Dhawan Singh and Viranjay M. Srivastava, "Metamaterial absorber based on concentric rings with shorted stubs," *IEEE International Conference on Engineering and Technology (ICET)*, Coimbatore, India, 16-17 December 2016, pp. 159-163.

[80] Joungyoung Lee, Young J. Yoon, and Sungjoon Lim, "Ultra-thin polarization independent absorber using hexagonal interdigital metamaterial," *Electronics and Telecommunications Research Institute Journal*, vol. 34, no. 1, pp. 126-129, February 2012.

[81] H. Tao, C. M. Bingham, A. C. Strikwerda, D. Pilon, D. Shrekenhamer, N. I. Landy, K. Fan, X. Zhang, W. J. Padilla, and R. D. Averitt, "Highly flexible wide angle of incidence terahertz metamaterial absorber: design, fabrication, and characteristics, *Physical Review B*, vol. 78, no. 24, pp. 1031-1034, December 2008.

[82] Osman Ayop, Mohamad Kamal A. Rahim, Noor A. Murad, and Noor A. Samsuri, "Polarization insensitive and wide operating angle metamaterial absorber at X-band,"

IEEE Asia-Pacific Conference on Applied Electromagnetics (APACE2014), Johor Bahru, Malaysia, 8-10 Dec 2014, pp. 245 – 249.

[83] Shobhit K. Patel, Christos Argyropoulos, and Yogeshwar P. Kosta, "Broadband compact microstrip patch antenna design loaded by multiple split ring resonator superstrate and substrate," *Waves in Random and Complex Media*, vol. 27, no. 1, pp. 92-102, June 2016.

[84] Jaypal Baviskar, Afshan Mulla, Amol Baviskar, Dinesh Auti, and Rohit Waghmare, "Performance enhancement of microstrip patch antenna array with incorporation of metamaterial lens," *IEEE Aerospace Conference*, Yellowstone, USA, 5-12 March 2016, pp. 1-10.

[85] Yang Li, Kunzhe Zhang, Lin A. Yang, and Lin Du, "Gain enhancement and wideband RCS reduction of a microstrip antenna using triple-band planar electromagnetic band-gap structure," *Progress In Electromagnetics Research Letters*, vol. 65, pp. 103-108, January 2017.

[86] Yi Zhao, Jun Gao, Xiangyu Cao, Tao Liu, Liming Xu, Xiao Liu, and Lili Cong, "In-band *RCS* reduction of waveguide slot array using metasurface bars," *IEEE Transactions on Antennas and Propagation*, vol. 65, no. 2, pp. 943-947, February 2017.

[87] Wei Li and Jason Valentine, "Metamaterial perfect absorber based hot electron photodetection," *Nano Letters*, vol. 14, no. 6, pp. 3510-3514, May 2014.

[88] Maria D. Astorino, Fabrizio Frezza, and Nicola Tedeschi, "Ultra-thin narrow-band, complementary narrow-band, and dual-band metamaterial absorbers for applications in the THz regime," *Journal of Applied Physics*, vol. 121, no. 6, pp. 1031-10310, January 2017.

[89] Li Yongqian, Su Lei, Xu Xiaolun, Zhang Chenglin, and Wang Binbin, "Energy conversion within infrared plasmonic absorption metamaterials for multi-band resonance," *Optics Communications*, vol. 342, pp. 247-252, May 2015.

[90] Si J. Li, Xiang Y. Cao, Jun Gao, Tao Liu, Yue J. Zheng, and Zhao Zhang, "Analysis and design of three-layer perfect metamaterial-inspired absorber based on double split-serration-rings structure," *IEEE Transactions on Antennas and Propagation*, vol. 63, no. 11, pp. 5155-5160, November 2015.

[91] Joon H. Lim, Yo H. Ryu, Sung S. Kim, "Influence of substrate on broadband microwave absorption of metamaterial absorbers composed of multi-scaled split cut wires," *9th International Congress on Advanced Electromagnetic Materials in Microwaves and Optics*, Oxford, United Kingdom, 7-12 September 2015, pp.145-147.

[92] Jingbo Sun, Lingyun Liu, Guoyan Dong, and Ji Zhou, "An extremely broadband metamaterial absorber based on destructive interference," *Optics Express*, vol. 19, no. 22, pp. 155-162, October 2011.

[93] Jianna Zhang, Guocui Wang, Bo Zhang, Ting He, Yanan He, and Jingling Shen, "Photo-excited broadband tunable terahertz metamaterial absorber," *Optical Materials*, vol. 54, pp. 32-36, April 2016.

[94] Hyung K. Kim, Dongju Lee, and Sungjoon Lim, "Frequency-tunable metamaterial absorber using a varactor-loaded fishnet-like resonator," *Applied Optics***,** vol. 55, no. 15, pp. 4113-4118, 2016.

[95] Jialin Li, Jianjun Jiang, Yun He, Wenhua Xu, Mi Chen, Ling Miao, and Shaowei Bie, "Design of a tunable low-frequency and broadband radar absorber based on active frequency selective surface," *IEEE Antennas and Wireless Propagation Letters*, vol. 15, pp. 774-777, March 2016.

[96] Limei Qi, Chao Li, and Guangyou Fang, "Tunable terahertz metamaterial absorbers using active diodes," *International Journal of Electromagnetics and Applications*, vol. 4, no. 3, pp. 57-60, April 2014.

[97] H. Yuan, Bo Zhu, Junming Zhao, and Yijun Feng, "Metamaterial absorber with active frequency tuning in X-band," *Proceedings of the International Symposium on Antennas & Propagation (ISAP)*, Nanjing, China, 23-25 October 2013, pp.1219-1221.

[98] M. H. B. Ucar, A. Sondas, and Y. E. Erdemli, "Switchable split- ring frequency selective surfaces," *Progress in Electromagnetics Research B*, vol. 6, pp. 65-79, 2008.

[99] Gargi Saha, Chandrakanta Kumar, and Venkataraman V. Srinivasan, "Frequency selective surface with improvised ring-resonator for flexible design," *Progress in Electromagnetics Research C*, vol. 56, pp.137-144, March 2015.

[100] Dhawan Singh and Viranjay M. Srivastava, “Design Implementation of Concentric Loops with Stubs Metamaterial Absorber,” *Wireless Personal Communications*, vol. 104, no. 1, pp 1-20, January 2019.

[101] Xudong Chen, Tomasz M. Grzegorczyk, Bae I. Wu, Joe Pacheco, and Jin A. Kong, “Robust method to retrieve the constitutive effective parameters of metamaterials,” *Physical Review E*, vol. 70, pp. 6081-6087, July 2004.

[102] Claire M. Watts, Xianliang Liu, and Willie J. Padilla, “Metamaterial electromagnetic wave absorbers,” *Advanced Optical Materials*, vol. 24, no. 23, pp. 98-120, June 2012.

[103] Shuowei Dai, Ding Zhao, Qiang Li, and Min Qiu, “Double-sided polarization-independent plasmonic absorber at near-infrared region,” *Optics Express*, vol. 21, no. 11, pp. 3125-33, June 2013.

[104] Wenwen Liu, “The study status and development of metamaterial absorber,” *International Conference on Logistics Engineering, Management and Computer Science (LEMCS 2015)*, Shenyang, China, 29-31 January 2015, pp. 1318-1322.

[105] D. R. Smith, D. C. Vier, Th. Koschny, and C. M. Soukoulis, “Electromagnetic parameter retrieval from inhomogeneous metamaterials,” *Physical Review E*, vol. 71, pp. 6171-61711, March 2005.

[106] Yashwanth R. Padooru, Alexander B. Yakovlev, Chandra S. R. Kaipa, Francisco Medina, and Francisco Mesa, “Circuit modeling of multiband high-impedance surface absorbers in the microwave regime,” *Physical Review B*, vol. 84, pp. 1081-11, July 2011.

[107] Gong Qiaoxia, Liu Xiaomin, Duan Zhiyong, Shi Xiaoqiang, Ma Fengying, and Liang Erjun, “Study on absorbing properties and mechanism of cross-shaped metamaterial absorber,” *Infrared and Laser Engineering*, vol. 42, no. 6, pp. 1528-1532, June 2013.

[108] N. I. Landy, C. M. Bingham, T. Tyler, N. Jokerst, D. R. Smith, and W. J. Padilla, “Design, theory, and measurement of a polarization-insensitive absorber for terahertz imaging,” *Physical Review B*, vol. 79, pp. 1041-1046, March 2009.

[109] Dongying Li, Zsolt Szabo, Xianming Qing, Ping Li, and Zhi Ning Chen, “A high gain antenna with an optimized metamaterial inspired superstrate”, *IEEE Transactions on Antennas and Propagation*, vol. 60, no. 12, pp. 6018-6023, December 2012.

[110] Zsolt Szabo, Gi H. Park, Ravi Hedge, and Ping Li, "A unique extraction of metamaterial parameters based on Kramers-kronig relationship," *IEEE Transactions on Microwave Theory and Techniques*, vol. 58, no. 10, pp. 2046-2653, October 2010.

[111] Claudio G. Parazzoli, Robert B. Greegor, and M. H. Tanielian, "physics of negative refraction and negative index materials," *Springer Berlin Heidelberg*, vol. 98, pp. 261-329, 2007.

[112] Davoud Zarifi, Mohammad Soleimani, and Vahid Nayyeri, "Parameter retrieval of chiral metamaterials based on the causality principle," *International Journal of RF and Microwave Computer-Aided Engineering*, vol. 23, no. 5, pp. 610-618, September 2012.

[113] Saptarshi Ghosh, Somak Bhattacharyya, Devkinandan Chaurasiya, and Kumar V. Srivastava, "An ultrawideband ultrathin metamaterial absorber based on circular split rings," *IEEE Antennas and Wireless Propagation Letters*, vol. 14, no.1, pp. 1172-1175, January 2015.

[114] J. Lee and S. Lim, "Bandwidth-enhanced and polarization-insensitive metamaterial absorber using double resonance," *Electronics Letters*, vol. 47, no. 1, pp. 8- 9, January 2011.

[115] Yahong Liu, Shuai Gu, Chunrong Luo, and Xiaopeng Zhao, "Ultra-thin broadband metamaterial absorber," *Applied Physics A*, vol. 108, no. 1, pp. 19-24, April 2012.

[116] Mohammad R. Soheilifar and Ramazan A. Sadeghzadeh, "Design, fabrication, and characterization of scaled and stacked layers planar metamaterial absorber," *IET Microwaves, Antennas & Propagation*, vol. 9, no. 1, pp. 86–93, August 2014.

[117] Yongzhi Cheng, Helin Yang, Zhengze Cheng, and Nan Wu, "Perfect metamaterial absorber based on a split-ring-cross resonator", *Applied Physics A*, vol. l02, no. 1, pp. 99-103, January 2011.

[118] Xiang J. Gao, Tong Cai, and Li Zhu, "Enhancement of gain and directivity for microstrip antenna using negative permeability metamaterial," *AEU-International Journal of Electronics and Communications*, vol. 70, no. 7, pp. 880-885, July 2016.

[119] Gerd Mrozynski and Matthias Stallein, *Electromagnetic Field Theory: A Collection of Problems*, 2nd Ed., Springer, Germany, 2013.

[120] Jean G. Van Bladel, *Electromagnetic Fields*, 2nd Ed., Wiley-IEEE press, USA, 2007.

[121] Kamil B. Alici, Filiberto Bilotti, Lucio Vegni, and Ekmel Ozbay, "Experimental verification of metamaterial based subwavelength microwave absorbers," *Journal of Applied Physics*. vol. 108, no. 8, pp. 131-136, October 2010.

[122] Osman Ayop, Mohamad Kamal A. Rahim, Noor A. Murad, and Noor A. Samsuri, " Dual band polarization insensitive and wide angle circular ring metamaterial absorber," *8th European Conference on Antennas and Propagation (EuCAP),* The Hague, Netherlands, 6-11 April 2014. pp. 955-957.

[123] Xiaopeng Shen, Yan Yang, Yuanzhang Zang, Jianqiang Gu, Jiaguang Han, Weili Zhang, and Tie J. Cui, "Triple-band terahertz metamaterial absorber: Design, experiment, and physical interpretation," *Applied Physics Letters*, vol. 101, no. 15, pp. 1021-1024, October 2012.

[124] Osman Ayop, Mohamad Kamal A. Rahim, Noor A. Murad, and Noor A. Samsuri, "Dual band polarization insensitive metamaterial absorber in X-band," *19th International Symposium on Antenna and Propagation (ISAP),* Kaohsiung, Taiwan, 2-5 Dec 2014, pp.1-2.

[125] D. J. Kern and D. H. Werne, "A genetic algorithm approach to the design of ultra-thin electromagnetic bandgap absorbers," *Microwave and Optical Technology Letters*, vol. 38, no. 1, pp. 61-64, July 2003.

[126] Saeid Jamilan, Mohammad N. Azarmanesh, and Davoud Zari, "Design and characterization of a dual-band metamaterial absorber based on destructive interferences," *Progress in Electromagnetics Research C*, vol. 47, pp. 95-101, 2014.

[127] Chitra Singh, Kumund R. Jha, Varinder Singh and Ghanshyam Singh, "Cross-polarization reduction of microstrip antenna using microwave absorbers," *International Journal of RF Microwave Computer-Aided Engineering*, vol. 27, no. 5, pp.1-10, January 2017.

[128] Qing L. Zhang, Yu T. Jin, Jia Q. Feng, Xin Lv, and Li M. Si, "Mutual coupling reduction of microstrip antenna array using metamaterial absorber," *IEEE MTT-S International Microwave Workshop Series on Advanced Materials and Processes for RF and THz Applications (IMWS-AMP),* Suzhou, China, 1-3 July 2015, pp.1-3.

[129] Zi X. Zhang and Jun C. Zhang, "RCS reduction for patch antenna based on metamaterial absorber," *Progress in Electromagnetic Research Symposium (PIERS)*, Shanghai, China, 8 - 11 August 2016, pp. 364-368.

[130] Shiv Narayan, Balasubramaniyam Sangeetha, Thattanvalappil V. Sruthi, Vadeyanapur Shambulingappa, and Raveendranath U. Nair, "Design of low observable antenna using active hybrid-element FSS structure for stealth applications," *AEU -International Journal of Electronics and Communications*, vol. 80, pp. 137-143, October 2017.

[131] Wenbo Pan, Cheng Huang, Po Chen, Xiaoliang Ma, Chenggang Hu, and Xiangang Luo, "A low-RCS and high-gain partially reflecting surface antenna," *IEEE Transactions on Antennas and Propagation*, vol. 62, no. 2, pp. 945-949, February 2014.

[132] Jiaming Hao, Lei Zhou, and Min Qiu, "Nearly total absorption of light and heat generation by plasmonic metamaterials," *Physical Review B*, vol. 83, pp. 1071-10712, April 2011.

[133] Zhi Hao Jiang, Seokho Yun, Fatima Toor, Douglas H. Werner, and Theresa S. Mayer, "Conformal dual-band near-perfectly absorbing mid-infrared metamaterial coating" *ACS Nano*, vol. *5*, no. 6, pp. 4641–4647, April 2011.

[134] Kadir Ozden, Okan M. Yucedag, and Hasan Kocer, "Metamaterial-based broadband RF absorber at X-band," *AEU-International Journal of Electronics and Communications*, vol. 70, no. 8, pp. 1062-1070, August 2016.

[135] Yong Ma, Qin Chen, James Grant, Shimul C. Saha, A. Khalid, and David R. S. Cumming, "A terahertz polarization insensitive dual-band metamaterial absorber," *Optics Letters*, vol. 36, no. 6, pp. 945-947, March 2011.

[136] Furkan Dincer, Muharrem Karaaslan, Emin Unal, Kemal Delihacioglu, and Cumali Sabah, "Design of polarization and incident angle insensitive dual-band metamaterial absorber based on isotropic resonator," *Progress in Electromagnetics Research*, vol. 144, pp. 123-132, January 2014.

[137] M. H. Li, H. L. Yang, and X. W. Hou, "Perfect metamaterial absorber with dual bands," *Progress in Electromagnetics Research*, vol. 108, pp. 37-49, September 2010.

[138] Shen X. Peng, Cui T. Jun, and Ye J. Xiang, "Dual band metamaterial absorber in microwave regime," *Acta Physica Sinica*, vol. 61, no. 5, pp. 1011-5, March 2012.

[139] Xiaoming Liu, Chuwen Lan, Bo Li, Qian Zhao, and Ji Zhou, “Dual band metamaterial perfect absorber based on artificial dielectric molecules,” *Scientific Reports*, vol. 6, no. 28906, pp.1-6, July 2016.

[140] Xiaopeng Shen, Tie J. Cui, Junming Zhao, Hui F. Ma, Wei X. Jiang, and Hui Li, “Polarization-independent wide-angle triple-band metamaterial absorber,” *Optics Express*, vol. 19, no. 10, pp. 9401-9407, May 2011.

[141] Alkesh Agrawal, Ashutosh Singh, and Mukul Misra1, “A multiband metamaterial absorber with concentric continuous rings resonator structure,” *International Journal of Advances in Microwave Technology (IJAMT)*, vol. 1, no. 1, pp. 5-9, May 2016.

[142] Dhawan Singh and Viranjay M. Srivastava, “Dual resonances shorted stub circular rings metamaterial absorber,” *AUE-International Journal of Electronics and Communication*, vol. 83, pp. 58-66, January 2018.

[143] Mehdi K. Hedayati, Franz Faupel, and Mady Elbahri, “Review of plasmonic nanocomposite metamaterial absorber,” *Materials*, vol. 7, no. 2, pp. 1221-1248, February 2014.

[144] Parul Dawar, Raghava Nallanthighal, and A. De, “Ultra-wideband, multi-resonance antenna using swastika metamaterial”, *International Journal of Microwave and Optical Technology*, vol. 11, no. 6, pp. 413-420, November 2016.

[145] Anand Kaushik, Jitendra Mohan, and H. Gupta, “Novel metamaterials with their applications to microstrip antenna”, *International Journal of Microwave and Optical Technology*, vol. 11, no. 3, pp. 188-195, May 2016.

[146] Osman Ayop, Mohamad Kamal A. Rahim, and Noor A. Murad, “Polarization-independent metamaterial absorber for single band and multi-band frequency,” Jurnal Teknologi, vol. 77, no. 10, pp. 99-106, July 2015.

[147] Emin Unal, Mehmet Bagmanci, Muharrem Karaslan, Oguzhan Akgol, Huseyin Turan Arat, and Cumali Sabah, “Zinc oxide-tungsten-based pyramids in construction of ultra-broadband metamaterial absorber for solar energy harvesting,” *IET Optoelectronics*, vol. 11, no. 3, pp. 114-120, June 2017.

[148] Jing Mu, Hao Wang, Haiqing Wang, and Yong Huang, “Low-RCS and gain enhancement design of a novel partially reflecting and absorbing surface antenna,”

IEEE Antennas and Wireless Propagation Letters, vol. 16, pp. 1903 - 1906, March 2017.

[149] Sajal Agarwal and Yogendra K. Prajapati, "Analysis of metamaterial-based absorber for thermos-photovoltaic cell applications," *IET Microwaves Antennas & Propagation*, vol. 11, no. 5, pp. 208-212, September 2017.

[150] Yue J. Zheng, Jun Gao, Yu L. Zhou, Xiang Y. Cao, Li M. Xu, Si J. Li, and Huan H. Yan, "Metamaterial-based patch antenna with wideband RCS reduction and gain enhancement using improved loading method," *IET Microwaves, Antennas & Propagation*, vol. 11, no. 9, pp. 1183-1189, July 2017.

[151] Si J. Li, Jun Gao, Xiang Y. Cao, Yi Zhao, Zhao Zhang, and Hong X. Liu, "'Loading metamaterial perfect absorber method for in-band radar cross section reduction based on the surface current distribution of array antennas," *IET Microwaves, Antennas & Propagation*, vol. 9, no. 5, pp. 399-406, April 2015.

[152] Si J. Li, Xiangyu Cao, Tao Liu, Huanhuan Yang, "Double-layer perfect metamaterial absorber and its application for RCS reduction of antenna," *Radio Engineering*, vol. 23, no. 1, pp. 222-228, April 2014.

[153] Alireza Shater and Davoud Zarifi, "Radar cross section reduction of microstrip antenna using dual-band metamaterial absorber", *Applied Computational Electromagnetics Society Journal* (*ACES)*, vol. 32, no.2, pp. 135-140, February 2017.

[154] Tao Liu, Xiangyu Cao, Jun Gao, Qiurong Zheng, Wenqiang Li, and Huanhuan Yang, "RCS reduction of waveguide slot antenna with metamaterial absorber," *IEEE Transactions on Antennas and Propagation*, vol. 61, no. 3, pp. 1479-1484, March 2013.

[155] Hong K. Jang, Jae H. Shin, and Chun G. Kim, "Low RCS patch array antenna with electromagnetic bandgap using a conducting polymer," *International Conference on Electromagnetics in Advanced Applications*," Sydney, Australia, 20-24 September 2010, pp. 140-143.

[156] Zhilong Miao, Cheng Huang, Qin Zhao, Mingbo Pu, Xiaoliang Ma, and Xiangang Luo, "Design of a patch antenna with dual-band radar cross section reduction," *International Conference on Microwave and Millimeter Wave Technology (ICMMT)*, Shenzhen, China, 5-8 May 2012, pp. 1-3.

[157] Hao Zhang, Xiang Y. Cao, Jun Gao, Huan H. Yang, and Qun Yang, "A novel dual-band metamaterial absorber and its application for microstrip antenna," *Progress in Electromagnetics Research Letters*, vol. 44, pp. 35- 41, November 2014.

[158] F. Costa, S. Genovesi, and A. Monorchio, "A frequency selective absorbing ground plane for low-RCS microstrip antenna arrays," *Progress in Electromagnetics Research*, vol. 126, pp. 317-332, March 2012.

[159] M. Zahir Joozdani, M. K. Amirhosseini, and A. Abdolali, "Wideband radar cross-section reduction of patch array antenna with miniaturized hexagonal loop frequency selective surface," *Electronics Letters*, vol. 52, no. 9, pp. 767–768, April 2016.

[160] W. He, R. Jin, and J. Geng, "Low radar cross-section and high performances of microstrip antenna using fractal unipolar compact electromagnetic bandgap ground," *IET Microwaves, Antennas & Propagation*, vol. 1, no. 5, pp. 986-991, October 2007.

[161] Wen Q. Li, Xiang Y. Cao, Jun Gao, Zhao Zhang, and Li L. Cong, "Broadband RCS reduction and gain enhancement microstrip antenna using shared aperture artificial composite material based on quasi-fractal tree," *IET Microwaves, Antennas & Propagation*, vol. 10, no. 4, pp. 370 – 377, March 2016.

[162] Simone Genovesi, Filippo Costa, and Agostino Monorchio, "Low profile array with reduced radar cross section by using frequency selective surfaces", *IEEE Transactions on Antennas and Propagation*, vol. 60, no. 5, pp. 2327– 2335, May 2012.

[163] Himangshu B. Baskey, Abhishek K. Jha, and M. Jaleel Akhtar, "Design of metamaterial based structure for the radar cross section reduction of a microstrip antenna," *IEEE International Microwave and RF Conference (IMaRC)*, Bangalore, India, December 2014, pp. 104-107.

[164] L. L. Cong, X. Y. Cao, W. Q. Li, and Y. Zhao, "A new design method for patch antenna with low RCS and high gain performance," *Progress in Electromagnetics Research Letters*, vol. 59, pp. 77-84, 2016.

[165] Aditi Sharma and Ghanshyam Singh, "Design of single pin shorted three-dielectric-layered substrates rectangular patch microstrip antenna for communication systems," *Progress in Electromagnetics Research Letter*, vol. 2, pp. 157-165, 2008.

[166] C. A. Balanis, *Antenna Theory, Analysis and Design*, 3rd Ed., John Wiley & Sons, USA, 2005.

[167] Aditi Sharma and Ghanshyam Singh, "Rectangular microstirp patch antenna design at THz frequency for short distance wireless communication systems," *Journal of Infrared, Millimeter, and Terahertz Waves*, vol. 30, no.1, pp.1, January 2009.

[168] R. Falguni, Y. P. Kosta, J. Makwana, and A. V. Patel, "Design & implementation of reduced size microstrip patch antenna with metamaterial defected ground plane," *International Conference on Communication and Signal Processing*, Melmaruvathur, India, 3-5 April 2013, pp.186-190.

[169] M. Taouzari, A. Mouhsen, J. E Aoufi, O. E Mrabet, and H. Nasraoui, "Designing and fabrication of microstrip ultra wideband planar antenna for diversity applications," *International Journal of Microwave and Optical Technology*, vol.10, no.6, pp. 421-425, November 2015.

[170] N. Jaglan and S. D. Gupta, "Designing and fabrication of microstrip patch antenna with EBG substrate", *International Journal of Microwave and Optical Technology*, vol.10, no.2, pp. 79- 88, March 2015.

[171] Dhawan Singh and Viranjay M. Srivastava, "Low radar cross section of patch antenna using shorted stubs metamaterial absorber," *International Journal of Microwave and Optical Technology (IJMOT)*, vol. 13, no. 3, pp. 194-202, May 2018.

[172] H. B. Baskey, A. K. Jha, and M. J. Akhtar, "Designing and fabrication of the radar cross-section reduction of a microstrip antenna," *IEEE International Microwave and RF Conference (IMaRC)*, Bangalore, India, 15-17 December 2014, pp. 104-107.

[173] V. A. Libi Mol and C. K. Aanandan, "An ultrathin microwave metamaterial absorber with enhanced bandwidth and angular stability," *Journal of Physics Communications*, vol. 1, no. 1, pp. 1-12, August 2017.

[174] Dhawan Singh and Viranjay M. Srivastava, "A comparative analysis for radar cross section of patch antenna using shorted stubs metamaterial absorber," *Journal of Engineering Science and Technology (JESTEC)*, vol. 13, no. 11, pp. 3532-3546, November 2018.

[175] Dhawan Singh and Viranjay M. Srivastava, "RCS reduction of patch array using shorted stubs metamaterial absorber," *Journal of Communication (JOCM)*, vol. 13, no. 12, pp. 702-711, December 2018.

[176] J. Zheng, S. Fang, Y. Jia, and Y. Liu, "RCS reduction of patch array antenna by complementary split-ring resonators structure," *Progress in Electromagnetics Research C*, vol. 51, pp. 95-101, June 2014.

[177] Jiejun Zhang, Junhong Wang, Meie Chen, and Zhan Zhang, "RCS reduction of patch array antenna by electromagnetic band-gap structure," *IEEE Antennas and Wireless Propagation Letters*, vol. 11, pp.1048-1051, August 2012.

[178] X. Liu, J. Gao, X. Cao, Y. Zhao, W. Li, S. Li, and N. Li, "A high-gain and low-scattering waveguide slot antenna of artificial magnetic conductor octagonal ring arrangement," *Radio Engineering*, vol. 25, no. 1, pp. 46-52, April 2016.

[179] W. Li, S. Yang, J. Zhang, S. Sai, H. Yuan and S. Qu, "The RCS reduction of microstrip antenna design based on multi-band metamaterial absorber," *IEEE MTT-S International Microwave Workshop Series on Advanced Materials and Processes for RF and THz Applications (IMWS-AMP)*, Suzhou, China, 1-3 July 2015, pp. 1-3.

[180] Igor V. Minin and Oleg V. Minin, *Basic Principles of Fresnel Antenna Arrays*, 1st Ed., Springer-Verlag, Berlin, Heidelberg, 2008.

[181] Jin S. Chen and Kin L. Wong, "A single-layer dual-frequency rectangular microstrip patch antenna using a single probe feed," *Microwave and Optical Technology Letters*, vol. 11, no. 2, pp. 83-84, February 1996.

[182] Aditi Sharma, Vivek K. Dwivedi, and Ghanshyam Singh, "THz rectangular patch microstrip antenna design using photonic crystal as substrate," *Progress in Electromagnetic Research Symposium*, Cambridge, USA, 2-6 July 2008, pp.161-165.

[183] Si J. Li, Jun Gao, Xiangyu Cao, Zhao Zhang, and Di Zhang, "Broadband and high-isolation dual-polarized microstrip antenna with low radar cross section," *IEEE Antennas and Wireless Propagation Letters*, vol. 13, pp. 1413-1416, July 2014.

[184] Settapong Malisuwan, Jesada Sivaraks, Navneet Madan, and Nattakit Suriyakrai, "Design of microstrip patch antenna for Ku-band satellite communication

applications," *International Journal of Computer and Communication Engineering*, vol. 3, no. 6, pp. 413-416, November 2014.

[185] M. R. Ahsan, Mohammad T. Islam, M. Habib Ullah, R. W. Aldhaheri, and M. M. Sheikh, "A new design approach for dual-band patch antenna serving Ku/K band satellite communications," *International Journal of Satellite Communications and Networking*, vol. 34, pp. 759-769, August 2015.

[186] Rezaul Azim, Mohammad T. Islam, and Norbahiah Misran, "Dual polarized microstrip patch antenna for ku-band application," *Informacije MIDEM*, vol. 41, no. 2, pp. 114-117, 2011.

[187] Y. Shang, S. Xiao, M. C. Tang, Y. Y. Bai, and B. Wang, "Radar cross-section reduction for a microstrip patch antenna using PIN diodes," *IET Microwaves Antennas & Propagation*, vol. 6, no. 6, pp. 670-679, June 2012.

[188] Yahong Liu and Xiaopeng Zhao, "Perfect absorber metamaterial for designing low-RCS patch antenna," *IEEE Antennas and Wireless Propagation Letters*, vol. 13, pp. 1473 -1476, August 2014.

[189] Wenhui Li, Shen Yang, Jieqiu Zhang, Sui sai, Hangying Yuan and Shaobo Qu, "The RCS reduction of microstrip antenna design based on multi-band metamaterial absorber," *IEEE MTT-S International Microwave Workshop Series on Advanced Materials and Processes for RF and THz Applications (IMWS-AMP)*, Suzhou, China, 1-3 July 2015, pp. 1-3.

[190] Vijaykumar V. Chodavadiya and Shivani S. Aggarwal, "Microstrip patch antenna design for Ku band application," *International Journal of Engineering Research & Technology (IJERT)*, vol. 3, no. 4, pp. 1707- 1710, April 2014.

[191] Chunling Chen, Yongxin Guo, and Hao Wang, "Dual-band circularly polarized microstrip patch antenna for RFID applications," *IEEE International Symposium on Antennas and Propagation & USNC/URSI National Radio Science Meeting*, Vancouver, Canada, 19-24 July 2015, pp.1584-1585.

[192] Mohammad M. Islam, Mohammad T. Islam, and Mohammad R. I. Faruque, "Design of a microstrip antenna on Duroid 5870 substrate material for Ku and K-band

applications," *Technical Gazette (Tehnicki Vjesnik),* vol. 22, no. 1, pp. 71-77, February 2015.

[193] Mukesh K. Khandelwal, Binod K. Kanaujia, Santanu Dwari, Sachin Kumar, and A. K. Gautam, "Analysis and design of dual band compact stacked Microstrip patch antenna with defected ground structure for WLAN/WiMax applications," *AEU - International Journal of Electronics and Communications,* vol. 69, no. 1, pp. 39-47, January 2015.

[194] M. T. Islam, M. H. Ullah, and M. B. I. Reaz, "A low profile dual band slotted patch antenna on dielectric material substrate," *Journal of Applied Global Research,* vol. 6, no. 18, pp. 12-21, 2013.

[195] Y. Sung, "Compact dual-band antenna for 2.4/5.2/5.8 GHz WLAN service for laptop computer applications," *Microwave and Optical Technology Letters*, vol. 57, no. 9, pp. 2207-2213, September 2015.

[196] Douglas H. Werner, Micah D. Gregory, Zhi H. Jiang, Donovan E. Brocker, Clinton P. Scarborough, and Pingjuan L. Werner, "An overview of several recent antenna designs utilizing nature-inspired optimization algorithms," *IEEE Symposium on Computational Intelligence for Communication Systems and Networks (CIComms),* Orlando, USA, 9-12 December 2014, pp. 1-7.

[197] Sunandan Bhunia, "Microstrip patch antenna's limitation and some remedies," *International Journal of Electronics & Communication Technology*, vol. 4, no. 1, pp. 38-39, March 2013.

[198] Kin L. Wong and Kai P. Yang, "Compact dual-frequency microstrip antenna with a pair of bent slots," *Electronics Letters*, vol. 34, no. 3, pp. 225-226, February 1998.

[199] S. Maci and G. Biffi Gentili, "Dual-frequency patch antennas," *IEEE Antennas and Propagation Magazine*, vol. 39, no. 6, pp. 13-19 December 1997.

[200] Dhawan Singh and Viranjay M. Srivastava, "An Analysis of RCS for Dual-Band Slotted Patch antenna with a thin dielectric using Shorted Stubs Metamaterial Absorber," *AUE-International Journal of Electronics and Communication,* vol. 90, pp. 53-62, June 2018.